

Master's thesis

2020

Master's thesis

Vebjørn André Solli

NTNU
Norwegian University of
Science and Technology
Faculty of Engineering
Department of Civil and Environmental Engineering

Vebjørn André Solli

3D-effects in Slope Stability Analysis

Sensitivity of Geometry in 2D and 3D Stability
Programs

June 2020



Norwegian University of
Science and Technology

3D-effects in Slope Stability Analysis

Sensitivity of Geometry in 2D and 3D Stability Programs

Vebjørn André Solli

Civil and Environmental Engineering

Submission date: June 2020

Supervisor: Steinar Nordal, IBM

Co-supervisor: Annette Jahr, Multiconsult

Norwegian University of Science and Technology
Department of Civil and Environmental Engineering

Preface

This master thesis is the assessment basis in the 30 study points course TBA4900 - Geotechnical Engineering, Master Thesis at the Department of Civil and Environmental Engineering, NTNU. The project is part of the Master of Science degree in Civil and Environmental Engineering and was carried out in the spring semester of 2020. The master thesis is a continuation of the prestudy project thesis written in the autumn semester of 2020.

Annette Jahr at Multiconsult in Oslo is behind the project proposal and she has also been the main contact person from Multiconsult. Steinar Nordal have been the main supervisor at NTNU. Arnfinn Emdal at NTNU and Jean-Sébastien L'Heureux at NGI have provided supplementary project input and data. Guidance have been conducted through meetings at NTNU in Trondheim with Steinar Nordal.

Trondheim, 2020-06-10

A handwritten signature in black ink, reading "Vebjørn A. Solli". The signature is written in a cursive style with a clear, legible font.

Vebjørn André Solli

Acknowledgment

I would like to thank Annette Jahr and Multiconsult for suggesting the project. The project has been very interesting and educational. Further, thanks to Steffen Giese for support and providing access to necessary software. In addition, I would like to thank Corneliu Athanasiu for help with finding relevant references.

Especially I want to thank Steinar Nordal for great guidance in the autumn and spring semester. Also thanks to Arnfinn Emdal for initial guidance in the autumn. I have obtained valuable input, which have been very useful in the project completion. Furthermore, I would like to thank Jean-Sébastien L'Heureux at NGI for providing case data for 3D modelling. Lastly, big thanks to family and friends for support and proofreading.

V.A.S.

Summary

This master thesis consisted of a literature study together with 2D and 3D numerical analyses, using both limit equilibrium and finite element programs. Earlier literature was searched for factors that impact the 3D-effects (F_{3D}). The 2D simulations were used to find plane strain solutions and to study applicability of the side shear input in GeoSuite Stability. Moreover, 2D axisymmetric analyses were completed to simulate simple axisymmetric curvatures. Three-dimensional simulations were used to quantify and evaluate potential 3D-effects due to finite slope widths and curvatures.

Significant 3D-effects were uncovered in literature. The importance of 3D analyses was emphasised to avoid overconservative safety factors, and thus save time and costs. By fixing a planar slope to develop a finite width, more than a doubling of safety factors may be obtained for narrow widths. Evaluations of curvature in literature have revealed mostly significant stabilising effects, especially for concave slopes.

The 2D plane strain simulations in this master project illustrated the functionality of the side shear input in GeoSuite Stability. The 3D-effects for a simulated finite width were significant, as found in previous literature. PLAXIS 2D with an axisymmetric model was used to simulate simple convex and concave curvatures. Slightly greater stability was observed for the concave slopes. However, the 3D-effects increased more rapidly for the convex cases when the slope flattened.

3D simulations of a planar slope with fixed width were completed to evaluate potential 3D-effects. Significant effects were found, similar to findings in literature and with GS Stability. Safety factors from PLAXIS 3D gave 3D-effects that ranged from approximately 1.08 for relative width $w = W/H = 6$ to 1.92 for $w = 1$. Safety factors increased more rapidly for decreased width, and greater 3D-effects were obtained for flatter slopes. 3D-effects found in GS Stability with the BEAST method were slightly higher than the PLAXIS 3D findings. Further, the 3D LE program Slide3 with Morgenstern-Price gave lower 3D-effects than PLAXIS 3D. The Slide3 failure mechanisms differ slightly from PLAXIS, which may be caused by LE assumptions or FE overshoot.

The 3D simulations of curved slopes are completed to evaluate the influence of curvature. The slopes are modelled to simulate a ridge (convex) or valley (concave) along a more extensive slope

system. All considered cases gave positive 3D-effects, and concave slopes were more stable than convex. Effects were larger for flatter slopes, greater rotation angle α and lower radius. More prominent, sharper and extensive curvatures provide increased stability. 3D-effects for $\alpha = 180^\circ$ ranged from approximately 1.07 to 1.14, while $\alpha = 90^\circ$ gave values between 1.05 and 1.08.

The Sørkjosen slide from 2015 was evaluated considering potential 3D-effects. Idealised concave curvature was used to estimate the influence by simply revolving the 2D reference profile. The analyses suggested significant curvature effect, with $F_{3D} = 1.20$ for a fully revolved model. In addition to the idealised curvature, a full scale model was constructed using bathymetry, which indicated potential restraining effects.

Literature and three-dimensional finite element simulations have revealed potentially significant 3D-effects. These are dependent and highly sensitive to various geometrical and geotechnical properties. All considered finite width and curved slope cases with undrained behaviour in the present thesis have shown stabilising effects. However, as found in literature on 3D-effects, convex curvature may be less stable than a planar or 2D slope. Moreover, 3D FE analysis may give erroneous results, such as an overshoot of safety factor.

The main objective of this master thesis was to evaluate and quantify the relationship between 2D and 3D slope stability analyses. 3D-effects are potentially significant, but can vary considerably. The impact is dependent on soil properties and degree of restraining effect from boundaries or curvature. Increased stability is obtained if the geometric attribute reduces the sliding mass relatively more than the total shear surface area. Sharper and more prominent curvatures have provided increased positive influence in 3D analysis.

The possibility of simulating 3D-effects in 2D LE software GeoSuite Stability was assessed. Slightly overestimated safety factors were obtained by using the definition of the side shear input as a function of slide width. The side shear factor should therefore be reduced and used with caution. Moreover, no apparent connection between curved slopes and the simulated finite widths in GS Stability is observed.

Sammendrag

Denne masteroppgaven har bestått av et litteraturstudie sammen med numeriske 2D- og 3D-analyser. Numeriske simuleringer er gjennomført med programmer basert på grenselikevekt og elementmetoden. Tidligere litteratur ble gjennomført etter faktorer som påvirker 3D-effekter (F_{3D}). 2D-simuleringene ble brukt til å finne løsninger for plan-tøyning og for å undersøke anvendbarheten til sideskjær-inputen i GeoSuite Stability. Videre ble aksesymmetriske 2D-analyser fullført for å simulere enkle aksesymmetriske kurvaturer. Tredimensjonale simuleringer ble brukt til å kvantifisere og evaluere potensielle 3D-effekter som et resultat av endelige skråningsbredder og kurvaturer.

Betydelige 3D-effekter ble avdekket i litteraturstudiet. Viktigheten av 3D-analyser ble vektlagt for å unngå overkonservative sikkerhetsfaktorer, og dermed spare tid og kostnader. Ved å tvinge en plan skråning til å utvikle en begrenset bredde, kan sikkerhetsfaktoren mer enn en dobles for smale bredder. Evalueringer av kurvatur i litteraturen har avdekket stort sett betydelige stabiliserende effekter, spesielt for konkave skråninger.

2D-simuleringene med plan-tøyning i denne masteroppgaven illustrerte funksjonaliteten til sideskjær-inputen i grenselikvektprogrammet GeoSuite Stability. 3D-effektene for en simulert endelig bredde var som kjent betydelig i litteraturen. Elementmetodeprogrammet PLAXIS 2D med en aksesymmetrisk modell ble brukt til å simulere enkle konvekse og konkave kurvaturer. Litt høyere stabilitet ble observert for de konkave skråningene. Imidlertid økte 3D-effektene raskere for de konvekse tilfellene når skråningshelningen minsket.

3D-simuleringer av en plan skråning med endelig bredde ble fullført for å evaluere potensielle 3D-effekter. Det ble funnet signifikante effekter, som ligner funn gjort i litteraturen og med GS Stability. Sikkerhetsfaktorer fra PLAXIS 3D ga 3D-effekter som varierte fra omtrent 1,08 for relativ bredde $w = W/H = 6$ til 1,92 for $w = 1$. Sikkerhetsfaktorene økte raskere for redusert bredde, og større 3D-effekter ble oppnådd for flatere skråninger. 3D-effekter funnet i GS Stability med BEAST-metoden var litt høyere enn verdiene fra PLAXIS 3D. Videre ga 3D grenselikevektsprogrammet Slide3 med Morgenstern-Price lavere 3D-effekter enn elementmetodeprogrammet PLAXIS 3D. Bruddmekanismene i Slide3 skiller seg litt fra PLAXIS, som kan være forårsaket av grenselikevektsantagelser eller overestimering med elementmetoden.

3D-simuleringene av buede skråninger er fullført for å evaluere påvirkning av kurvatur. Skråningene er modellert for å simulere en rygg (konveks) eller dal (konkav) langs et omfattende skråningssystem. Alle vurderte tilfeller ga positive 3D-effekter, og konkave skråninger var mer stabile enn konvekse. Effektene var større for flatere helninger, større rotasjonsvinkel α og lavere radius. Mer fremtredende, skarpere og omfattende kurvaturer gir økt stabilitet. 3D-effekter for $\alpha = 180^\circ$ varierte fra omtrent 1,07 til 1,14, mens $\alpha = 90^\circ$ ga verdier mellom 1,05 og 1,08.

Skredet i Sørkjosen fra 2015 ble evaluert med tanke på potensielle 3D-effekter. Idealisererte konkave buer ble brukt til å estimere påvirkningen ved å dreie 2D-referanseprofilen. Analysene antydde betydelig krumningseffekt, med $F_{3D} = 1,20$ for en modell med hele profilen dreid. I tillegg til den idealiserte kurvaturen ble en modell i full skala konstruert ved bruk av batymetri før skredet. Denne indikerte mulige effekter som begrenser bruddmekanismen.

Litteraturen og tredimensjonale simuleringer ved bruk av elementmetoden har avdekket potensielt betydelige 3D-effekter. Disse er avhengige og svært følsomme for forskjellige geometriske og geotekniske egenskaper. Alle skråninger analysert i den nåværende oppgaven med endelige bredder og buer med udrenert oppførsel har vist stabiliserende effekter. Imidlertid, som funnet i litteratur om 3D-effekter, kan konveks kurvatur være mindre stabil enn en plan eller 2D-skråning. Dessuten kan 3D elementmetodeanalyser gi feilaktige resultater, for eksempel et overestimert av sikkerhetsfaktoren.

Hovedmålet med denne masteroppgaven var å evaluere og kvantifisere forholdet mellom 2D og 3D skråningsstabilitetsanalyser. 3D-effekter er potensielt signifikante, men kan variere betydelig. Påvirkningen er avhengig av jordegenskaper og grad av begrensende effekter fra grensebetingelser eller krumning. Økt stabilitet oppnås hvis geometriske egenskaper reduserer glide-massen relativt mer enn det totale skjæroverflatearealet. Skarpere og mer fremtredende kurvaturer ga økt positiv innflytelse i 3D-analyser.

Muligheten for å simulere 3D-effekter i 2D-grenselikevektsprogramvaren GeoSuite Stability ble vurdert. Litt overestimerte sikkerhetsfaktorer ble funnet ved å bruke definisjonen av sideskjærinputen som funksjon av skredbredde. Sideskjærfaktoren bør derfor reduseres og brukes med forsiktighet. Dessuten er det ikke observert en åpenbar forbindelse mellom buede skråninger og de simulerte endelige breddene i GS Stability.

Contents

Preface	i
Acknowledgment	ii
Summary	iii
Sammendrag	v
1 Introduction	1
1.1 Background	1
1.2 Objectives	3
1.3 Limitations	4
1.4 Approach	4
1.5 Structure of the Report	4
2 Theory	6
2.1 Soil Model	7
2.1.1 Mohr-Coulomb	7
2.1.2 NGI-ADP	8
2.2 Slope Stability Analysis	9
2.2.1 Slope Stability Definition	9
2.2.2 Limit Equilibrium Method	14
2.2.3 Stability Charts	18
2.2.4 Finite Element Method	19
2.2.5 Finite Difference Method	21
2.2.6 Limit Analysis Method	21
2.3 GeoSuite Stability	22

2.4	Rocscience Slide3	27
2.5	PLAXIS	34
2.5.1	PLAXIS 2D	34
2.5.2	PLAXIS 3D	34
3	Literature Study on 3D-effects	49
3.1	3D-effects	50
3.2	Finite Element Analysis - Fixed Width and Undrained Behaviour	50
3.3	Limit Equilibrium Analysis - Fixed Width and Undrained Behaviour	54
3.4	Upper Bound Limit Analysis - Fixed Width and Undrained Behaviour	58
3.5	Limit Equilibrium Analysis - Translational Slide and Drained Behaviour	61
3.6	Finite Difference Analysis - Curved Geometry and Drained Behaviour	67
3.7	Finite Element Analysis - Curved Geometry and Drained Behaviour	74
3.8	Limit Equilibrium Analysis - Curved Geometry and Drained Behaviour	80
3.9	Summary and Discussion of Literature Study	86
4	Two-dimensional Simulations	90
4.1	Plane Strain Analyses	91
4.1.1	Slope Model	91
4.1.2	PLAXIS 2D	94
4.1.3	GeoSuite Stability	95
4.1.4	Plane Strain Results	96
4.1.5	Discussion	100
4.2	PLAXIS 2D - Axisymmetric Model	103
4.2.1	Slope Model	103
4.2.2	Results	105
4.2.3	Discussion	108
5	Three-dimensional Simulations - Validation and Mesh Sensitivity Analysis	109
5.1	Validation - PLAXIS 3D	110
5.1.1	Example 1 - Drained Analysis with Fixed Width	110
5.1.2	Example 2 - Drained Analysis with Unrestrained Sides for AF and NAF	112
5.1.3	Example 3 - Undrained Analysis with Fixed Widths	114

5.2	Mesh Sensitivity Analysis	121
5.2.1	Mesh Density	122
5.2.2	Mesh Sensitivity for Fixed Width and Curved Geometry	128
5.2.3	Convergence in Safety Analysis	131
6	Three-dimensional Simulations - Planar Slope with Finite Width	132
6.1	3D Modelling of Planar Slope with Finite Width	132
6.1.1	Model Geometry	133
6.1.2	Soil Strength	134
6.1.3	Mesh and Convergence	135
6.1.4	Rocscience Slide3	136
6.2	Results for Planar Slope with Fixed Width	138
6.2.1	PLAXIS 3D - Effect of Fixed Width and Inclination	138
6.2.2	Slide3 - Effect of Fixed Width and Inclination	143
6.2.3	Effect of Fixed Width and Cohesion	146
6.2.4	Comparison of Solutions for Fixed Width	148
6.3	Discussion on Effect of Finite Width	150
7	Three-dimensional Simulations - Slope with Curvature	154
7.1	3D Modelling of Slope with Curvature	155
7.1.1	Model Geometry	155
7.1.2	Soil Strength	158
7.1.3	Mesh and Convergence	159
7.2	Results for Slope with Curvature	160
7.2.1	Convex Curvature	160
7.2.2	Concave Curvature	165
7.2.3	Convex Curvature with 10 m Planar Extension	169
7.2.4	Concave Curvature with 10 m Planar Extension	172
7.2.5	Comparison of Results for Curved Slopes	176
7.2.6	PLAXIS 2D Axisymmetric vs. PLAXIS 3D	179
7.3	Case - Sørkjosen Slide 2015	181
7.3.1	Causal Factors and Conclusion	181

7.3.2	Bathymetry Analysis and Area Description	182
7.3.3	Two-dimensional Stability Analysis	185
7.3.4	Three-dimensional Stability Analysis	189
7.4	Discussion on Effect of Curvature	198
8	Method and Model Limitations	203
8.1	Accuracy and Numerical Limitations	203
8.2	Realistic Conditions	204
8.3	Method Assumptions	205
9	Summary	206
9.1	Summary	206
9.2	Conclusion	209
9.3	Recommendations for Further Work	211
	References	212
A	Model and Parameter Definition	216
A.1	PLAXIS Model and Calculation Definition	216
A.2	PLAXIS 2D/3D Parameters	217
A.3	GeoSuite Stability Parameters	217
A.4	Slide3 Parameters	217
B	PLAXIS 2D Results	218
B.1	Safety Analysis	218
B.2	Failure Mechanism	219
C	GeoSuite Stability Failure Mechanism	222
C.1	Case 1 - $b=1.5$	223
C.2	Case 2 - $b=2$	228
C.3	Case 3 - $b=3$	233
D	PLAXIS 3D Failure Mechanism - Planar Slope with Finite Width	238
D.1	Case 1 - $b=1.5$	238
D.2	Case 2 - $b=2$	240

D.3 Case 3 - b=3	242
E Slide3 Failure Mechanism - Planar Slope with Finite Width	245
E.1 Case 1 - b=1.5	245
E.2 Case 2 - b=2	247
E.3 Case 3 - b=3	249
F PLAXIS 3D Failure Mechanism - Slope with Curvature	252
F1 Convex - b=1.5	252
F2 Convex - b=3	256
F3 Concave - b=1.5	260
F4 Concave - b=3	264
F5 Convex - 10 m extension	268
F6 Concave - 10 m extension	272

List of Figures

2.1	Undrained strength, Tresca criterion	8
2.2	Two-dimensional slope definitions	10
2.3	Some possible slide surfaces in slope stability analysis	10
2.4	Base, toe and slope rotational slides	11
2.5	2D slope geometry	11
2.6	3D planar slope geometry	12
2.7	Convex and concave arches	13
2.8	Slope with a circular slip surface divided into slices	15
2.9	Slice as defined in the Simplified Bishop method	16
2.10	Slice with interslice forces $Z_i + Z_{i+1} = Q$ according to Spencer's procedure	16
2.11	Non-circular slip surface defined by Spencer and a single slice	17
2.12	Stability chart for $\phi = 0$ by Janbu (1954).	19
2.13	Slice with forces and moments used in BEAST.	25
2.14	Column with forces and sliding direction used in Slide3	28
2.15	Slide3 force equilibrium in the horizontal x-y plane	29
2.16	Slide3 horizontal force equilibrium in the x-direction	29
2.17	Slide3 horizontal force equilibrium in the y-direction	29
2.18	Spherical surface available in Slide3	32
2.19	Ellipsoidal surface available in Slide3	32
2.20	Slope geometry modelled in PLAXIS 3D	35
2.21	The 10-node tetrahedral element used by PLAXIS 3D.	41
2.22	Fixed hexagonal cone illustrating MC failure surface with $c = 0$	44

3.1	3D geometry definition	51
3.2	3D-effects vs. H/W for various b and d	52
3.3	Comparison of 3D FE and 2D LE analyses for SF vs. W/H	53
3.4	3D cylindrical slide of width $L = W$ and slope cross-section	55
3.5	3D cylindrical slide with curved ends	55
3.6	3D-effects for various end surface curves	56
3.7	Stability number chart for $w = W/H = 1$	57
3.8	Proposed rotational failure mechanism with curved cylinder shape	59
3.9	Slope with slide width $B = W$ for a torus symmetry plane and plane insert	59
3.10	Critical values of $\frac{\gamma H}{c} = \frac{\gamma H}{S_u}$ for various inclinations and width-height ratios	60
3.11	The 3D slope defined for a rounded translational slide	62
3.12	The 3D slope defined for a idealised translation slide	63
3.13	Comparison of the effects of shear resistance in 3D analysis	64
3.14	Comparison of the effects of shear resistance in 3D analysis using K_τ and K_0	65
3.15	Comparison of the effects of shear resistance in 3D LE analysis with FE and FD	66
3.16	Example of a (a) concave slope (left) and a (b) convex slope (right)	68
3.17	Normalised SF vs. curvature radius R_{av} for concave and convex slopes	69
3.18	Boundary surfaces for a 3D (concave) slope model	70
3.19	Results for a curved slope surface with inclination $b = 1$	71
3.20	Geometry definition for convex (left) and concave (right) arch	72
3.21	Results for curved arches with inclination $b = 2$	73
3.22	3D turning corners with slope inclination $b = 2$	74
3.23	3D-effects for convex turning corner angles of 90° , 135° and 180°	76
3.24	Fully restrained 90° (left) and 135° (right) turning corner shear contours	76
3.25	3D-effects of convex turning corner angles for vertical slope	78
3.26	Fully restrained vertical 90° (left) and 135° (right) turning corner shear contours	78
3.27	Fully restrained vertical 90° concave turning corner shear contours	79
3.28	Convex (left) and concave (right) corner with angle α	80
3.29	Comparison of 3D-effects with different slope corner angles	81
3.30	Convex $\alpha = 90^\circ$ (left) and concave $\alpha = 270^\circ$ (right) corner with failure surface	81
3.31	Convex (left) and concave (right) models with corner angle α	82

3.32	Comparison of plane, convex and concave slopes for various soil strength properties	83
3.33	Failure surfaces with $c' = 10 \text{ kPa}$, $\phi' = 30^\circ$ and $\phi^b = 20^\circ$	84
3.34	Failure surfaces with $c' = 40 \text{ kPa}$, $\phi' = 10^\circ$ and $\phi^b = 5^\circ$	84
3.35	Comparison of safety factors for various soil properties and slope geometry	85
4.1	2D slope geometry	93
4.2	Example of the <i>Very fine</i> mesh selected for the defined model geometries	94
4.3	Comparison of SF obtained in GS Stability for various w -values	97
4.4	A comparison of the SF plots for each inclination	98
4.5	Incremental shear strains obtained in PLAXIS 2D for $b = 1.5$	99
4.6	Failure surface obtained in GS Stability for $b = 1.5$ and no side shear	99
4.7	Convex axisymmetric model in PLAXIS 2D	104
4.8	Concave axisymmetric model in PLAXIS 2D	104
4.9	Comparison of safety factors from the axisymmetric calculations	107
4.10	Plots showing 3D-effects for various convex axisymmetric curvature	107
4.11	Plots showing 3D-effects for various concave axisymmetric curvature	108
5.1	2D geometry for Example 1	111
5.2	Shear mechanism obtained in present study with PLAXIS 3D for Example 1	111
5.3	Geometry with shear contours for Example 2, illustrated by Kelesoglu (2015)	113
5.4	Shear mechanism obtained in present study with PLAXIS 3D for Example 2	113
5.5	Defined 3D geometry, retrieved from (Jostad & Lacasse, 2015)	115
5.6	Results from a safety analysis conducted in PLAXIS 3D on Example 3 with $w = 4$	116
5.7	Results from a safety analysis conducted in PLAXIS 3D on Example 3 with $w = 1$	116
5.8	Shear mechanism for $b = 3$ and $d = 1$, retrieved from (Jostad & Lacasse, 2015)	117
5.9	Half-model shear mechanism obtained in present study for $w = 4$ and $d = 1$	117
5.10	Half-model shear mechanism obtained in present study for $w = 1$ and $d = 1$	118
5.11	Validation of 3D-effects for example 3	120
5.12	3D slope geometry	121
5.13	Comparison of safety analysis for three element distributions	123
5.14	Effect of the model width and mesh coarseness	125
5.15	Effect of model depth with a <i>Very fine</i> mesh	126

5.16	Effect of model depth with a <i>Very fine</i> mesh with coarseness factor 0.75	126
5.17	Effect of the model depth and volume for a different coarseness factors	128
5.18	Mesh options $Vfx0.50 - 1.0$ and $Vfx0.25 - 0.50$ for $w = 1$	129
5.19	Safety analysis for $w = 1$ with meshes $Vfx0.50 - 1.0$ and $Vfx0.25 - 0.50$	129
5.20	Mesh options $Vfx0.50 - 1.0$ and $Vfx0.25 - 0.50$ for $r_u = 1$	130
5.21	Safety analysis for convex slope with meshes $Vfx0.50 - 1.0$ and $Vfx0.25 - 0.50$. .	131
6.1	3D geometry of finite width planar slope	133
6.2	Planar slope connectivity plot from PLAXIS 3D	136
6.3	Safety factors obtained using PLAXIS 3D with fixed widths	139
6.4	3D-effects for the three cases with fixed widths	140
6.5	Half-model plot of incremental displacements for $w = 1$ and $b = 1.5$	141
6.6	Half-model plot of incremental displacements for $w = 6$ and $b = 1.5$	141
6.7	Half-model plot of incremental displacements for $w = 1$ and $b = 3$	142
6.8	Half-model plot of incremental displacements for $w = 6$ and $b = 3$	142
6.9	Safety factor obtained by the four LE-methods available in Slide3	143
6.10	3D-effects obtained in Slide3 for varying width-height ratio w	144
6.11	Slip surface with Slide3 Morgenstern-Price for $b = 1.5$ and $w = 1$	145
6.12	Slip surface with Slide3 Morgenstern-Price for $b = 1.5$ and $w = 6$	145
6.13	Slip surface with Slide3 Morgenstern-Price for $b = 3$ and $w = 1$	146
6.14	Slip surface with Slide3 Morgenstern-Price for $b = 3$ and $w = 6$	146
6.15	3D-effects F_{3D} for strength profiles S_u^1 , S_u^2 and S_u^3	147
6.16	Comparison of 3D-effects for varying w and inclination $b = 1.5$	148
6.17	Comparison of 3D-effects for varying w and inclination $b = 2$	149
6.18	Comparison of 3D-effects for varying w and inclination $b = 3$	149
7.1	Top view of convex (left) and concave (right) curvature	156
7.2	PLAXIS 3D models of a convex and a concave slope with $\alpha = 90^\circ$	157
7.3	PLAXIS 3D models of a convex and a concave slope with $\alpha = 180^\circ$	157
7.4	3D-effects for convex curvature	161
7.5	Incremental displacements for $b = 1.5$ and $\alpha = 90^\circ$ with $r_u = 1$ and $r_u = 6$	162
7.6	Incremental displacements for $b = 1.5$ and $\alpha = 180^\circ$ with $r_u = 1$ and $r_u = 6$	163

7.7	Incremental displacements for $b = 3$ and $\alpha = 90^\circ$ with $r_u = 1$ and $r_u = 6$	164
7.8	Incremental displacements for $b = 3$ and $\alpha = 180^\circ$ with $r_u = 1$ and $r_u = 6$	164
7.9	3D-effects for concave curvature	166
7.10	Incremental displacements for $b = 1.5$ and $\alpha = 90^\circ$ with $r_l = 1$ and $r_l = 6$	167
7.11	Incremental displacements for $b = 1.5$ and $\alpha = 180^\circ$ with $r_l = 1$ and $r_l = 6$	168
7.12	Incremental displacements for $b = 3$ and $\alpha = 90^\circ$ with $r_l = 1$ and $r_l = 6$	168
7.13	Incremental displacements for $b = 3$ and $\alpha = 180^\circ$ with $r_l = 1$ and $r_l = 6$	169
7.14	3D-effects for convex curvature with planar extension	170
7.15	Incremental displacements for 10 <i>m</i> ext., $b = 1.5$, $\alpha = 90^\circ$, $r_u = 1$ and $r_u = 6$	172
7.16	Incremental displacements for 10 <i>m</i> ext., $b = 1.5$, $\alpha = 180^\circ$, $r_u = 1$ and $r_u = 6$	172
7.17	3D-effects for concave curvature with planar extension	173
7.18	Incremental displacements for 10 <i>m</i> ext., $b = 1.5$, $\alpha = 90^\circ$, $r_l = 1$ and $r_l = 6$	175
7.19	Incremental displacements for 10 <i>m</i> ext., $b = 1.5$, $\alpha = 180^\circ$, $r_l = 1$ and $r_l = 6$	175
7.20	3D-effects for curvature with inclination $b = 1.5$	176
7.21	3D-effects for curvature with inclination $b = 3$	177
7.22	3D-effects for all curved slopes without planar extension	178
7.23	3D-effects for all curved slopes with planar extension	179
7.24	Curvature effects for PLAXIS 2D Axisymmetric and PLAXIS 3D, where $b = 1.5$	180
7.25	Curvature effects for PLAXIS 2D Axisymmetric and PLAXIS 3D, where $b = 3$	180
7.26	Overview of Sørkjosen and slide area	181
7.27	Bathymetry before the slide	182
7.28	Illustration of slide stages, where 1 is the initial slide	183
7.29	Pictures of the breakwater construction stages over the years	184
7.30	Considered profiles through the initial slide	186
7.31	Profile 31 showing the parking extent in 1994, 2006 and 2015	187
7.32	Failure mechanism obtained for case 1 in PLAXIS 2D	187
7.33	Approximated replica of profile 31	188
7.34	Incremental shear strains for profile 31	189
7.35	Proposed approximate radius and curvature angle for an idealised model	190
7.36	Fully revolved model of profile 31	191
7.37	Incremental displacements for the fully revolved model of profile 31	191

7.38	3D model of profile 31 where fillings from 2006 and 2014 are not revolved	192
7.39	Incremental displacements of revolved profile 31 with extruded fillings	193
7.40	Incremental displacements of the profile 31 cross-section in the 3D-model	193
7.41	3D model of a simplified breakwater and a realistic seabed	194
7.42	Small model showing the assumed contours of the three clays	195
7.43	Illustration of the sand spot developed in the safety analysis	196
7.44	Incremental displacements at collapse with three defined clays	197
7.45	Failure mechanism at the beginning of the safety analysis	197
9.1	Selected plots illustrating potential 3D-effects for finite and curved slopes	208
A.1	Phases run in PLAXIS 2D to obtain failure mechanism and SF	216
A.2	Phases run in PLAXIS 3D to obtain failure mechanism and SF for a finite slope . . .	216
A.3	Phases run in PLAXIS 3D to obtain failure mechanism and SF for a curved slope . .	217
B.1	Result from safety analysis conducted in PLAXIS 2D	218
D.1	Failure mechanism from PLAXIS 3D for a finite slope where $b = 1.5$ and $w = 1$. . .	238
D.2	Failure mechanism from PLAXIS 3D for a finite slope where $b = 1.5$ and $w = 2$. . .	239
D.3	Failure mechanism from PLAXIS 3D for a finite slope where $b = 1.5$ and $w = 4$. . .	239
D.4	Failure mechanism from PLAXIS 3D for a finite slope where $b = 1.5$ and $w = 6$. . .	240
D.5	Failure mechanism from PLAXIS 3D for a finite slope where $b = 2$ and $w = 1$	240
D.6	Failure mechanism from PLAXIS 3D for a finite slope where $b = 2$ and $w = 2$	241
D.7	Failure mechanism from PLAXIS 3D for a finite slope where $b = 2$ and $w = 4$	241
D.8	Failure mechanism from PLAXIS 3D for a finite slope where $b = 2$ and $w = 6$	242
D.9	Failure mechanism from PLAXIS 3D for a finite slope where $b = 3$ and $w = 1$	242
D.10	Failure mechanism from PLAXIS 3D for a finite slope where $b = 3$ and $w = 2$	243
D.11	Failure mechanism from PLAXIS 3D for a finite slope where $b = 3$ and $w = 4$	243
D.12	Failure mechanism from PLAXIS 3D for a finite slope where $b = 3$ and $w = 6$	244
E.1	Slip surface from Slide3 for a fixed width planar slope where $b = 1.5$ and $w = 1$. . .	245
E.2	Slip surface from Slide3 for a fixed width planar slope where $b = 1.5$ and $w = 2$. . .	246
E.3	Slip surface from Slide3 for a fixed width planar slope where $b = 1.5$ and $w = 4$. . .	246
E.4	Slip surface from Slide3 for a fixed width planar slope where $b = 1.5$ and $w = 6$. . .	247

E.5	Slip surface from Slide3 for a fixed width planar slope where $b = 2$ and $w = 1$	247
E.6	Slip surface from Slide3 for a fixed width planar slope where $b = 2$ and $w = 2$	248
E.7	Slip surface from Slide3 for a fixed width planar slope where $b = 2$ and $w = 4$	248
E.8	Slip surface from Slide3 for a fixed width planar slope where $b = 2$ and $w = 6$	249
E.9	Slip surface from Slide3 for a fixed width planar slope where $b = 3$ and $w = 1$	249
E.10	Slip surface from Slide3 for a fixed width planar slope where $b = 3$ and $w = 2$	250
E.11	Slip surface from Slide3 for a fixed width planar slope where $b = 3$ and $w = 4$	250
E.12	Slip surface from Slide3 for a fixed width planar slope where $b = 3$ and $w = 6$	251
F.1	Failure mechanism for a convex slope with $b = 1.5$, $\alpha = 90^\circ$ and $r_u = 1$	252
F.2	Failure mechanism for a convex slope with $b = 1.5$, $\alpha = 90^\circ$ and $r_u = 2$	253
F.3	Failure mechanism for a convex slope with $b = 1.5$, $\alpha = 90^\circ$ and $r_u = 4$	253
F.4	Failure mechanism for a convex slope with $b = 1.5$, $\alpha = 90^\circ$ and $r_u = 6$	254
F.5	Failure mechanism for a convex slope with $b = 1.5$, $\alpha = 180^\circ$ and $r_u = 1$	254
F.6	Failure mechanism for a convex slope with $b = 1.5$, $\alpha = 180^\circ$ and $r_u = 2$	255
F.7	Failure mechanism for a convex slope with $b = 1.5$, $\alpha = 180^\circ$ and $r_u = 4$	255
F.8	Failure mechanism for a convex slope with $b = 1.5$, $\alpha = 180^\circ$ and $r_u = 6$	256
F.9	Failure mechanism for a convex slope with $b = 3$, $\alpha = 90^\circ$ and $r_u = 1$	256
F.10	Failure mechanism for a convex slope with $b = 3$, $\alpha = 90^\circ$ and $r_u = 2$	257
F.11	Failure mechanism for a convex slope with $b = 3$, $\alpha = 90^\circ$ and $r_u = 4$	257
F.12	Failure mechanism for a convex slope with $b = 3$, $\alpha = 90^\circ$ and $r_u = 6$	258
F.13	Failure mechanism for a convex slope with $b = 3$, $\alpha = 180^\circ$ and $r_u = 1$	258
F.14	Failure mechanism for a convex slope with $b = 3$, $\alpha = 180^\circ$ and $r_u = 2$	259
F.15	Failure mechanism for a convex slope with $b = 3$, $\alpha = 180^\circ$ and $r_u = 4$	259
F.16	Failure mechanism for a convex slope with $b = 3$, $\alpha = 180^\circ$ and $r_u = 6$	260
F.17	Failure mechanism for a concave slope with $b = 1.5$, $\alpha = 90^\circ$ and $r_l = 1$	260
F.18	Failure mechanism for a concave slope with $b = 1.5$, $\alpha = 90^\circ$ and $r_l = 2$	261
F.19	Failure mechanism for a concave slope with $b = 1.5$, $\alpha = 90^\circ$ and $r_l = 4$	261
F.20	Failure mechanism for a concave slope with $b = 1.5$, $\alpha = 90^\circ$ and $r_l = 6$	262
F.21	Failure mechanism for a concave slope with $b = 1.5$, $\alpha = 180^\circ$ and $r_l = 1$	262
F.22	Failure mechanism for a concave slope with $b = 1.5$, $\alpha = 180^\circ$ and $r_l = 2$	263
F.23	Failure mechanism for a concave slope with $b = 1.5$, $\alpha = 180^\circ$ and $r_l = 4$	263

E24	Failure mechanism for a concave slope with $b = 1.5$, $\alpha = 180^\circ$ and $r_l = 6$	264
E25	Failure mechanism for a concave slope with $b = 3$, $\alpha = 90^\circ$ and $r_l = 1$	264
E26	Failure mechanism for a concave slope with $b = 3$, $\alpha = 90^\circ$ and $r_l = 2$	265
E27	Failure mechanism for a concave slope with $b = 3$, $\alpha = 90^\circ$ and $r_l = 4$	265
E28	Failure mechanism for a concave slope with $b = 3$, $\alpha = 90^\circ$ and $r_l = 6$	266
E29	Failure mechanism for a concave slope with $b = 3$, $\alpha = 180^\circ$ and $r_l = 1$	266
E30	Failure mechanism for a concave slope with $b = 3$, $\alpha = 180^\circ$ and $r_l = 2$	267
E31	Failure mechanism for a concave slope with $b = 3$, $\alpha = 180^\circ$ and $r_l = 4$	267
E32	Failure mechanism for a concave slope with $b = 3$, $\alpha = 180^\circ$ and $r_l = 6$	268
E33	Failure mechanism for an extended convex slope with $\alpha = 90^\circ$ and $r_u = 1$	268
E34	Failure mechanism for an extended convex slope with $\alpha = 90^\circ$ and $r_u = 2$	269
E35	Failure mechanism for an extended convex slope with $\alpha = 90^\circ$ and $r_u = 4$	269
E36	Failure mechanism for an extended convex slope with $\alpha = 90^\circ$ and $r_u = 6$	270
E37	Failure mechanism for an extended convex slope with $\alpha = 180^\circ$ and $r_u = 1$	270
E38	Failure mechanism for an extended convex slope with $\alpha = 180^\circ$ and $r_u = 2$	271
E39	Failure mechanism for an extended convex slope with $\alpha = 180^\circ$ and $r_u = 4$	271
E40	Failure mechanism for an extended convex slope with $\alpha = 180^\circ$ and $r_u = 6$	272
E41	Failure mechanism for an extended concave slope with $\alpha = 90^\circ$ and $r_l = 1$	272
E42	Failure mechanism for an extended concave slope with $\alpha = 90^\circ$ and $r_l = 2$	273
E43	Failure mechanism for an extended concave slope with $\alpha = 90^\circ$ and $r_l = 4$	273
E44	Failure mechanism for an extended concave slope with $\alpha = 90^\circ$ and $r_l = 6$	274
E45	Failure mechanism for an extended concave slope with $\alpha = 180^\circ$ and $r_l = 1$	274
E46	Failure mechanism for an extended concave slope with $\alpha = 180^\circ$ and $r_l = 2$	275
E47	Failure mechanism for an extended concave slope with $\alpha = 180^\circ$ and $r_l = 4$	275
E48	Failure mechanism for an extended concave slope with $\alpha = 180^\circ$ and $r_l = 6$	276

List of Tables

3.1	Material properties in (Y. Zhang, Chen, Zheng, Li, & Zhuang, 2013)	70
3.2	Safety factors for convex turning corners with inclination $b = 2$	75
3.3	Safety factors for convex turning corners with slope inclination $b = 0$	77
3.4	Safety factors for concave turning corners with slope inclination $b = 0$	79
4.1	Defined geometries for a simple 2D slope	93
4.2	Calculated side shear factor input for the defined width-height ratios	95
4.3	Safety factor (SF) for all cases considered in the project 2D analyses	97
4.4	Safety factors for different r_u using axisymmetric model	105
4.5	Safety factors for different r_l using axisymmetric model	106
5.1	Relevant soil parameters retrieved from Example 1 in (Xing, 1988)	110
5.2	Comparison of safety factors and methods for Example 1	112
5.3	Relevant soil parameters for Example 2	112
5.4	Comparison of safety factors and methods for Example 2	114
5.5	Relevant soil parameters for Example 3, retrieved from (Jostad & Lacasse, 2015).	114
5.6	Comparison with Jostad and Lacasse (2015) for $b = 2$ and $\frac{S_u}{\gamma H} = 0.20$	118
5.7	Defined geometrical attributes for a simple 3D slope	122
5.8	Evaluation of mesh and model width dependency	124
5.9	Evaluation of mesh and depth dependency	125
5.10	Evaluation of volume and depth dependency	127
6.1	Defined geometrical properties for a simple 3D slope	134
6.2	Safety factor (SF) for all cases with fixed width and shear strength S_u^1	138

6.3	Safety factor (SF) for all cases using Slide3	143
6.4	Safety factors for undrained strength profiles S_u^1 , S_u^2 and S_u^3	147
7.1	Defined geometrical properties for curved 3D slope	156
7.2	Safety factors for convex slopes with $\alpha = 90^\circ$, $\alpha = 180^\circ$, $b = 1.5$ and $b = 3$	161
7.3	Safety factors for a concave slope with $\alpha = 90^\circ$, $\alpha = 180^\circ$, $b = 1.5$ and $b = 3$	165
7.4	Safety factors for a convex extended slope with $\alpha = 90^\circ$, $\alpha = 180^\circ$ and $b = 1.5$	170
7.5	Safety factors a concave extended slope with $\alpha = 90^\circ$, $\alpha = 180^\circ$ and $b = 1.5$	173
7.6	Relevant soil parameters for materials with drained behaviour	185
7.7	Relevant soil parameters for clay	186
A.1	PLAXIS model definitions	216
A.2	Relevant soil parameters in the Mohr-Coulomb model with <i>Undrained B</i>	217
A.3	Relevant soil parameters for undrained analysis in GS Stability	217
A.4	Relevant soil parameters for undrained analysis in Slide3	217

Notations

Latin Symbols

A Area

b Slope inclination

c Cohesion

D Depth below slope toe to slip surface base

E Young's modulus

G Shear modulus

H Slope height

K_0 At-rest earth pressure coefficient

K_A Active earth pressure coefficient

R Radius

S_u Undrained shear strength

W Slope width (or weight of slide mass/slice, specified where present)

u Pore pressure (or displacement, specified where present)

N_0 Stability number

Greek Symbols

α Rotation angle of curved slope surface (or slice base angle, specified where present)

α_{SS} Side shear factor

β Slope angle ($\arctan(1/b)$)

γ Material unit weight (or shear strain, specified where present)

ϕ Friction angle

ϕ^b Unsaturated shear strength angle

ψ Dilatancy angle

σ Total stress

σ' Effective stress

ϵ Strain

ν Poisson's ratio

τ Shear stress

Abbreviations

2D Two-dimensional

3D Three-dimensional

AF Associated Flow

CAD Computer-Aided Design

DOF Degree of Freedom

DSS Direct Simple Shear

FDM Finite Difference Method

FEM Finite Element Method

GLE General Limit Equilibrium

GSS GeoSuite Stability

LAM Limit Analysis Method

LEM Limit Equilibrium Method

MC Mohr-Coulomb

NAF Non-Associated Flow

SAO Surface Altering Optimisation

SF Safety Factor

SRM Strength Reduction Method

Chapter 1

Introduction

1.1 Background

Slope stability analysis is an important area in geotechnical engineering. Traditionally, two-dimensional limit equilibrium methods (LEM) have been the basis for the calculations. As computational power has developed, so have the methods of analysis. More advanced computer software is available, which for instance uses limit equilibrium methods or the finite element method (FEM). Two of the most commonly used 2D programs by geotechnical consultants in Norway is GeoSuite Stability and PLAXIS 2D. GeoSuite Stability is based on LE considerations, and PLAXIS 2D is based on the FE method.

Two-dimensional programs are suitable for simple slope stability problems. However, these assume an infinitely wide slope. This assumption is often unrealistic, since natural topography and slopes are three-dimensional systems. Slopes have a three-dimensional failure mechanism, which may require different assumptions compared to a 2D plane strain model. The ratio between a 3D and 2D slope failure property, such as safety factor (SF), is often called 3D-effect.

Literature studies have been carried out to assess the 3D-effects for different geometries and conditions. Significant effects are observed for certain slopes, with the 3D SF being higher than the 2D SF. The consequence is an overconservative safety factor from 2D-analyses, which may be costly. In addition, back-calculation of the slide may result in overestimated strength properties.

A three-dimensional problem may be solved with a 3D program, which can be based on various

methods, such as LEM or FEM. One of the most popular three-dimensional finite element programs is PLAXIS 3D, which can be used to acquire an accurate representation of reality. However, the analyses consume a lot of time and are costly, especially for complex problems. Moreover, numerical issues may occur. Therefore, an evaluation of the three-dimensionality of a slope stability problem may be required.

Problem Formulation

Slope stability analyses completed in two-dimensional programs may underestimate the safety factor. Studies have shown 3D-effects for several slope geometries and soil conditions, see the literature survey below and chapter 3. However, a clear connection between 2D and 3D programs for practical use is hard to obtain. An accurate estimate of safety factor using two-dimensional software can save considerable time and costs. In addition, a realistic simulation will minimise the problem of overestimated shear strength in back-analysis of slope failure.

A comparison between the realistic shear surfaces in PLAXIS software and the simplified plane strain program GeoSuite Stability may be used as a tool to optimise slope stability analysis. GeoSuite Stability has an optional input for additional side shear forces, which is dependent of slide width. A connection may exist to simulate 3D-effects in 2D software.

Topography and soil properties may create complex slope systems. A sensitivity study of different geometries and curvatures in slopes can be useful. This may reveal a relation between 2D and 3D calculations with LEM and FEM, which can potentially be used by geotechnical engineers. It may become easier to evaluate stability problems and to choose a suitable analysis method, if factors that influence 3D-effects are recognised and understood.

Literature Survey

Several studies in earlier literature have been completed to evaluate 3D-effects. Some have assessed simple planar slopes with finite width to assess the difference between 2D and 3D analyses. Others have studied slopes with varying material properties and three-dimensional curvature, both convex and concave.

Jostad and Lacasse (2015) and Griffiths and Marquez (2007) studied simple undrained slope stability cases by 2D LE and 3D FE analyses in order to quantify the 3D-effects. They established

a trend between the width-height ratio W/H and the safety factor.

Gens, Hutchinson, and Cavounidis (1988) and Michalowski and Drescher (2009) obtained 3D stability charts for undrained conditions using LE and limit analysis (LA) method, respectively. The charts were dependent on attributes such as slide width, inclination and depth.

Stark and Eid (1998), Arellano and Stark (2000) and Akhtar and Stark (2017) studied how 3D-effects could be implemented in practice. They tested how earth pressure coefficients K_0 and K_A could be used in 3D methods to create the side shear resistance needed to simulate 3D-effects.

Kelesoglu (2015), Y. Zhang et al. (2013), Nian, Huang, Wan, and Chen (2012) and L. L. Zhang, Fredlund, Fredlund, Lu, and Wilson (2015) and Chaudhary, Domingos, Gitirana, Fredlund, and Lu (2016) studied curvature effect on slope stability for complex geometries. Several 3D geometries were analysed, such as concave and convex curvatures, along with various soil properties.

What Remains to be Done?

The existence of 3D-effects are established in the literature, with varying magnitude depending on soil and geometry properties. A wide range of cases remains to be evaluated. This thesis will focus on simple planar slopes with finite widths to quantify potential effects. Moreover, to assess the possibility of using the side shear input in GS Stability to simulate 3D-effects. Furthermore, the impact of curvature and its restraining effect remains to be studied. 3D simulations are used to quantify 3D-effects and the corresponding failure mechanisms.

1.2 Objectives

The main objective of this master thesis is to evaluate and quantify the relationship between 2D and 3D slope stability analyses. By this, explore the possibility of simulating 3D-effects in 2D LE software GeoSuite Stability. Moreover, study how three-dimensional curvature and boundary conditions affect the slope stability. The project research questions are defined as follows:

1. What is the magnitude of 3D-effects for different slopes and curvatures in stability analysis?
2. How do geometric slope properties influence the 3D-effects and the failure mechanism?
3. How can the side shear input in GeoSuite Stability be used to simulate the 3D slope stability problem in practice?

1.3 Limitations

Study limitations are related to the choice of simple and idealised slope cases. A homogeneous soil with undrained shear strength profile is selected. Drained conditions are not included, which may influence 3D-effects differently. Furthermore, only one slope height is considered. The effects on the safety factor may vary for different heights in undrained analysis. In addition, only rotational slides with toe failure are analysed. Other rotational slip surfaces and larger translational slides may be relevant in the assessment of 3D-effects.

1.4 Approach

Relevant literature on 3D-effects was found by help of supervisors and by the search engine Google Scholar. Several articles and other helpful literature were provided by Steinar Nordal from previous research of 3D-effects. Remaining articles were found by searching relevant keywords in Google Scholar. The literature extent was narrowed by finding project relevant sources. Each source was evaluated for trustworthiness by checking author, publisher/journal and reliability of content. Most studies were found to be objective. The content deemed relevant in the literature selection was summarised.

Calculation programs GeoSuite Stability and PLAXIS 2D were used to conduct two-dimensional simulations. PLAXIS 3D and Slide3 were used to analyse three-dimensional stability problems. Programs were learned by reading the software manuals and testing simple slope stability calculations. Software licenses were provided through Multiconsult and NTNU.

Models were defined for use in the calculation programs. Simplicity was emphasised when creating the soil and geometrical model. Consequently, it becomes easier to reproduce the analyses and accurately compare methods. The obtained results were compared to earlier studies in literature for validation and to establish a broader knowledge platform on 3D-effects.

1.5 Structure of the Report

The rest of the report is structured as follows. In chapter 2, a fundamental introduction to relevant theory in slope stability analysis is provided. The chapter includes some soil model theory, slope stability methods and a brief description of the calculation programs. In chapter 3, a lit-

erature study on 3D-effects is completed, including a summary and discussion of findings. The two-dimensional numerical simulations conducted in this project are presented in chapter 4, for both plane strain and axisymmetric models. Findings and limitations of the 2D analyses are discussed in the end of the chapter.

A series of three-dimensional simulations are completed in this thesis, and are divided and described in several chapters. A validation and mesh sensitivity analysis is provided in chapter 5. In chapter 6, 3D simulations of a planar slope model with fixed width are provided. Three-dimensional simulations of slopes with curvature are presented in chapter 7, together with a real 3D case. The simulation chapters include method of analysis, results and discussion of findings and limitations. In chapter 8, method and model limitations are briefly discussed. The project findings are summarised in chapter 9. Furthermore, a conclusion and recommendations for further work are established.

Chapter 2

Theory - Slope Stability Analysis

Slope stability is one of the major disciplines within geotechnical engineering. Several stability methods have developed throughout the years since early 1900s. Different problems may require different techniques. For any geotechnical issue there are factors influencing the results in slope stability analyses. Such factors may be choice of soil model, stability analysis method and type of software.

In the following subsections a general description of soil models and different slope stability methods is presented. The Mohr-Coulomb (MC) material model and undrained analysis are mainly used in the present study. However, the NGI-ADP is briefly presented due to its use in the case study. Furthermore, both Limit Equilibrium Method (LEM) and Finite Element Method (FEM) are utilised to analyse slope stability. Moreover, certain literature studies have applied other slope definitions and stability methods. A lot of the following theory is formed during the prestudy project thesis (Solli, 2019) and is therefore directly transferred to save time.

Analysis programs in the present study are based on LE and FE procedures defined for both two- and three-dimensional space. GeoSuite (GS) Stability is a program frequently used by Norwegian consultant companies and is the 2D LEM tool for this thesis. PLAXIS delivers some of the most frequently used FEM programs in geotechnical engineering. PLAXIS 2D was the main FEM tool for the project thesis, while PLAXIS 3D is the main calculation tool for the present master thesis. To supplement the 3D FE analyses, some slopes are studied using the 3D limit equilibrium software Slide3.

2.1 Soil Model

How the soil behaves under various conditions depends on the soil model and properties. Different types of analysis require different emphasis on soil parameters. For example, a settlement evaluation from load on a horizontal surface needs accurate values of stiffness parameters, such as Young's Modulus E . A safety factor analysis of slope stability evaluates the shear strength along a failure surface. Therefore, the strength parameters are of focus. Moreover, different soils may need different material models and type of analysis. For example, sand is often a drained or long term problem, while clay is often of the undrained or short term type.

2.1.1 Mohr-Coulomb

The Mohr-Coulomb (MC) soil model available in PLAXIS is a simple model that simulates linear elastic-perfectly plastic behaviour. The elastic part is based on Hooke's law on isotropic elasticity. The Mohr-Coulomb failure criterion is the basis of the perfectly plastic part, which leads to irreversible strains. A yield function is created as the failure criterion, and is dependent on effective stresses (σ'), cohesion (c) and friction angle (ϕ). (Brinkgreve, Kumarswamy, Swolfs, Zampich, & Ragi Manoj, 2019)

The MC-model in PLAXIS allows analysis of different soil behaviour by the calculation functions *Drained*, *Undrained A*, *Undrained B* and *Undrained C*. Both *Drained* and *Undrained A* utilise the effective strength parameters c' and ϕ' , and an effective stress analysis is conducted. *Undrained A* requires zero volumetric strain during loading. The effective strength parameters are used to model the undrained shear strength in *Undrained A*. However, it might deviate from real S_u . *Undrained B* combines undrained shear strength with effective stress stiffness, where excess pore pressures can be calculated. *Undrained C* is based on total stresses and excess pore pressures are not calculated. (Brinkgreve et al., 2019)

When using drainage type *Undrained B* or *Undrained C* in PLAXIS, the undrained shear strength is a direct input. The friction angle is defined as $\phi = 0$ and cohesion is $c = S_u$. These assumptions reduce the Mohr-Coulomb failure criterion to the Tresca criterion (Brinkgreve et al., 2019). The PLAXIS input allows for an inclination of S_u with depth, which is directly controlled by the user. The undrained shear strength profile is defined from a user decided reference elevation y in 2D or z in 3D. Consequently, the S_u is constant in the horizontal direction for each layer for this

model, unless the strength profile is rotated using a defined program command. The theoretical basis of Mohr-Coulomb in PLAXIS is further elaborated in subsection 2.5.2.

The parameters that influence the plasticity in the elastoplastic MC model, are cohesion c , friction angle ϕ and dilatancy angle ψ . For undrained analysis, the friction angle is defined as zero, and the cohesion becomes the undrained shear strength $c = S_u$, as illustrated in Figure 2.1. With $\phi = 0$ the failure criterion is reduced to the Tresca criterion. (Brinkgreve et al., 2019)

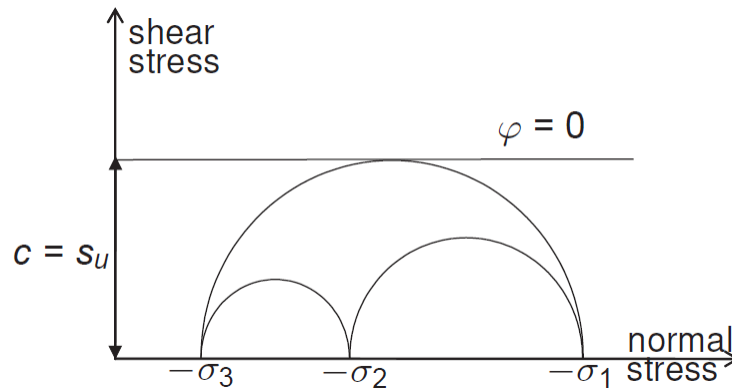


Figure 2.1: Mohr-Coulomb reduced to the Tresca criterion when $\phi = 0$ and cohesion equals undrained shear strength $c = S_u$, retrieved from (Brinkgreve et al., 2018).

The dilatancy angle ψ is central when including plastic strains, and may affect the analysis. However, clay soils usually show negligible dilatancy, i.e. $\psi \approx 0$. In undrained analysis a positive dilatancy angle will, in combination with no volume changes, result in a tensile pore stress generation. Consequently, the soil strength will become overestimated in effective undrained analysis. Therefore, the dilatancy angle for *Undrained B* and *Undrained C* is set as zero. (Brinkgreve et al., 2019)

2.1.2 NGI-ADP

NGI-ADP is an elasto-plastic constitutive material model formulated by Grimstad, Andresen, and Jostad (2011), which implements anisotropic undrained shear strength. To account for the inherent anisotropic traits of undrained shear strength and stiffness, the undrained shear strength for active (A), direct simple shear (DSS) and passive (P) stress paths are included. An approximated Tresca criterion with von Mises plastic potential function is implemented as failure criterion. This remedies the sharp corners of the previously mentioned Tresca yield criterion

that may lead to numerical problems. (Grimstad et al., 2011)

The NGI-ADP model is available in PLAXIS 3D, and is custom made for analyses with direct input of undrained shear strength. The model can be used for simulations using undrained loading of clay in problems concerning capacity, deformation and soil-structure interaction. Isotropic elasticity is given by the input unloading-reloading shear modulus over active shear strength ratio G_{ur} . Further, the remaining required stiffness parameters are shear strain at failure in triaxial compression γ_f^C , triaxial extension γ_f^E and direct simple shear γ_f^{DSS} . The active shear strength profile is defined by reference active shear strength $S_{u,ref}^A$, reference elevation z_{ref} and shear strength increase with depth $S_{u,inc}^A$. Furthermore, the strength inputs are triaxial compressive shear strength over active shear strength ratio $S_u^{C,TX}/S_u^A$, passive shear strength over active shear strength ratio S_u^P/S_u^A , initial mobilisation τ_0/S_u^A and direct simple shear strength over active shear strength ratio S_u^{DSS}/S_u^A . (Brinkgreve et al., 2018)

2.2 Slope Stability Analysis

The usual method of evaluating slope stability is by 2D plane strain analysis, which involves the assumption of an infinite slope width. However, slopes have varying properties in the third dimension, which leads to a three-dimensional slope failure mechanism. Limit Equilibrium Method has been the most popular technique in 2D analysis (Wei, Cheng, & Li, 2009; L. L. Zhang et al., 2015). Other numerical methods exist within the area, such as the Finite Element Method, Finite Difference Method (FDM) and Limit Analysis Method (LAM).

2.2.1 Slope Stability Definition

A slope definition is required when evaluating a potential slide in slope stability analysis. Figure 2.2 shows a simple overview of a slope cross-section, where the inclination of the slope surface is described by the parameters b , which is the corresponding horizontal unit per one vertical unit. The slope height is defined as the vertical distance from the slope toe (bottom) to the slope crest (top). The side surface is included since it will be used to explain various restraint measures and fix the slide width.

Slopes may be natural or man-made. Examples of natural slopes are valleys, mountain sides and cliffs. Man-made slopes maybe embankments and excavations, or other structures that have

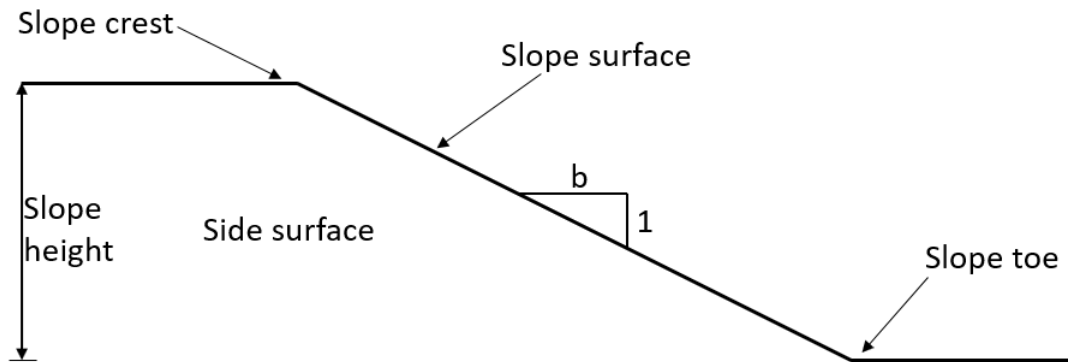


Figure 2.2: Two-dimensional slope definitions.

been built or removed. The various slope types may cause a range of movements associated with stability, with examples such as rock fall, toppling, debris flow or slide. Within geotechnical slope stability analysis the methods are aimed at slides, and how the relation between mass and resistance acts in the soil. Several reasons for failure are possible, such as a building on top of a slope, excavation or change in groundwater levels.

Slides may be described by their failure modes or mechanisms, which depend on soil type and slope geometry. Failure happens when the weight of the sliding mass exceeds the shear resistance along the slip surface, i.e. the driving forces are greater than the resisting shear forces. In geotechnical engineering it is common to divide slides into translational and rotational.

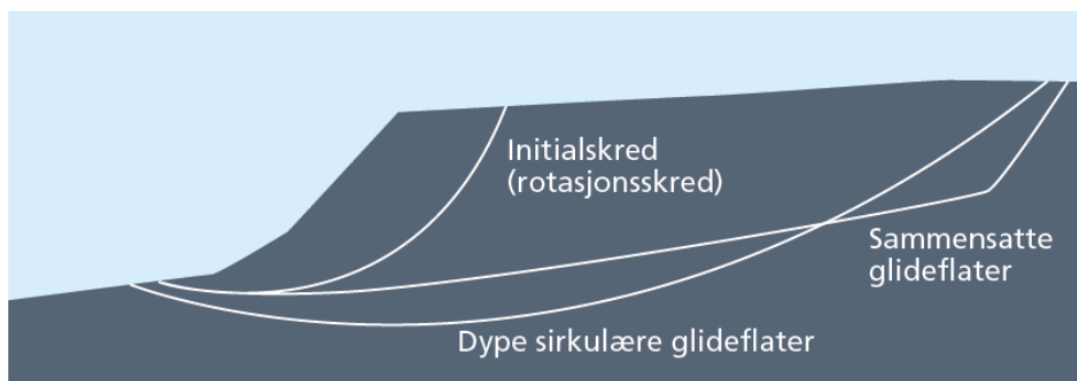


Figure 2.3: Possible slides assessed in slope stability analysis, where a rotational slide, a deep circular slide and a combined slide surface alternative are presented, retrieved from (NVE, 2014).

Figure 2.3 shows a rotational slide, a deep circular (rotational) slide and a combined slide surface alternative (mainly translational). A rotational slide is characterised by the mass moving down along the slip surface and outwards from the slope in a rotational movement. A transla-

tional is characterised by the mass 'loosening' from the back of the slope and being driven in a approximately straight movement along the slide surface, e.g. along a weak layer. The slope and soil conditions determine where the critical failure surface occurs. Rotational slides are the main focus in this study, however, some literature studies presents findings related to translational slides. Figure 2.4 illustrates the three kinds of rotational slides defined in slope stability analysis, which are base (or deep) failure B , toe failure T and slope failure S .

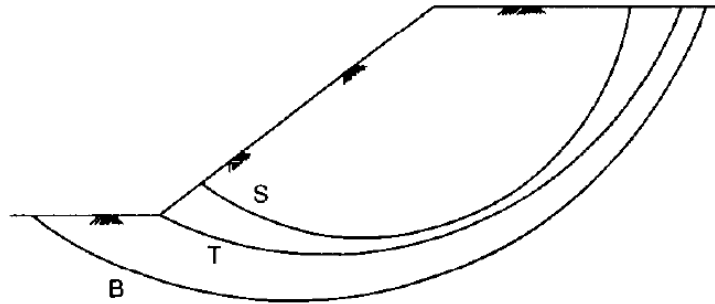


Figure 2.4: The three types of rotational slides, where B is base failure, T is toe failure and S is slope failure, retrieved from (Gens et al., 1988).

Slope Geometry

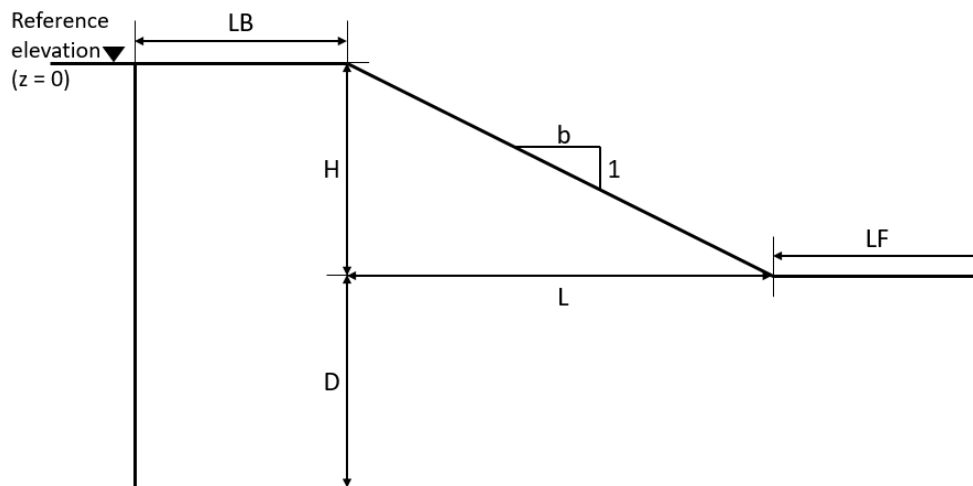


Figure 2.5: 2D slope geometry, where the shear strength reference elevation is at $z = 0$, H is the slope height, D is the depth below slope toe, b is the slope inclination, L is the horizontal length of the slope surface, LB is the model length behind the slope crest and LF is the length in front of the slope toe.

The relevant 2D slope geometry is defined in Figure 2.5, where H is slope height and b (or $1 : b$) is slope inclination. D is the depth below toe to bottom boundary (e.g. bedrock), L is the

horizontal length of the slope, LB is the length of the slope model behind the crest and LF is the length of the slope model in front of the toe. In 2D calculations the plane strain assumption is present, which implies that the slope is infinitely wide perpendicular to the plane. Figure 2.2 defines the different parts of the slope.

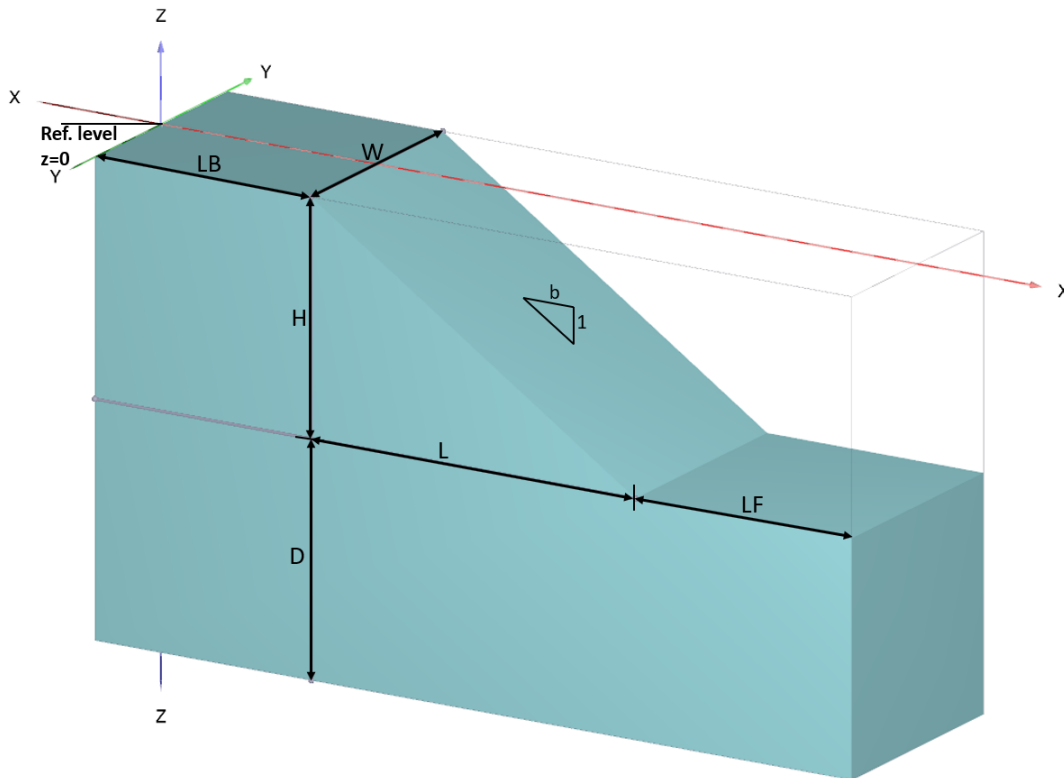


Figure 2.6: 3D planar slope geometry, where the shear strength reference elevation is at $z = 0$, H is the slope height, D is the depth below slope toe, b is the slope inclination, L is the horizontal length of the slope surface, LB is the model length behind the slope crest and LF is the length in front of the slope toe.

In three-dimensional space the slope width W is added as a finite geometrical attribute. Figure 2.6 shows how the geometry is defined in the PLAXIS 3D model. All properties are defined similar as in two-dimensional space except the width W . W is the model width and may be fully fixed or only normally fixed, depending on the analysis. If the model is not fully fixed with only normal restraints the side surfaces are called 'smooth' boundaries. This case simulates an infinitely wide slope. However, the safety factor may vary for different model widths with 'smooth' sides, due to insufficiently fine mesh or other numerical issues. Fully fixed boundaries are called 'rough', and means that the width is fixed and the slide cannot develop wider than the restraints. When the width-height ratio $w = W/H$ is used in the simulations, the slope width is fixed. The

width is not fully fixed if only W is used in model comparisons, unless otherwise specified.

In reality slopes may have more complex 3D curvatures compared to the simple 2D slope. These may be divided into convex and concave curvatures. Convex curvatures have an outward curve, such as a mountain ridge. Concave curvatures have an inward curve, such as a mountain valley. Figure 2.7 shows a convex arch (left) and a concave arch (right). Turning arches are smooth slope surfaces with convex or concave curvature. Furthermore, turning corners are convex or concave surfaces with a distinct centred edge (corner) along the slope length.

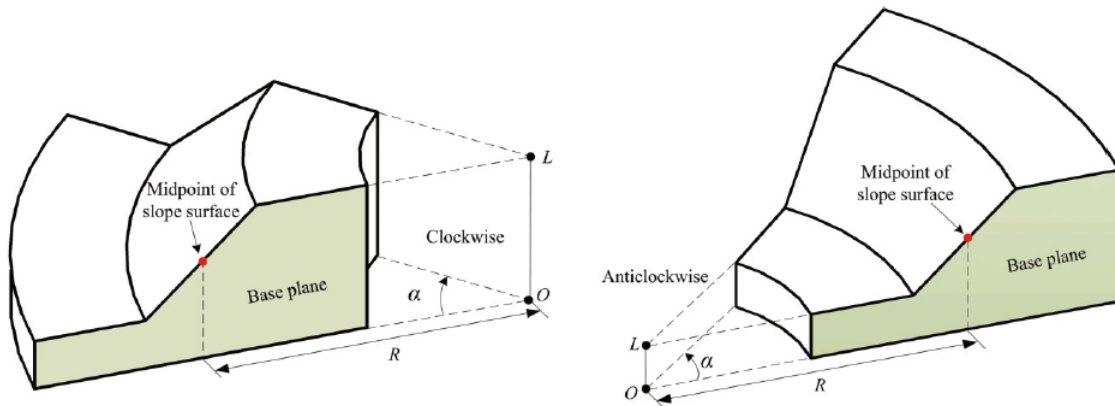


Figure 2.7: Left slope shows a convex arch and right slope shows a concave arch rotated a curvature angle α with a radius R , retrieved from (Y. Zhang et al., 2013).

Safety Factor

The safety factor (SF) is a common output parameter when analysing slope stability problems with possible slide failure. In LEM the SF is calculated by assuming a slip/failure surface and defining equilibrium equations for the system. The slip surface is where sliding may occur if SF is less than 1, i.e. shear stresses exceed shear strength. It can be defined as the available shear strength S of the soil divided by equilibrium shear stress τ :

$$SF = \frac{S}{\tau} \quad (2.1)$$

where $S = c + \sigma \tan \phi$ for total stress and $S = c' + \sigma' \tan \phi'$ for effective stresses. c is soil cohesion, σ is normal stress on the shear surface and ϕ is soil friction angle mobilised along the assumed slip surface. (Duncan, Wright, & Brandon, 2014)

Plane Strain

Two-dimensional slope stability analysis assume plane strain conditions. The assumption implies infinite slide width in a direction orthogonal to the cross-section plane, with no curvatures. Furthermore, the slide movement is directed parallel to the plane. As a result of the assumption of an infinite wide slope, the end effects from side shear resistance are neglected. Only the mobilised shear strength along the failure surface is used to determine the safety factor. (Akhtar & Stark, 2017)

2.2.2 Limit Equilibrium Method

The Limit Equilibrium Method (LEM) is based on satisfying static equilibrium on the slide mass to obtain the safety factor (Duncan et al., 2014). Various methods have been established that use different assumptions and simplifications, where limit equilibrium is the basis. LEM started out as a two-dimensional procedure. Later several methods have been expanded to three-dimensional analysis, as a measure to more accurately solve 3D problems where the plane strain assumption may be inadequate (Kalatehjari & Ali, 2013).

The methods may be divided into two approaches: *single free-body procedures* and *procedure of slices*. Examples of *single free-body procedures* are Infinite Slope, Logarithmic Spiral and Swedish Circle. These assess the entire soil body enclosed by the soil surface and the slip surface. Equilibrium equations are set up and solved for the entire soil body. (Duncan et al., 2014)

The *procedure of slices* involves dividing the soil mass into a series of vertical or horizontal slices. Each slice is evaluated for equilibrium, which results in equations that can be solved for each slice. Examples are Force Equilibrium procedures, Simplified Bishop and Ordinary Method of Slices. (Duncan et al., 2014)

The various procedures use different assumptions and solve for unknowns in equilibrium equations. Their usefulness and accuracy differ between the methods, and an evaluation of the slope stability problem should be carried out in advance. The assumptions relate to their approach of solving the equations with regards to the unknowns. A method may assume one value of an unknown, such as SE , and then iterate to obtain a static determinate system. (Duncan et al., 2014)

To show how the methods may differ from each other, four common methods are briefly presented. The methods are Simplified Janbu, Simplified Bishop, Spencer and Morgenstern-Price, which are the methods available in the slope stability program Slide3. These methods are only used for three-dimensional analysis using vertical columns in the present study, not for two-dimensional analysis. However, as the transformation from 2D to 3D is simple and analogous the methods are presented for 2D space, which means vertical slices will be used for illustration. A two-dimensional slope with a circular slip surface divided into slices is shown in Figure 2.8.

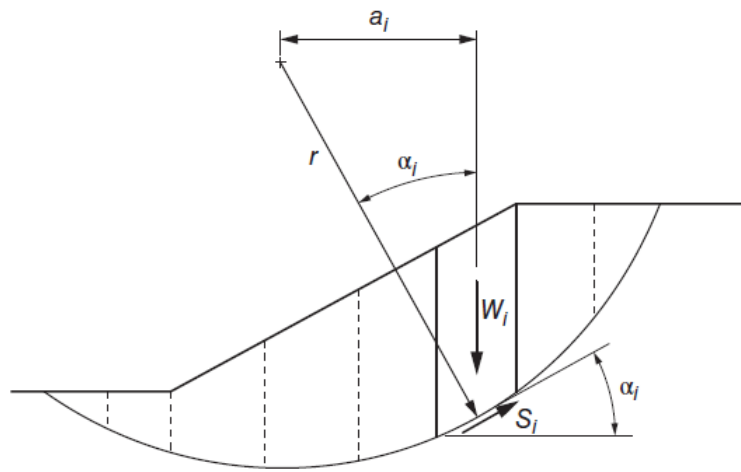


Figure 2.8: Slope with a circular slip surface divided into slices, retrieved from (Duncan et al., 2014). r is the circle radius, a_i is the horizontal moment arm for the slice, α_i is the base angle of the slice, S_i is the shear force on the slice base and W_i is the slice weight.

Simplified Janbu is part of the force equilibrium methods within the procedure of slices, i.e. only force equilibrium is satisfied. The method assumes horizontal interslice forces and no shear stress between slices. Consequently, the safety factor becomes lower compared to more rigorous methods where all equilibrium conditions are satisfied. Correction factors are available to account for this error in safety factor. (Duncan et al., 2014)

Simplified Bishop satisfies moment equilibrium and vertical force equilibrium for each slice. The method assumes a circular slip surface and horizontal forces between the slices. Shear forces between slices are therefore not included. Moment equilibrium is satisfied about the center of the circle. With the forces defined and equilibrium satisfied by the mentioned as-

sumptions, the safety factor can be expressed on an effective stress basis as:

$$SF = \frac{\sum \left[\frac{c' \Delta l \cos \alpha + (W - u \Delta l \cos \alpha) \tan \phi'}{\cos \alpha + (\sin \alpha \tan \phi') / SF} \right]}{\sum W \sin \alpha} \quad (2.2)$$

where c' is the cohesion, Δl is the length of the slice base, α is the base angle of the slice, W is the slice weight, u is the pore pressure and ϕ' is the friction angle. Figure 2.9 shows some geometrical properties (left) and the acting forces (right) on a single slice as defined by the Simplified Bishop method. (Duncan et al., 2014)

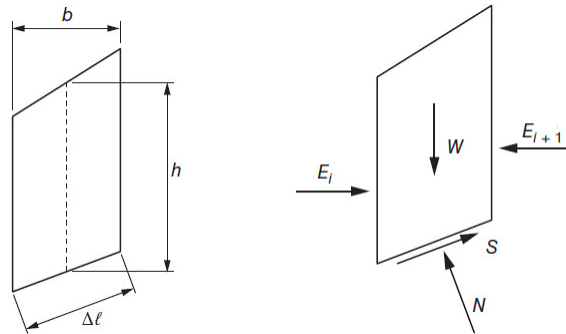


Figure 2.9: Slice with geometrical properties (left) and acting forces (right) as defined in the Simplified Bishop method, retrieved from (Duncan et al., 2014). b is the horizontal slice width, h is the slice middle height and Δl is the slice base length. W is the slice weight, E_i and E_{i+1} are the interslice horizontal forces on slice i , S is the shear force acting along the slice base and N is the normal force on the slice base.

Spencer's procedure is the simplest method that satisfies both force and moment equilibrium. The method assumes parallel interslice forces, which can be defined as in Figure 2.10 where the interslice forces Z_i and Z_{i+1} are expressed by the resultant Q . All interslice forces have the same inclination θ , which is an unknown in the equilibrium equations. Also, the normal force N is assumed acting on the center of the slice base. (Duncan et al., 2014)

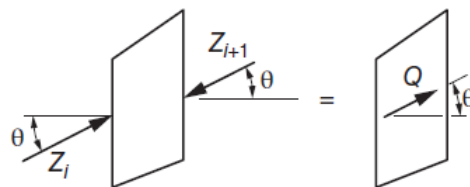


Figure 2.10: Slice with interslice forces Z_i and Z_{i+1} that gives the resultant Q according to Spencer's procedure, retrieved from (Duncan et al., 2014). θ is the inclination angle of the interslice forces.

Figure 2.11 shows an arbitrary slip surface in the defined coordinate system together with a single vertical slice applied with relevant forces. These definitions together with force and moment equilibrium form the basis of the sets of equations to be solved. Force equilibrium can be expressed as:

$$\sum Q_i = 0 \quad (2.3)$$

where Q_i is the interslice resultant for slice i . Moment equilibrium can be expressed as following, with the moment center point being the origin of the Cartesian coordinate system defined in Figure 2.11:

$$\sum Q(x_b \sin \theta - y_Q \cos \theta) = 0 \quad (2.4)$$

where x_b is the horizontal point of the slice base center, y_Q is the vertical coordinate of the resultant Q and θ is the interslice force inclination. By summing forces perpendicular and normal to each slice base, and including the Mohr-Coulomb shear force, an equation for Q is obtained:

$$Q = \frac{-F_v \sin \alpha - F_h \cos \alpha - (c' \Delta l / F) + (F_v \cos \alpha - F_h \sin \alpha + u \Delta l)(\tan \phi' / SF)}{\cos(\alpha - \theta) + [\sin(\alpha - \theta) \tan \phi' / SF]} \quad (2.5)$$

where c' is the cohesion, ϕ' is the friction angle Δl is the length along the slice base and u is pore pressure. The unknown parameters in the equations are the safety factor SF and the resultant inclination θ . These are solved for in Equation 2.3 and Equation 2.4 by trial-and-error methods until tolerated convergence. (Duncan et al., 2014)

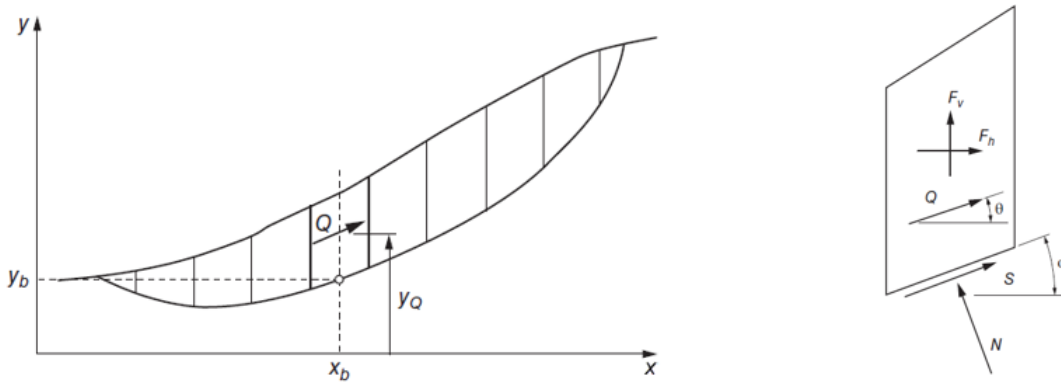


Figure 2.11: Non-circular slip surface divided in the defined coordinate system (left) defined by Spencer and a single slice with forces, retrieved from (Duncan et al., 2014). Q is the interslice force resultant, y_Q is the vertical point of Q , y_b and x_b are the vertical and horizontal coordinates of the slice base center. θ is the interslice resultant inclination, α is the slice base angle, F_v and F_h are the known vertical and horizontal forces, S is the slice base shear force and N is the slice base normal force.

The Morgenstern-Price method is similar to Spencer, and satisfies force and moment equilibrium. The main difference regarding unknowns is how interslice forces are defined. While the interslice force inclination θ is a single unknown in Spencer's method, Morgenstern-Price assumes a pattern of inclinations and an unknown scaling factor λ . The method assumes the relation between interslice shear forces and normal forces as:

$$X = \lambda f(x)E \quad (2.6)$$

where X is the vertical interslice force and E is the horizontal interslice force. $f(x)$ is an assumed function that describes the interslice force relation and inclination at the boundary of each slice. Examples of function types are half-sine and constant. If $f(x)$ is constant the results obtained by Spencer and Morgenstern-Price are almost identical. Equation 2.6 provides flexibility when predicting interslice forces compared to the method of Spencer. (Duncan et al., 2014)

Limitations

Several limitations and assumptions are linked with the use of LEM. For 2D LE analysis the plane strain assumption is not valid for many cases where the problem is three-dimensional. This can be improved by 3D LE analysis. However, the 3D methods also contain assumptions, for example related to shear strength on the side of the slide. LEM does not satisfy displacement compatibility due to the use of simple statics and equilibrium of moments and forces. Moreover, the methods involves indeterminate static conditions, unrealistic distributions of stress and the interaction between soil and structures may be troublesome. (Kelesoglu, 2015)

Furthermore, it is necessary to assume a slip surface to obtain the safety factor. Consequently, several slip surfaces should be tested to locate the critical case and SF. Moreover, the SF is assumed constant along the presumed failure surface. The methods often solve a statically indeterminate problem, which leads to the need of assuming some internal forces. (Duncan et al., 2014)

2.2.3 Stability Charts

Various stability charts have been suggested as a quick preliminary assessment of slope stability. Stability charts depend on dimensionless relations between the safety factor and other relevant

parameters, such as geometry, shear strengths and groundwater conditions. The Direct Method by Janbu (1954) uses stability charts to obtain a useful indication for idealised slopes, see Figure 2.12. For example the safety factor expression for homogeneous and fully cohesive ($\phi = 0$) soil is: (Duncan et al., 2014)

$$SF = N_0 \frac{c}{\gamma H} \tag{2.7}$$

where N_0 is a stability number, c is cohesion, γ is soil unit weight and H is slope height. Duncan et al. (2014) stated that using stability charts are usually as accurate as the accuracy of shear strength evaluation.

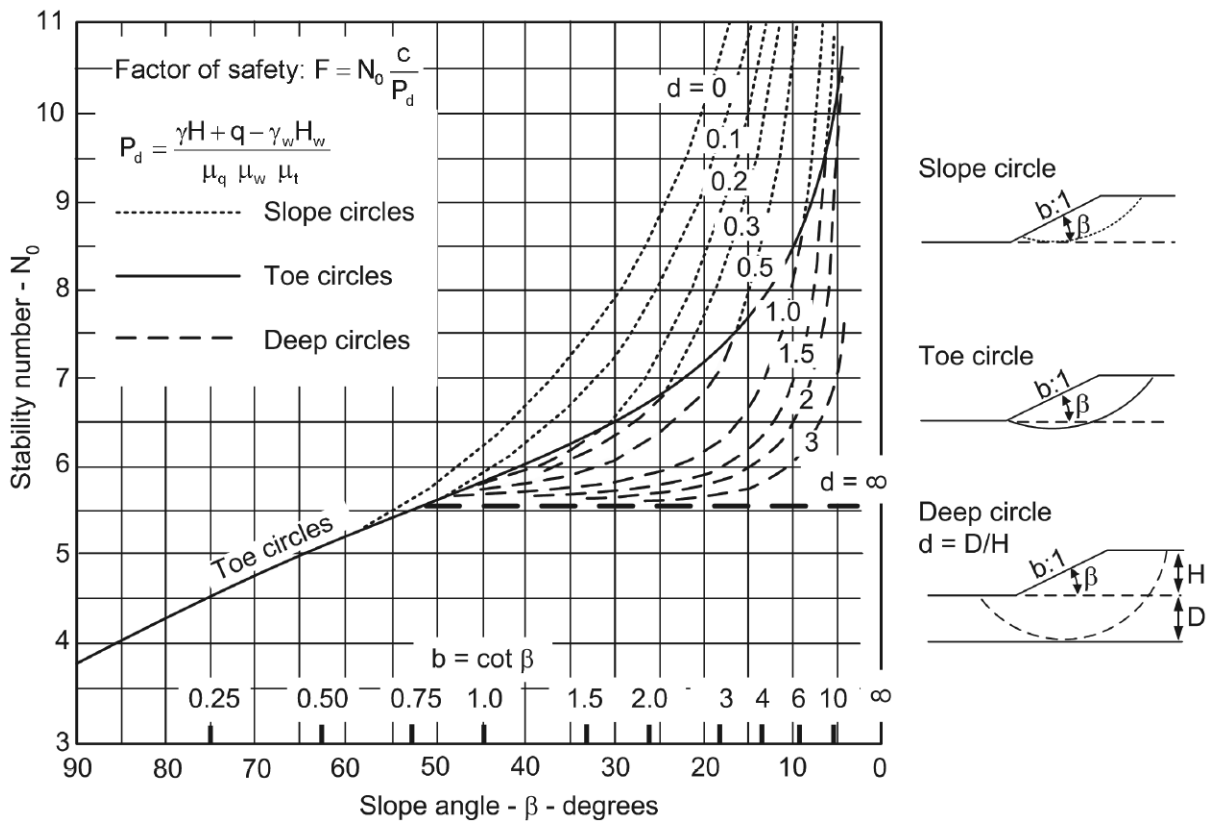


Figure 2.12: Stability chart for $\phi = 0$ by Janbu (1954).

2.2.4 Finite Element Method

The Finite Element Method (FEM) is a method that can be used for a range of engineering problems. It is based on finite elements with equations linking stresses and displacements. The structure could potentially create a comprehensive system of equations to be solved numerically. The model may be exposed to a load action and the method solves the system of equa-

tions to find the resulting response. FEM makes it possible to model non-linear stress-strain behaviour. Consequently, more realistic solutions may be obtained (Duncan, 1996). PLAXIS 2D and 3D are examples of FE software developed for geotechnical practice, such as slope stability analysis.

Slope stability analyses using FEM are regarded as an accurate and versatile option. It requires less assumptions compared to LEM, which include finding the critical failure mechanism. Analyses using FE software will automatically locate the natural failure surface, where the soil shear strength is less than the affecting shear stresses. (Griffiths & Lane, 1999)

Griffiths and Lane (1999) summarised several advantages of FEM over LEM when comparing the methods:

- As mentioned above, it is not necessary to assume the critical failure surface, since it is located naturally when obtained using FE software.
- LEM requires assumptions about the present slice side forces. This is unnecessary in FEM as the method does not use slices. Global equilibrium is maintained in FEM until failure has occurred.
- Deformations can be obtained using FEM if stiffness data are available.
- Progressive failure mechanism can be monitored using FE software.

Some potential disadvantages related to the finite element approach include increased calculation time and numerical issues. One potential problem regarding false stiffness and overshoot is elaborated on in subsection 2.5.2. The efficiency of the FE approach may be reduced for problems containing complex soil properties and model geometries, or if the analysis is three-dimensional. Increased time and cost could be the consequence, when increased accuracy is desirable. Moreover, if modelled incorrectly or the problem is complex, numerical issues may arise, e.g. singularity and discretisation errors. (Jostad & Lacasse, 2015)

Slope stability analysis conducted using FEM will give more accurate results provided correct modelling, compared to LEM. Calculation time for FE analyses may be significant, especially in 3D. However, as computational power increases, the effectiveness of FE analysis will increase compared to LEM (Griffiths & Lane, 1999).

Strength Reduction Method

The definition of the safety factor is the same for FE analysis as for LE analysis, see Equation 2.1. However, the solution procedure differs. FE software (e.g. PLAXIS 2D) and software based on the Finite Difference Method (FDM) use the Strength Reduction Method (SRM) in safety analysis. It is based on what factor that the original shear strength must be divided by to achieve slope failure, which presents as:

$$c_f = \frac{c}{SF} \quad (2.8)$$

$$\phi_f = \arctan \frac{\tan \phi}{SF} \quad (2.9)$$

where c_f is the cohesion and ϕ_f is the friction angle at failure. The strength parameters cohesion and friction angle are reduced until the slope fails. (Griffiths & Lane, 1999)

2.2.5 Finite Difference Method

The Finite Difference Method (FDM) is a numerical tool that is similar to the Finite Element Method (FEM). As in FEM, the model is discretised using a mesh of elements and a strength reduction technique is used to find the safety factor. A popular geotechnical software that utilise FDM is FLAC by ITASCA Consulting Group, where FLAC stands for Fast Lagrangian Analysis of Continua (ITASCA, 2008). The main difference between FDM and FEM is how the partial differential equations are solved. Governing equations are replaced by algebraic expressions containing field variables, such as stress or displacements, at discrete points. These variables are undefined within each element. However, in FEM the variables are varying throughout each element, which are described by specific functions. FDM solves the equations explicitly without a global stiffness matrix in contrast to FEM. Consequently, the FD calculations does not require excessive memory capacity for extensive problems. (Damians, Bathurst, Josa, & Lloret, 2013)

2.2.6 Limit Analysis Method

Limit Analysis Method (LAM) is based on finding bounds for limit load or resistance of a slope with perfectly plastic material obeying an associated flow rule. Bounds can be found with respect to various factors affecting the stability, such as the slope height, external loads or soil weight. Upper bound limit analysis can provide critical values for factors affecting the slope sta-

bility, such as the dimensionless ratio $\frac{\gamma H}{S_u}$ and safety factor. For load or height an upper bound limit can be found by the kinematic method (Michalowski & Drescher, 2009). The approach involves equalling the work done by external loads along the failure mechanism with the work by internal stresses. Potential inaccuracies with the upper bound approach are a potential lack of equilibrium of external loads and internal stresses, and the assumed failure mechanism could be wrong (Yu, Salgado, Sloan, & Kim, 1998). In addition, limit analysis may be restricted to simple slopes, since it is difficult to construct accurate failure mechanism for a complex three-dimensional slope (Y. Zhang et al., 2013).

Lower bound limit analysis requires that applied stresses balance external loads and do not exceed the strength criterion of the soil. If so, the external loads are not greater than the collapse loads. A limitation concerning the lower bound approach is that strains and displacements are not considered. Moreover, the stress state is possibly not the true collapse stress state. (Yu et al., 1998)

Another type of limit analysis is finite element limit analysis, which can be used for both upper and lower bounds. The plasticity theorems are formed on the basis of finite element formulations. The method is suitable for finding the bounds of the true collapse loads. Upper and lower bound solutions will approach each other as the mesh is refined, which means that an accurate estimate can be obtained. (Tschuchnigg, Schweiger, Sloan, Lyamin, & Raissakis, 2015)

2.3 GeoSuite Stability

Novapoint GeoSuite Stability is a 2D slope stability program developed by Trimble Solutions, based on LE-methods. It consists of a user interface, calculation engine and report generator. The user interface is used to create appropriate input for the calculation engine. With the help of CAD-tool, a suitable slope geometry and soil layering can be represented. Furthermore, undrained, drained or combined analysis can be defined, where strength parameters are the input. A shear strength profile with depth can be created. Another property of GS Stability is the input of end surface shear stresses, which can be used to simulate 3D-effects. Furthermore, the program allows for groundwater, pore pressures and loads to be selected. (Trimble, 2018)

When geometries, soil conditions and loads are defined, the calculation method is selected. The

choices consist of the LE-techniques BEAST 2003, Bishop Simplified, Bishop Modified and Force Equilibrium. The default calculation strategy is BEAST 2003, which is further described below. When the calculation is executed the results are presented. The user can document the results by using the report generator. In addition, various calculation strategies may be selected, such as creating a quadratic search area by *Tangent* or selecting exit points for failure surface using *Points*. (Trimble, 2018)

Soil Strength

GS Stability allows for total and effective stress analyses, and can be used with both drained and undrained strengths, or a combination. Input for drained conditions are friction angle ϕ' and cohesion c' . Undrained analysis requires input of cohesion $c = S_u$. A strength profile can be made by the user in different horizontal locations in the soil layer. If there are several shear strength profiles, the strength is interpolated between profile points. As a result, it is possible to make an inclination in shear strength. (Trimble, 2018)

BEAST

The default calculation engine in GS Stability is BEAST 2003 (current version). The LE-program utilises a general procedure of slices to analyse problems related to slope stability, bearing capacity and earth pressure. The output may be safety factor or earth pressure, solution quality and forces/stresses for individual slices. It can cope with shear surfaces as planes, circles, combined or general surfaces that are specified by points. The program can use both effective and total stresses. BEAST provides force and moment equilibrium for each slice, and have an automatic quality control. The method is based on plane strain conditions, and end surface shear stresses can be included as optional input. BEAST creates a simple finite element type mesh, which can be used as a reference for different soil properties. (Trimble, 2018)

According to the BEAST-manual the program is based on limit equilibrium, with plane strain geometry. BEAST finds a solution with both force and moment equilibrium in each slice. It calculates an initial force equilibrium and then modifies the solution to get overall moment equilibrium. The obtained moment equilibrium for each slice is used to find the interslice normal forces. Interslice roughness distribution is a program input for the force equilibrium solution. The soil strength is assumed fully mobilised along the entire shear surface. A quality check

is conducted by the program and the solution receives a score. If the initial assumptions are wrong, e.g. regarding normal force location, BEAST can alter these based on the score feedback. (Trimble, 2018)

BEAST creates slices between the shear surface and the soil surface. Equal slices are normally used, unless otherwise is specified by the user. When slices and elements are defined, it is necessary to appoint soil properties to points and faces of the slices. Soil properties, for example undrained shear strength S_u , are assigned to the point and averaged along the faces between the points. (Trimble, 2018)

Side Shear Forces

In regular 2D calculations with plane strain conditions, the slope failure is assumed infinite in the direction orthogonal to the paper plane, here defined as the Y-direction. In reality the slides are of finite length, which are due to 3D-effects caused by end shear stresses. In GS Stability there is an input option that accounts for these end effects. The input is the side shear factor α_{SS} . BEAST finds the side shear force SS for each slice by the following procedure: (Trimble, 2018)

1. Calculate the average effective unit weight at the centre point of the slice.
2. Assume resting pressure coefficient $K'_0 = 0.5$ and calculate the average horizontal stress σ_y in the Y-direction.
3. Calculate the horizontal force $F_y = \sigma_y \cdot A$, where A is the area of the slice.
4. Calculate the side shear force according to the following equations:

Drained conditions:

$$SS = (c \cdot A + F_y \cdot \tan \phi) \alpha_{SS} \quad (2.10)$$

where c is the cohesion and ϕ is the friction angle.

Undrained conditions:

$$SS = S_u \cdot A \cdot \alpha_{SS} \quad (2.11)$$

where S_u is the undrained shear strength.

The input factor α_{SS} depends on the length of the failure system in Y-direction, or width of the

slide. For BEAST to include full shear at both end surfaces of the system length B , the factor is given as:

$$\alpha_{SS} = \frac{2}{B} \quad (2.12)$$

Where B is given the unit corresponding to the length unit defined for the Y-direction. (Trimble, 2018)

There are some assumptions regarding the side shear force SS . It is assumed acting $\frac{2}{3}$ deep into the average slice height. Moreover, the force direction is assumed parallel to the shear surface and against the displacements, as illustrated in Figure 2.13. (Trimble, 2018)

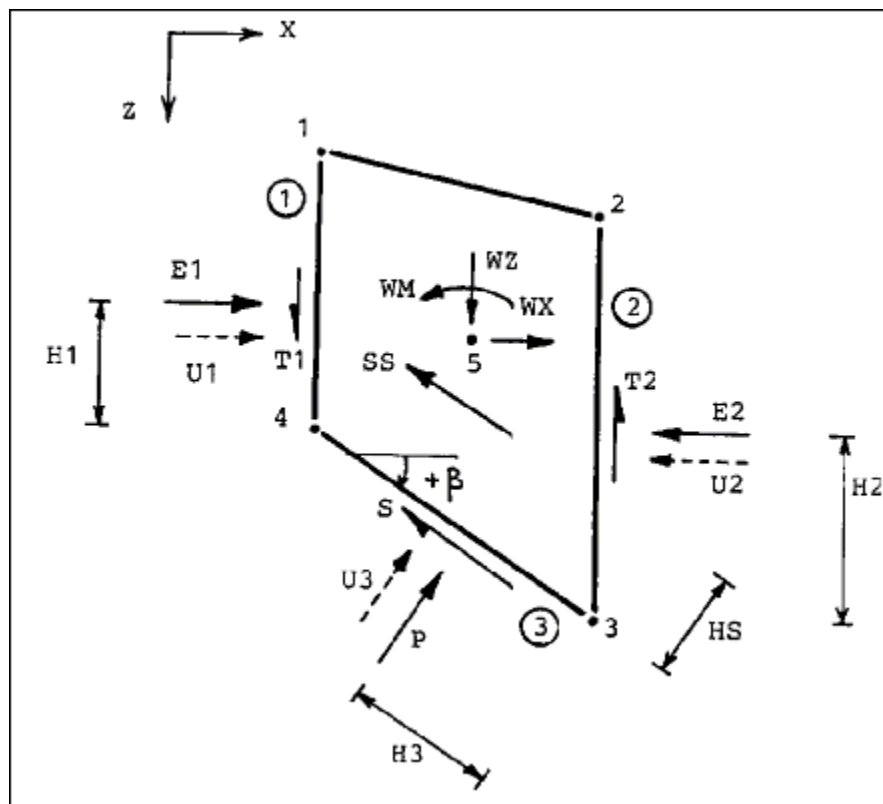


Figure 2.13: Slice with forces and moment arms used in BEAST according to GS Stability manual (Trimble, 2018).

Equations

Figure 2.13 is used to derive and calculate the equations for the limit equilibrium system for a single slice. First, the equation sets are found by force and moment equilibrium. The forces and geometrical properties of a general slice are described as:

- E_1, E_2, P : Effective normal forces.

- T_1, T_2, S : Shear forces.
- W_X, W_Z, W_M : Forces and moments that are known, with slice centre as reference point.
- SS : Side shear force.
- H_1, H_2, H_3 : Location of normal forces.
- H_S : Location of side shear force.
- β : Shear surface inclination.

Equations defined for the BEAST method are given as follows (Trimble, 2018):

$$\Sigma F_X = 0:$$

$$E_1 + W_X + E_2 + P \sin \beta - (S + SS) \cos \beta = 0 \quad (2.13)$$

$$\Sigma F_Y = 0:$$

$$T_1 + W_Z - T_2 - P \cos \beta - (S + SS) \sin \beta = 0 \quad (2.14)$$

$$\Sigma M = 0:$$

$$T_1 \cdot B - E_1(H_1 + H_4) + W_M + W_Z \cdot B_5 - W_X \cdot H_5 + SS \cdot H_S + E_2 \cdot H_2 - P \cdot H_3 = 0 \quad (2.15)$$

Where $B = x_2 - x_1$, $H_4 = z_3 - z_4$, $B_5 = x_3 - x_5$ and $H_5 = z_3 - z_5$. Numbers in subscript refers to each numbered point in the slice.

Furthermore, the failure shear stress is defined by the equation for fully mobilised shear strength at face 3:

$$S = \frac{C_3 \cdot L_{34} + P \tan(\phi_3)}{SF} \quad (2.16)$$

Where C_3 is cohesion of face 3, ϕ_3 is friction angle of face 3, L_{34} is shear surface length and SF is the safety factor. The equation assumes application of Mohr-Coulomb failure criterion, and a constant safety factor through the system of slices. (Trimble, 2018)

The presented equations above are solved by iteration until the desired/sufficient accuracy and critical failure is obtained. The BEAST iteration algorithm is explained in further detail in (Trimble, 2018). Consequently, the process results in an estimate of the slope safety factor.

2.4 Rocscience Slide3

Slide3 is a three-dimensional slope stability program based on limit equilibrium methods (LEM) and is developed by Rocscience. The software is similar to the equivalent 2D program Slide, with additions like modelling of complex 3D geometry and anisotropic materials. A range of material models are available, such as Mohr-Coulomb, Anisotropic strength and SHANSEP. The soil model called Mohr-Coulomb in Slide3 only accounts for drained analysis. A separate model called Undrained may be used to study undrained behaviour. Here the friction angle is set as zero, and the failure criterion is reduced to the Tresca criterion.

The three-dimensional calculation methods are directly analogous to the traditional two-dimensional LE methods. The vertical slices used in 2D are extended to vertical columns in 3D. Slide3 provides four 3D limit equilibrium methods, which are Janbu Simplified, Simplified Bishop, Spencer and Morgenstern-Price (referred to as Generalised Limit Equilibrium (GLE) in the software). Janbu Simplified satisfies force equilibrium and Bishop Simplified satisfies moment equilibrium. Spencer and Morgenstern-Price satisfy both force and moment equilibrium. The difference between the two latter is that Spencer uses a constant intercolumn force angle and Morgenstern-Price uses an intercolumn force function that can be constant or defined with a half-sine function. (Duncan et al., 2014)

Three-dimensional limit equilibrium methods using vertical columns solve forces and moments in two orthogonal directions. Further, normal and shear forces are found by vertical forces on the base of the columns. However, accurate solutions are not easily obtained in 3D space for more complex and non-symmetrical problems. Several limitations are found in early numerical methods based on 3D LEM, as summarised in (Rocscience, 2017):

- Assumed sliding direction
- Assumed plane of symmetry
- Transverse force and/or moment equilibrium not satisfied
- Local coordinate system required
- Simple search methods for critical surfaces, such as spherical or planar

Equations

Efficient and accurate methods have been proposed the last decades, including those implemented in Slide3. Huang, Tsai, and Chen (2002) and Cheng and Yip (2007) improved the LE methods by including a statically determinate 3D system of equations, a solver for a unique sliding direction and force and moment equilibrium in two orthogonal directions. A brief introduction to the method is presented below. For a more elaborated review the reader is referred to (Huang et al., 2002) and (Cheng & Yip, 2007). The system of forces defined is illustrated in Figure 2.14, with different components described as: (Rocscience, 2017)

- N, U : Effective normal force and pore pressure force on column base
- S : Mobilised shear force on column base
- a : Sliding direction
- E : Intercolumn normal forces
- X : Intercolumn vertical shear forces
- H : Intercolumn horizontal shear forces
- P : Vertical external force
- W : Column weight

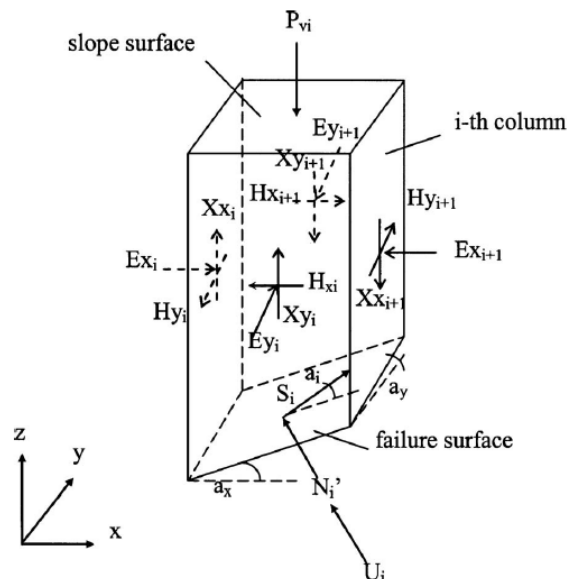


Figure 2.14: Column with forces and sliding direction used in Slide3 according to (Cheng & Yip, 2007).

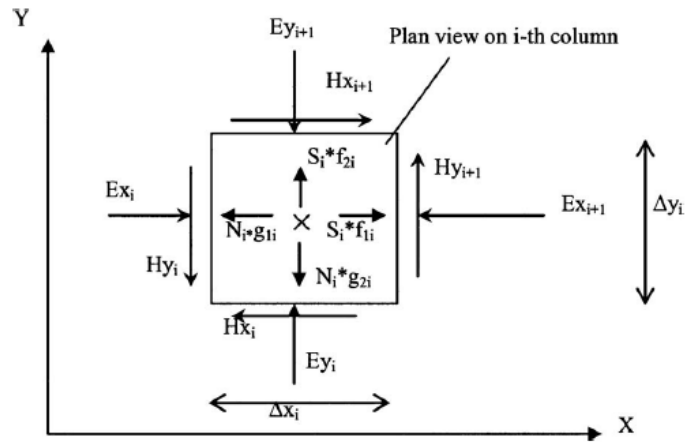


Figure 2.15: Slide3 force equilibrium in the horizontal x-y plane, retrieved from (Cheng & Yip, 2007).

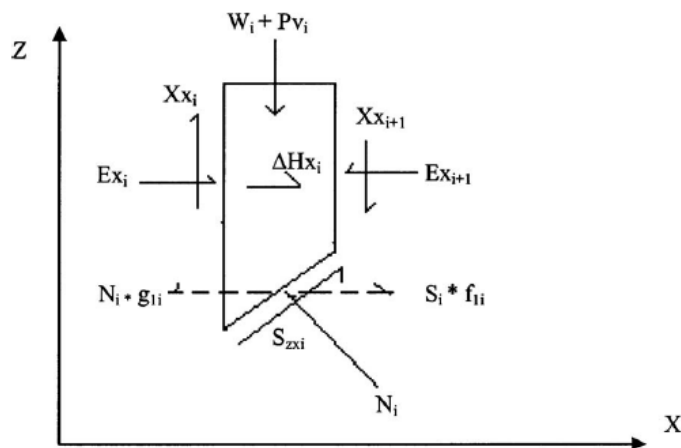


Figure 2.16: Slide3 horizontal force equilibrium in the x-direction, retrieved from (Cheng & Yip, 2007).

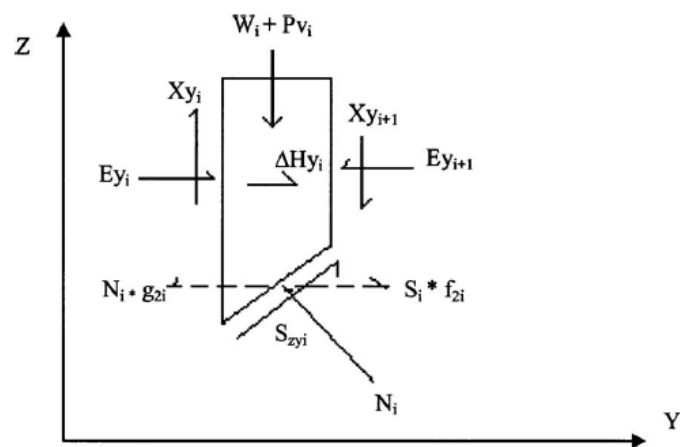


Figure 2.17: Slide3 force equilibrium in the y-direction, retrieved from (Cheng & Yip, 2007).

Figure 2.15, Figure 2.16 and Figure 2.17 shows the forces that are used to obtain force and moment equilibrium for the three planes. The z-axis defines the vertical direction and the x-y plane is the horizontal plane. f_1, f_2, f_3, g_1, g_2 and g_3 are directional unit vectors of the shear force S_i and normal force N_i . The components apply to a single vertical column i . (Cheng & Yip, 2007)

The figures above makes up the basis of the equilibrium equations for the Morgenstern-Price method proposed by Cheng and Yip (2007), as a continued development from Huang et al. (2002). The procedure can be reduced to Janbu Simplified or Bishop Simplified. First, vertical force equilibrium for a single column i :

$$\Sigma F_z = 0 \rightarrow N_i g_{3i} + S_i f_{3i} - (W_i + P_{vi}) = (X x_{i+1} - X x_i) + (X y_{i+1} - X y_i) \quad (2.17)$$

where the base normal stress is:

$$N_i = A_i + B_i S_i \quad (2.18)$$

and shear stress is defined with the Mohr-Coulomb failure criterion as:

$$S_i = \frac{C_i + (A_i - U_i) \tan \phi_i}{F [1 - (B_i \tan \phi_i / F)]} \quad (2.19)$$

where $C_i = c A_i$ with c being cohesion and A_i being the area of the column base, ϕ_i is the friction angle, F is the safety factor and $B_i = -\frac{f_{3i}}{g_{3i}}$. Further:

$$A_i = \frac{W_i + P_{vi} + \Delta E x_i \lambda_x + \Delta E y_i \lambda_y}{g_{3i}} \quad (2.20)$$

Second, force and moment equilibrium in the horizontal directions are defined. Force equilibrium in x-direction is expressed as:

$$-\Sigma H x_i + \Sigma N_i g_{1i} - \Sigma S_i f_{1i} = 0 \quad (2.21)$$

Moment equilibrium in x-direction gives:

$$\Sigma (W_i + P_{vi} - N_i g_{3i} - S_i f_{3i}) R X + \Sigma (N_i g_{1i} - S_i f_{1i}) R Z = 0 \quad (2.22)$$

where $R X$ and $R Z$ are lever arms to the moment point.

In y-direction force equilibrium is given as:

$$-\sum Hy_i + \sum N_i g_{2i} - \sum S_i f_{2i} = 0 \quad (2.23)$$

Moment equilibrium in y-direction gives:

$$\sum(Hy_i + P_{vi} - N_i g_{3i} - S_i f_{3i})RY + \sum(N_i g_{2i} - S_i f_{2i})RZ = 0 \quad (2.24)$$

where RY and RZ are lever arms to the moment point.

Third, equations for directional safety factors F_x , F_y , F_{mx} and F_{my} can be established and solved for by:

$$F_y - F_x = 0 \quad (2.25)$$

$$F_{mx} - F_y = 0 \quad (2.26)$$

$$F_{my} - F_x = 0 \quad (2.27)$$

Last, values of the safety factor F , λ_x , λ_y and sliding direction a is found that satisfy the last three equations. The value of F will be the overall three-dimensional safety factor for a given slip surface. (Rocscience, 2017)

The procedure of Cheng and Yip (2007) reproduced above is used in Slide3 with further improvements. For better and faster calculations a more efficient solver is used for 3D LE equations. Moreover, fast search methods are implemented for general three-dimensional failure surfaces. The failure criteria are not limited to Mohr-Coulomb, and a wide range of soil models may be used. In addition, the program allows for complex geometry modelling and data interpretation tools. (Rocscience, 2017)

Surface Search

As previously mentioned earlier 3D limit equilibrium methods were limited by their ability to find the slip surface and assumptions were needed. Slide3 may represent a variety of three-dimensional slip surfaces and advanced search methods are available. The supported slip surface shapes are: (Rocscience, 2019)

- Sphere
- Ellipsoid
- Multi-planar
- Wedge
- Non-Uniform Rational B-Spline (NURBS)

The default slip surface type in Slide3 is the ellipsoidal surface, which is a suitable fit for a 3D rotational slide. An ellipsoid with 9 parameters is more flexible compared to a sphere with 4 parameters. The spherical shape, see Figure 2.18, uses less computation time than the ellipsoidal shape, see Figure 2.19. However, the difference is not significant and thus the ellipsoidal surface is default.

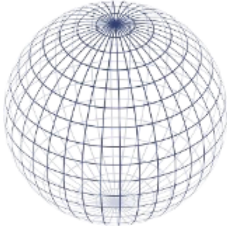
Shape	Parameters
	<ul style="list-style-type: none"> - 3D point centroid - Radius
	Total
	4 parameters

Figure 2.18: Spherical surface available in Slide3 with geometrical parameters, retrieved from (Rocscience, 2019).

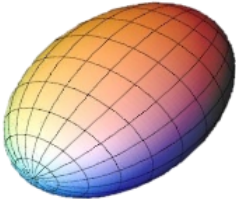
Shape	Parameters
	<ul style="list-style-type: none"> - 3D point centroid - 3 Radii - 3 rotation angles
	Total
	9 parameters

Figure 2.19: Ellipsoidal surface available in Slide3 with geometrical parameters, retrieved from (Rocscience, 2019).

An efficient and accurate search method is necessary to find the critical slip surface in 3D. The optimisation procedure is a challenging objective where a range of parameters are involved.

The objective function have non-linear behaviour with discontinuities and may have several local critical solutions. The search algorithms available in Slide3 is as follows:

- Grid Search - Deterministic
- Auto-Refine Search - Deterministic
- Cuckoo Search - Stochastic
- Particle Swarm Search - Stochastic

The search method can be divided into deterministic and stochastic. The deterministic methods search the region by creating many surfaces based on sphere or wedge, and then selects the failure mechanism with the lowest safety factor. The stochastic methods are nature-inspired meta-heuristic optimisation methods. Cuckoo Search is the default search technique in Slide3 and works with all surface types. The procedure uses 'random-walk' technique to generate new solutions in spaces that give lower safety factor. The stochastic processes dodge the solutions that are reduced to the local optima. Therefore, the stochastic are well suited for finding the global optimal solution. (Rocscience, 2019)

Following the failure mechanism search the Surface Altering Optimisation (SAO) further minimises the safety factor. SAO is a method that optimises at a local level by modifying the geometry established by the search methods. The approach converts any surface into NURBS and transforms the geometry until the safety factor is minimised within the defined iterations and numerical settings. (Rocscience, 2019)

2.5 PLAXIS

2.5.1 PLAXIS 2D

PLAXIS 2D is a two-dimensional calculation software based on the Finite Element Method (FEM). It can be used to analyse geotechnical problems related to deformation, stability and flow (Brinkgreve et al., 2019). The 2D program may utilise both plane strain and axisymmetric conditions. The user can select either 6-noded or 15-noded triangular elements, and define how coarse or fine the mesh should be. The theory behind the finite element method and how it is implemented in PLAXIS 2D is similar to PLAXIS 3D, where the main difference regards the type of element. Therefore, the theory description is limited to the theoretical basis of PLAXIS 3D found in (Brinkgreve et al., 2018), which is briefly described below in subsection 2.5.2

Several material models can be used, which are found in the material sets, or as user-defined models like the SHANSEP-MC model. Each model have various material properties as input, such as stiffness and strength parameters. Examples of standard soil models in PLAXIS are Mohr-Coulomb, Hardening Soil and NGI-ADP. Moreover, other materials (structures in the soil) can be defined and used in the model, such as plates and anchors. In addition, groundwater and flow conditions may be defined as wanted.

2.5.2 PLAXIS 3D

PLAXIS 3D is the three-dimensional equivalent to PLAXIS 2D. The plane strain assumption is not necessary and problems can be analysed in 3D space. The program utilises 10-noded tetrahedral finite elements. A simple slope model is illustrated in Figure 2.20 with the defined axis system in 3D space, where z-axis is in the vertical direction and x- and y-axis covers the horizontal plane. The program shares most functions with PLAXIS 2D. Furthermore, a range of 3D surfaces and properties can be implemented. A converter tool allows for implementation of a PLAXIS 2D model into PLAXIS 3D by extrusion. In addition, CAD-files can be imported and used to model soil volumes. (Brinkgreve et al., 2018)

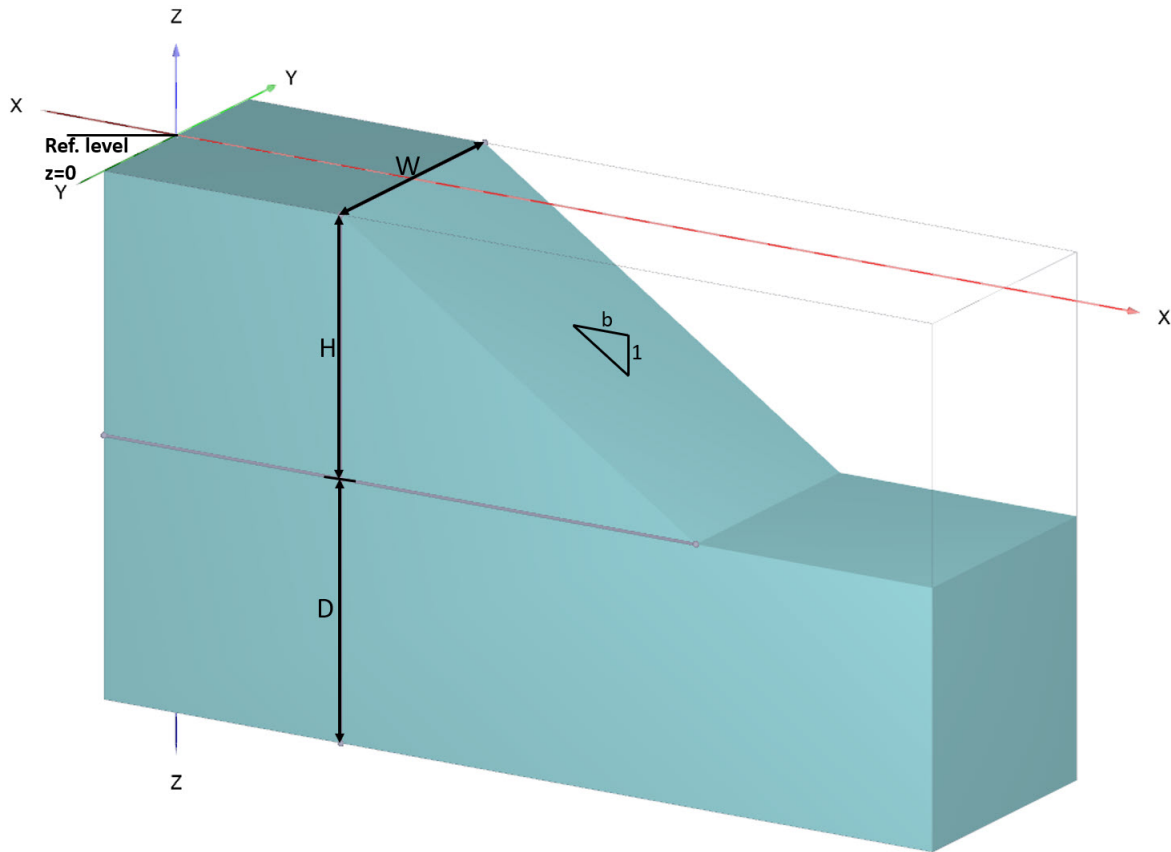


Figure 2.20: Slope geometry modelled in PLAXIS 3D, where W is slope width, H is slope height, D is depth below toe to model bottom and b is slope slope inclination.

Safety Analysis

PLAXIS 2D and 3D use *phi/c reduction* in their safety analyses to obtain a safety factor, which is based on SRM. Global safety factors are obtained by reducing the shear strength parameters c and $\tan \phi$ until failure occurs. The programs use the total multiplier ΣMsf to do the calculation:

$$\Sigma Msf = \frac{\tan \phi_{input}}{\tan \phi_{reduced}} = \frac{c_{input}}{c_{reduced}} = \frac{S_{u,input}}{S_{u,reduced}} \quad (2.28)$$

where ϕ = friction angle, c = cohesion and S_u = undrained shear strength. *Input* values are the user input soil strengths. ΣMsf starts at the initial state with value of 1. The SF is defined as the values of ΣMsf at failure. (Brinkgreve et al., 2019)

Numerical Control Parameters

Numerical control parameters define how the simulation is run for a specific calculation type. These can be altered to optimise the calculation for certain problems. The default settings are often adequate. Examples of default numerical parameters are solver type *Picos*, max steps 100 and tolerated error 0.01. These can be changed for each calculation phase, e.g. gravity loading (initial phase), plastic loading and safety analysis. For a safety analysis, the numerical control parameters should not significantly impact the results. (Brinkgreve et al., 2018)

Deformation Theory

To understand how PLAXIS 3D (and 2D) uses FEM to solve slope stability problems, the deformation theory behind the software is briefly reviewed. The following subsections are reproduced from (Brinkgreve et al., 2018), where all quantities are functions of the 3D space position. A range of symbols are used below, such as single underline for vectors, double underline for matrices and dot above symbol for rate (small increment). The same procedures and equations are applicable for 2D space (PLAXIS 2D). However, in PLAXIS 2D the volume elements are replaced with area elements. The equations are part of continuum mechanics, are further discretised according to the finite element method. Static equilibrium in continuum mechanics is defined as:

$$\underline{\underline{L}}^T \underline{\underline{\sigma}} + \underline{\underline{b}} = \underline{\underline{0}} \quad (2.29)$$

where $\underline{\underline{\sigma}}$ is the six stress components ($[\sigma_{xx} \ \sigma_{yy} \ \sigma_{zz} \ \sigma_{xy} \ \sigma_{yz} \ \sigma_{zx}]^T$), $\underline{\underline{b}}$ is the three body forces and $\underline{\underline{L}}^T$ is the transposed matrix of a differential operator in 3D space. $\underline{\underline{L}}^T$ is defined as:

$$\underline{\underline{L}}^T = \begin{bmatrix} \frac{\partial}{\partial x} & 0 & 0 & \frac{\partial}{\partial y} & 0 & \frac{\partial}{\partial z} \\ 0 & \frac{\partial}{\partial y} & 0 & \frac{\partial}{\partial x} & \frac{\partial}{\partial z} & 0 \\ 0 & 0 & \frac{\partial}{\partial z} & 0 & \frac{\partial}{\partial y} & \frac{\partial}{\partial x} \end{bmatrix}$$

Further, the kinematic equation is defined as:

$$\underline{\underline{\epsilon}} = \underline{\underline{L}} \underline{\underline{u}} \quad (2.30)$$

where $\underline{\underline{\epsilon}}$ contains the six strain components ($[\epsilon_{xx} \ \epsilon_{yy} \ \epsilon_{zz} \ \gamma_{xy} \ \gamma_{yz} \ \gamma_{zx}]^T$) and $\underline{\underline{u}}$ has the

three displacements components u_x , u_y and u_z . The general relation between stress and strain is defined as:

$$\underline{\dot{\sigma}} = \underline{\underline{M}} \underline{\dot{\epsilon}} \quad (2.31)$$

where $\underline{\dot{\sigma}}$ is the stress rate vector, $\underline{\dot{\epsilon}}$ is the strain rate vector and $\underline{\underline{M}}$ is the material stiffness matrix. Further, the equilibrium equation (2.29) is reformulated according to Galerkin's variation principle in weak form as follows:

$$\int \delta \underline{u}^T \left(\underline{\underline{L}}^T \underline{\sigma} + \underline{b} \right) dV = 0 \quad (2.32)$$

where $\delta \underline{u}$ is a kinematically admissible variation of displacements and V is volume.

Partial integration by Green's theorem is applied to the first term of Equation 2.32, and the following boundary integral known as the virtual work equation is created:

$$\int \delta \underline{\epsilon}^T \underline{\sigma} dV = \int \delta \underline{u}^T \underline{b} dV + \int \delta \underline{u}^T \underline{t} dS \quad (2.33)$$

where \underline{t} contains the three boundary traction components.

The stress state $\underline{\sigma}$ is developed by the following incremental procedure:

$$\underline{\sigma}^i = \underline{\sigma}^{i-1} + \Delta \underline{\sigma} \quad \text{where:} \quad \Delta \underline{\sigma} = \int \underline{\dot{\sigma}} dt \quad (2.34)$$

where $\underline{\sigma}^i$ is the present unknown stress state and $\underline{\sigma}^{i-1}$ is the known previous stress state. The stress rate $\underline{\dot{\sigma}}$ is integrated over a time increment t to obtain the stress increment $\Delta \underline{\sigma}$.

By regarding Equation 2.33 as the actual or present state i , the unknown present stresses $\underline{\sigma}^i$ is eliminated using Equation 2.34. As a result, the relation may be formulated as:

$$\int \delta \underline{\epsilon}^T \Delta \underline{\sigma} dV = \int \delta \underline{u}^T \underline{b}^i dV + \int \delta \underline{u}^T \underline{t}^i dS - \int \delta \underline{\epsilon}^T \underline{\sigma}^{i-1} dV \quad (2.35)$$

Element Discretisation

Next step is to apply finite element discretisation to the obtained relation. In FEM a continuum is divided into elements, in 3D volume elements. The elements consist of nodes with degrees of freedom (dofs) corresponding to discrete unknowns of problem. The degrees of freedom in

deformation theory correspond to displacements of the element. The finite element method relates the displacements \underline{u} to the discrete nodal values \underline{v} by shape functions (or interpolation functions) in the matrix \underline{N} . The relation is formulated as:

$$\underline{u} = \underline{N}\underline{v} \quad (2.36)$$

By inserting Equation 2.36 into Equation 2.30 the following relation to the strains is achieved:

$$\underline{\epsilon} = \underline{L}\underline{N}\underline{v} = \underline{B}\underline{v} \quad (2.37)$$

where \underline{B} becomes the strain interpolation matrix, relating the nodal displacements to the strains.

Discretised, Equation 2.35 may be formulated as:

$$\int (\underline{B}\delta\underline{v})^T \Delta\underline{\sigma} dV = \int (\underline{N}\delta\underline{v})^T \underline{b}^i dV + \int (\underline{N}\delta\underline{v})^T \underline{t}^i dS - \int (\underline{B}\delta\underline{v})^T \underline{\sigma}^{i-1} dV \quad (2.38)$$

$\delta\underline{v}^T$ can be placed outside the integrals, and the equation can be rewritten as follows if Equation 2.38 hold for any kinematically admissible displacement variation $\delta\underline{v}^T$:

$$\int \underline{B}^T \Delta\underline{\sigma} dV = \int \underline{N}^T \underline{b}^i dV + \int \underline{N}^T \underline{t}^i dS - \int \underline{B}^T \underline{\sigma}^{i-1} dV \quad (2.39)$$

Equation 2.39 is the discretised equilibrium condition, where the first two terms on the right sides are the present external force vectors. The last term on the right side is the internal reaction vector from the previous step. The external forces and the internal reaction should be balanced by the stress increment $\Delta\underline{\sigma}$.

Iterative Procedure

The stress-strain increment relation is often non-linear, and may not be directly calculated. Therefore, a global iterative procedure is introduced to achieve equilibrium in all points. If the stress-strain relation $\Delta\underline{\sigma} = \underline{M}\Delta\underline{\epsilon}$ is substituted into Equation 2.39, the following expression is introduced:

$$\underline{K}^i \Delta\underline{v}^i = \underline{f}_{ex}^i - \underline{f}_{in}^{i-1} \quad (2.40)$$

where $\underline{\underline{K}}$ is a stiffness matrix, $\Delta \underline{v}$ is the incremental displacement vector, \underline{f}_{ex}^i is the external force vector and \underline{f}_{in}^{i-1} is the internal reaction vector for the step number i . The formulation for the global iteration procedure is written as:

$$\underline{\underline{K}}^j \delta \underline{v}^j = \underline{f}_{ex}^i - \underline{f}_{in}^{j-1} \quad (2.41)$$

where j is the iteration number and i is the step number. $\delta \underline{v}$ is the sub-incremental displacements that makes up the incremental displacements for each step:

$$\Delta \underline{v}^i = \sum_{j=1}^n \delta \underline{v}^j \quad (2.42)$$

where n is the number of iterations in each step i . The stiffness matrix $\underline{\underline{K}}$ approximates the material behaviour. If $\underline{\underline{K}}$ is accurate fewer iterations are necessary to achieves equilibrium. A tolerated error is defined, which is used to determine if a solution is accurate enough or if a new iteration is necessary.

The stiffness matrix for linear-elastic response is defined as:

$$\underline{\underline{K}} = \int \underline{\underline{B}}^T \underline{\underline{D}}^e \underline{\underline{B}} dV \quad (2.43)$$

where $\underline{\underline{D}}^e$ is the elastic material matrix and $\underline{\underline{B}}$ is the strain interpolation matrix. The iteration process becomes robust when using an elastic stiffness matrix, provided no increase in material stiffness, even for non-associated plasticity models. Various techniques are implemented to improve the iteration, such as arc-length control, over-relaxation and extrapolation. For linear-elastic material models such as Mohr-Coulomb the elastic stiffness is especially suitable in the iteration procedure, since $\underline{\underline{K}}$ is only formed and decomposed before the first calculation step. (Brinkgreve et al., 2018)

Plasticity

The stress increments $\Delta \underline{\sigma}$ is found by Equation 2.34, and can be written as follows for differential plasticity models:

$$\Delta \underline{\sigma} = \underline{\underline{D}}^e (\Delta \underline{\epsilon} - \Delta \underline{\epsilon}^p) \quad (2.44)$$

where $\underline{\underline{D}}^e$ is the elastic material matrix and $\Delta \underline{\underline{\epsilon}}^p$ is the plastic strain increment vector. The strain increments $\Delta \underline{\underline{\epsilon}}$ are found using the expression $\Delta \underline{\underline{\epsilon}} = \underline{\underline{B}} \Delta \underline{\underline{v}}$.

The plastic strain increment $\Delta \underline{\underline{\epsilon}}^p$ is zero for elastic behaviour and non-zero for plastic behaviour, according to the following expression:

$$\Delta \underline{\underline{\epsilon}}^p = \Delta \lambda \left[(1 - \omega) \left(\frac{\partial g}{\partial \underline{\underline{\sigma}}} \right)^{i-1} + \omega \left(\frac{\partial g}{\partial \underline{\underline{\sigma}}} \right)^i \right] \quad (2.45)$$

where $\Delta \lambda$ is the plastic multiplier increment and g is the plastic potential. $\frac{\partial g}{\partial \underline{\underline{\sigma}}}$ is the partial derivative of the plastic potential with regard to the stresses. ω indicates the type of time integration, with $\omega = 0$ being explicit integration and $\omega = 1$ being implicit integration. Implicit integration is found to be favourable and is the utilised integration type, which reduces Equation 2.45 to:

$$\Delta \underline{\underline{\epsilon}}^p = \Delta \lambda \left(\frac{\partial g}{\partial \underline{\underline{\sigma}}} \right)^i \quad (2.46)$$

Equation 2.46 (or the flow rule) can be inserted into Equation 2.44 and further into Equation 2.34, which becomes:

$$\underline{\underline{\sigma}}^i = \underline{\underline{\sigma}}^{tr} - \Delta \lambda \underline{\underline{D}}^e \left(\frac{\partial g}{\partial \underline{\underline{\sigma}}} \right)^i \quad \text{where:} \quad \underline{\underline{\sigma}}^{tr} = \underline{\underline{\sigma}}^{i-1} + \underline{\underline{D}}^e \Delta \underline{\underline{\epsilon}} \quad (2.47)$$

where $\underline{\underline{\sigma}}^{tr}$ is an auxiliary stress vector (elastic or trial stresses). For a purely elastic material behaviour $\underline{\underline{\sigma}}^{tr}$ is the new stress state.

The plastic multiplier increment $\Delta \lambda$ can be solved for the yield criterion of the new stress state:

$$f(\underline{\underline{\sigma}}^i) = 0 \quad (2.48)$$

which lead to the following equation for perfectly plastic and linear hardening models:

$$\Delta \lambda = \frac{\underline{\underline{\sigma}}^{tr}}{d + h} \quad \text{where:} \quad d = \left(\frac{\partial f}{\partial \underline{\underline{\sigma}}} \right)^{\underline{\underline{\sigma}}^{tr}} \underline{\underline{D}}^e \left(\frac{\partial g}{\partial \underline{\underline{\sigma}}} \right)^i \quad (2.49)$$

where h is the hardening parameter, which is zero for perfectly plastic models and constant for linear hardening.

Element Formulation

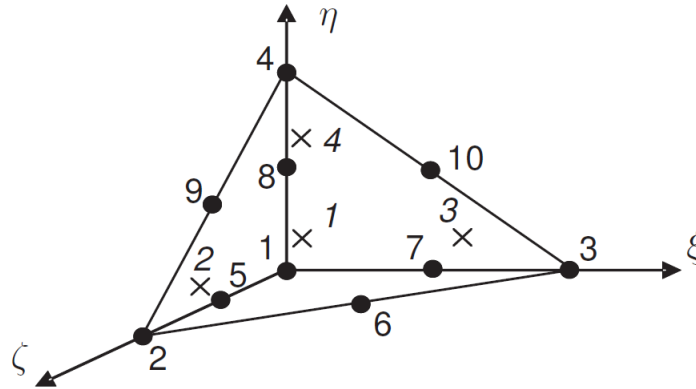


Figure 2.21: The 10-node tetrahedral element used by PLAXIS 3D, retrieved from (Brinkgreve et al., 2018). \times are integration points and \bullet are nodes.

In PLAXIS 2D the user may use 6-node triangular or 15-node triangular elements, which are area elements, while in PLAXIS 3D only the 10-node tetrahedral (volume) element is available. The 10-node tetrahedral element will be of focus here, also known as *Tet10*. The element can represent a second-order interpolation of displacements. Tetrahedral elements have three local axes/coordinates, ξ , η and ζ , as Figure 2.21 illustrates. The element has ten interpolation functions, which are functions of ξ , η and ζ :

$$N_1 = (1 - \xi - \eta - \zeta)(1 - 2\xi - 2\eta - 2\zeta)$$

$$N_2 = \zeta(2\zeta - 1)$$

$$N_3 = \xi(2\xi - 1)$$

$$N_4 = \eta(2\eta - 1)$$

$$N_5 = 4\zeta(1 - \xi - \eta - \zeta)$$

$$N_6 = 4\xi\zeta$$

$$N_7 = 4\xi(1 - \xi - \eta - \zeta)$$

$$N_8 = 4\eta(1 - \xi - \eta - \zeta)$$

$$N_9 = 4\eta\zeta$$

$$N_{10} = 4\xi\eta$$

Each node of the element has three degrees of freedom, which are u_x , u_y and u_z . Consequently, \underline{N}_i becomes the 3×3 -matrix defined as:

$$\underline{N}_i = \begin{bmatrix} N_i & 0 & 0 \\ 0 & N_i & 0 \\ 0 & 0 & N_i \end{bmatrix} \quad (2.50)$$

and the nodal displacements vector \underline{v} is:

$$\underline{v} = \begin{bmatrix} v_{ix} & v_{iy} & v_{iz} \end{bmatrix}^T \quad (2.51)$$

To calculate Cartesian strains from displacements, the interpolation functions are differentiated with regards to the global axis system with Cartesian coordinates. The Jacobian matrix J is used to define the relation between the local and the global (Cartesian) coordinate system. The relation between strains and nodal displacements is $\underline{\epsilon} = \underline{B}_i \underline{v}_i$, and \underline{B}_i is calculated as follows:

$$\underline{B}_i = \begin{bmatrix} \frac{\partial N_i}{\partial x} & 0 & 0 \\ 0 & \frac{\partial N_i}{\partial y} & 0 \\ 0 & 0 & \frac{\partial N_i}{\partial z} \\ \frac{\partial N_i}{\partial y} & \frac{\partial N_i}{\partial x} & 0 \\ 0 & \frac{\partial N_i}{\partial z} & \frac{\partial N_i}{\partial y} \\ \frac{\partial N_i}{\partial z} & 0 & \frac{\partial N_i}{\partial x} \end{bmatrix} \quad (2.52)$$

With the strain-displacement relation established, the element stiffness matrix may be estimated. The elastic stiffness matrix is as defined in Equation 2.43. To simplify the calculation, the stiffness matrix is calculated in the local coordinate system as:

$$\underline{K}^e = \int \underline{B}^T \underline{D}^e \underline{B} j dV^* \quad (2.53)$$

where j is the Jacobian determinant and V^* is the volume defined with the local axes.

Numerical integration is utilised to calculate over the volume according to the following general formulation:

$$\int \int \int F(\xi, \eta, \zeta) d\xi d\eta d\zeta \approx \sum_{i=1}^k F(\xi_i, \eta_i, \zeta_i) w_i \quad (2.54)$$

where F is a general function of the local coordinates and w_i is the weight factor for point i . PLAXIS uses Gaussian integration base on 4 sample points withing the tetrahedral element. Applied on Equation 2.53, the stiffness matrix is estimated by submatrices $\underline{\underline{K}}_{ij}^e$ as:

$$\underline{\underline{K}}_{ij}^e = \sum_k \underline{\underline{B}}_i^T \underline{\underline{D}}^e \underline{\underline{B}}_j w_k \quad (2.55)$$

If plastic soil deformations occur, only the elastic part of the soil stiffness is used in the stiffness matrix, since the plasticity is iteratively solved. (Brinkgreve et al., 2018)

Mohr-Coulomb Soil Model

The Mohr-Coulomb (MC) soil model is a linear elastic-perfectly plastic model, and is a simple 'first-order' approximation of soil behaviour. The five basic input parameters of the model represent the soil elasticity (E and ν), the soil plasticity (ϕ and c) and soil dilatancy (ψ). Hooke's law of isotropic elasticity is the basis of the linear elastic part of the model. The Mohr-Coulomb failure criterion forms the perfectly plastic part, with plastic yielding for a yield function $f = 0$. The yield surface is fixed and not affected by plastic straining.

The strains in an elastoplastic model contains an elastic part $\underline{\underline{\epsilon}}^e$ and a plastic part $\underline{\underline{\epsilon}}^p$:

$$\underline{\underline{\epsilon}} = \underline{\underline{\epsilon}}^e + \underline{\underline{\epsilon}}^p \quad (2.56)$$

By substitution into Hooke's law, the stress rates relates to the strains rates as:

$$\underline{\underline{\dot{\sigma}}} = \underline{\underline{D}}^e \underline{\underline{\dot{\epsilon}}}^e = \underline{\underline{D}}^e (\underline{\underline{\dot{\epsilon}}} - \underline{\underline{\dot{\epsilon}}}^p) \quad (2.57)$$

Plastic strain rates are proportional to the yield function differentiated with regards to the stresses. Therefore, it is possible to represent the plastic strain rates as vectors that are perpendicular to the yield surface, which is associated plasticity. However, using the MC yield criterion the associated plasticity overestimates the dilatancy. As a remedy, a plastic potential function g is added as an addition to the yield function f . Non-associated plasticity (or non-associated flow - NAF) occurs if $g \neq f$, i.e. when the dilatancy angle is not equal to the friction angle, $\psi \neq \phi$. Associated

flow (AF) is the case when $\psi = \phi$. The plastic strain rates can be defined as:

$$\underline{\dot{\epsilon}}^p = \lambda \frac{\partial g}{\partial \underline{\sigma}'} \quad (2.58)$$

where λ is the previously introduced plastic multiplier. $\lambda = 0$ for purely elastic behaviour and $\lambda > 0$ for plastic. Equation 2.58 is known as the flow rule with regards to strain rates. (Brinkgreve et al., 2018)

There are six yield functions in the MC soil model, defined as follows for principal effective stresses:

$$\begin{aligned} f_{1a} &= \frac{1}{2}(\sigma'_2 - \sigma'_3) + \frac{1}{2}(\sigma'_2 + \sigma'_3) \sin \phi - c \cos \phi \leq 0 \\ f_{1b} &= \frac{1}{2}(\sigma'_3 - \sigma'_2) + \frac{1}{2}(\sigma'_3 + \sigma'_2) \sin \phi - c \cos \phi \leq 0 \\ f_{2a} &= \frac{1}{2}(\sigma'_3 - \sigma'_1) + \frac{1}{2}(\sigma'_3 + \sigma'_1) \sin \phi - c \cos \phi \leq 0 \\ f_{2b} &= \frac{1}{2}(\sigma'_1 - \sigma'_3) + \frac{1}{2}(\sigma'_1 + \sigma'_3) \sin \phi - c \cos \phi \leq 0 \\ f_{3a} &= \frac{1}{2}(\sigma'_1 - \sigma'_2) + \frac{1}{2}(\sigma'_1 + \sigma'_2) \sin \phi - c \cos \phi \leq 0 \\ f_{3b} &= \frac{1}{2}(\sigma'_2 - \sigma'_1) + \frac{1}{2}(\sigma'_2 + \sigma'_1) \sin \phi - c \cos \phi \leq 0 \end{aligned}$$

where ϕ is the friction angle and c is the cohesion. For the yield function $f_i = 0$ as hexagonal cone represents the failure criterion in principal stress space, see Figure 2.22.

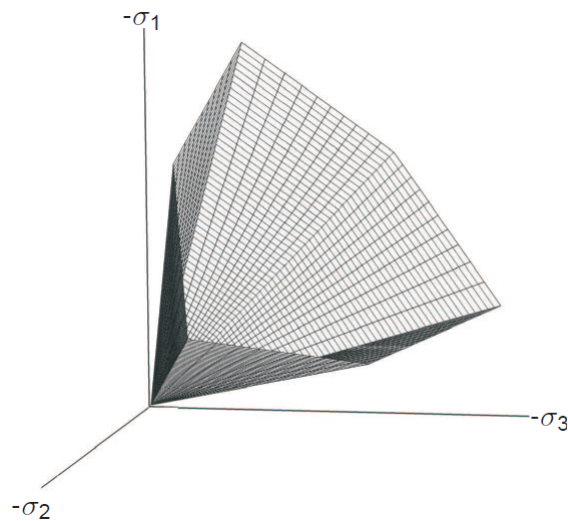


Figure 2.22: Fixed hexagonal cone illustrating MC failure surface with $c = 0$, retrieved from (Brinkgreve et al., 2018).

The plastic potential functions of the MC model are listed under for completeness:

$$\begin{aligned}
 g_{1a} &= \frac{1}{2}(\sigma'_2 - \sigma'_3) + \frac{1}{2}(\sigma'_2 + \sigma'_3) \sin \psi \\
 g_{1b} &= \frac{1}{2}(\sigma'_3 - \sigma'_2) + \frac{1}{2}(\sigma'_3 + \sigma'_2) \sin \psi \\
 g_{2a} &= \frac{1}{2}(\sigma'_3 - \sigma'_1) + \frac{1}{2}(\sigma'_3 + \sigma'_1) \sin \psi \\
 g_{2b} &= \frac{1}{2}(\sigma'_1 - \sigma'_3) + \frac{1}{2}(\sigma'_1 + \sigma'_3) \sin \psi \\
 g_{3a} &= \frac{1}{2}(\sigma'_1 - \sigma'_2) + \frac{1}{2}(\sigma'_1 + \sigma'_2) \sin \psi \\
 g_{3b} &= \frac{1}{2}(\sigma'_2 - \sigma'_1) + \frac{1}{2}(\sigma'_2 + \sigma'_1) \sin \psi
 \end{aligned}$$

where ψ is the dilatancy angle, which is used to model positive plastic volumetric strain increments. (Brinkgreve et al., 2018)

Potential Numerical Issues with Elasto-plasticity in FEM

Failure loads in FEM calculations may become overestimated with elasto-plastic soil models, such as the Mohr-Coulomb model. Nordal and Antonsen (1985) showed that a conflict between the plastic flow rule and the FE discretisation may occur, which may cause overshoot. The theoretical basis below is partly reproduced from (Nordal & Antonsen, 1985) and partly repeated from earlier subsections.

The yield criterion formulated in Equation 2.48 becomes the failure criterion since the ultimate stress state is studied. Moreover, no hardening is present for the collapse. The failure criterion, as a function of stresses $\underline{\sigma}$, is repeated as:

$$f(\underline{\sigma}) = 0 \quad (2.59)$$

and the plasticity is introduced with the previously defined flow rule, which provides a unique deformation mode:

$$d\underline{\epsilon}^p = d\lambda \frac{\partial g}{\partial \underline{\sigma}} \quad (2.60)$$

where $\underline{\epsilon}^p$ contains the plastic strains, λ is the plastic multiplier and g is the plastic potential.

Equation 2.56 shows how elasto-plastic theory assumes the strains $\underline{\epsilon}$ as the sum of elastic and plastic strains:

$$d\underline{\epsilon} = d\underline{\epsilon}^e + d\underline{\epsilon}^p \quad (2.61)$$

At failure for attempted loading the stress increments cannot have components outwards from the failure surface. Therefore, the following equation must be satisfied:

$$\frac{\partial f^T}{\partial \underline{\sigma}} d\underline{\sigma} = 0 \quad (2.62)$$

By reformulating Equation 2.57 the stress increments can be defined as:

$$d\underline{\sigma} = \underline{\underline{D}} d\underline{\epsilon}^e = \underline{\underline{D}} \left(d\underline{\epsilon} - d\lambda \frac{\partial g}{\partial \underline{\sigma}} \right) \quad (2.63)$$

which when used together Equation 2.62 creates the following elasto-plastic stress strain relation:

$$d\underline{\sigma} = \left[\underline{\underline{D}} - \frac{\underline{\underline{D}} \frac{\partial g}{\partial \underline{\sigma}} \frac{\partial f^T}{\partial \underline{\sigma}} \underline{\underline{D}}}{\frac{\partial f^T}{\partial \underline{\sigma}} \underline{\underline{D}} \frac{\partial g}{\partial \underline{\sigma}}} \right] d\underline{\epsilon} = \underline{\underline{D}}_{ep} d\underline{\epsilon} \quad (2.64)$$

where $\underline{\underline{D}}_{ep}$ is the new elasto-plastic matrix that relates the stresses and strains.

The flow rule in Equation 2.60 specifies the direction of plastic deformation. In 3D space six linear independent strain vectors are needed for completeness of the deformation modes, since $\underline{\epsilon} = [\epsilon_{xx} \ \epsilon_{yy} \ \epsilon_{zz} \ \gamma_{xy} \ \gamma_{yz} \ \gamma_{zx}]^T$. If $\underline{\epsilon}^p$ is one of these, five more linearly independent vectors are needed to complete Equation 2.61. The six deformation modes create complete the strain increment $d\underline{\epsilon}$, where only one controls the plastic deformation, $d\underline{\epsilon}^p$.

At failure there are no stresses to act as resistance against $\underline{\epsilon}^p$. Consequently:

$$\underline{\underline{\sigma}} = \underline{\underline{D}}_{ep} d\underline{\epsilon}^p = \left[\underline{\underline{D}} - \frac{\underline{\underline{D}} \frac{\partial g}{\partial \underline{\sigma}} \frac{\partial f^T}{\partial \underline{\sigma}} \underline{\underline{D}}}{\frac{\partial f^T}{\partial \underline{\sigma}} \underline{\underline{D}} \frac{\partial g}{\partial \underline{\sigma}}} \right] \left(d\lambda \frac{\partial g}{\partial \underline{\sigma}} \right) = \underline{\underline{0}} \quad (2.65)$$

Furthermore, the five remaining components will create purely elastic reactions:

$$\underline{\underline{D}}_{ep} d\underline{\epsilon}^e = \underline{\underline{D}} d\underline{\epsilon}^e - \frac{\underline{\underline{D}} \frac{\partial g}{\partial \underline{\sigma}} \frac{\partial f^T}{\partial \underline{\sigma}} \underline{\underline{D}}}{\frac{\partial f^T}{\partial \underline{\sigma}} \underline{\underline{D}} \frac{\partial g}{\partial \underline{\sigma}}} \left(\underline{\underline{D}}^{-1} d\underline{\sigma} \right) = \underline{\underline{D}} d\underline{\epsilon}^e \quad (2.66)$$

$d\underline{\epsilon}^e$ and $d\underline{\sigma}$ is here reduced to five 'dimensions'. As a results, the following equation holds for failure stress state:

$$d\underline{\sigma} = \underline{D}_{ep}\underline{\epsilon} = \underline{D}_{ep}d\underline{\epsilon}^e = \underline{D}d\underline{\epsilon}^e \quad (2.67)$$

This requires \underline{D}_{ep} to be singular, since $d\underline{\epsilon}^p$ is an eigenvector of \underline{D}_{ep} with an eigenvalue of is zero. To illustrate the elasticity of the components, the stress and strain components are formulated with six eigenvectors and eigenvalues:

$$\begin{aligned} d\underline{\sigma} &= d\sigma_1\underline{n}_1 + d\sigma_2\underline{n}_2 + \dots + d\sigma_6\underline{n}_6 \\ d\underline{\epsilon} &= d\epsilon_1\underline{n}_1 + d\epsilon_2\underline{n}_2 + \dots + d\epsilon_6\underline{n}_6 \end{aligned}$$

where \underline{n}_k is the unit eigenvectors of \underline{D}_{ep} with eigenvalues λ_k for each component $k = 1, 2, \dots, 6$. $d\sigma_k$ is value and \underline{n}_k is direction. For each component k the following relations are obtained:

$$\begin{aligned} d\sigma_k\underline{n}_k &= \underline{D}_{ep}d\epsilon_k\underline{n}_k \\ d\sigma_k &= (\underline{n}_k^T \underline{D}_{ep} \underline{n}_k) d\epsilon_k = \lambda_k d\epsilon_k \end{aligned}$$

These relations describe the resistance against the deformation mode defined by \underline{n}_k . With the \underline{n}_k that corresponds to the plastic deformation $\underline{\epsilon}^p$ at failure stress state, the eigenvalue becomes $\lambda_k = \underline{n}_k^T \underline{D}_{ep} \underline{n}_k = 0$, i.e. no resistance against plastic deformation. However, the rest of the eigenvalues λ_k are non-zero elastic moduli. Moreover, a symmetric matrix \underline{D}_{ep} is only obtainable for associated flow, i.e. when $\psi = \phi$.

The deformation mode defined in elasto-plasticity must be transferred to the finite element discretisation. As defined in Equation 2.37, the elements couple the nodal displacements with strains as:

$$d\underline{\epsilon} = \underline{B}d\underline{v} \quad (2.68)$$

Elasto-plastic theory defines the strains at failure for each point in the soil with Equation 2.60, while FEM defined the stress field for each element according to Equation 2.68. To model the elasto-plastic model with FEM, it is required at impending failure that:

$$d\underline{\epsilon} = \underline{B}d\underline{v} = d\lambda \frac{\partial \underline{g}}{\partial \underline{\sigma}} = d\underline{\epsilon}^p \quad (2.69)$$

This equation should be satisfied in all points within a soil element. However, the finite element method estimates the stiffness relations by numerical integration in the set integration points. The number of Gauss integration points for solving the equations affect the capability of the element to model pure plastic failure. The relation between the number of constraints (equations) and the number of available degrees of freedom (unknowns) should be assessed. The consequence of too many constraints may be that the system locks, and it becomes impossible to obtain a purely plastic failure mechanism. For some elements a reduced Gaussian integration rule may be a way of reducing the constraints. Necessary considerations may vary for different elements, and also locations in the meshed model. For example the number of available dofs in a corner of a restrained model may be reduced since the nodal displacements are fixed.

Nordal and Antonsen (1985) tested out several element types with various number of integration points. Each case was evaluated using a stiffness ratio factor, which measured the degree of elasticity (or plasticity) of the stiffness at failure. The results varied, where some cases showed a bad performance with a lot of elastic response. All cases expressed some elastic stiffness. However, some were satisfactorily.

As discussed by Nordal and Antonsen (1985), elasto-plastic soil models may overshoot collapse loads in finite element analyses. The conflict may arise if the shape functions and available degrees of freedom in an element struggles to exactly mode the plastic deformations defined by the flow rule. In the attempt to satisfy Equation 2.69, a 'false' elastic stiffness may occur in the numerical integration. Consequently, the 'added' stiffness may cause a failure convergence to overshoot.

Chapter 3

Literature Study - Articles and Research

Most of the following literature study was conducted as part of the project thesis completed in the autumn of 2019, which was the pre-study of this master thesis, see (Solli, 2019). Some alterations have been made to the summary and discussion of the studies. In addition, literature is added as supplementary knowledge, which is deemed relevant for the topic of the present study. The literature studies and their assumptions are discussed in the end of the chapter to avoid unnecessary repetition, since results and limitations may be similar.

Several studies have been carried out with the aim of quantifying 3D-effects (F_{3D}) for different geometries and conditions. Some have assessed simple slopes with finite width to evaluate the difference between 2D and 3D analyses. Others have studied slopes with three-dimensional curvature, both convex and concave. As more accurate calculation models and powerful software have developed, the understanding of these effects have increased. Especially the implementation of finite element (FE) programs have opened up for more accurate calculations. This can be used as a tool to assess the 3D-effects, along with limit equilibrium methods (LEM), limit analysis methods (LAM) and the finite difference method (FDM).

A range of notations and definitions are used in the various studies. New symbols found in article figures are attempted explained and connected with the slope definition in subsection 2.2.1, which is similar in the study by Jostad and Lacasse (2015). 3D-effect is defined as $F_{3D} = SF_{3D}/SF_{2D}$. However, some studies present the difference between 3D and 2D in percentage. Moreover, curved geometries may be compared with the 3D planar slope, instead of a 2D slope. These are still regarded as 3D-effects, due to the three-dimensionality of curvature.

3.1 3D-effects

Cavounidis (1987) stated that a three-dimensional slope always has a greater safety factor compared to the corresponding two-dimensional slope. This statement was supported by Duncan (1996), who summarised relevant studies that compared 2D and 3D slope stability analyses. All studies showed a 3D SF greater than 2D SF, with some exceptions with inaccurate assumptions. Therefore, the safety factor may become overconservative for a range of cases by using 2D analysis. Further, the back-calculated shear strength will be overestimated by neglecting 3D-effects.

Leshchinsky and Baker (1986) tested failure mechanisms when accounting for end effects (side shear resistance). It was pointed out that 2D and 3D analyses should result in the same safety factor for homogeneous soil with zero cohesion. Furthermore, the study indicated more prominent end effects for cohesive soils. The increased influence for cohesive soils were also found by Sun, Chai, Xu, and Qin (2017), where various slope geometries and material properties were analysed.

Wei et al. (2009) concluded that slope failures are most often 3D in reality, as a result of varying geometry and not completely homogeneous soil properties. To account for the three-dimensionality of a problem, 3D programs are developed. These are often based on limit equilibrium or limit analysis methods, or the strength reduction method (SRM). Examples of methods that use a strength reduction technique are FDM and FEM.

3.2 Finite Element Analysis - Fixed Width and Undrained Behaviour

Jostad and Lacasse (2015)

Jostad and Lacasse (2015) analysed different slope cases to assess the 3D-effects using a 2D LE and a 3D FE program. For the different cases the authors varied the slope inclination b , the ratio between slide width W and slope height H and the ratio between slide depth D and slope height H , see Figure 3.1. The 3D-effects (F_{3D}) were presented as a function of the inverse width ratio $\frac{1}{w} = \frac{H}{W}$. The study is used as an validation example in section 5.1, where the prerequisites and results are further discussed.

The 3D finite element code used was developed as a part of a research project. The analysis was conducted using clay and undrained shear strength. Jostad and Lacasse (2015) implied that

avoiding overconservative safety factors is the main motivation to include 3D-effects, and by this decrease project costs. Classical 2D LE analyses use the most critical cross-section, without taking varying topography and soil properties in the third dimension into account. The side shear or end effects are not included, which will for most cases result in failure at a lower SF than in reality.

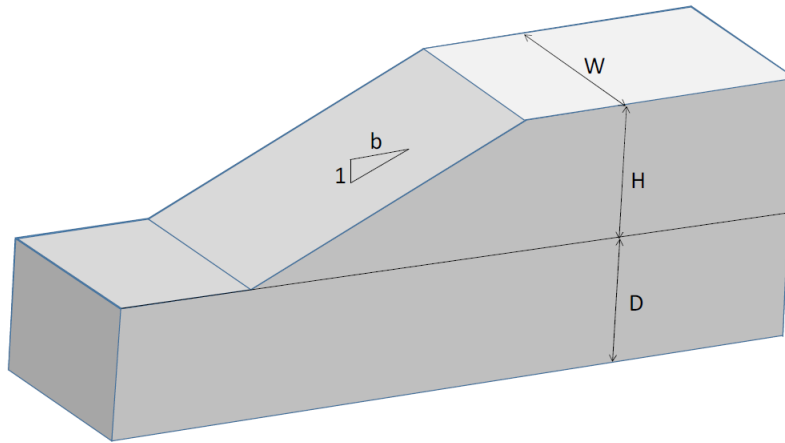


Figure 3.1: Geometry definition in 3D, where W = slide width, H = slope height, D = depth from slope toe to bottom boundary and b = slope inclination, retrieved from (Jostad & Lacasse, 2015).

The study was conducted on idealised geometries with different slip surface depths $d = \frac{D}{H}$, slide width $w = \frac{W}{H}$ in 3D and slope gradient b , see Figure 3.1. The soil strength was defined by a constant undrained shear strength $S_u = 20kPa$, with the elasto-plastic material model NGI-ADP. Moreover, $\gamma = 20kN/m^3$ and $\frac{S_u}{\gamma H} = 0.20$. Failure surfaces were found for $d = 0$ and $d = 1$, and the bottom boundary was fully fixed. Due to the constant undrained shear strength, the slip surface reached the bottom boundary and the failure mechanisms became comparable. The widths were fixed by restraining the model on one of the model side surfaces, and having a symmetrical slope model with the width $W/2$.

The elements used in the FE model were 20-noded brick elements with (2x2x2) reduced Gaussian. This choice of element properties was found suitable for a simple slope with undrained behaviour, with low shear locking. Furthermore, Jostad and Lacasse (2015) stated that the 10-noded tetrahedral elements, which are suitable for complex geometries, require significantly finer discretisation to avoid overshoot of resistance.

The 3D-effects ($F_{3D} = SF_{3D}/SF_{2D}$) were estimated by comparing the 3D finite element safety

factors with the 2D limit equilibrium safety factors. 3D-effects from the study are shown in Figure 3.2 for slip surface depth ratios of $d = 0$ and $d = 1$. The study showed that the 3D-effects increased with the inverse width ratio H/W , where $H/W = 0$ (or $w = W/H = \infty$) corresponds to plane strain as in 2D. When the ratio W/H is larger than 4, the 3D-effects are less than 1.2. For narrower slides of $W/H = 1$, the 3D safety factor was approximately between 1.5 and 2 times greater than the 2D LE safety factor.

Variations in effect are observed for the data sets included in Figure 3.2 and the rest of the study findings. Firstly, the 3D-effects increase for increased b , i.e. flatter slope. However, the difference between the slope inclinations decreases with higher width-height ratio w . Secondly, the difference between the two values of depth-height factor $d = D/H$ is significant. For $w = 1$ and $b = 2$, the F_{3D} is approximately 24% higher for $d = 1$ than $d = 0$. As w increases, the effect of slide depth decreases. It appears that inclination b and depth-height ratio d may have a significant influence on the 3D-effects.

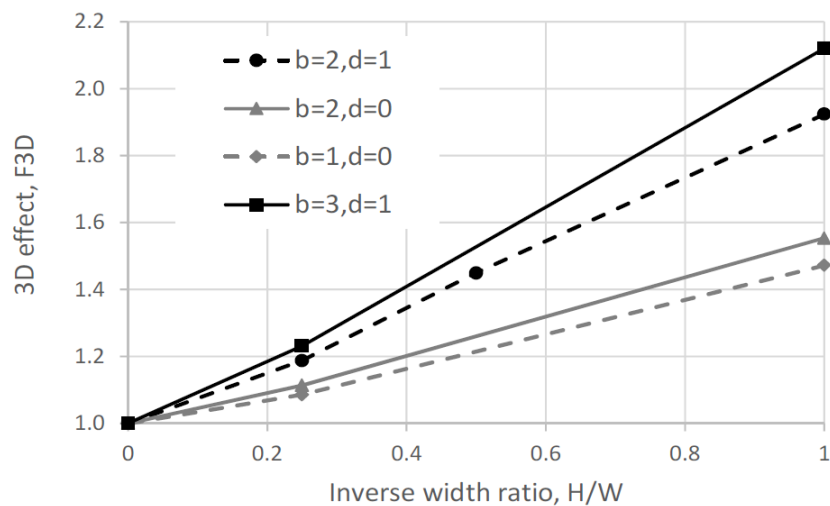


Figure 3.2: 3D-effects vs. the inverse width-height ratio H/W for different inclinations b equal 1, 2 and 3 and depth ratios $d = D/H$ equal 0 and 1, retrieved from (Jostad & Lacasse, 2015).

Jostad and Lacasse (2015) stated that the study is meant as help for estimating 3D-effects and to show when 3D FE analyses should be used. Including 3D-effects can reduce cost and risk, especially when the problem is complex and 3D in nature. FE analysis should be considered when the complexity increases. LE analysis may suffice for simpler geometries and soil conditions.

Griffiths and Marquez (2007)

Griffiths and Marquez (2007) studied the use of three-dimensional elasto-plastic finite element method (FEM) compared to other 2D and 3D methods. The width of the slope was varied for the 3D analyses and compared to 2D limit equilibrium (LE) analyses. Among the results, a comparison of safety factors between 3D FE and 2D LE as a function of the width-height ratio $w = W/H (= L/H)$. Some of the results are reproduced in the validation example in subsection 5.1.3 together with (Jostad & Lacasse, 2015) and the present study for comparison.

The 3D FE software used an elastic-perfectly plastic soil model with Mohr-Coulomb failure criterion. Soil resistance was defined by undrained shear strength. The strength was defined with the dimensionless parameter $\frac{S_u}{\gamma H} = 0.20$, and the dilatancy angle ψ was set to zero. The depth-height ratio $d = D/H$ was set as 0.5, and slope inclination as $b = 2$. The mesh contained 20-noded hexahedral elements with (2x2x2) reduced Gaussian. Griffiths and Marquez (2007) compared coarser and finer meshes, and studied how different boundary conditions affect the SF. The finer mesh gave a slightly lower value of SF. However, the difference did not exceed 2%.

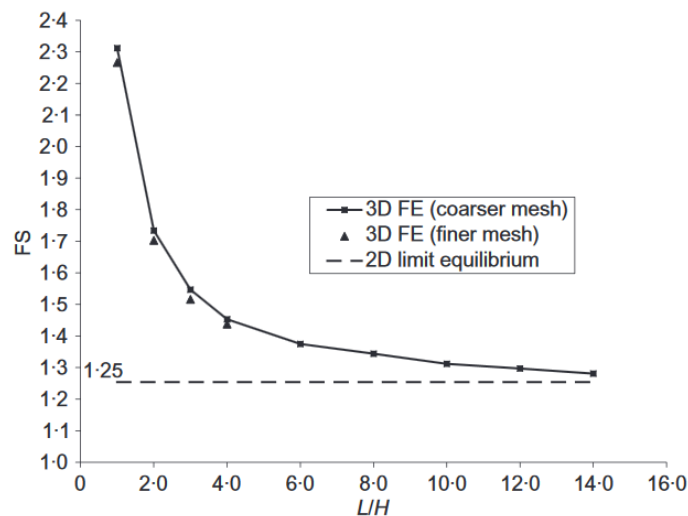


Figure 3.3: Comparison of 3D FE and 2D LE analyses for SF vs. width-height ratio $L/H = W/H$ with $\frac{S_u}{\gamma H} = 0.20$ and $b = 2$, retrieved from (Griffiths & Marquez, 2007).

Different width-height ratios W/H were analysed. The results show how the safety factor decreases with higher values of W/H and trends towards the 2D LE solution for the same cross-section, as shown in Figure 3.3. At $W/H = 4$ the 3D-effects (F_{3D}) are approximately 1.15 and

rapidly increasing for lower width-height ratios. The 3D-effect for $W/H = 1$ was approximately 1.8. Griffiths and Marquez (2007) emphasised the benefits of a 3D FE analysis. They concluded that a three-dimensional analysis is more realistic and helpful in understanding how slope failures occur and develop.

3.3 Limit Equilibrium Analysis - Fixed Width and Undrained Behaviour

Gens et al. (1988)

Gens et al. (1988) conducted three-dimensional limit equilibrium analyses of cohesive soils to assess end effects in slope stability. A cylindrical slip surface was assumed with various end surfaces. Analytical calculations were used to obtain design charts for simple evaluations of 3D-effects in slopes that contain fully cohesive soil, e.g. clay.

Equations for 3D safety factors were deduced analytically using limit equilibrium considerations for slope, toe and base failures. These assumed a rotational cylindrical slip surface and plane side surfaces (see Figure 3.4 (a)), with isotropic, homogeneous cohesive soil. The LEM type may be characterised as a single free-body procedure (Duncan et al., 2014), and is similar to the Swedish Circle method (Kalatehjari & Ali, 2013). A computer program is used to search after the critical slip surface for slide widths $L = W$, slope angles $i = \beta = \arctan(1/b)$ and depth factor D . D is defined as depth from crest to slide base DH divided by slope height H . The depth and depth factor definitions are different from what is described in subsection 2.2.1, where D is the depth below toe to slide base and depth factor is $d = D/H$. For instance, a depth factor $d = 1$ used by e.g. Jostad and Lacasse (2015) is equivalent to $D = 2$ in the study by Gens et al. (1988). See Figure 3.4 for geometrical definitions.

The use of plane ends of the cylindrical slip surface provided approximated estimates. Furthermore, Gens et al. (1988) tested several shapes of curved ends to find critical failure mechanisms, where plane ends gave a higher safety factor compared to curved sides. Figure 3.5 shows a 3D cylindrical slide with curved ends, where total slide width $W = L$ is the sum of cylinder width l_c and width of both end shapes l_e . The curved end analyses led to 'power curves', which yield lower safety factors compared to other geometries. Ellipsoidal ends are the best description of these critical sides surfaces.

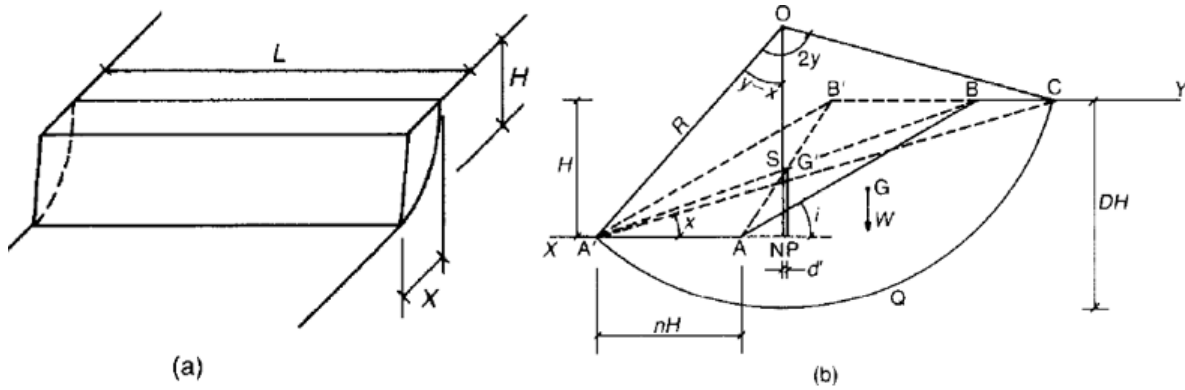


Figure 3.4: (a) 3D slope with height H and a cylindrical slide of width $L = W$ with plane ends. (b) 2D cross-section with relevant geometrical parameters, such as height H , depth from crest to slide base and slope angle $i (= \beta)$.

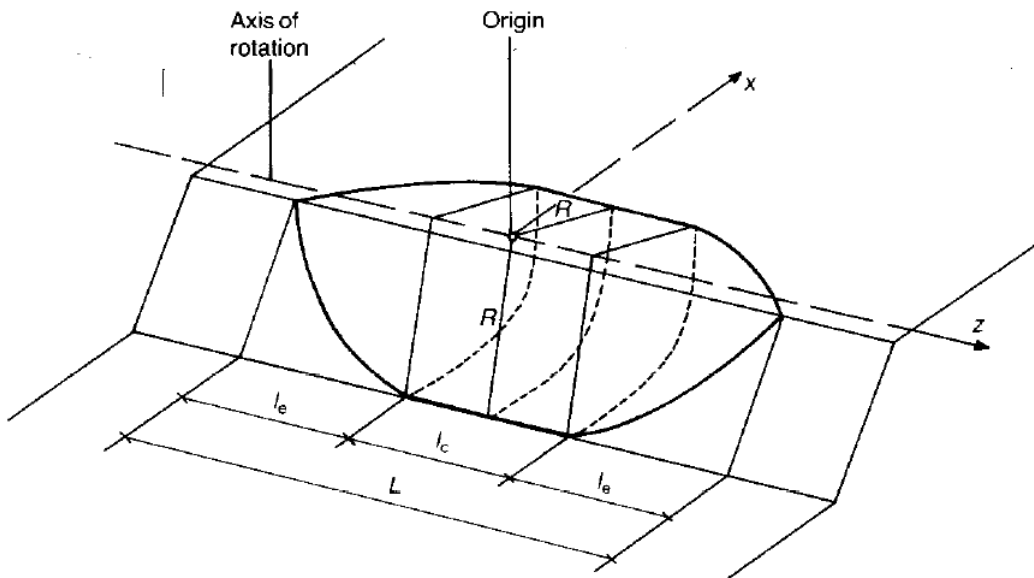


Figure 3.5: 3D cylindrical slide with curved ends, retrieved from (Gens et al., 1988). The slip surface is rotated around the axis of rotation, with a radius R from surface to origin. Total slide width $W = L = l_c + 2l_e$, where l_c is the width of the cylindrical surface and l_e is the width of the end shapes.

Figure 3.6 shows the difference between 3D SF (F_3) and 2D SF (F_2) for various end surface curves. (a) is for a slope angle of 30° and depth factor $D = 1$ (or $d = 0$). (b) is for a slope angle of 90° and any depth factor D . Plane ends yield the largest safety factors, while power curves yield the lowest. Moreover, the curves illustrate the rapid increase of 3D-effect for narrower slides. The 3D-effects for power curve ends in Figure 3.6 (a) appear similar to those obtained by Jostad and Lacasse (2015) using $d = 0$ and $b = 2$ ($\approx \beta = i = 26.57^\circ$). Gens et al. (1988) obtained a 3D-effect

slightly below 1.6 for $W/H = L/H = 1$ and approximately 1.13 for $W/H = 4$. Jostad and Lacasse (2015) obtained a 3D-effect (F_{3D}) of 1.55 for $W/H = 1$ and 1.11 for $W/H = 4$ for $d = 0$. Values of Gens et al. (1988) were slightly higher.

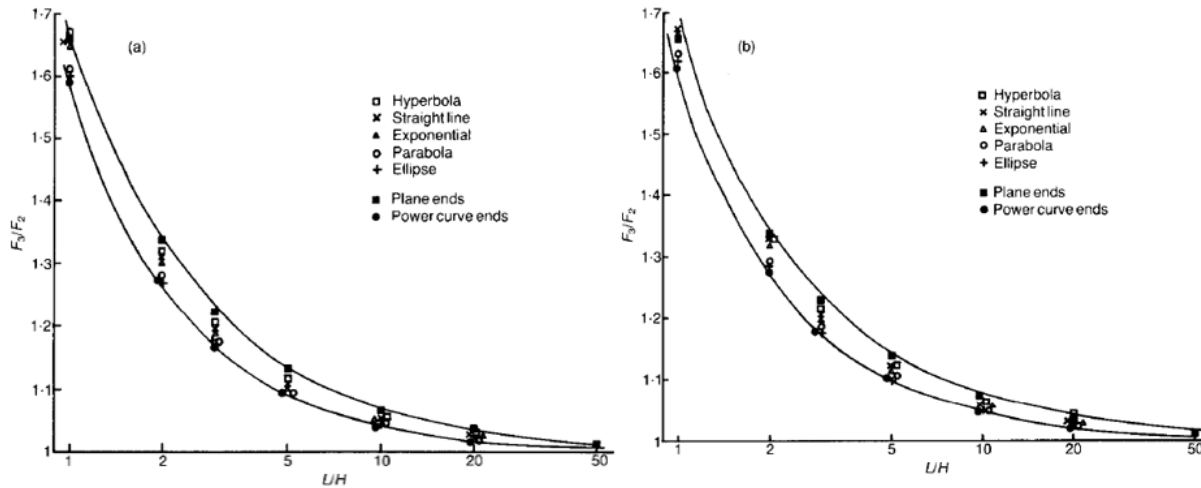


Figure 3.6: 3D-effects with various end surface curves for (a) slope angle $i = 30^\circ$ and $D = 1$ and (b) slope angle $i = 90^\circ$ and any D , retrieved from (Gens et al., 1988). The ratio between 3D SF (F_3) and 2D SF (F_2) is found along the vertical axis and the width-height ratio $W/H = L/H$ long the horizontal axis.

The 'power curves' and optimisation techniques were used to establish charts with the stability number $\frac{S_u}{F\gamma H}$ as output. Depth factor D and slope angle i are input parameters for the charts that correspond to a width-height ratio W/H (L/H in the paper). The charts are based on simplifications and may be used as an approximated assessment of three-dimensional slope stability.

A couple of cases are used to compare the values from the charts to other studies. Figure 3.7 shows a chart for $w = W/H = 1$, which for depth-height ratio $d = 1$ ($D = 2$ in the paper) and a slope inclination $b = 2$ (slope angle $\approx 26.57^\circ$) provides a stability number $\frac{S_u}{F\gamma H} \approx 0.084$. S_u is the undrained shear strength, F is the safety factor (SF), γ is the soil unit weight and H is the slope height. In (Jostad & Lacasse, 2015) $\frac{S_u}{\gamma H}$ was set as 0.20. This value provides a safety factor $SF = 2.38$ according to the chart by Gens et al. (1988) for $w = 1$. The same soil properties gave a safety factor of 2.27 in the analysis by Jostad and Lacasse (2015). The safety factors are similar, however, some deviation is present. The result obtained using the chart may provide an overestimate of the three-dimensional SF.

Cases with $w = 2$ and $w = \infty$ are also compared. With the same conditions as mentioned above,

except the width-height ratio, the stability number for $w = 2$ is obtained as $\frac{S_u}{F\gamma H} \approx 0.113$ from the relevant chart by Gens et al. (1988). This results in a safety factor approximately 1.77, which is close to $SF = 1.71$ obtained by Jostad and Lacasse (2015). However, still a higher value. The last case to be compared is an infinitely wide slope ($w = \infty$), where Jostad and Lacasse (2015) obtained a safety factor of 1.18. The chart gives a stability number $\frac{S_u}{F\gamma H} \approx 0.168$, which provides a safety factor of 1.19. The safety factors of the two studies approach each other as W/H increase, which may imply a greater uncertainty for narrower slides in the charts by Gens et al. (1988). As stated the solutions are limited by the assumption of slip surface and the approximated end surface shapes in the three-dimensional slope geometry.

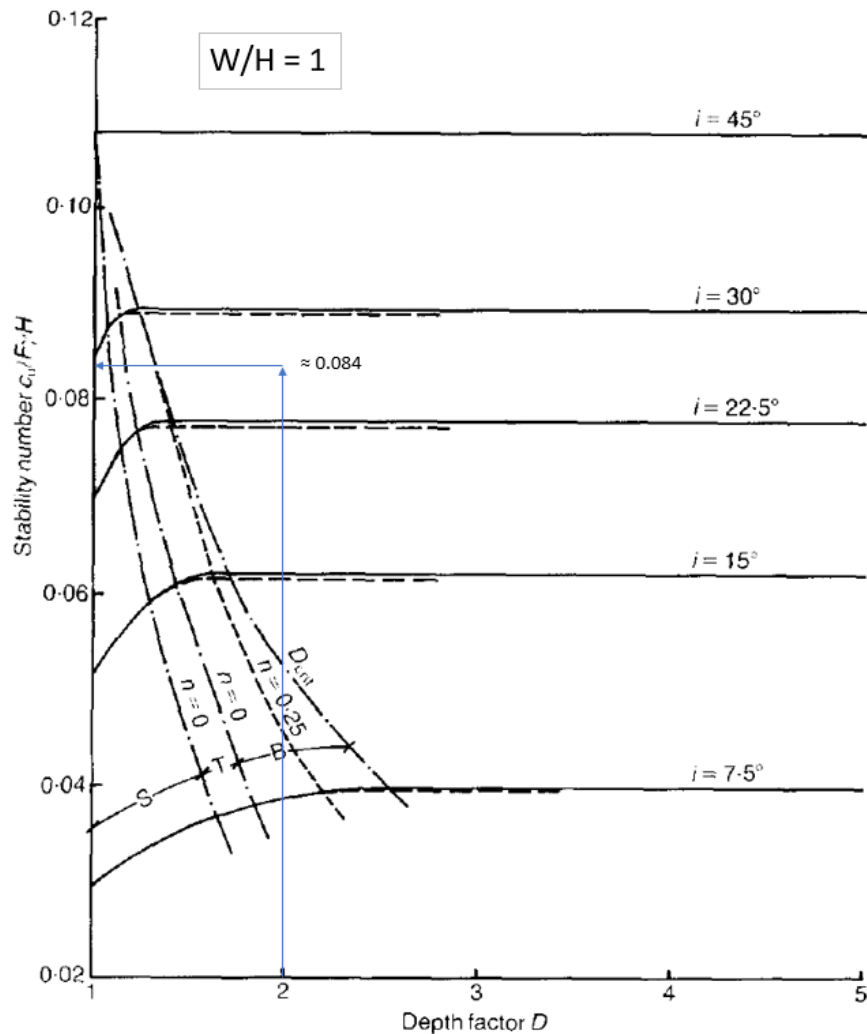


Figure 3.7: Stability number chart for $w = W/H = 1$ depending on depth factor D and slope angle i , retrieved from (Gens et al., 1988). c_u is undrained shear strength S_u , F is 3D safety factor, γ is soil unit weight and H is slope height.

3.4 Upper Bound Limit Analysis - Fixed Width and Undrained Behaviour

Michalowski and Drescher (2009)

Michalowski and Drescher (2009) studied three-dimensional slope stability using upper bound Limit Analysis Method (LAM). The upper bound limit analysis was completed using the kinematic approach, which is analytic. Furthermore, the most critical mechanism was found by analytical or numerical optimisation. Both cohesive-frictional (drained) and cohesive (undrained) cases were analysed. Rotational failure mechanisms were assumed for both the drained and the undrained analyses. Critical values of $\frac{\gamma H}{S_u}$ for a range of slope angles and width-height ratios $W/H = B/H$ were presented.

The kinematic approach of limit analysis was used to find critical values of $\frac{\gamma H}{S_u}$, with the Mohr-Coulomb yield criterion to define failure. An upper bound solution was obtained by the kinematic method, where limit load or resistance is evaluated for perfectly plastic materials. Bounds can be found with respect to various factors affecting the stability, such as the slope height, external loads or soil weight. The potential failure mechanism is defined by a kinematically admissible velocity field from the affecting elements. Admissible means that the velocity field strain rates are required to satisfy the flow rule of the failure criterion. Moreover, the boundary conditions must be satisfied by the velocities.

The upper bound limit load or height is obtained by setting the work along an admissible failure surface from external forces (weight) greater than or equal to internal stresses. Michalowski and Drescher (2009) evaluated the critical height by using the dimensionless $\frac{\gamma H}{c}$, where γ is the soil unit weight, H is the slope height and c is the cohesion. Cohesion c equals undrained shear strength S_u for undrained conditions. The safety factor can be found as $SF = \frac{c}{c_d} = \frac{\tan \phi}{\tan \phi_d}$, where c_d and $\tan \phi_d$ are the critical strength values for the slope to become unstable.

Different rotational failure mechanisms that are kinematically admissible are considered for drained and undrained soil conditions. The rotational failure surfaces suggested for drained and undrained material are a curvilinear cone (horn) and a curved cylinder (torus), respectively. Only a brief review of the undrained failure mechanism is provided here, which is simple compared to the drained construction due to no volume change of the soil. As a consequence, any rotational surface will satisfy the requirements for an admissible failure surface. Michalowski

Figure 3.10 presents critical values of $\frac{\gamma H}{S_u}$ for different slope angles β and width-height ratios $w = W/H = B/H$. The upper bound solution is obtained by numerical optimisation for the various geometrical parameters of the slide mechanism, where the minimum value of $\frac{\gamma H}{S_u}$ is found. The critical value is denoted $\left(\frac{\gamma H}{S_u}\right)_d$. A decrease in $\left(\frac{\gamma H}{S_u}\right)_d$ leads to a decrease in SF, since the safety factor can be found by multiplying $\left(\frac{\gamma H}{S_u}\right)_d$ with the actual value of $\frac{S_u}{\gamma H}$.

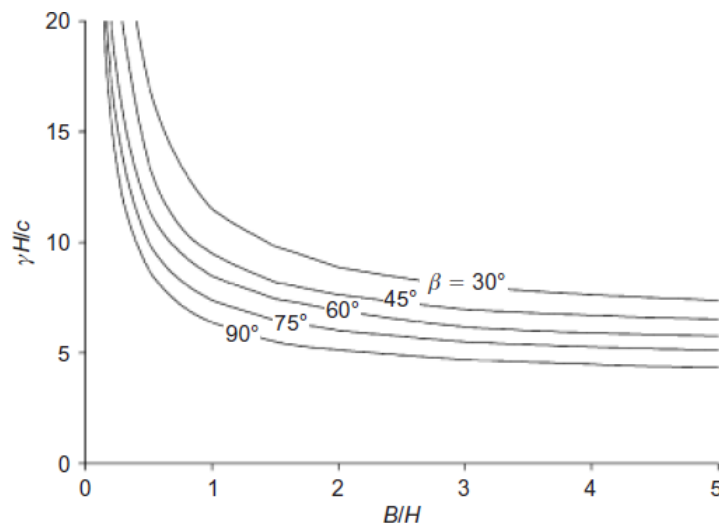


Figure 3.10: Critical values of $\frac{\gamma H}{c} = \frac{\gamma H}{S_u}$ for various slope inclinations and width-height ratios $B/H = W/H$ ($B = W$) for purely cohesive soil ($\phi = 0$), retrieved from (Michalowski & Drescher, 2009).

Similar to other previous, the results obtained by Michalowski and Drescher (2009) illustrates a decreasing SF for decreasing width-height ratio. Moreover, the rate of change is more significant for lower values of W/H , especially for $W/H < 2$. To verify the results, the actual value of $\frac{S_u}{\gamma H}$ is defined as 0.2 similar to the studies by Jostad and Lacasse (2015) and Griffiths and Marquez (2007). However, the commonly utilised slope inclination $b = 2$ approximates to a slope angle $\beta = 26.57^\circ$, and $\beta = 30^\circ$ is therefore a slightly steeper slope in comparison. A couple of safety factors for $\beta = 30^\circ$ are calculated as follows to compare with other studies. Width-height ratio $W/H = 1$ provides $\left(\frac{\gamma H}{S_u}\right)_d \approx 12$, which gives $SF = 12 \times 0.2 = 2.4$. Further, $W/H = 4$ provides $\left(\frac{\gamma H}{S_u}\right)_d \approx 7.7$, which gives $SF = 7.7 \times 0.2 = 1.54$.

The mentioned findings are not directly comparable with studies such as those by Jostad and Lacasse (2015) or Griffiths and Marquez (2007). Michalowski and Drescher (2009) suggested a toe failure mechanism, while Jostad and Lacasse (2015) and Griffiths and Marquez (2007) used base and/or slope failures. If compared to the slope angle $\beta = 26.57^\circ$ ($b = 2$), the slope angle $b =$

30° should provide slightly lower safety factors for the same slope and soil properties. Moreover, the safety factors for a toe failure should be in-between the safety factors of slope ($d = 0$) and base ($d > 0$) failure, which is supported by stability charts (see Figure 2.12). The mentioned width-height ratio examples satisfy this requirement. Jostad and Lacasse (2015) obtained $SF = 2.27$ for $w = 1$ and $d = D/H = 1$, and $SF = 2.51$ for $w = 1$ and $d = 0$. The safety factor of 2.4 by Michalowski and Drescher (2009) fits well in-between. Furthermore, for $w = 4$ Jostad and Lacasse (2015) obtained $SF = 1.40$ for $d = 1$ and $SF = 1.79$ for $d = 0$. $SF = 1.54$ by Michalowski and Drescher (2009) for toe failure fit reasonably well. However, the interval is wide and does not provide a rigorous verification. In addition, the study is limited by the assumption of a toe failure. In reality, a set of soil and slope properties could develop a deeper base slide. The assumption of toe failure may then overestimate the safety factor.

3.5 Limit Equilibrium Analysis - Translational Slide and Drained Behaviour

Stark and Eid (1998)

Stark and Eid (1998) evaluated the performance of three-dimensional slope stability methods in practice. Available 3D limit equilibrium (LE) slope stability software was assessed to determine limitations when not including side shear resistance for a translational slide. Moreover, it was assessed how 2D and 3D analyses change with soil strength properties and side resistance.

The study used various 2D and 3D software based on LE considerations, with the methods Simplified Janbu, Simplified Bishop and Spencer. These programs did not consider shear resistance on the vertical sides of the slope slide. The slope was defined as shown in Figure 3.11, where the slide sides are assumed vertical. As illustrated, the vertical columns along the sides are only subjected to shear resistance along the base and not the sides. The slope was modelled to achieve a translational slide, which is pictured in Figure 3.11 with a planar base failure surface. A lower and an upper soil layer was created, with properties and inclinations that would initiate a translational slide. The slide mass consisted of the upper payer. The lower layer had a small downward inclination in the sliding direction, and was meant to imitate a natural bedding plane or a landfill liner.

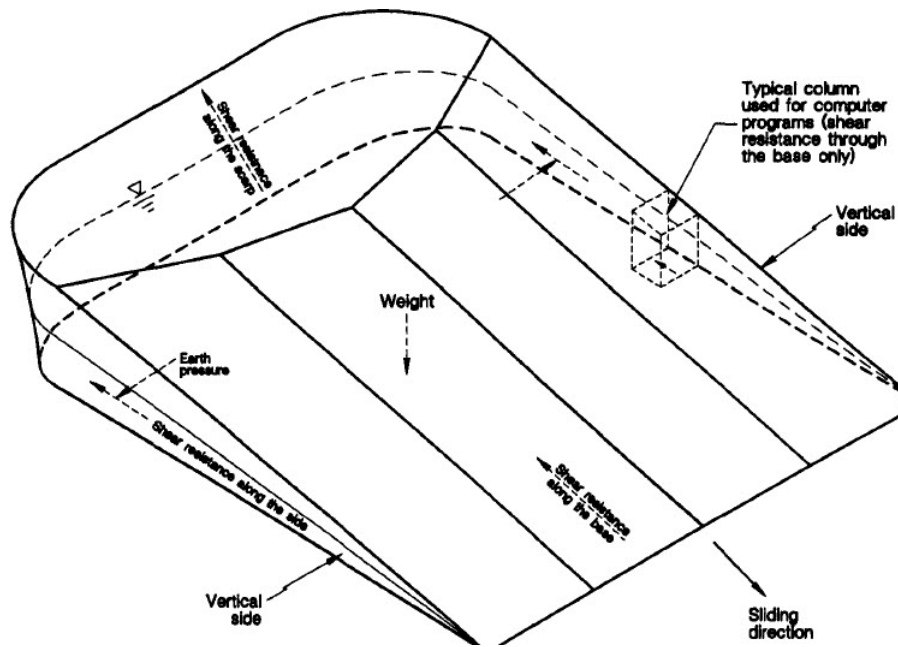


Figure 3.11: The slope defined for a translational slide with the acting shear resistances and rounded back-corners, retrieved from (Stark & Eid, 1998).

The model input was altered to include a shear force to simulate the actual resistance in 3D. To create the shear resistance, an imaginary layer with different strength properties was proposed only on the slide sides. This material had friction angle equal zero and cohesion from the at-rest earth pressure $K_0 = 1 - \sin \phi'$ on the slide sides. This cohesion was defined as:

$$c'_i = K_0 \sigma'_v \tan \phi' \quad (3.1)$$

Where σ'_v is the average vertical effective stress over the side depth and ϕ' is the secant friction angle of the upper material. The vertical sides of the slide mass were given a small outward inclination to obtain a row of columns in the analyses, which includes the effect of cohesion.

Adding the side resistance led to approximately 13% increase of safety factor compared to the 3D analyses without side shear. The different LE methods provided similar safety factors. Moreover, the difference between 3D SF and average 2D SF (from different slide cross sections) without side resistance is small. Stark and Eid (1998) emphasised the importance of conducting three-dimensional analysis with side resistance to avoid overestimated shear strength when back-calculating failure.

Arellano and Stark (2000)

Arellano and Stark (2000) implemented side shear resistance in 3D LE software to emphasise the importance of three-dimensional analysis in practice, as a continuation from the study of Stark and Eid (1998). Side resistance was implemented by using earth pressure coefficient K_0 and stresses at the sides of the slide. Similar material properties and layering was used as in (Stark & Eid, 1998).

To obtain the side shear force, Arellano and Stark (2000) multiplied cohesion c' from the imaginary layer with the area of the vertical slide side. External horizontal and vertical shear force equivalents of the imaginary material resistance were placed at the centroid of the two vertical sides of the slide. The translational slide was defined as in Figure 3.12, with sharp back-corners. The programs and methods are similar to what Stark and Eid (1998) used in their study. The variation of 3D-effects was presented, depending on material friction angle, slope angle and width-height ratio W/H .

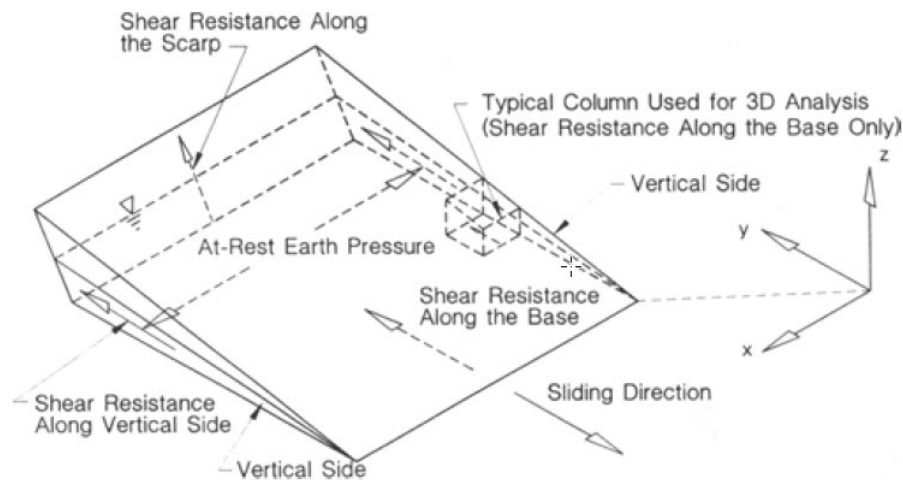


Figure 3.12: The slope defined for a translation slide with the acting shear resistances and sharp back-corners, retrieved from (Arellano & Stark, 2000).

As Figure 3.13 shows, the 3D-effects are considerable when including the shear resistance (end effects) in the 3D model. $F_{3D} = SF_{3D}/SF_{2D}$ (3D-effect) decreases with increasing W/H , with a significant effect for $W/H < 4$. The explanation for the trend is that decreased width provides less slide mass, and also less shear surface under the slide. For vertical sides the side resistance remains the same and obtains a greater influence compared to the driving force of weight.

Furthermore, the influence of end effects increases for decreasing slope inclination, see Figure 3.13. The 3D/2D safety factor ratio is approximately 1.30 for inclination $b = 1$ (1H:1V) and approximately 3.2 for $b = 5$ (5H:1V) when using the at-rest earth pressure coefficient K_0 and $W/H = 1$. The reason for the large variation of 3D-effects is partly due to an increase in side area when inclination flattens and slope length increases. A larger side area results in more shear resistance. The difference between the inclinations decreases with increasing W/H , as the slide mass to side area relation decreases. Moreover, limitations associated with choice of earth pressure coefficient in a slide may influence the discrepancy in 3D-effects. This is further studied in (Akhtar & Stark, 2017).

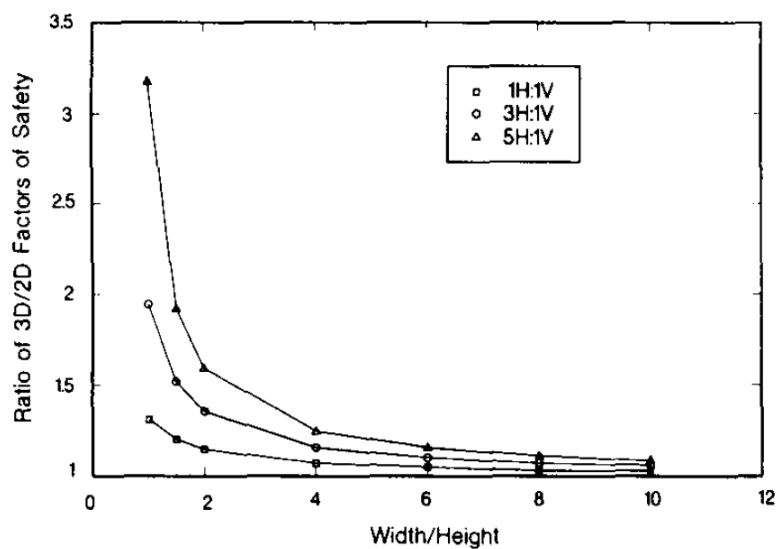


Figure 3.13: Comparison of the effects of shear resistance in 3D analysis, with SF_{3D}/SF_{2D} vs. W/H plotted for different inclinations, retrieved from (Arellano & Stark, 2000).

Akhtar and Stark (2017)

Akhtar and Stark (2017) evaluated the importance of side resistance in three-dimensional stability analysis by comparing LE, FD and FE programs for 2D and 3D. At rest (K_0) and active (K_A) earth pressure coefficients were used to establish side shear resistance in 3D LE analyses. The paper presents how different methods, coefficients and slope geometries affect the ratio of 3D/2D safety factor or 3D-effects. The study is a further continuation of the studies of Stark and Eid (1998) and Arellano and Stark (2000), extended to use of FDM, FEM and LEM with active earth pressure coefficient K_A .

Akhtar and Stark (2017) wanted to verify the use of at-rest earth pressure coefficient K_0 to obtain the shear resistance, which was used by Stark and Eid (1998) and Arellano and Stark (2000). Therefore, Akhtar and Stark (2017) conducted 2D and 3D analyses with FE software PLAXIS 3D and FD software FLAC/FLAC3D to achieve more realistic results. 2D and 3D LE analyses were conducted using CLARA-W.

To implement the side resistance in the 3D LE analysis, the earth pressure coefficients were calculated as $K_0 = 1 - \sin \phi'$ and $K_A = \frac{1 - \sin \phi'}{1 + \sin \phi'}$. The suggested in-between earth pressure coefficient is defined as $K_\tau = 0.5(K_0 + K_A)$. K_τ was implemented to simulate the side shear forces as used in (Arellano & Stark, 2000). Moreover, the slope model and material properties are similar to those used by Arellano and Stark (2000). FE and FD modelling are carried out differently compared to LE, e.g. it is important to model boundaries correctly when using FE and FD programs. In FE and FD models the side boundaries must be fully fixed to obtain the wanted slide width. The maximum width for 3D LE models with vertical columns are automatically restricted to the designed model width. More information on the adaption of models between the methods is found in (Akhtar & Stark, 2017).

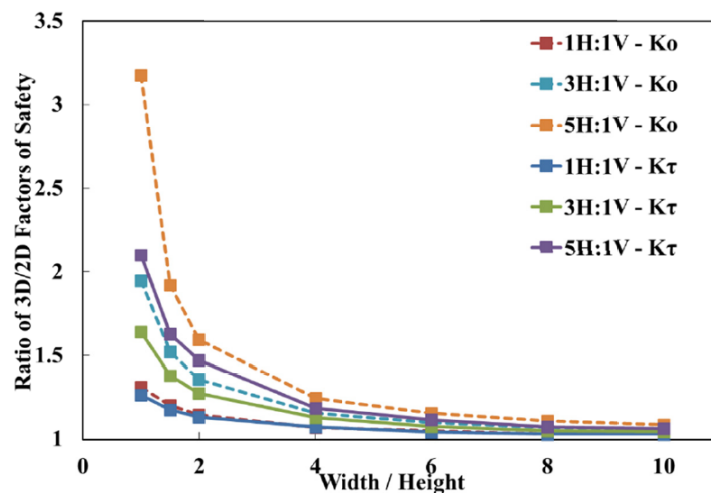


Figure 3.14: Comparison of the effects of shear resistance in 3D-analysis using K_τ and K_0 , with SF_{3D}/SF_{2D} SF vs. W/H plotted for different inclinations, retrieved from (Akhtar & Stark, 2017).

The analyses were presented as a comparison of SF_{3D}/SF_{2D} and width-height ratios for different inclinations. Figure 3.14 shows the effects of inclinations when using the in-between earth pressure coefficient K_τ to determine shear resistance compared to the at-rest earth pressure co-

efficient K_0 in LE calculations. The narrower slides show significant difference between the two earth pressure coefficient, especially for the flatter slopes. Still, the flatter slopes led to greater 3D-effects, due to the larger side area.

The choice of an in-between earth pressure coefficient K_τ is according to Akhtar and Stark (2017) supported by field observations. It is observed that the slide mass is cracked near the surface and the cracks shrink with depth. This may imply that an active earth pressure coefficient K_A matches the behaviour near the surface, while an at-rest coefficient K_0 is a better match near the slide mass base. Therefore, K_τ could be an appropriate average value for simulating the side shear resistance in three-dimensional limit equilibrium calculations.

Figure 3.15 presents the results from FE, FD and LE analysis using K_0 , K_τ and K_A . The inclination is 5H:1V. FE and FD analyses show a similar trend compared to the 3D LE analyses. FE results are slightly lower than FD-results, and are used as lower and upper bounds, respectively. For $W/H = 1$, the FE analysis obtained SF_{3D}/SF_{2D} equal to 2.04 and the FD analysis obtained 2.05. For this width-height ratio, both the LE analyses with K_0 and K_A are outside the bounds. The $LE(K_0)$ SF is as high as 3.2, while the $LE(K_A)$ SF is less than 2. Higher W/H values provided less difference between the LE results and stayed inside the bounds.

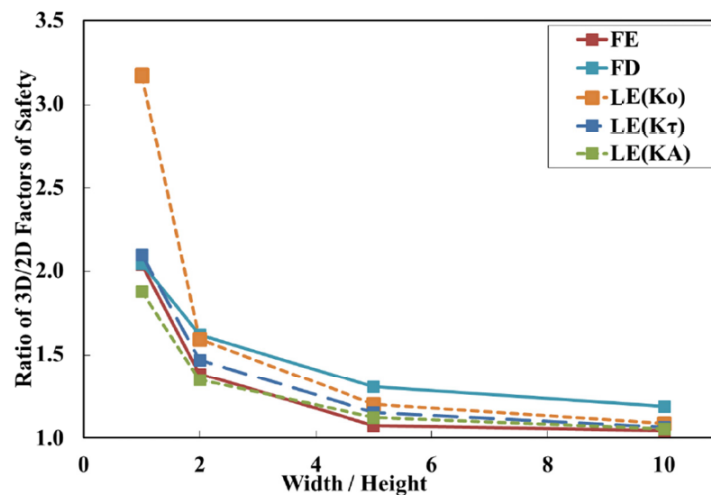


Figure 3.15: Comparison of the effects of shear resistance in 3D LE analysis with FE and FD, where SF_{3D}/SF_{2D} vs. W/H is plotted, retrieved from (Akhtar & Stark, 2017).

LE calculations using K_τ provide reasonable estimates for shear resistance according to Akhtar and Stark (2017). The $\frac{3D}{2D}$ ratios for SF fit inside the bounds for all W/H values, and are in-

between the overestimated K_0 results and underestimated K_A results. The trend of decreasing 3D-effects using side resistance for increased W/H ratio remains unchanged.

A translational slide with varying width-height ratios and inclinations shows how simple slope geometry impacts the 3D-effects. If the width of a slide is decreased, the mass is increased. However, for the same inclination the side area remains the same. Therefore, the ratio of slide mass and side area decreases. Consequently, the side resistance obtains a greater influence on the safety factor and the 3D-effects increase. Similar for a change in inclination, since flatter slopes have increased side area. The increase in side area results in greater influence of the side shear forces on the slide, and thus increased 3D-effects.

3.6 Finite Difference Analysis - Curved Geometry and Drained Behaviour

Kelesoglu (2015)

Kelesoglu (2015) evaluated the three-dimensional effects in slope stability by using the finite difference method (FDM). Various stability factors related to 3D problems were studied, such as convex and concave curvatures. The results of the analyses were presented as a comparison between safety factors obtained for plane, convex and concave slopes. Moreover, how SF changes with the curvature radius was assessed.

The analyses were conducted using FDM with the strength reduction method (SRM) to find the safety factor. A fine meshing configuration was found to be a suitable option. The soil properties and failure criterion were defined with the linear elastic-fully plastic Mohr-Coulomb model. Drained analyses were conducted using various sets of soil properties. The models were given boundary conditions that restrained displacements in all directions in the bottom of the model. The surfaces on the side, front and back of the model were restrained in the direction perpendicular to the surface.

Kelesoglu (2015) used seven cases with different slope inclinations b , soil unit weights γ , cohesions c , friction angles ϕ and groundwater levels GW . Furthermore, the effect of associated flow was studied. Both analyses with associated flow (AF) with a dilatancy angle equal to the friction angle and non-associated flow (NAF) with zero dilatancy angle were included. A small difference in SF was observed, where AF analyses resulted in slightly greater safety factors.

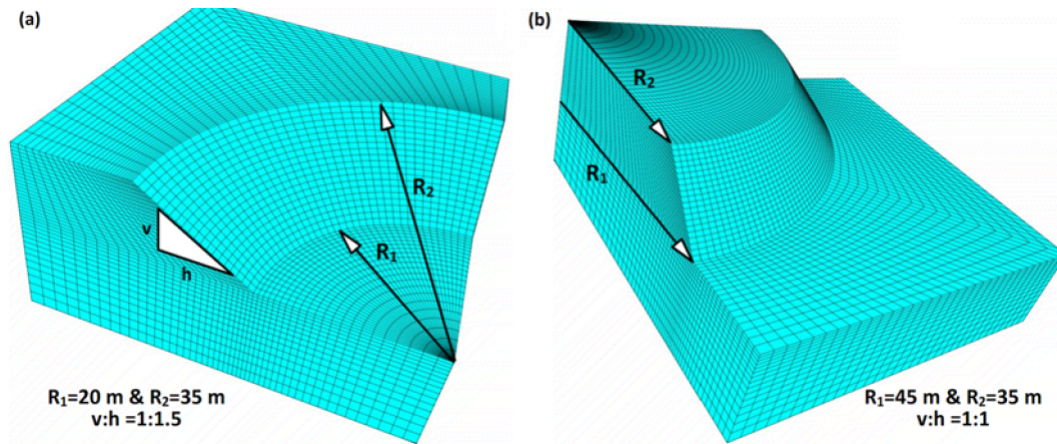


Figure 3.16: Example of a (a) concave slope (left) and a (b) convex slope (right), retrieved from (Kelesoglu, 2015). R_1 and R_2 are the curvature radii from the axis of rotation to the slope toe and slope crest, respectively. $v : h$ is the slope inclination equivalent to $1 : b$ for inclination parameter b .

To define the influence of curved slope surfaces, a series of analyses were conducted with varying geometry for a 90° curved model ($\alpha = 90^\circ$). Curvature radius R_{av} and inclination $v : h = 1 : b$ are the main variables that were compared to the normalised safety factor. R_{av} is the average radius for toe radius R_1 and crest radius R_2 , $R_{av} = \frac{R_1 + R_2}{2}$, from the axis of revolution. Figure 3.16 illustrates a concave slope example (left) and a convex slope example (right). The normalised SF is defined as the obtained 3D curved surface SF divided by the safety factor of a planar slope. Figure 3.17 shows the findings from the study.

The analyses completed by Kelesoglu (2015) show a significant influence of curvature radius R_{av} on the 3D safety factor. For concave curvatures with $R_{av} < 20 \text{ m}$ the stabilising effect ranges between 15% and 25%. With R_{av} between 20 m and 90 m the effect ranges between 5% and 10%. Convex slopes did not provide significant effects. However, some stabilising was observed, and slightly increasing with decreasing R_{av} . Furthermore, it is difficult to observe a clear difference in 3D-effects between the various sets of soil properties, due to the large selection and similar values. Some variations are visible, and the data is scattered by a few percent. However, the effect of each attribute cohesion c , friction angle ϕ , inclination b ($v : h$) and groundwater level GW is hard to evaluate.

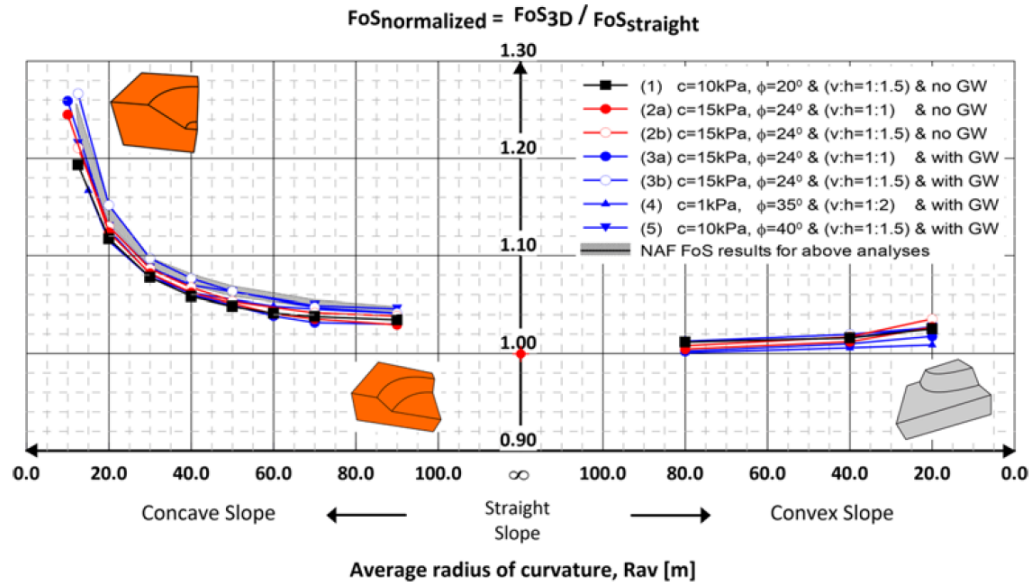


Figure 3.17: Normalised SF vs. curvature radius R_{av} for concave and convex slopes, retrieved from (Kelesoglu, 2015). Several sets of geometrical and geotechnical properties are included. Infinite radius implies a planar slope.

Zhang et al. (2013)

Y. Zhang et al. (2013) studied the effect of complex geometries on three-dimensional slope stability, using the Finite Difference Method (FDM) with a strength reduction technique (SRM). Various cases were analysed, and included geometries such as curving slope surfaces and turning corners. Among the findings, the paper presents safety factors for different curvatures and boundary conditions.

The analyses with the FD code used elastic-perfectly plastic soil with Mohr-Coulomb failure criterion. The associated flow (AF) rule was included with a dilatancy angle ψ equal to the friction angle ϕ . SRM was used to find the safety factor. Three slope examples were utilised, with drained behaviour and soil properties as reproduced in Table 3.1. Various mesh sizes and forms were tested, which showed that the safety factor ranged widely for the alternatives. Both hexahedral (8-noded) and tetrahedral (4-noded) elements were tested with coarse, optimised and fine mesh refinements. The value of SF varied remarkably between the two elements forms, where the tetrahedral element provided significantly higher values of SF. The hexahedral elements were used, because they were found to be more accurate and time saving for the relevant analyses.

Table 3.1: Material properties for examples used in (Y. Zhang et al., 2013).

Material properties	Example 1 - $b = 0$ (vert.)	Example 2 - $b = 1$	Example 3 - $b = 2$
Soil unit weight, γ	17.64 kN/m^3	20 kN/m^3	18.8 kN/m^3
Young's modulus, E	10 MPa	10 MPa	10 MPa
Poisson's ratio, ν	0.25	0.25	0.25
Cohesion, c	24.5 kPa	20 kPa	29 kPa
Friction = Dilatancy angle, $\phi = \psi$	20°	20°	20°

Y. Zhang et al. (2013) stated several reasons for the performance and choice of element type. In general, fewer nodes result in lower accuracy and calculation time. For the same element size the hexahedral element has more nodes than the tetrahedral, and finer discretisation provides more elements and nodes. For the same model scale and mesh configuration, the hexahedrons provide less elements and nodes compared to the tetrahedrons. Therefore, time and memory is saved for hexahedral elements. Further, the hexahedral element deforms at a lower strain energy state, and is thus more accurate than the tetrahedral. In addition, the grid discretisation using tetrahedral elements in FDM becomes less uniform compared to hexahedral. Consequently, greater discretisation errors may occur for tetrahedrons.

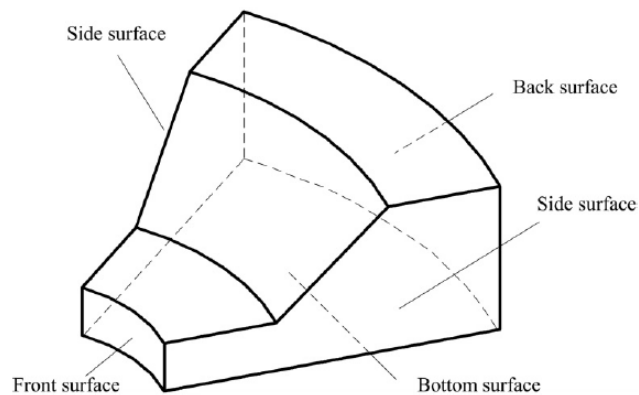


Figure 3.18: Boundary surfaces for a 3D (concave) slope model, retrieved from (Y. Zhang et al., 2013).

The 3D models had side surface boundary conditions defined as smooth-smooth (SS), rough-smooth (RS) or rough-rough (RR), see Figure 3.18. Smooth means that the displacements are restrained only in the direction normal to the surface, while rough (fully fixed) implies restrained in all directions. The bottom boundary was fully restrained, while back and front surfaces were restrained normally. Rough-smooth (RS) means that one side is smooth and one is rough, which

is used for half-models of RR, where the model is symmetrical about the smooth surface.

Effect of Curved Slope Surface

One slope type in the study was characterised by simple curved slope surface, see (Y. Zhang et al., 2013) for how the degree of curvature is presented. Figure 3.19 presents selected findings including safety factors and shear strain contours. Convex, concave and common (plane) surfaces were tested with different side surface boundary conditions. Using the SS boundary, both convex and concave surfaces are more stable. However, the effect is less than 3% compared to the common slope. With RR boundaries the effects range between -10% and $+11\%$ compared to the common slope, where the effects increase with concavity.

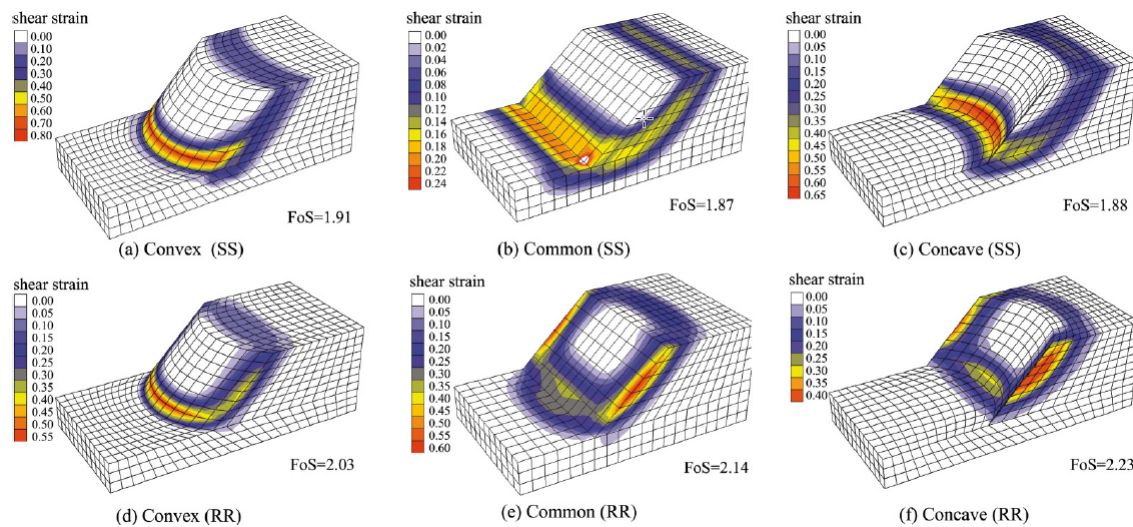


Figure 3.19: Results for a curved slope surface with inclination $b = 1$, retrieved from (Y. Zhang et al., 2013). Results include shear strains and safety factor (FoS) for convex and concave curvature with either smooth-smooth or rough-rough boundaries.

Figure 3.19 shows certain differences between the effects obtained with SS and RR boundaries. A positive stabilising effect is observed for the smooth-smooth boundary conditions, i.e. only fixed perpendicular to the side surfaces. Figure 3.19 illustrates how the slip surface shape is similar to the shape of the curved slope surface. Consequently, the contact area between the slide mass and stable mass for the curved slopes is greater compared to the common slope, due to the curving slip surface. For the rough-rough (fully fixed) cases the failure surface changes and is fixed inside the boundaries. This leads to a change in slide mass volume, which becomes

larger for the convex case compared to the common and concave slopes. As a consequence, a significant destabilising (negative) effect was found compared to the common slope, which was as high as 10%. A significant stabilising effect was found for the concave rough-rough cases, due to less slide mass in the concave curvature within the restrained boundaries.

Effect of Turning Arc

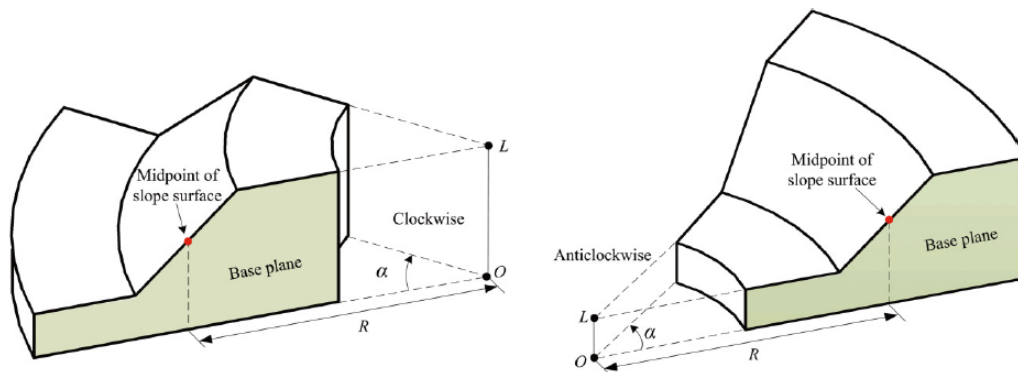


Figure 3.20: Geometry definition for convex (left) and concave (right) arch, retrieved from (Y. Zhang et al., 2013). The base plane is rotated with an angle α about the OL axis. R is the radius from OL to the slope surface midpoint.

Another slope surface type is the turning arc (see Figure 3.20), with curvature angles $\alpha = 45^\circ$, $\alpha = 90^\circ$ and $\alpha = 180^\circ$. The study obtained lower safety factors for convex arches with vertical slope compared to the common slope (planar), where destabilising effects increased from SS to RR boundary conditions. It increased to a positive effect for the slopes with inclination $b = 1$ and $b = 2$. The SF for the concave surface is greater than the planar slope SF for all cases. The stabilising effect of the concave slopes is greater than of the convex slopes. The safety factor increases from SS boundary to RR boundary. For RS and RR boundary conditions, the SF decreases with larger curvature angles α . A change in curvature angle α does not affect the SF for slopes with smooth-smooth boundaries, due to symmetry. One set of results for turning arches is shown in Figure 3.21 for $b = 2$, where restraining effects were observed for all curved slopes.

Y. Zhang et al. (2013) showed that convex and concave surfaces may influence stability with varying degree, depending on slope steepness, arch angle and boundaries. A concave surface will give a higher safety factor than a planar slope. However, the degree varies for the boundary conditions and inclinations. A convex surface may result in a lower SF than the planar slope. Under the right conditions and geometry the study showed that curvature may be beneficial.

Moreover, the impact of side restraints is reduced as the slide model is widened. The effects are simply explained by changes in slip surface area and slide mass volume when the geometry and boundary conditions are altered. More turning corners and forms are studied in the paper.

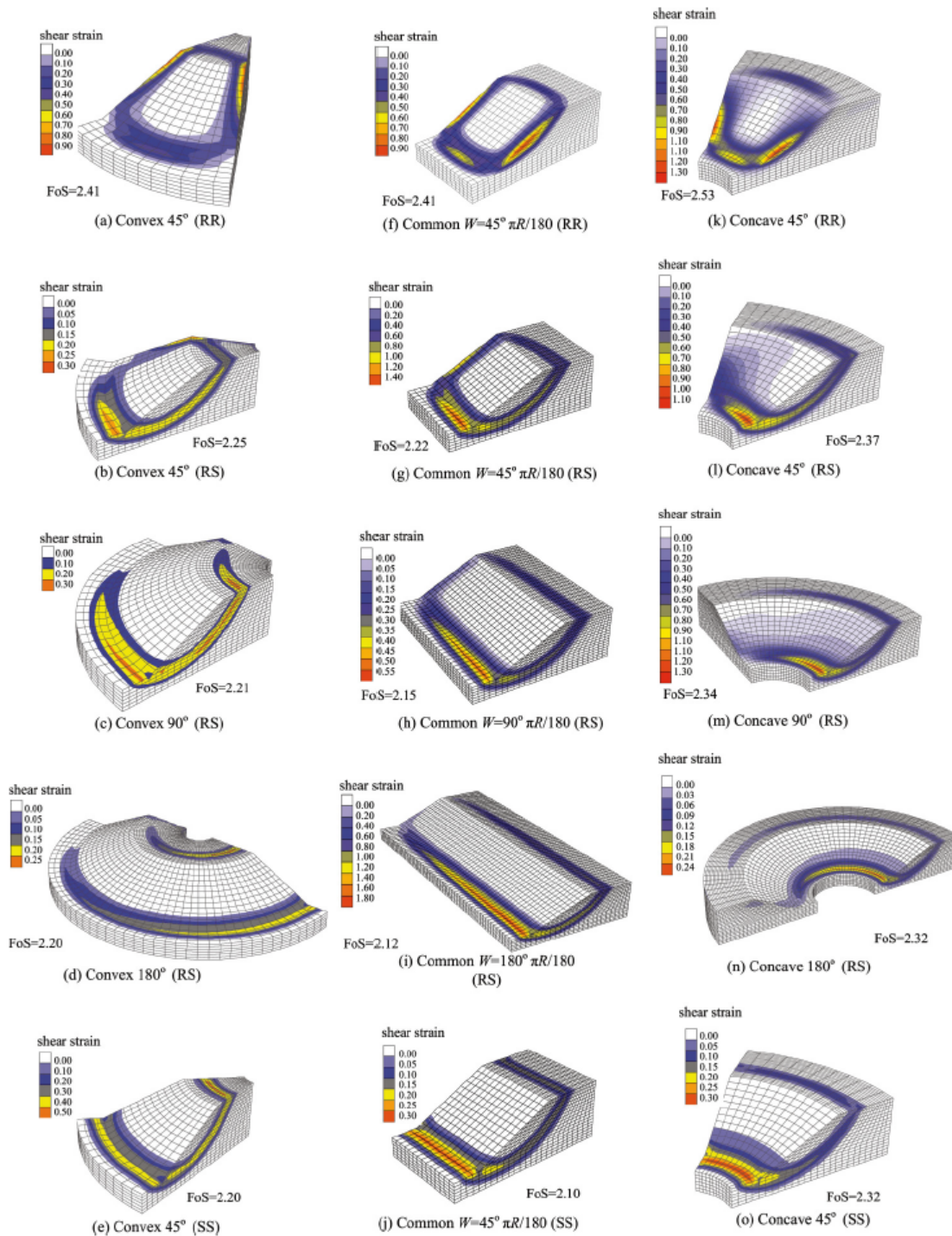


Figure 3.21: Results for curved arches with inclination $b = 2$, retrieved from (Y. Zhang et al., 2013). Results include shear strains and safety factor (FoS) for curvatures with SS or RR boundaries.

3.7 Finite Element Analysis - Curved Geometry and Drained Behaviour

Nian et al. (2012)

Nian et al. (2012) conducted a three-dimensional slope stability analysis for the assessment of geometric effects, using the finite element method (FEM) with a strength reduction technique (SRM). 3D slopes with varying geometrical attributes were analysed, such as turning corners/arcs, slope angles and curvatures. The results included impact on the obtained safety factors for the geometries with various restraining boundaries.

Analyses were conducted using the finite element program Abaqus. The soil model was defined as elastic-perfectly plastic with Mohr-Coulomb failure criterion. Material properties of the slope were defined with friction angle $\phi' = 20^\circ$, cohesion $c' = 40 \text{ kPa}$, dilatancy angle $\psi = 0$, Young's modulus $E' = 100 \text{ MPa}$, Poisson's ratio $\nu' = 0.3$ and unit weight $\gamma = 20 \text{ kN/m}^3$. The model mesh consisted of 20-noded hexahedral elements with reduced integration.

Effect of Turning Corner Angle

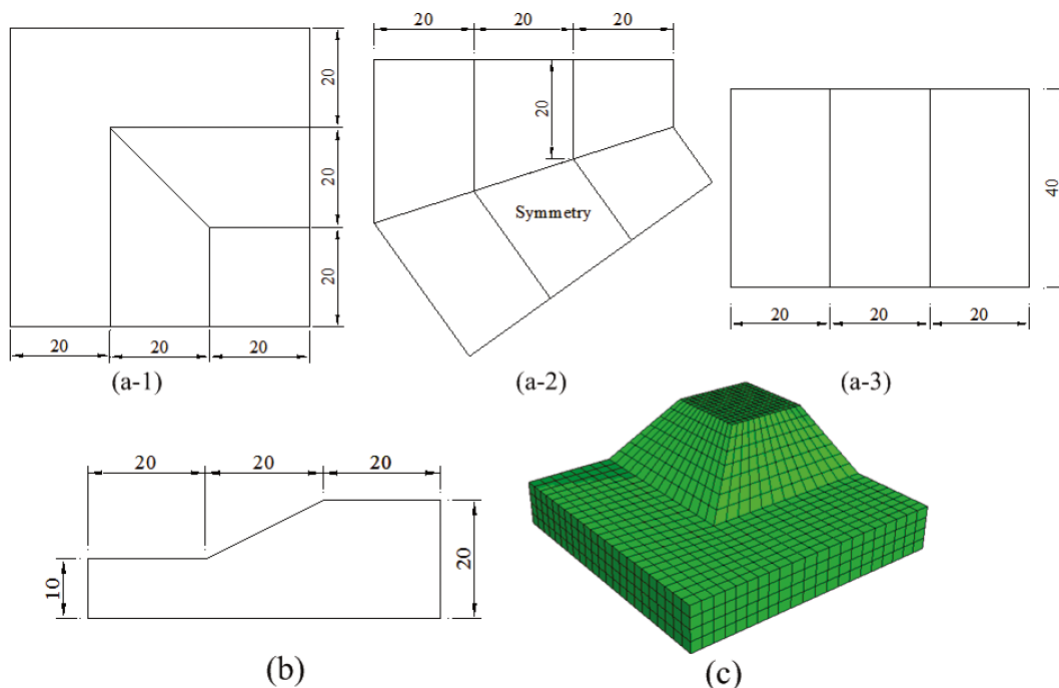


Figure 3.22: 3D turning corners with slope inclination $b = 2$, retrieved from (Nian et al., 2012). (a-1) is the 90° corner, (a-2) is the 135° corner and (a-3) is the 180° corner (planar slope). (b) shows the 2D profile and (c) is the meshed 90° tuning corner slope.

To assess the effects of turning corner angles, three cases were evaluated for a given slope inclination. In practice, turning corners could be constructed for instance at the intersection of two embankments. 90°, 125° and 180° (planar slope) corners were analysed with unrestrained (SS), semi-restrained (RS) and fully restrained (RR) boundary conditions, which acted on the slope side surfaces. Figure 3.22 describes the geometry of the tuning corner slopes with inclination $b = 2$. (a-1) is the 90° corner, (a-2) is the 135° corner and (a-3) is the 180° corner or planar slope. (b) shows the 2D profile and (c) is the meshed 90° tuning corner slope.

Safety factors for a slope inclination of $b = 2$ (or 1V:2H) are reported in Table 3.2 together with the plane strain solutions. Increase in corner angle (from 90°) leads to a decreasing SF for all boundaries. The difference in SF is less than 5% between 180° and 90°. For fully restrained boundaries, the safety factors are less than 10% higher compared to unrestrained. Moreover, the safety factors for the 3D analyses are greater than for the plane strain solution, especially for fully restrained.

Table 3.2: Safety factors for convex turning corners with inclination $b = 2$, reproduced from (Nian et al., 2012).

Turning corners of slope	Safety factor		
	Unrestrained (SS)	Semi-restrained (RS)	Fully restrained (RR)
90°	2.690	2.710	2.860
135°	2.655	2.695	2.810
180° (planar slope)	2.590	2.655	2.780
Plane strain solution	2.555	2.555	2.555

Figure 3.23 shows the 3D-effects (F_{3D}) of convex turning corners with inclination $b = 2$ for rough-rough (RR), rough-smooth (RS) and smooth-smooth (SS). The 3D-effect is defined as the the 3D safety factor divided by the plane strain solution, $F_{3D} = SF_{3D}/SF_{2D}$. The plots show how the effects decrease with increasing convex corner angle for all boundary conditions. Moreover, the fully fixed (RR) boundary conditions provide a significantly higher effect compared to the RS and SS boundaries. The reason is the narrower slides caused by the restraints, which provides less slide mass compared to the change in slip surface area.

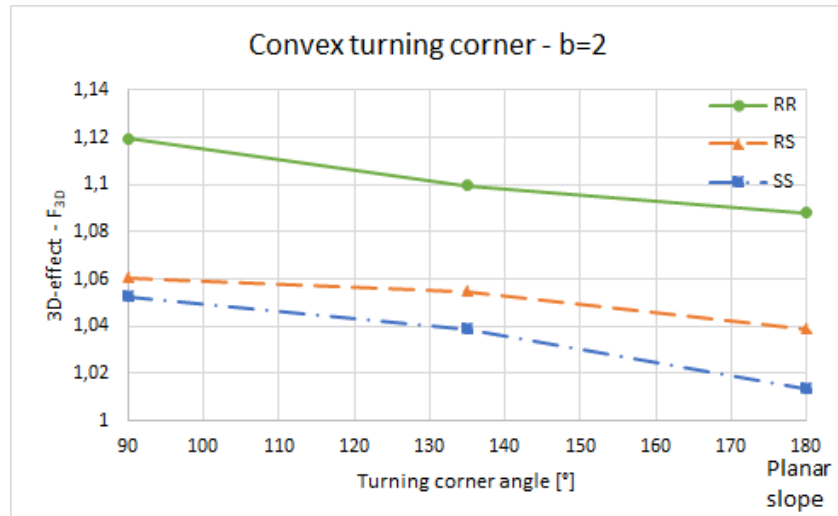


Figure 3.23: 3D-effects for convex turning corner angles of 90°, 135° and 180° (planar) for inclination $b = 2$, calculated from results in (Nian et al., 2012).

Figure 3.24 illustrates how the slide will develop using shear contours for a 90° corner (left) and a 135° corner (right) under fully restrained boundaries. The 90° turning corner displays how the slide is divided on each side of the corner, which is due to the restraining effect of the sharp corner. At the corner the slide mass is minimal, which is caused by the convex inclined slope corner. The slide propagates as one slide for the 135° corner, since the corner is wider with more slide mass compared to the 90°. Further, the restraining effect from the corner vanishes for the planar slope, where only the boundary conditions and the three-dimensionality of the model provides 3D-effects.

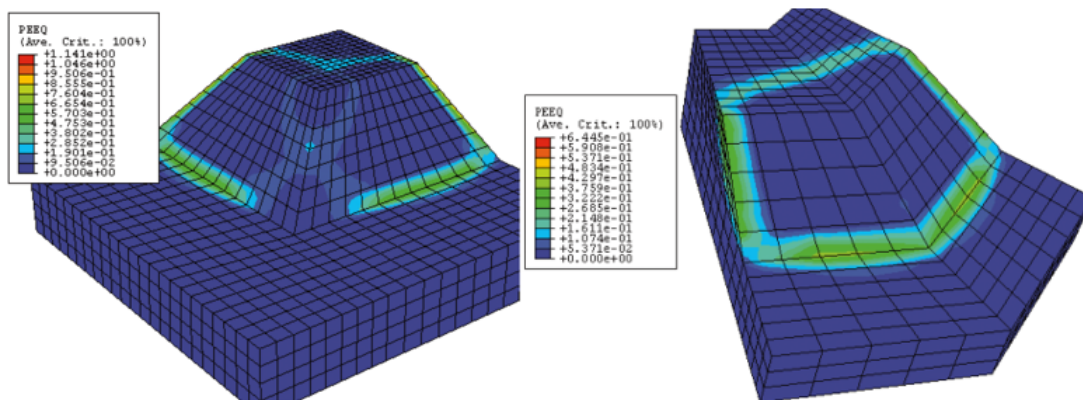


Figure 3.24: 90° (left) and 135° (right) turning corner shear contours with slope inclination $b = 2$ and fully restrained side surface boundaries (RR), retrieved from (Nian et al., 2012).

Effect of Slope Inclination

To assess the influence of inclination, a vertical slope ($b = 0$) was analysed with the same corner angles of 90° , 135° and 180° . Table 3.3 shows a different trend compared to the gentle slope. When the corner angle increases, the SF increases. Moreover, the SF is lower for the 90° and 135° corner angle with unrestrained boundaries compared to the 2D plane strain solution. The increase in inclination has significantly reduced the safety factor compared to the gentle slope, and the SF can be lower than the plane strain result.

Table 3.3: Safety factors for convex turning corners with slope inclination $b = 0$ (vertical), reproduced from (Nian et al., 2012).

Turning corners of slope	Safety factor		
	Unrestrained (SS)	Semi-restrained (RS)	Fully restrained (RR)
90°	1.172	1.197	1.209
135°	1.205	1.215	1.240
180° (planar slope)	1.210	1.235	1.273
Plane strain solution	1.206	1.206	1.206

Figure 3.25 shows the 3D-effects (F_{3D}) of convex turning corners on vertical slopes for rough-rough (RR), rough-smooth (RS) and smooth-smooth (SS). The plots show how the effects increase with increasing convex corner angle for all boundary conditions, which is an opposite trend compared to the slopes with inclination $b = 2$. The fully fixed (RR) boundary conditions still provide a significantly higher effect compared to the RS and SS boundaries. Moreover, the effect increases more rapidly compared to $b = 2$ for increasing corner angle. However, the difference in effect between the boundary conditions is lower. In addition, several results provide safety factor below the plane strains solution, which imply a negative effect for certain convex corner angles on a vertical slope.

Figure 3.26 illustrates how the slide will develop using shear contours for a 90° corner (left) and a 135° corner (right) under fully restrained boundaries. The 90° turning corner displays how the slide develops at the corner and not on each side as for $b = 2$. Compared to the $b = 2$ case, the vertical slope develops a shorter slip surface that concentrates at the corner toe, and thus a

smaller slip surface contact area is mobilised. There is less resistance from the crest to the toe than for flatter slopes. The shear surface contact area increases for higher corner angles, which is the reason for the trend in Figure 3.25. The unrestrained (SS) and semi-restrained (RS) cases will obtain less restraining aid from the boundaries. Further, the 3D-effect becomes negative if the three-dimensional ratio between the driving slide mass and the shear resistance becomes more critical compared to the equivalent ratio in 2D. This appear to be the situation for the vertical slope with the given material properties.

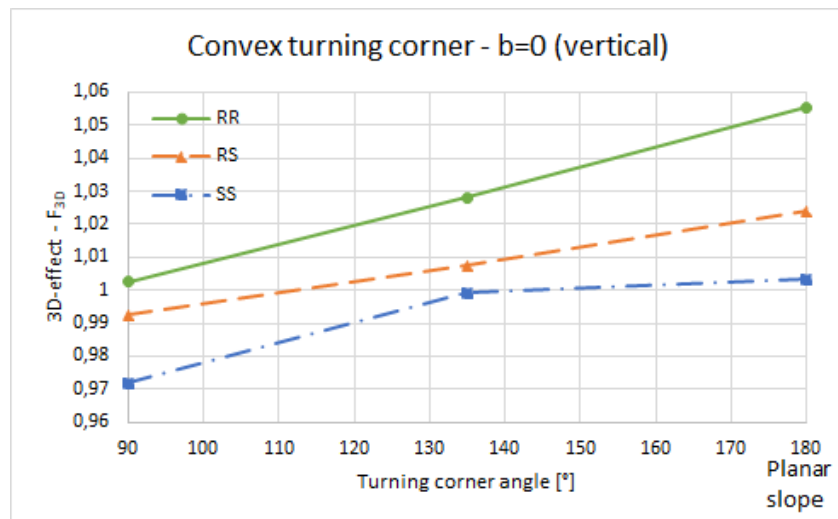


Figure 3.25: 3D-effect for convex turning corner angles of 90°, 135° and 180° (planar) for inclination $b = 0$ (vertical slope), calculated from results in (Nian et al., 2012).

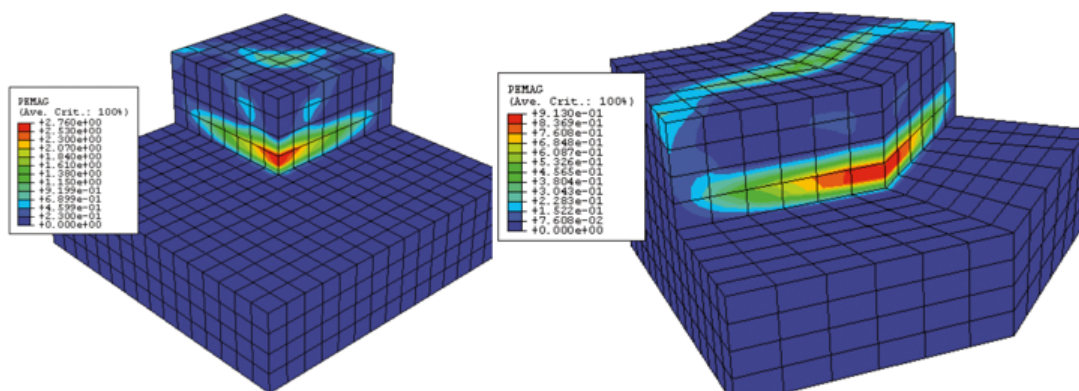


Figure 3.26: 90° (left) and 135° (right) turning corner shear contours with slope inclination $b = 0$ (vertical) and fully restrained side surface boundaries (RR), retrieved from (Nian et al., 2012).

Convex vs. Concave

To compare a concave and a convex corner, a vertical concave slope with 90° corner angle is analysed. As an example, such vertical slopes with sharp corners could be present for excavations. Table 3.4 shows a higher safety factor for all boundary conditions compared to the convex equivalent. The greatest difference for the 90° corners is 15% for fully restrained boundaries. All safety factors obtained from the concave corner analyses are greater than the plane strain solution. The 3D-effects are ranging from 1.06 and 1.14, which also are higher than those obtained for slope inclination $b = 2$.

Table 3.4: Safety factors for concave turning corners with slope inclination $b = 0$ (vertical), reproduced from (Nian et al., 2012).

Turning corner of slope	Safety factor		
	Unrestrained (SS)	Semi-restrained (RS)	Fully restrained (RR)
90°	1.274	1.275	1.380

Figure 3.27 shows the shear contours of the fully restrained concave 90° corner angle. Due to the restraining nature of the concave corner, the slide is divided and concentrated on each side of the corner, similar to the convex $b = 2$ case. Consequently, the driving mass has been split and reduced, and the shear surface area has increased. Moreover, in the concave corner the two perpendicular sides may act as support against each other. Therefore, higher 3D-effects are achieved for the concave corner.

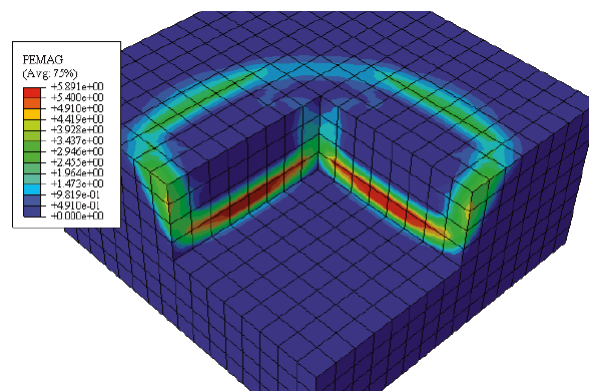


Figure 3.27: Concave 90° turning corner shear contours with slope inclination $b = 0$ (vertical) and fully restrained side surface boundaries (RR), retrieved from (Nian et al., 2012).

3.8 Limit Equilibrium Analysis - Curved Geometry and Drained Behaviour

Zhang et al. (2015)

L. L. Zhang et al. (2015) studied the influence of unsaturated soil in 2D and 3D slope stability analyses. Different ground water conditions and geometries are tested using 2D and 3D limit equilibrium software. Presented are convex and concave curvatures, and how the 3D-effects vary for the curvature corner angle when matric suction from unsaturated soil is introduced.

The analyses were conducted using the 3D LE software SVSlope and the 2D general limit equilibrium (GLE) method by Fredlund and Krahn (1977). The three-dimensional analysis utilised a 3D extension of the mentioned GLE method, which was proposed by Lam and Fredlund (1993). An intercolumn force function is required in the method, which is similar to the one proposed by Morgenstern and Price (1965). The study assumed the intercolumn force function as a half-sine function. Furthermore, an ellipsoidal failure surface was assumed for the 3D analysis.

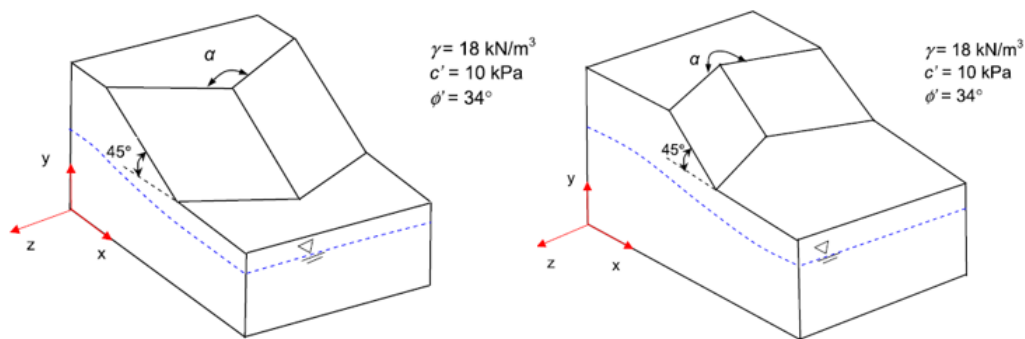


Figure 3.28: Convex (left) and concave (right) corner with angle α , slope angle $\beta = 45^\circ$ ($b = 1$) and the dotted ground-water level (GWL), retrieved from (L. L. Zhang et al., 2015).

Both convex and concave corners were modelled and evaluated for different corner angles and groundwater conditions. Figure 3.28 shows the convex (left) and concave (right) corner with angle α and slope angle 45° ($b = 1$). The soil strength was defined using the Mohr-Coulomb model with cohesion $c' = 19 \text{ kPa}$ and friction angle $\phi' = 34^\circ$, including the shear strength increase rate relative to matric suction ϕ^b . Moreover, the soil unit weight was given as $\gamma = 18 \text{ kN/m}^3$. The slope height was set as 30 m and the groundwater level was placed approximately 5 m below the slope toe. Values of α between 0° and 180° were defined as convex and $\alpha = 180^\circ$ defined a simple planar slope surface. α between 180° and 360° defined a concave corner.

Figure 3.29 presents the difference between 3D and 2D SF $\left(\frac{SF_{3D}-SF_{2D}}{SF_{2D}}\right)$ for different corner angles and rate of shear strength increase relative to matric suction ϕ^b . The slope angle is set as 45° ($b = 1$). For $\phi^b = 15^\circ$ the 3D-effects increase when the corner angle is increasing, i.e. increase with concavity. Moreover, the effect is greatest for concave corners, with approximately a 60% difference for a 270° angle. $\phi^b = 0$ provides a slight decrease in $\frac{SF_{3D}-SF_{2D}}{SF_{2D}}$ for convex geometry. The concave corners still result in a significant increase. However, the maximum difference is reduced to approximately 35%. Matric suction in unsaturated soil appears to have a significant positive 3D-effect on slope stability.

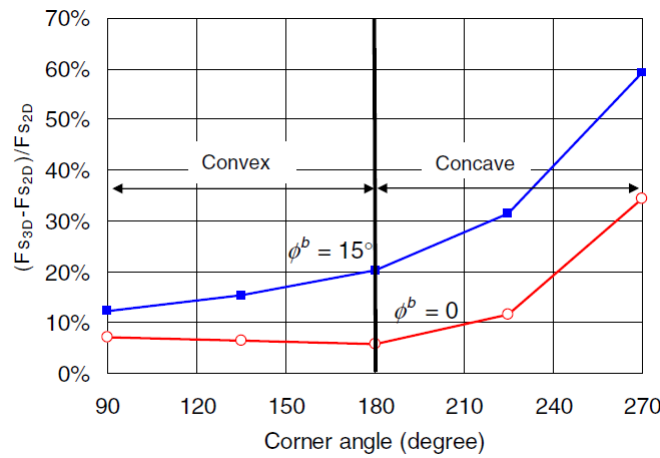


Figure 3.29: Comparison of 3D-effects $\left(\frac{SF_{3D}-SF_{2D}}{SF_{2D}}\right)$ with different slope corner angles, for $\phi^b = 0^\circ$ and $\phi^b = 15^\circ$, retrieved from (L. L. Zhang et al., 2015). Concavity increases from left to right.

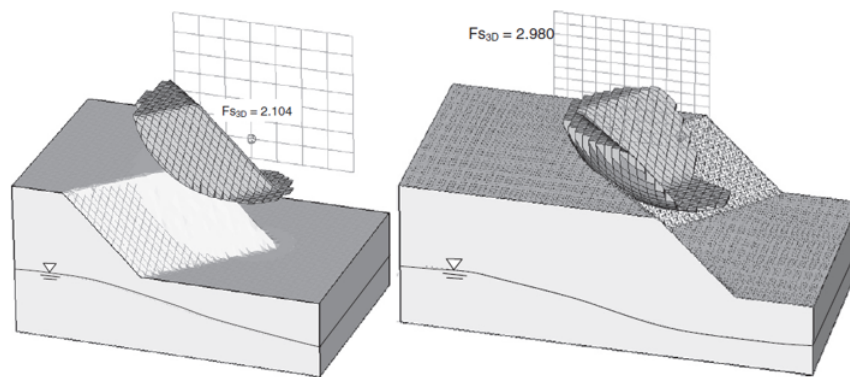


Figure 3.30: Convex $\alpha = 90^\circ$ (left) and concave $\alpha = 270^\circ$ (right) corner with corresponding failure surface for $\phi^b = 15^\circ$, retrieved from (L. L. Zhang et al., 2015).

Figure 3.30 illustrates how the convex (left) and concave (right) geometry affects the critical

slip surface for the defined soil with $\phi^b = 15^\circ$. The convex corner ($\alpha = 90^\circ$) obtained a three-dimensional safety factor of 2.104 and the concave corner ($\alpha = 270^\circ$) a safety factor of 2.980, which is a significant difference. For the defined slope and soil properties, the concave geometry appears to develop a wider slip surface compared to the convex. Consequently, more shear surface contact area is mobilised. In addition, the concave corner 'cuts' and removes parts of the slide mass, and thus the concave geometry obtains a smaller slide mass relative to the shear contact area compared to the convex geometry.

Chaudary et al. (2016)

Chaudhary et al. (2016) studied the effects of complex geometries in 3D slope stability analysis. Slopes with different convex and concave curvature angles were analysed, and the results related to safety factor and failure mechanism were compared. Furthermore, a sensitivity analysis of soil properties were conducted to find how these affect the slope stability. Three-dimensional limit equilibrium (LE) software was used to assess the various scenarios.

The stability analysis tool in the study was based on the limit equilibrium method (LEM). As 2D LE analyses use slices, the 3D LE analyses use columns. The LEM of columns was implemented in the software SVOFFICE 2009, with a pre-established slip direction. The grid and radius method was used to search for ellipsoidal slip surfaces. The LE methods used were Simplified Bishop, Simplified Janbu, Spencer, Morgenstern-Price and Generalised Limit Equilibrium (GLE) by Fredlund, Krahn, and Pufahl (1981). Only GLE results are presented.

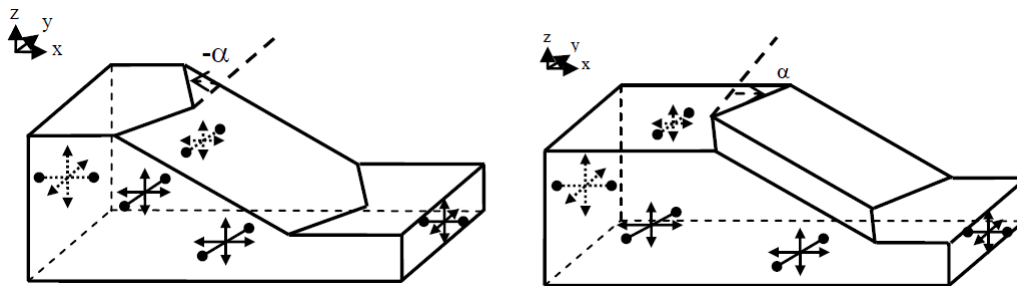


Figure 3.31: Convex (left) and concave (right) models with corner angle α , retrieved from (Chaudhary et al., 2016).

Idealised planar, convex and concave geometries were evaluated to study the effects on safety factor and failure mechanism. The study used slope surfaces with either a convex or a concave corner in the middle of the surface, see Figure 3.31. These corner angles α varied between 45°

(concave) to -45° (convex), with $\alpha = \pm 22.5^\circ$ and $\alpha = 0$ (planar) as intermediate angles. The slope height was 10 m and the slope inclination was defined as $b = 2$.

Various soil properties were analysed to study their sensitivity on the SF. Drained strength parameters were defined, where cohesion c' ranged between 10 kPa and 40 kPa and friction angle ϕ' ranged from 10° to 30° . In addition, the unsaturated shear strength angle ϕ^b , which impacts the effect of matric suction on the shear strength in unsaturated zones, ranged from 5° to 20° .

Effect of Turning Corner

Figure 3.32 shows the stabilising effects of curved slope surface. The safety factors increase as the absolute values of corner angle increase for convex (10 – 25%) and concave (32 – 38%) geometry compared to the planar slope. The increase is greatest for concave geometry, which can be explained by the arching effect that increase with concavity. Chaudhary et al. (2016) found that the slip surfaces exceeded the side boundaries for the planar three-dimensional model, and continued sideways as the model width was increased. It went towards 'infinite' width, similar to 2D analysis. Therefore, the planar slope results were retrieved from 2D LE analyses.

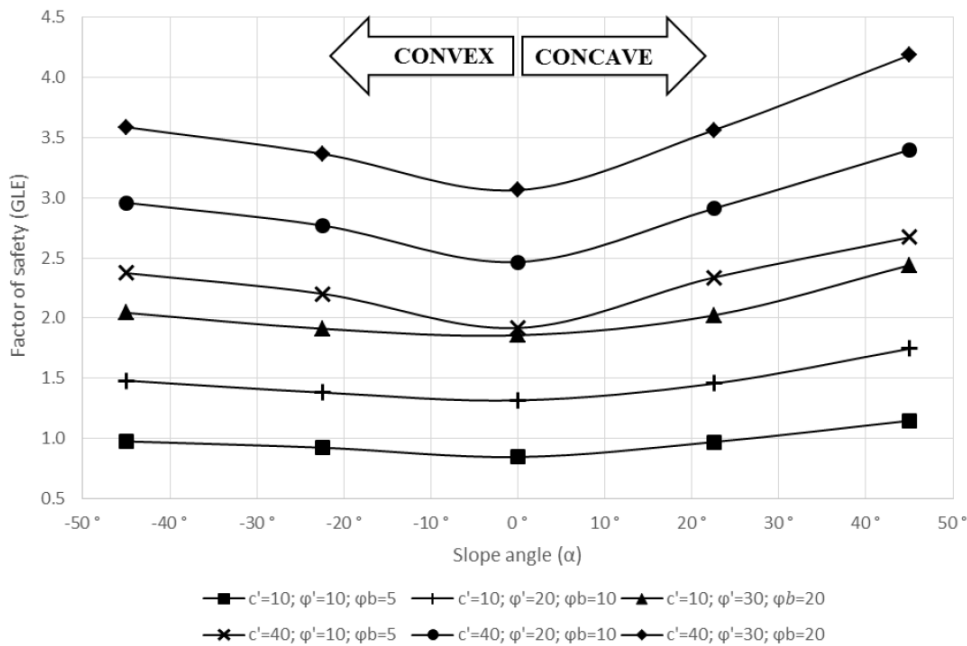


Figure 3.32: Comparison of plane, convex and concave slope surfaces for different soil strength properties, retrieved from (Chaudhary et al., 2016). Safety factors are obtained using the Generalised Limit Equilibrium (GLE) method.

Figure 3.33 and Figure 3.34 shows critical slip surfaces for the three corner angles $\alpha = 45^\circ$ (con-

cave), $\alpha = 22.5^\circ$ (concave), $\alpha = -22.5^\circ$ (convex) and $\alpha = -45^\circ$ (convex). In general, the slip surfaces propagate wider for corners closer to plane, both for convex and concave geometry. Further, as the slide widens, the slide appears to increase in mass. Additional driving mass is a destabilising factor. Moreover, the convex slip surfaces exit at or close to the toe of the slope. Concave slip surfaces exit further downwards from the slope toe. This may create a longer slip surface and a greater shear contact area, which is a stabilising factor.

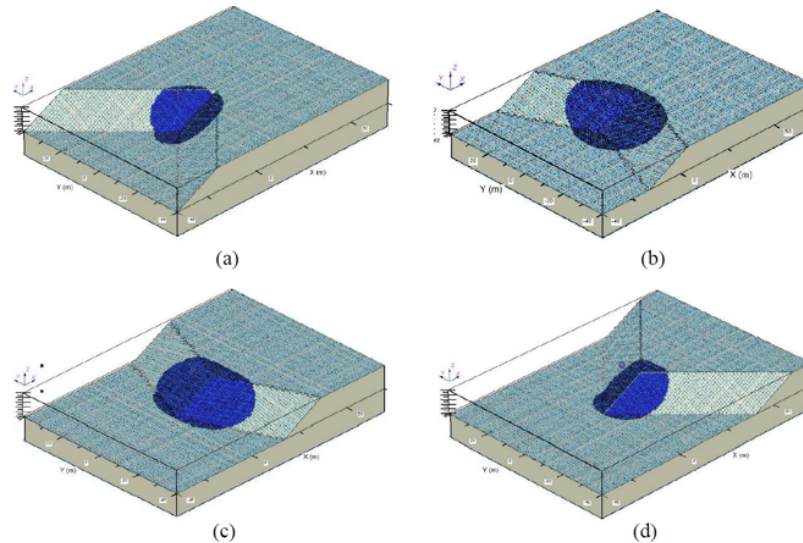


Figure 3.33: Slip surfaces with $c' = 10 \text{ kPa}$, $\phi' = 30^\circ$ and $\phi^b = 20^\circ$ for (a) concave $\alpha = 45^\circ$, (b) concave $\alpha = 22.5^\circ$, (c) convex $\alpha = -22.5^\circ$ and (d) convex $\alpha = -45^\circ$ corners, retrieved from (Chaudhary et al., 2016).

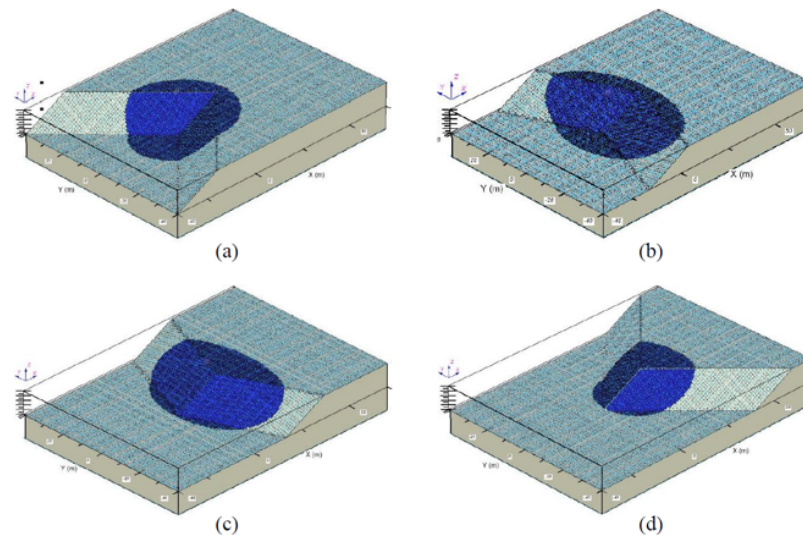


Figure 3.34: Slip surfaces with $c' = 40 \text{ kPa}$, $\phi' = 10^\circ$ and $\phi^b = 5^\circ$ for (a) concave $\alpha = 45^\circ$, (b) concave $\alpha = 22.5^\circ$, (c) convex $\alpha = -22.5^\circ$ and (d) convex $\alpha = -45^\circ$ corners, retrieved from (Chaudhary et al., 2016).

Effect of Strength Properties

Soil strength in Figure 3.33 is defined by cohesion $c' = 10\text{ kPa}$, friction angle $\phi' = 30^\circ$ and unsaturated shear strength angle $\phi^b = 20^\circ$. In Figure 3.34 the strength properties are defined by cohesion $c' = 40\text{ kPa}$, friction angle $\phi' = 10^\circ$ and unsaturated shear strength angle $\phi^b = 5^\circ$. The figures display a clear difference between the sets of material properties. Slopes in Figure 3.34 with the increased cohesion have significantly wider and deeper failure surfaces for the same corner angles. This strength set provides higher safety factors compared to the strength set in Figure 3.33, see Figure 3.32. The reason may be a greater increase in shear contact area relative to the increased slide mass.

By evaluating cases with a range of soil properties and curvatures, some elements were found to influence the safety factor. The effect from slope geometry on the safety factor is greater for more cohesive soils. Figure 3.35 shows how the concave and convex models result in a larger difference from the planar slope as the cohesion c' increases. Furthermore, concave slopes are easier affected by changes in shear strength. In addition, the study stated that the 3D safety factors are greater than the 2D safety factors for the described cases. It was found that the 3D-effect varied between 3% and 30%, with an average of 13.9%.

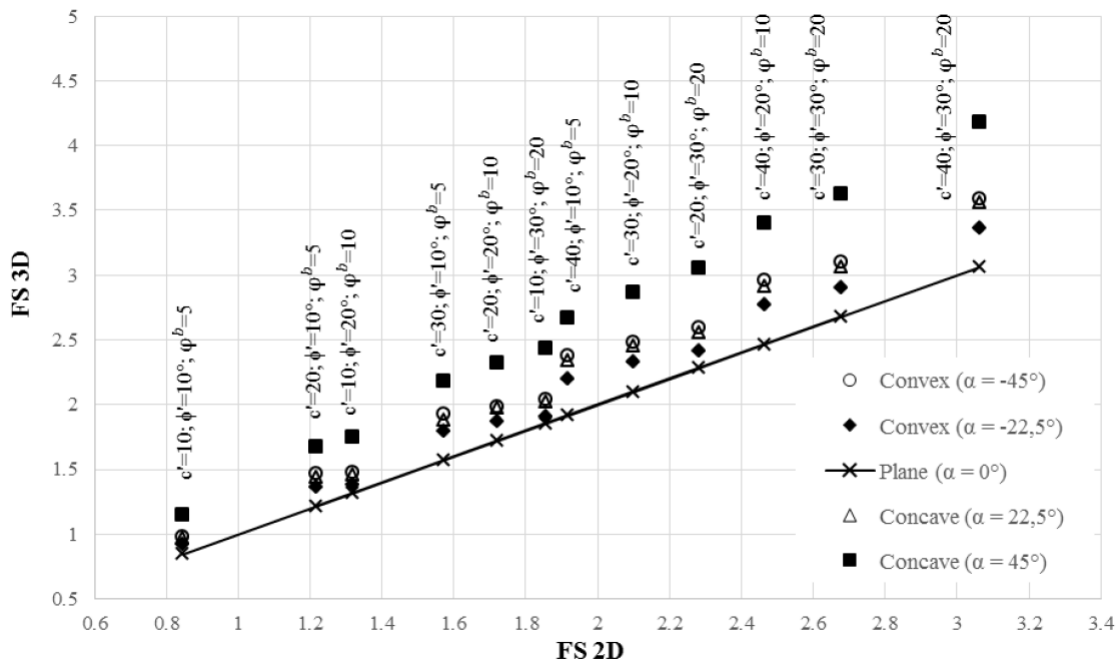


Figure 3.35: Comparison of safety factors for various soil properties and slope geometry, retrieved from (Chaudhary et al., 2016). 2D and 3D safety factors are defined along the horizontal and vertical axis, respectively.

3.9 Summary and Discussion of Literature Study

The main point from the review of some literature studies is that 3D-effects may be significant, especially when curvatures are present. As Cavounidis (1987), Duncan (1996) and others have suggested, the 3D safety factor will be greater than the 2D safety factor for most cases. This can be supported by the fact that problems are 3D in nature and an infinite slope is rarely encountered, as emphasised by Wei et al. (2009). It is difficult to imagine how the relation between driving forces and resisting forces can lead to a infinite slide width in reality. Three-dimensional variations in topography, layering and soil conditions are often present, and are neglected in two-dimensional analysis.

Effect of Fixed Width

Jostad and Lacasse (2015) and Griffiths and Marquez (2007) showed how the width-height ratio $w = W/H$ affected the safety factor using undrained conditions. The authors simulated three-dimensional geometries and slides by restraining the boundaries on the vertical sides of the FE model to obtain the desired finite width. Such idealised conditions may not be fully compatible to reality with regards to the actual slide width. However, it is a useful indication on how geometries in 3D may significantly affect the real safety factor. The studies show how sensitive the slope stability is to a decrease of slide width. Moreover, a significant increase of 3D-effects was found for flatter and deeper slopes.

Gens et al. (1988) assessed the effect of finite three-dimensional slide widths using limit equilibrium considerations for undrained conditions. The main difference from the studies of Jostad and Lacasse (2015) and Griffiths and Marquez (2007) is the part where a failure mechanism must be assumed. While FEM automatically locates the natural shear slip surface, Gens et al. (1988) assumed a rotational cylindrical slip surface. The study found critical slide ends that create a slip surface similar to an ellipsoidal shape, which is the default slip surface in Slide3. However, the solution may be inaccurate due to the idealised geometry and assumed failure surface. The study provided similar 3D-effects as Jostad and Lacasse (2015) and Griffiths and Marquez (2007), however, with as slight overshoot.

The study by Michalowski and Drescher (2009) used a limit analysis method to obtain critical values of $\frac{\gamma H}{S_u}$ for finite slide widths. The results are similar to those of Jostad and Lacasse (2015)

and Griffiths and Marquez (2007). However, the failure mechanism is not entirely comparable. Further, Michalowski and Drescher (2009) illustrated how the shape of failure mechanism for drained and undrained conditions differs. In addition, the study found that the stabilising effect of narrowing widths is enhanced for flatter slopes, and thus supporting other study findings.

Stark and Eid (1998), Arellano and Stark (2000) and Akhtar and Stark (2017) presented a practical solution to 3D LE analysis with side shear resistance for a translational slide. Their studies showed the potential impact of end effects for a range of width-height ratios. Similar to Jostad and Lacasse (2015) and Griffiths and Marquez (2007), the effect was significant for W/H less than 4. Moreover, the positive impact increased for flatter slopes, due to more area where the side shear resistance can act. Akhtar and Stark (2017) found that an earth pressure coefficient K_r in-between at-rest K_0 and active K_A coefficients in the 3D limit equilibrium analyses provided reasonable safety factors. Finite element analysis and finite difference analysis were used as lower and upper bound, respectively. The LE solutions using K_r fell between these bounds. This proves the usefulness of several analysis types when evaluating a 3D problem.

Effect of Curvature

Several studies have focused on the effect of curvature in slope stability. Kelesoglu (2015) showed a significant influence for small radii in concave slopes, especially for average radius less than 30 m. Convex slope radius had less of an impact. Y. Zhang et al. (2013) found that curved surfaces almost always had a beneficial impact, and that decreasing inclination provides increased SF. The effects varied significantly depending on the boundary conditions. Certain convex slope surfaces led to negative effects compared to a planar slope. However, most curvatures had positive effects for both smooth-smooth and rough-rough boundaries, especially concave. The extent and shape of the shear surface were dependent on the boundary conditions and curvature.

Nian et al. (2012) presented how slope inclination and turning corners affect the SF in FE analysis. For $b = 2$ the SF increased with decreased convex corner angle. However, for $b = 0$ (vertical slope) the corner angle had a reverse impact on the SF. This may indicate a boundary inclination between positive and negative effects, depending on soil properties. However, a convex vertical slope is rarely realistic in many places. Furthermore, the 3D-effects are greater for a flatter slope and fully fixed boundaries. In addition, the study supports the increased stabilising effect of a concave curvature.

L. L. Zhang et al. (2015) supported the variation between concave and convex, and added the stabilising influence of matric suctions for drained conditions. Similar to Nian et al. (2012) different corner angles were analysed. Significant positive 3D-effects were obtained, especially for the sharp concave angles. The 3D-effects increased further by including a shear strength increase from matric suction in unsaturated soil. The convex slopes had less 3D-effects than the planar slope with matric suction, and approximately equal for $\phi^b = 0$.

Chaudhary et al. (2016) used limit equilibrium considerations to assess 3D-effects of corner angles, similar to L. L. Zhang et al. (2015). The same trend for convex and concave corner angles were observed, where concave curvature acted more stabilising. Furthermore, Chaudhary et al. (2016) inspected the influence of varying drained soil properties. Larger effect was found for more cohesive soils, which matches the findings of Leshchinsky and Baker (1986) and Sun et al. (2017). In addition, the study illustrated how the shear surface and slide shape increase for higher cohesion, and how the slide changes with curvature.

Discussion

The studies suggest a potentially significant connection between safety factor and slope inclination, width and curvature. Conditions and properties may vary a lot, and undrained and drained analyses may have different impact on results. However, an indication on how the 3D SF behaves for certain conditions and geometries may be obtained. Narrower widths will give less weight for almost the same side area. Consequently, the 3D-effects increase. Flatter inclination will increase the slope side area and shear surface, which will increase the acting shear resistance. Consequently, again increased stabilising effects. These are factors that should be accounted for when comparing 2D and 3D analyses.

The depth-height ratio d and inclination b are parameters in both 2D and 3D models. However, their value affects the 3D-effects, since an increase in both will prolong the slip surface, and thus extend the three-dimensional shear surface. With a finite slide width, the shear surface obtains a greater influence compared to the driving slide mass. This may be the reason for the increased 3D-effects for narrower slides. Another explanation for the larger 3D-effects obtained for narrow widths ($w < 2$) may be that the slip surface becomes shallower and flatter (less curved), which may decrease the slide mass more than the shear surface.

Additional restraining effect may be observed when convex or concave curvature is introduced. Certain cases have found negative effects from convex slope surfaces, which may be intuitive due to a concentration of mass in the protruding ridge. However, for moderate slope inclinations, there is less mass near the crest for the convex surface. As summarised, the effect is greatest for concave shapes, which may be due to the arching effect. The shear surface extends around and below the surface and there is less slide mass due to the hollowed concave (valley) shape.

These studies used idealised situations and boundary conditions that not necessarily reflect reality. For the planar slopes with fixed width, i.e. fully fixed side boundaries, it is unlikely that such restraints are present. If present, it is probably a man-made construction that creates a near-fixed geometry. In nature there may be a semi-fixed situation, where a different material or a rapid change of soil properties is present that initiates a finite width failure mechanism.

A range of curvature types have been analysed, such as corners and arches. A corner may be more common for man-made structures, while arches are common in nature. Natural curvatures are often not as smooth and idealised as in the presented studies. However, they give an indication of how the curvatures impact different 3D problems. Furthermore, it may be necessary to create a more comprehensive model where the geometry is extended on the sides. This will be more realistic in areas where e.g. ridges (convex) or valleys (concave) are part of a larger natural slope structure. This is attempted to investigate in the three-dimensional simulations of curvature in chapter 7.

Although similar findings may be observed in the various studies, some deviation is present that may be due to the method of calculation. It is difficult to be sure of the accuracy of the finite element and finite difference analyses without a thorough verification analysis. These approaches should yield an accurate slip surface. However, the possibility of an overshoot of safety factor is present, due to potential numerical errors or too coarse element distribution. The main limitation regarding the limit equilibrium and limit analysis procedures is the assumption of slip surface. Optimisation procedures may find a critical solution that is quite accurate. Still, some uncertainty must be accounted for.

Chapter 4

2D Simulations - Modelling and Calculations

Most of this chapter includes the two-dimensional analyses completed in the project thesis that was the prestudy of this master thesis, see (Solli, 2019). The results found in the project thesis will be used to compare 2D and 3D slope stability analysis. Therefore, the 2D plane strain analysis conducted in the project thesis is transferred to the present thesis. The plane strain ($w = \infty$) findings will be used as reference 2D SF when the 3D-effect is calculated as $F_{3D} = SF_{3D}/SF_{2D}$. Moreover, the simulated width-height ratio safety factor found in GS Stability is compared to 3D fixed widths in chapter 6. In addition, axisymmetric calculations are added to the 2D analyses in the present master thesis. The axisymmetric model in PLAXIS 2D is used to simulate convex and concave curvatures with varying radii.

The two-dimensional numerical simulations were conducted to compare FE software PLAXIS 2D and LE software GS Stability. Moreover, GS Stability was used to test how the side shear input functions. To obtain a valid comparison a simple 2D model was created, which could be implemented in both PLAXIS 2D and GS Stability. Calculations using the programs were completed when similar model conditions were obtained. Furthermore, several width-height ratios ($w = W/H$) were defined for the side shear input in GS Stability and calculations were run to assess the effect.

In addition, a hand-calculated slope stability analysis was conducted as a simple comparison.

The Direct Method with stability charts by Janbu (1954) was used to estimate the safety factor given the same parameters defined for PLAXIS 2D and GS Stability analyses. Results from these calculations are summarised with the other safety factors in subsection 4.1.4.

4.1 Plane Strain Analyses

Plane strain analysis assume an infinite slide width in the direction perpendicular to the 2D profile plane. PLAXIS 2D offers both a plane strain model or a axisymmetric model. In the first part of the 2D analysis, the plane strain option in PLAXIS 2D is used. GeoSuite Stability and 2D LEM assumes plane strain. However, the infinite width can be artificially restricted by including side shear, which is shown in the following subsections.

4.1.1 Slope Model

To achieve an accurate estimation and comparison of different methods, the model must be unambiguously defined throughout the analysis. Therefore, an undrained strength profile and a 2D soil volume with defined geometrical attributes are created. These are implemented in PLAXIS 2D and GS Stability. These analyses are elaborated on in the following sections.

The models contain some assumptions that simplifies the simulations. Firstly, it is assumed fully homogeneous soil in the width of the slope, perpendicular to the plane. Furthermore, the soil strength is simplified to a linearly increasing S_u -profile with depth, without any other change in properties. Secondly, as this prestudy analysis focuses on 2D, the plane strain assumptions is present. Thirdly, the geometrical attributes are idealised, with straight surfaces. Moreover, the strength is defined with equal value in the horizontal direction for each depth value.

Strength Profile

As the main goal for this study is to assess 3D-effects, it is deemed sufficient to use a simplified undrained shear strength (S_u) profile. Soil strength is an important property when evaluating failure mechanism and safety factor in slope stability analysis. The simple S_u -profile used in the analyses is defined as follows:

$$S_u = 20 + 2z \quad [kPa] \quad (4.1)$$

Where z is the depth below ground surface at the defined reference elevation, given in meter.

The Mohr-Coulomb soil model with *Undrained B* is utilised to achieve a suitable comparison between PLAXIS and GS Stability. The result is that for both the LE-calculations and FE-calculations the soil strength is defined with a depth-dependent S_u -profile. Therefore, the strength defined by Equation 4.1 can be directly implemented in GS Stability and PLAXIS 2D.

GS Stability can easily define several strength profiles along the slope and interpolate strength between the profiles. However, PLAXIS have no easy solution to differences in soil strength along the slope, except from rotating the strength profile. Therefore, the analyses are simplified by defining the top ground surface (highest elevation) as reference point for the profile, for both GS Stability and PLAXIS. This strength assumption may not be realistic. Natural strengths may follow the slope inclination with altering reference points, depending on type of slope.

Geometry

A simple geometry is defined for the analyses to achieve an accurate comparison of the methods. The geometries are presented in Figure 4.1 and Table 4.1, where LB = Length of back surface, LF = Length of front surface, L = Horizontal length of slope, H = Height of slope, D = Depth under slope toe and b = slope inclination. The dimensionality of the problem is of importance. Other length/depth parameters are chosen to obtain a sufficiently large soil volume for the FE-analyses, without using fixed boundaries on the front and back. Otherwise, the failure may occur through the entire volume instead of as a natural slide in the slope.

Three cases were studied to assess different geometries. For the two-dimensional focus of this paper, only the slope inclination (b) is varied. The slope height (H) is highly important in anal-

yses using undrained shear strength. However, the magnitude of height alone is of less importance when the width-height ratio (W/H) is used as relative measure. To get a comprehensive picture of effects in undrained analysis, several slope heights should be analysed.

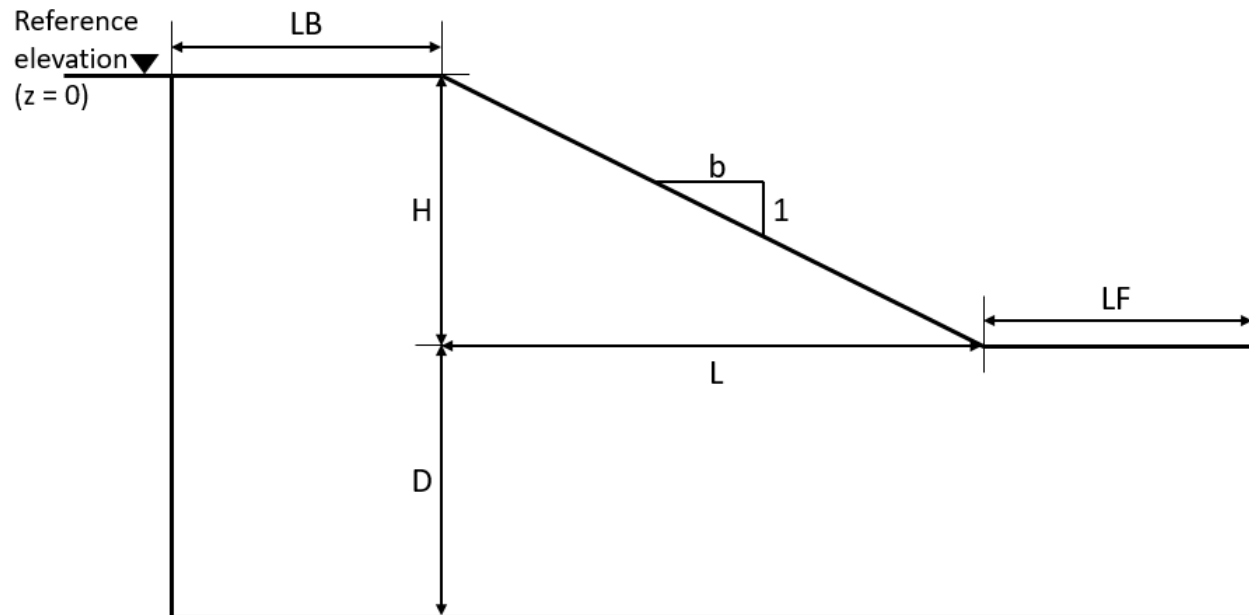


Figure 4.1: 2D slope geometry, where the shear strength reference elevation is at $z = 0$, H is the slope height, D is the depth below slope toe, b is the slope inclination, L is the horizontal length of the slope surface, LB is the model length behind the slope crest and LF is the length in front of the slope toe.

Table 4.1: Defined geometries for a simple 2D slope, see Figure 4.1.

Geometrical attribute	Symbol	Value
Slope inclination	b	1.5 (Case 1)
		2 (Case 2)
		3 (Case 3)
Slope height	H	10 m
Depth below slope toe	D	20 m
Length of surface behind the slope	LB	20 m
Length of surface in front of slope	LF	20 m
Horizontal length of slope	L	$H \cdot b$

4.1.2 PLAXIS 2D

PLAXIS 2D is used to compare two-dimensional FEM and LEM. The model type selected is the *plane strain* with 15-noded triangular elements (default). There is no input of side resistance in the program, which leads to normal plane strain conditions when a plane strain model is selected. Therefore, results from PLAXIS 2D are only comparable with the infinite width-height ratios defined for the GS Stability analyses.

Mohr-Coulomb is chosen as the soil model. It was deemed unnecessary to choose a more advanced soil model when comparing to simple LEM with Mohr-Coulomb failure criterion. Drainage type *Undrained B* is selected due to the input of only S_u -profile. Input parameters for Mohr-Coulomb *Undrained B* are reported in Table A.2 in Appendix A.

Three analyses were conducted using PLAXIS 2D, one for each case, see Table 4.1. Figure 4.1 shows the element mesh for Case 1. The *Very fine* element distribution with coarseness factor 1.0 was used for all cases. A brief sensitivity test of finer element distributions were completed using a reduced coarseness factor. However, no significant difference was obtained. Moreover, the safety analysis 'converged' well with an approximately horizontal curve in the $\Sigma Msf - |u|$ plot retrieved from PLAXIS. Model properties and calculated phases are reported in Appendix A.

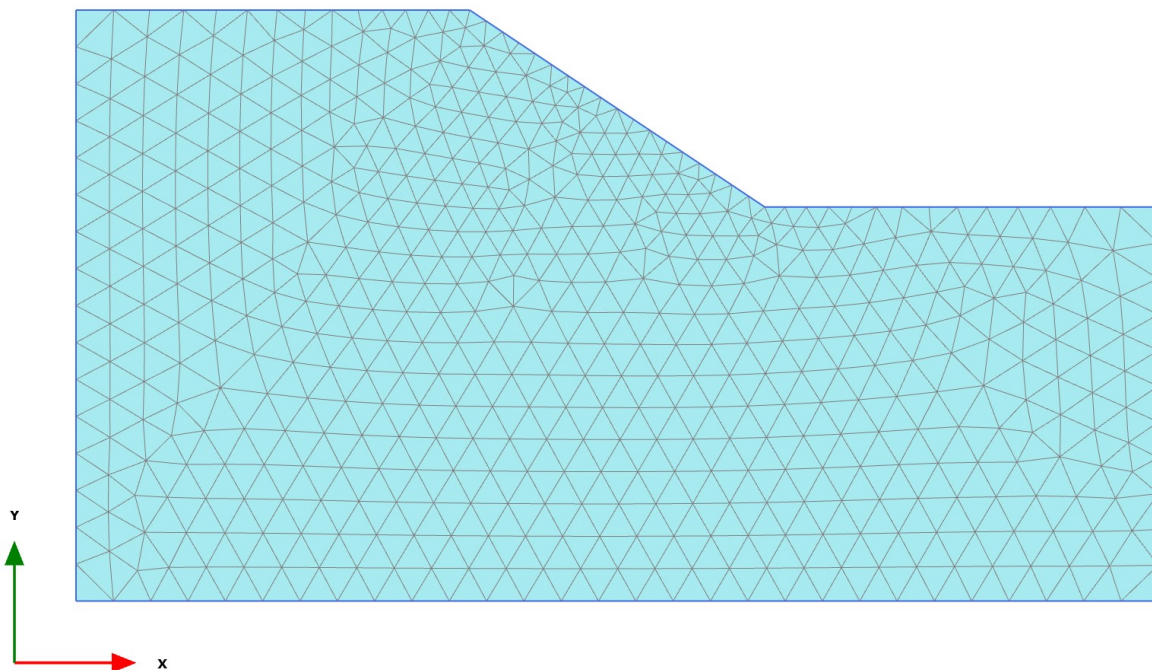


Figure 4.2: Example of the *Very fine* mesh selected for the defined model geometries in PLAXIS 2D, where $b=1.5$.

4.1.3 GeoSuite Stability

The analyses conducted in GS Stability were carried out using the same soil parameters as for PLAXIS 2D with a slightly different input, see Table A.3 in Appendix A. E and ν are not of importance for slope safety analysis, and are therefore not available input in GS Stability. An undrained shear strength profile is manually created in GS Stability, where $c = S_u$ as defined in Equation 4.1.

To find the critical mechanism in GS Stability, the critical surface is assumed as toe failure. The reason is that the calculations conducted in PLAXIS 2D showed toe failure for all the three cases. PLAXIS 2D is able to locate the natural failure surface by using FE calculations, and therefore toe failure should be the case for the 2D plane strain analyses done in GS Stability. Moreover, it is a likely assumption with the slightly increasing undrained strength with depth.

The assumption of toe failure is further investigated by checking several search areas in GS Stability. The calculation strategies *Tangent* and *Points* were used to find the most critical failure and the corresponding lowest safety factor. The evaluation showed that the assumption of toe failure is accurate. Therefore, the solutions were found by fixing the slope toe as the critical surface exit using *Points* strategy. A comparison of results are more accurate when the failure type remains the same.

To assess the effect of the side shear input in GS Stability, different widths W are inserted into Equation 2.12 where width $B = W$. Since the width of a slide is depending on height of the slope, the width-height ratio $w = W/H$ is introduced. As a result, different w can be analysed to see effects of side shear resistance on these relations as defined by GS Stability. By implementing the width-height ratios in Equation 2.12, the side shear factor α_{SS} becomes a function of H . With $H = 10\text{ m}$, the side shear factors used in the GS Stability analyses are as presented in Table 4.2.

Table 4.2: Calculated side shear factor input for the defined width-height ratios and a height $H = 10\text{ m}$.

Width-height ratio $w = W/H$	Side shear factor $\alpha_{SS}(H)$	Value side shear factor $\alpha_{SS}(H = 10\text{ m})$
1	$2/H$	0.2
2	$1/H$	0.1
4	$1/2H$	0.05
6	$1/3H$	0.033
∞	$2/\infty$	0

4.1.4 Plane Strain Results

The findings from the simulations are summarised in Table 4.3. The results for finite width-height ratios w are found using the side shear input in GS Stability. Figure 4.4 shows all safety factors plotted for each case. Figure 4.3 presents a comparison between the different inclinations for different width-height ratios. Figure 4.5 shows the failure surface from safety analysis in PLAXIS 2D for $b = 1.5$. Figure 4.6 shows the toe failure surface obtained in GS Stability for $b = 1.5$ without side shear.

The remaining PLAXIS slip surfaces are found in Appendix B along with the safety analysis results in Figure B.1. These are represented by the incremental shear strains from the *c/phi reduction* technique. The rest of the analyses conducted in GS Stability are found in Appendix C. These present the located slip surfaces with the corresponding safety factor. Moreover, the obtained accuracy score is included.

Safety Factor

For all cases, the plane strain solutions (infinite width) are quite similar for the different methods, see Table 4.3. GS Stability with BEAST and PLAXIS 2D with FEM obtained practically the same SF. Janbu Direct Method gave slightly lower values, with a maximum deviation of 4% compared to BEAST and FEM.

Different finite slope widths are simulated by using the side shear input with the values defined in Table 4.2. The results in Table 4.3 shows how a decreasing w gives an increased safety factor. For $b = 1.5$, the difference between $w = \infty$ and $w = 6$ is approximately 11%. The difference between $w = \infty$ and $w = 1$ is approximately 66%. With $b = 3$, the difference between $w = \infty$ and $w = 6$ is approximately 16%. While SF for $w = 1$ is 91% larger than for $w = \infty$. The effects when $b = 2$ and $w = 4$ is approximately 20%.

The incremental increase in SF shows the trend, as exemplified by Case 2. The difference between $w = 4$ and $w = 6$ is approximately 6%. For $w = 2$ versus $w = 4$ the change is approximately 16%. The last increment shows a difference of 26%, where the step is $W/H = 1$. The trend shows an increase in SF gradient for a decrease in w . The total difference between $w = \infty$ and $w = 1$ is approximately 74%.

Table 4.3: Safety factor (SF) for all cases considered in the project 2D analyses.

Width-height ratio (W/H)	Safety factor (SF)		
	Case 1: $b = 1.5$	Case 2: $b = 2$	Case 3: $b = 3$
$w = 1$	2.048	2.363	3.003
$w = 2$	1.650	1.877	2.324
$w = 4$	1.441	1.624	1.964
$w = 6$	1.370	1.539	1.829
$w = \infty$ (GS Stability)	1.232	1.357	1.570
$w = \infty$ (PLAXIS 2D)	1.233	1.359	1.567
$w = \infty$ (Hand calc. - Janbu Direct Method)	1.187	1.327	1.522

Figure 4.3 compares the plane strain solution ($w = \infty$) with the different W/H ratios for the three cases. The plot shows how SF increases more rapidly for decreasing W/H . Furthermore, the difference between the solutions increases with increasing b (decreasing slope angle). In addition, the safety factors trend towards the plane strain solution as w goes towards infinity.

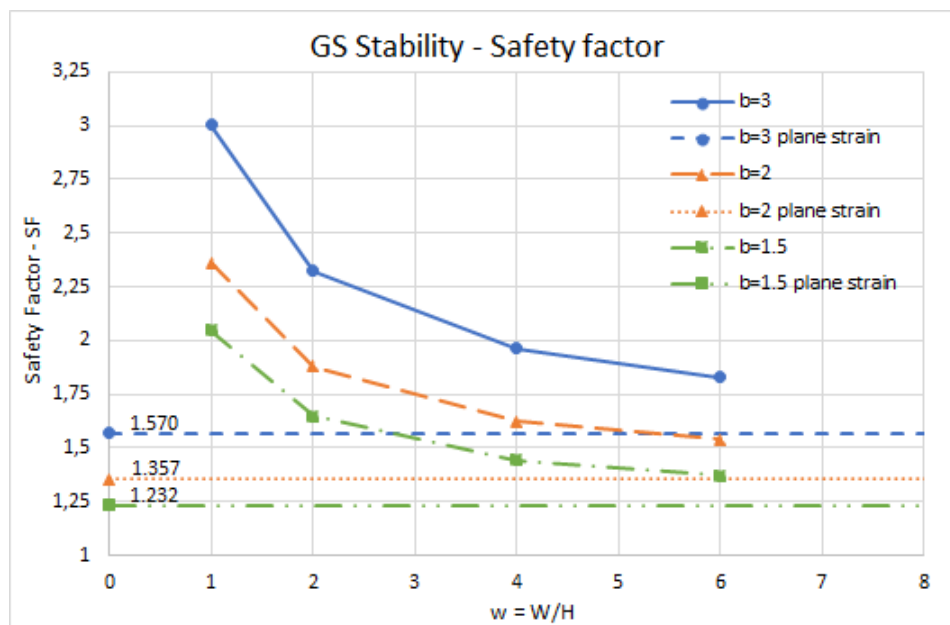
Figure 4.3: Comparison of SF obtained in GS Stability between different inclinations for various w -values.

Figure 4.4 presents all obtained safety factors in plots for each case. It shows a similar trend for all cases, where the SF increases more rapidly with greater W/H . The PLAXIS 2D solution and the GS Stability solution with no side shear are almost indistinguishable. The hand calculation using Janbu's Direct Method provides slightly lower SF compared to PLAXIS 2D and GS Stability.

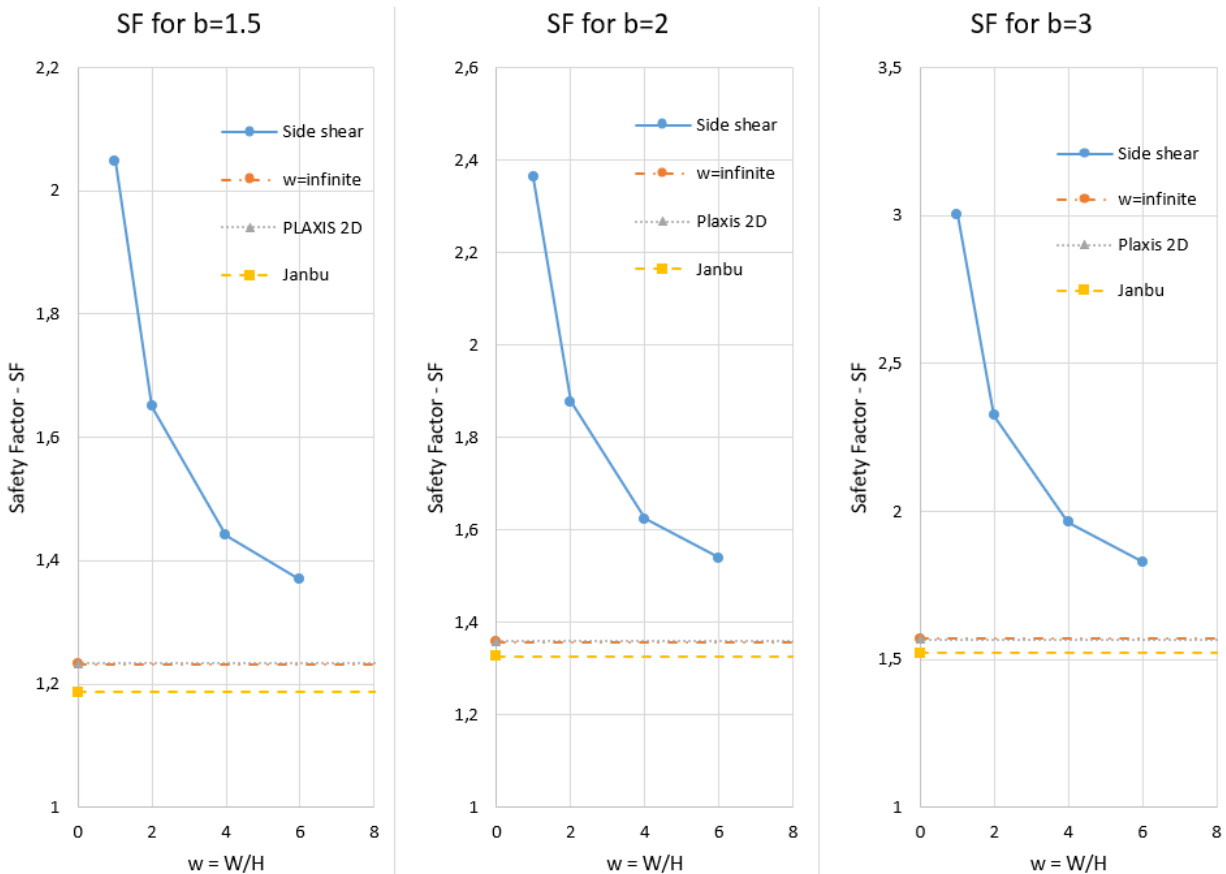


Figure 4.4: A comparison of the plots for each inclination. All calculated safety factors are included.

Failure Mechanism

Figure 4.5 displays the failure surface by incremental strains from the PLAXIS 2D safety calculation. For all the cases, FE analysis results in a toe failure for the defined slope properties. All failure mechanisms from PLAXIS 2D are available in Appendix B. The findings show that the extent or 'radius' of the slip surface increases with decreasing slope angle.

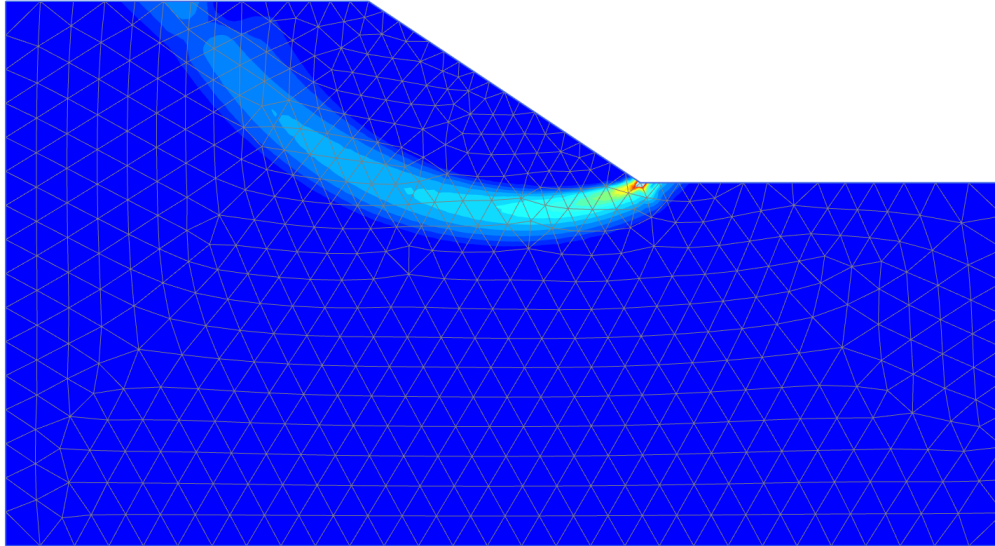


Figure 4.5: Incremental shear strains showing failure surface obtained in PLAXIS 2D for $b = 1.5$.

Figure 4.6 presents the CAD-output from GS Stability when a calculation has run. The example is for $b = 1.5$ and shows the extent of the failure mechanism when it is fixed at the toe of the slope. The increase in 'radius' for increased value of b is similar for GS Stability and PLAXIS 2D. All analyses completed in GS Stability are found in Appendix C.

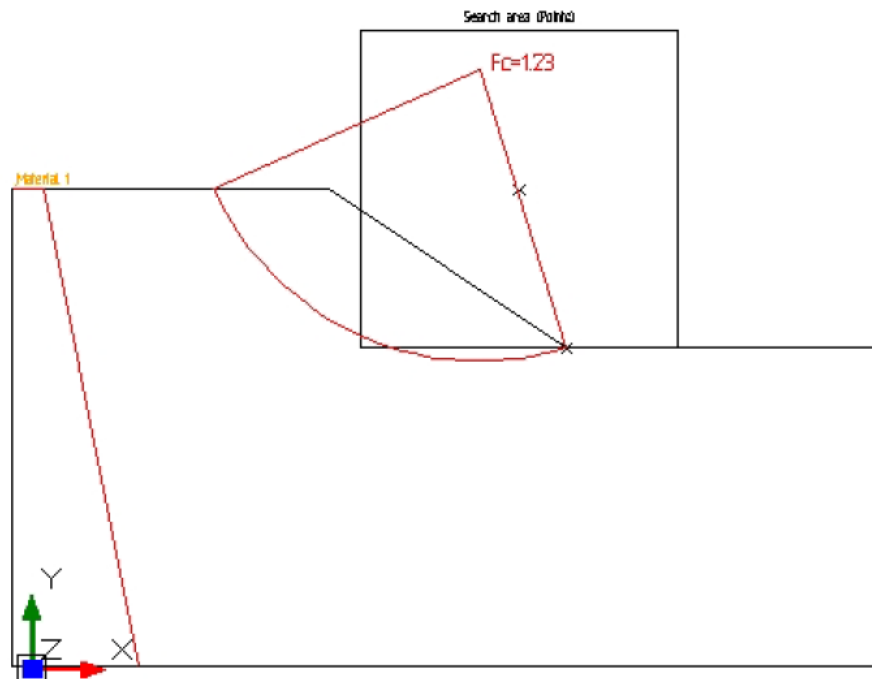


Figure 4.6: Failure surface obtained in GS Stability for $b = 1.5$ and no side shear.

4.1.5 Discussion

Model Limitations

A homogeneous soil profile is used in the simulations, with a simple undrained strength profile. Often there is some variation in layering, e.g. a drained dry crust near the surface, which is neglected here. The main limitation with the defined S_u profile is the constant horizontal value in the entire soil volume. This assumption is often not realistic in nature as the strength more or less follows the slope. However, if the slope is a product of an excavation or similar man-made structures, the assumption may be tolerable.

The model for this project analysis covers only a small set of cases. The slope height H is an important factor in slope stability analysis with undrained strength. Therefore, several heights should be tested to evaluate a potential difference in effect. However, the limitation is reduced by focusing on the width-height ratio. In addition, Leshchinsky and Baker (1986) stated that the 3D-effects were more prominent for cohesive soils. By restricting to analysis of one value of cohesion, the effect of cohesion is not sufficiently explored.

The simulations are restricted to undrained conditions, which exclude any impact of drained strength. To properly assess slope stability with drained conditions, several cases must be analysed. Drained analyses introduce the effect of groundwater, since effective stresses are used. The effect of groundwater in drained conditions can be significant, especially when curvatures are present in 3D space. For a convex ridge, the groundwater level may be located further into the soil. While for a concave valley, the groundwater can be higher elevated on the sides of the valley bottom, which may lead to over-pressure. These aspects may be critical when evaluating 2D versus 3D slope stability problems.

The simple hand-calculations using Janbu's Direct Method proved to comply well with the software calculations. Several limitations are associated with the method, which may decrease accuracy. The method consists of reading charts to obtain the necessary values. Consequently, inaccurate reading may lead to inaccurate values. Furthermore, for the undrained case the shear strength must be averaged along the failure surface. This strength estimate may decrease the accuracy. However, if it is done carefully with enough points it should be tolerable.

PLAXIS 2D

PLAXIS 2D serves as a useful tool in the slope stability analyses. The FEM feature of locating the natural failure mechanism is a valuable aspect when assessing 'realistic' slides. Consequently, PLAXIS 2D is helpful in finding the slip surface in GS Stability. However, correct modelling is vital for accurate estimates. This includes definition of boundaries and extent of the model, especially for correct development of failure surface.

Suitable meshing is one important factor in FE modelling. The accuracy of the obtained safety factor may differ from one mesh type to another. The estimate depends on the coarseness/density of the mesh. The *Very fine mesh* can be used for this analysis, since the simple 2D calculation will be completed in a short time. Coarser meshes could be sufficient for this case. If time is an issue, an evaluation of efficiency and accuracy for different meshes should be completed. This is highly relevant for 3D FE analyses.

The choice of element type is another factor in FE analysis. The efficiency and suitability of elements may differ between certain problems. The default 15-noded triangular elements used in PLAXIS 2D are generally a good option. However, errors may occur when PLAXIS calculates plastic displacements at failure. Therefore, it is essential to be aware of element selection and the numerical strategy, especially for the more complex 3D FEM.

GeoSuite Stability

Under 2D plane strain conditions both PLAXIS 2D and GS Stability gave similar safety factors. The FE analyses are expected to be more accurate, because of the progressive global equilibrium and the automatic searching for failure surface. When the location of slip surface is known, it can be transferred to the LE software. Since GS Stability 'knows' where the critical surface is, the safety factor becomes practically equal as for PLAXIS 2D in this case. A variation of geometries and conditions should be tested to verify this.

The aspect that separates previous analyses in literature from the present simulations is that the W/H relation is used in 2D software instead of 3D. BEAST defines the side shear factor as a function of the system width. The present analyses have assumed the system width as the slide width, where the sides of the slide are assumed vertical in BEAST. The widths used in the 3D models in literature are defined as the width between the boundaries of the soil volume.

Therefore, the width is not necessarily defined equally for GS Stability and the 3D analyses in previous papers.

The method in GS Stability resembles the method used by Akhtar and Stark (2017); Arellano and Stark (2000); Stark and Eid (1998), where the 3D software was based on LEM. These studies assume vertical slide sides, equivalent with BEAST. However, the shear resistance on the sides are defined differently. The authors only define shear resistance for drained strength parameters. Therefore, the method cannot be connected directly with the method of BEAST for undrained conditions. A comparison between these analyses and drained analyses in GS Stability may be useful, since the side shear forces are dependent on the earth pressure coefficient.

3D-effects

The testing of side shear factors as functions of W/H in GS Stability showed a significant variation from the plane strain solutions. SF became more sensitive as W/H decreased, especially for $W/H < 4$. This trend matches literature results. The difference is as great as 91% for $b = 3$ and $w = 1$. However, it is unlikely that a regular planar slope will have a width equal the height. On the other hand, if the problem is a three-dimensional valley or ridge, the potential slide width may become similar to the slope height. An explanation for the trend is that the slide mass decreases significantly when w decreases compared to the area affected by shear resistance.

The findings comply well with literature, where different width-height ratios have been analysed in 3D. Jostad and Lacasse (2015) and Griffiths and Marquez (2007) obtained 3D-effects approximately between 16% and 20% for $b = 2$ and $w = 4$, which fit well with the present study where a 20% effect was observed. Compared to the study of Akhtar and Stark (2017), the present study effect for $b = 3$ is significantly higher. The reason may be due to difference between drained and undrained analyses. A comparison between Jostad and Lacasse (2015) and the present study reveals approximately the same result for the same inclination and W/H . Similar values and trend compared to the literature indicate a potentially accurate definition of the side shear resistance in BEAST.

Earlier literature and the present study suggest a similar trend for SF versus w depending on the slope inclination. The 3D-effects seem to increase with flatter slopes. This may be caused by an increase in slope extent and area, which results in greater shear resistance.

4.2 PLAXIS 2D - Axisymmetric Model

Axisymmetric model is the alternative to plane strain in PLAXIS 2D. Axisymmetric implies that the model is symmetric around the axis of origin (reference axis). The profile modelling is the same as for plane strain, since PLAXIS 2D is a two-dimensional program. This axisymmetric analysis is used as a simple study of curvature effects, where both convex and concave curved slope surfaces are simulated.

4.2.1 Slope Model

The soil strength profile and slope geometry is defined similar as in the plane strain analysis in subsection 4.1.1. The shear strength is defined using material model Mohr-Coulomb and drainage type *Undrained B* with strength profile $S_u = 20 + 2z$ [kPa]. The three cases are still described with slope inclination $b = 1.5$, $b = 2$ and $b = 3$. The slope height H is 10 m in all analyses in the present study. Furthermore, the element type is 15-noded triangular and element distribution is *Very fine* with varying coarseness factors. Some of the larger models are given a smaller coarseness factor in the slope area to maintain similar element sizes.

The new variable is the simulated radius R from the reference axis in the axisymmetric model. When the radius increases, i.e. the length from the reference axis increases, the degree of curvature decreases. Consequently, the slope approaches a planar slope for higher curvature radius. Figure 4.7 shows the definition of the convex model, where the upper radius R_u that stretches between the reference axis to the slope crest. Figure 4.8 shows the concave model, which is defined by the lower radius R_l that stretches from the reference axis to the slope toe. Radii ranging from 20 m to 500 m are analysed.

The curvature could be defined by an average radius to the middle of the slope, instead of to different radii. However, two different definitions are used to not mix the two types of curved surface, since the failure mechanisms may differ significantly. Consequently, a direct comparison of the radii may not be entirely comparable. Therefore, two definitions are used to separate the two types. Still, the radii are compared to each other in the present study to see the variation between the two curvatures. Similar to the width-height ratios $w = W/H$, the curvature is presented using the dimensionless radius-height ratio $r = R/H$, since the height is an important factor in undrained analysis.

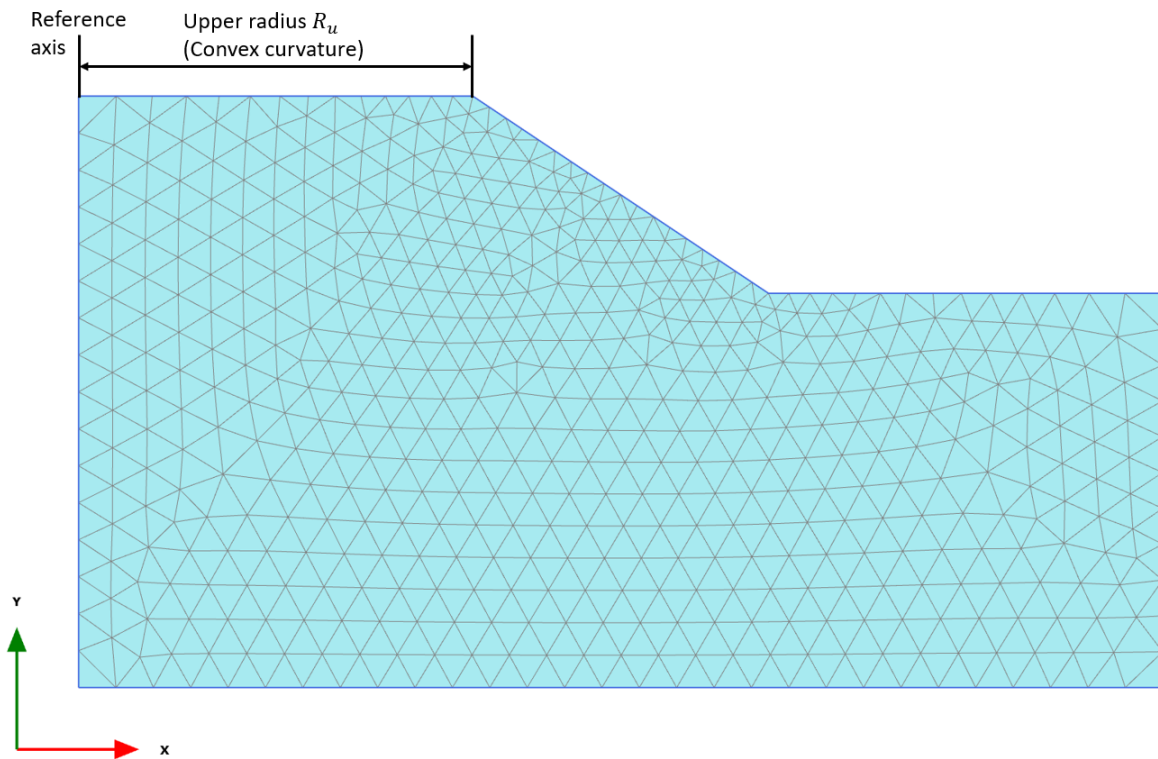


Figure 4.7: Axisymmetric model in PLAXIS 2D. For convex curvature the upper radius R_u is used to define the arching.

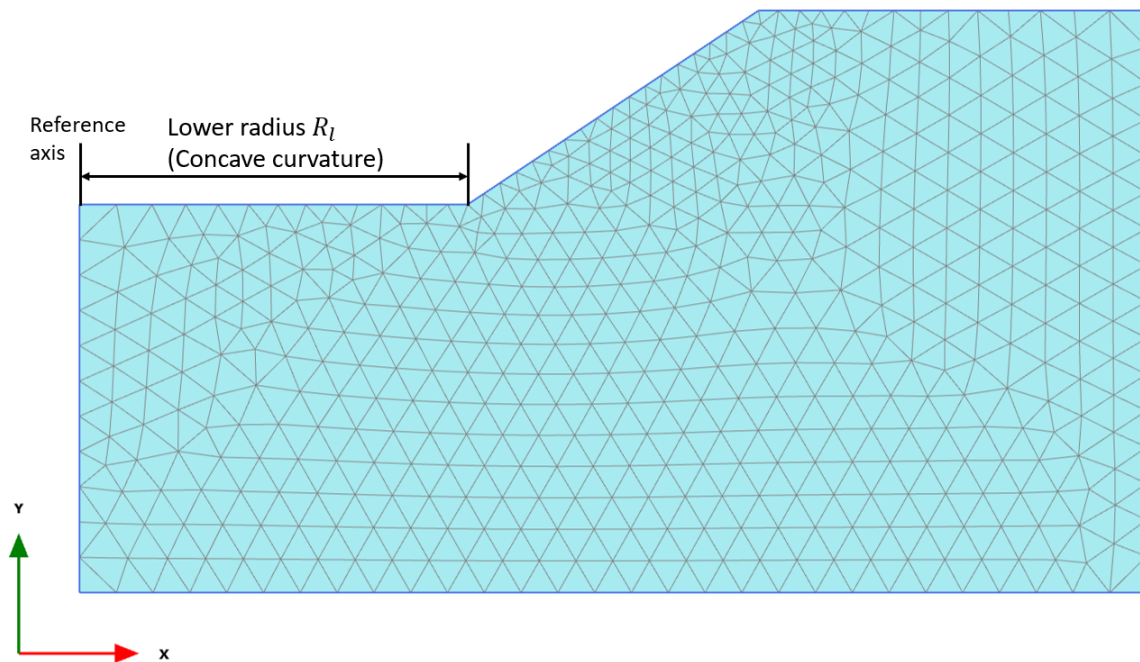


Figure 4.8: Axisymmetric model in PLAXIS 2D. For concave curvature the lower radius R_l is used to define the arching.

4.2.2 Results

On the basis of the models described in subsection 4.2.1 seven analyses are run for each slope inclination case and curvature type. Table 4.4 summarises the findings for the convex curved surfaces, where their relative arches are defined with $r_u = R_u/H$. Similar, Table 4.5 included the result for simulated concave curvatures with varying $r_l = R_l/H$. The studied values for r_u and r_l are 2, 3, 4, 6, 10, 20 and 50. These are compared with the plane strain results obtained in section 4.1. Deviation from plane strain solution is calculated using the GS Stability findings. Obtained slip surfaces resemble those obtained in section 4.1, and are thus not included.

The safety factors decrease as the convex radius-height ratio r_u increases, see Table 4.4. The safety factor for $r_u = 50$ is close to the plane strain results with a difference of approximately 0.5% for all cases. For the most convex curvature with $r_u = 2$, the difference is approximately 8% for $b = 1.5$. This is increased to $\approx 10\%$ for $b = 2$, and $\approx 13\%$ for $b = 3$.

Table 4.4: Safety factors (SF) for different simulated convex radius-height ratios $r_u = R_u/H$ using axisymmetric model in PLAXIS 2D. The three bottom rows contain plane strain calculations.

Convex arch - $r_u = R_u/H$	Safety factor (SF)		
	Case 1: $b = 1.5$	Case 2: $b = 2$	Case 3: $b = 3$
$r_u = 2$	1.334	1.499	1.777
$r_u = 3$	1.302	1.459	1.726
$r_u = 4$	1.289	1.438	1.694
$r_u = 6$	1.272	1.416	1.660
$r_u = 10$	1.256	1.395	1.629
$r_u = 20$	1.244	1.376	1.600
$r_u = 50$	1.237	1.364	1.580
$w = \infty$ (GS Stability)	1.232	1.357	1.570
$w = \infty$ (PLAXIS 2D)	1.233	1.359	1.567
$w = \infty$ (Hand calc. - Janbu Direct Method)	1.187	1.327	1.522

Table 4.5 summarises the findings from the concave axisymmetric simulations. Similar to the convex cases the safety factors decrease for increased concave radius-height ratio r_l . However, the safety factors are greater for the concave shape. The positive effect for $r_l = 50$ is approximately 1%, compared to the plane strain solution. $r_l = 2$ provided stabilising effects of approxi-

mately 14.6%, 15.0% and 15.3% for $b = 1.5$, $b = 2$ and $b = 3$, respectively.

Table 4.5: Safety factors (SF) for different simulated concave radius-height ratios $r_l = R_l/H$ using axisymmetric model in PLAXIS 2D. The three bottom rows contain plane strain calculations.

Concave arch - $r_l = R_l/H$	Safety factor (SF)		
	Case 1: $b = 1.5$	Case 2: $b = 2$	Case 3: $b = 3$
$r_l = 2$	1.412	1.560	1.810
$r_l = 3$	1.367	1.511	1.760
$r_l = 4$	1.344	1.486	1.729
$r_l = 6$	1.312	1.452	1.691
$r_l = 10$	1.288	1.423	1.650
$r_l = 20$	1.264	1.395	1.611
$r_l = 50$	1.243	1.374	1.586
$w = \infty$ (GS Stability)	1.232	1.357	1.570
$w = \infty$ (PLAXIS 2D)	1.233	1.359	1.567
$w = \infty$ (Hand calc. - Janbu Direct Method)	1.187	1.327	1.522

Figure 4.9 compares all the axisymmetric analyses completed in the present study. As already mentioned, the effect of concave curvature is greater than convex. Moreover, the safety factor approaches the plane strain solution for large values of $r = R/H$. The safety factors increase more rapidly as the radius decreases, similar to the trend of fixed widths. Furthermore, the difference between the two surface shapes decreases with flatter slope, i.e. the convex solution closes in on the concave with increasing value of b .

Figure 4.10 presents the 3D-effects as defined by $F_{3D} = SF_{3D,axi}/SF_{2D,GSS}$ for convex curvature. $SF_{3D,axi}$ is the value obtained in PLAXIS 2D with axisymmetric model and $SF_{2D,GSS}$ is the plane strain solution obtained in GeoSuite Stability. All effects are positive ($F_{3D} > 1$) and flatter slopes result in greater 3D-effects. The stabilising influence of flatter slopes increase for more prominent curvature, i.e. smaller radii.

3D-effects for the concave simulations are plotted in Figure 4.11. The general trend of increased F_{3D} for decreased r_l is similar to that of the convex curvature. However, the influence of slope inclination has significantly diminished compared to the convex models. The curves nearly follows each other with the same difference for all value of r_l .

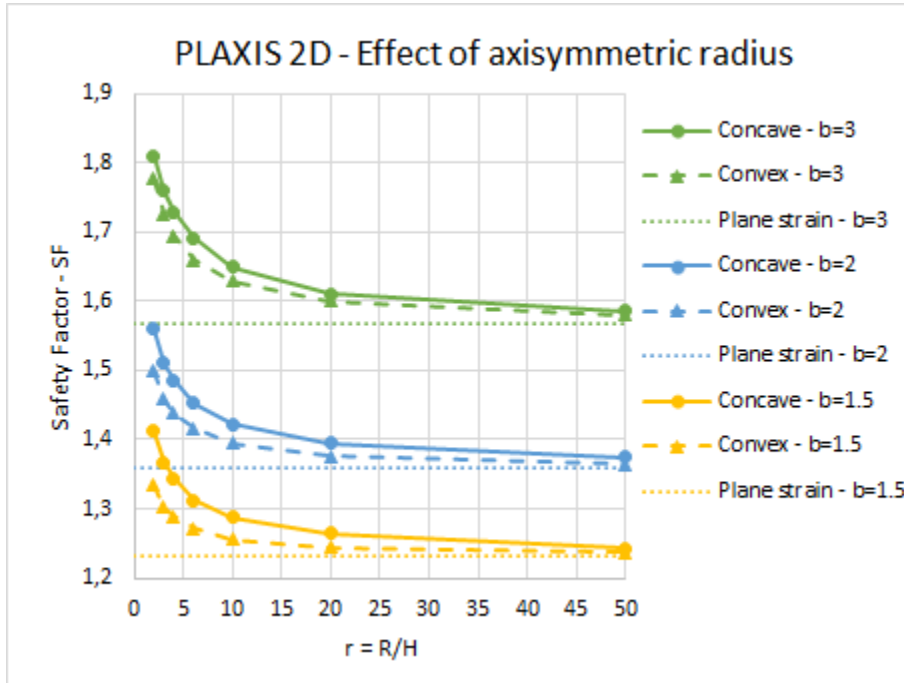


Figure 4.9: Comparison of safety factors from the axisymmetric calculations. The convex models use a radius from the top of the slope, while the concave models use a radius from the toe. The plane strain analyses from GS Stability are included.

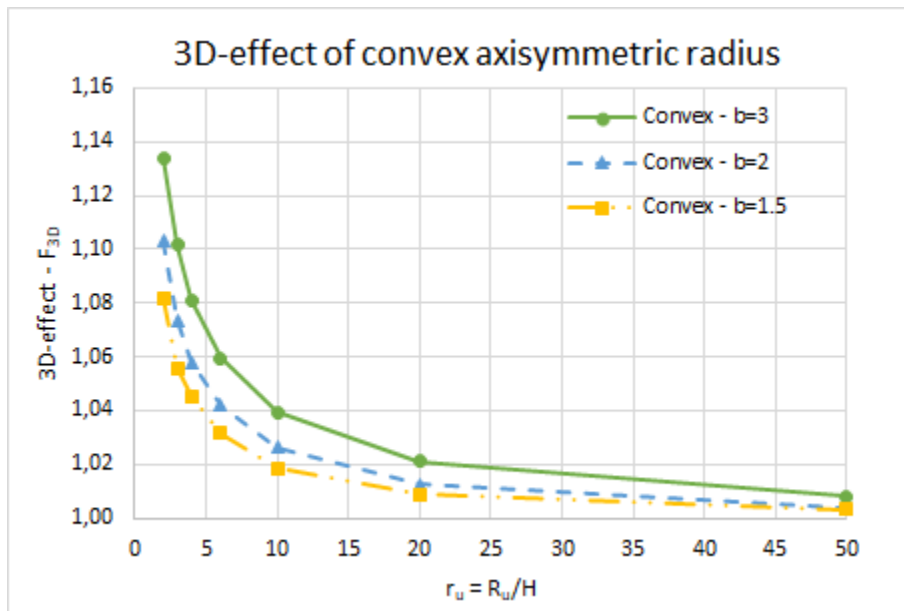


Figure 4.10: Plots showing 3D-effects for various convex axisymmetric radius-height ratios $r_u = R_u/H$ and the three slope inclination cases. The 3D-effect is defined as the 2D plain strain SF divided by the SF obtained with axisymmetrical simulated '3D' curvature.

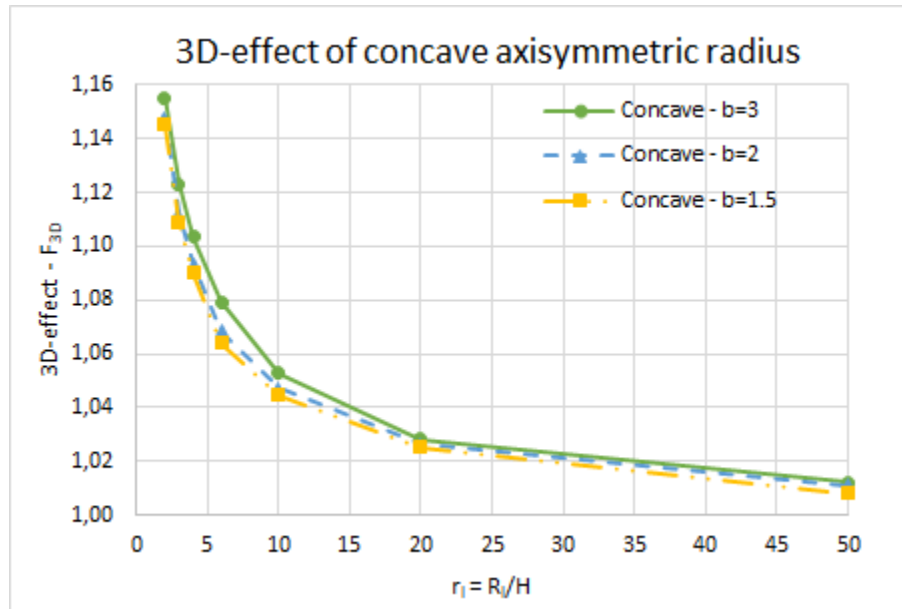


Figure 4.11: Plots showing 3D-effects for various concave axisymmetric radius-height ratios $r_l = R_l/H$ and the three slope inclination cases. The 3D-effect is defined as the 2D plain strain SF divided by the SF obtained with axisymmetrical simulated '3D' curvature.

4.2.3 Discussion

The axisymmetric model available in PLAXIS 2D offers an efficient tool for assessing effect of curvature in slope stability. Similar to what is observed for decreasing finite slide widths, a decrease in curvature radius will increase the safety factor. Moreover, the increase will develop more rapidly, especially for $r < 10$. The effect is significantly lower compared to relative size, which is due to no fully fixed sides in the axisymmetric models. However, the positive effects indicate that prominent curvatures may have a restraining effect.

The influence is more significant for concave geometry, which may be a result of more arching effect. The concave surface with a 'valley' may have greater shear surface to slide mass ratio compared to the convex surface with a 'ridge'. The reason for stabilising effect for convex curvature is that the slide mass near the slope crest is reduced due to the arching.

The 3D-effects for the two curved surface types reveal some different mechanisms for altering geometry. Convex arches provide a noticeable positive effect for flatter slopes. This indicate a higher sensitivity of slope inclination for convex surfaces compared to concave. More comprehensive 3D analyses should be conducted to assess geometry impact on the failure mechanism.

Chapter 5

3D Simulations - Validation and Mesh

Sensitivity Analysis

PLAXIS 3D is the main three-dimensional calculation program used in the present study. The limitation of the plane strain assumption is avoided, and varying geometry in the third dimension is possible. However, 3D modelling is more complex and time consuming, and errors more easily occur. This is especially a hazard in 3D finite element calculations, and careful modelling is essential. To improve the certainty of accurate solution, a brief validation and mesh sensitivity analysis is included.

The main aim of 3D slope stability calculations is to see the variation from a 2D plane strain analysis. These 3D-effects F_{3D} can be presented as difference in percentage or a ratio between the 3D SF and the 2D SF: $F_{3D} = SF_{3D}/SF_{2D}$. A ratio greater than 1 implies a positive stabilising effect. The GeoSuite Stability (GSS) SF found in chapter 4 is chosen as the two-dimensional reference safety factor for each slope case. All safety factors obtained by a 3D software are labelled as SF_{3D} , both with and without restraints or curvature.

5.1 Validation - PLAXIS 3D

Cases used in literature are replicated and calculated to secure accurate and suitable modelling in PLAXIS 3D. Three different example cases are used. The majority of validation examples are cases that use drained strength, i. e. cohesion c and friction angle ϕ as shear strength parameters. Examples 1 and 2 focus on drained conditions, where Example 2 also incorporates associated flow (AF) by using dilatancy angle ψ equal to the friction angle ϕ . Undrained strength is used in Example 3 to get a more accurate comparison with the relevant analyses in the present study.

5.1.1 Example 1 - Drained Analysis with Fixed Width

Example 1 was described by Xing (1988) and has been used in several studies as a validation example. Table 5.1 shows the relevant soil parameters, and the Mohr-Coulomb soil model was used in the present study with *Drained* conditions. Figure 5.2 shows references with method and safety factors are summarised in Table 5.1.

Figure 5.1 shows the 2D slope geometry for Example 1. The height H of the slope was 12.2 m , the depth D was 6.1 m , the slope inclination was $b = 2$ and the width W was 60 m with RR (rough-rough) boundary conditions. RR boundary conditions imply fully fixed boundaries on the side surfaces of the model. Only half the width was modelled due to symmetry, which leads to one rough side (fully fixed) and one smooth side (normally fixed) in the half-model, as illustrated in Figure 5.2. The *Very fine* automatic meshing was utilised in PLAXIS 3D.

Table 5.1: Relevant soil parameters retrieved from Example 1 in (Xing, 1988). The radius R for the circular slip surface in the figure is the original slip surface obtained by Xing (1988).

Parameter description	Value
Soil unit weight, γ	$18.8\text{ kN}/\text{m}^3$
Young's modulus, E	$10000\text{ kN}/\text{m}^2$
Poisson's ratio, ν	0.25
Cohesion, c	$29\text{ kN}/\text{m}^2$
Friction angle, ϕ	20°
Dilatancy angle, ψ	0°

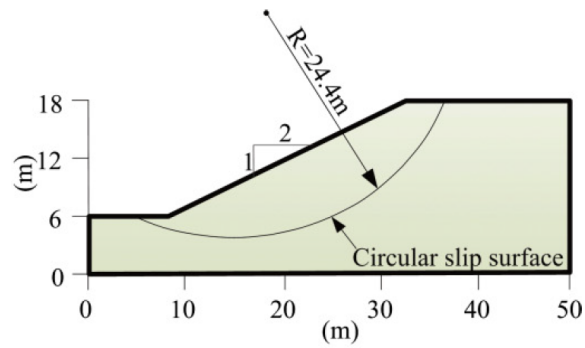


Figure 5.1: 2D geometry for Example 1, illustrated by Y. Zhang et al. (2013).

The findings from the present study is comparable with those from literature. The obtained slip surface in Figure 5.2 appears as a toe failure mechanism near the symmetry line. As Figure 5.1 shows, the slip surface exit from Xing (1988) was located further downwards from the toe, i.e. it propagated deeper. Results summarised in Table 5.2 show consistent safety factors between the different studies. The present study obtained a safety factor of 2.14, which is close to the other studies. e.g. $SF = 2.122$ by Xing (1988). The 3D FEM and FDM analyses have provided approximately the same safety factor. The analysis by Chen, Wang, Haberfield, Yin, and Wang (2001) using the UB-LAM (Upper-bound Limit Analysis Method) resulted in a higher SF, which is expected for an upper-bound analysis.

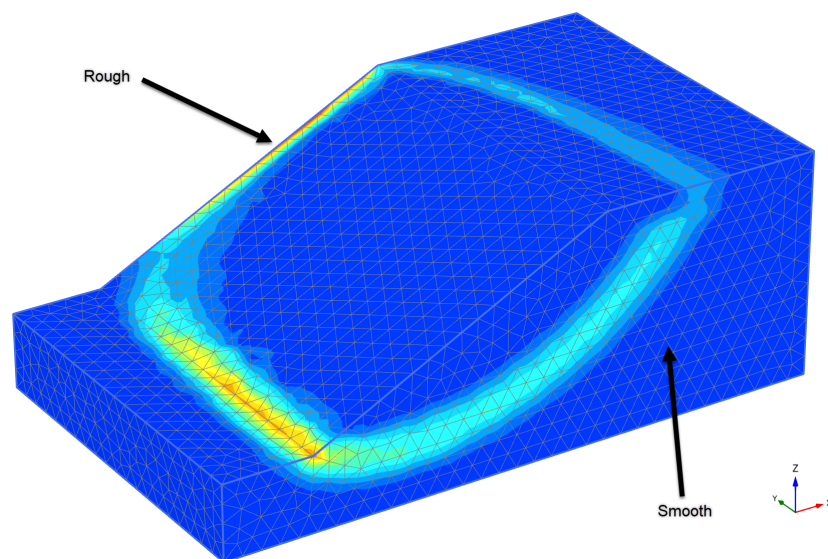


Figure 5.2: Shear mechanism obtained in present study with PLAXIS 3D for Example 1. The width is $W/2 = 30m$ with rough boundary on the far side and smooth on the near symmetry side of the model.

Table 5.2: Comparison of safety factors and methods for Example 1 described by Xing (1988).

Reference	Method	Safety Factor
Fredlund and Krahn (1977)	2D (Average)	2.034
Xing (1988)	3D LEM	2.122
Chen et al. (2001)	3D UB-LAM*	2.262
Chen, Mi, Zhang, and Wang (2003)	3D LEM	2.187
Griffiths and Marquez (2007)	3D FEM (SRM)	2.17
Nian et al. (2012)	3D FEM (SRM) ABAQUS	2.15
Y. Zhang et al. (2013)	3D FDM (SRM) FLAC3D	2.18
Sun et al. (2017)	3D FEM (SRM) ABAQUS	2.133
Present study	3D FEM (SRM) PLAXIS 3D	2.14

*Upper-Bound Limit Analysis Method (UB-LAM)

5.1.2 Example 2 - Drained Analysis with Unrestrained Sides for AF and NAF

Example 2 was described by Cai and Ugai (2000) and used as a validation example in other studies such as (Kelesoglu, 2015). Table 5.3 provides given soil parameters, including dilatancy angle for the associated flow (AF) case. The present study utilised the Mohr-Coulomb model with *Drained* conditions. Figure 5.1 shows the geometry with the shear mechanism obtained by Kelesoglu (2015).

Table 5.3: Relevant soil parameters for Example 2, retrieved from (Kelesoglu, 2015). AF = Associated Flow.

Parameter description	Value
Soil unit weight, γ	$20 \text{ kN}/\text{m}^3$
Stiffness, E	$200000 \text{ kN}/\text{m}^2$
Poisson's ratio, ν	0.25
Cohesion, c	$10 \text{ kN}/\text{m}^2$
Friction angle, ϕ	20°
Dilatancy angle for AF, ψ	20°

Figure 5.3 shows the cross-section geometry with the shear contours. The slope height H is 10 m , the slope depth D is 10 m and the slope inclination was $b = 1.5$. Boundary conditions was

defined as smooth-smooth (SS) in both side surfaces, i.e. not width restraints. In the present study the model width was set to 5 m. The element meshing was defined with the *Very fine* automatic mesh configuration in PLAXIS 3D.

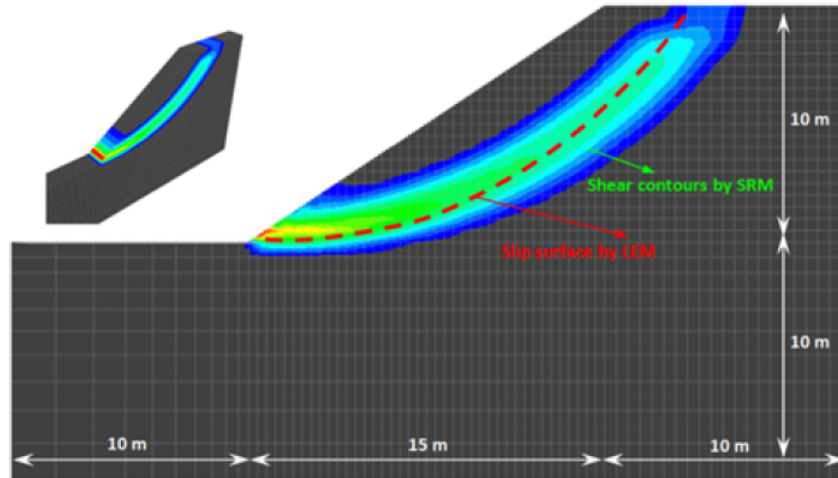


Figure 5.3: Geometry with shear contours for Example 2, illustrated by Kelesoglu (2015).

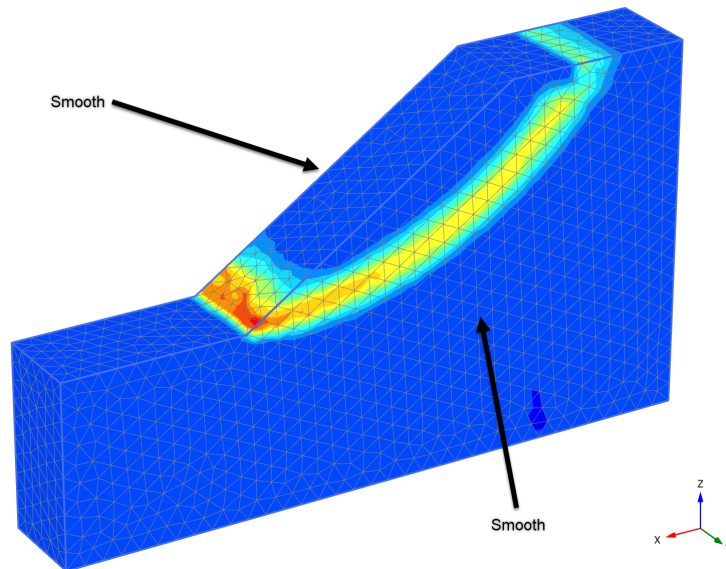


Figure 5.4: Shear mechanism obtained in present study with PLAXIS 3D for Example 2.

The findings from the present study compare well with those from literature. Kelesoglu (2015) included the slip surfaces from both SRM (FDM) and LEM analyses. Figure 5.3 shows a toe failure mechanism, which coincides well with the obtained shear surface from the present study in Figure 5.4. Furthermore, results from the validation example for the various studies are sum-

marised with method and safety factors in Table 5.4. Analyses in the present study obtained a safety factor of 1.18 and 1.16 for the associated case (AF) and the non-associated case (NAF), respectively. The values are in the range between $SF = 1.14$ and $SF = 1.20$ for all cases. Therefore, the modelling appears accurate.

Table 5.4: Comparison of safety factors and methods for Example 2 described by Cai and Ugai (2000).

Reference	Method	Safety Factor
Cai and Ugai (2000)	3D FEM (SRM) - NAF	1.14
Won, You, Jeong, and Kim (2005)	3D FDM (SRM) - NAF	1.15
Wei and Cheng (2009)	3D FDM (SRM) FLAC3D - AF	1.20
	3D LEM	1.18
Kelesoglu (2015)	3D FDM (SRM) FLAC3D - AF	1.18
	3D FDM (SRM) FLAC3D - NAF	1.15
	2D LEM	1.14
Present study	3D FEM (SRM) PLAXIS 3D - AF	1.18
	3D FEM (SRM) PLAXIS 3D - NAF	1.16

5.1.3 Example 3 - Undrained Analysis with Fixed Widths

The study conducted by Jostad and Lacasse (2015) was earlier elaborated in chapter 3. A comparison between 2D LEM and 3D FEM analysis was obtained for different slope inclinations b and depth-height ratios $d = D/H$. Varying width-height ratios $w = W/H$ were tested to evaluate 3D-effects. The parameters given in the paper is reproduced in Table 5.5. Geometric lengths were not provided. The height H was found from the given relation $\frac{S_u}{\gamma H} = 0.20$, which requires $H = 10$ with the defined soil parameters, such that $\frac{S_u}{\gamma H} = \frac{40 kPa}{20 kN/m^3 \cdot 10 m} = 0.20$. Stiffness parameters E and ν are set as $10000 kPa$ and 0.3 , respectively. Figure 5.5 shows the defined slope geometry.

Table 5.5: Relevant soil parameters for Example 3, retrieved from (Jostad & Lacasse, 2015).

Parameter description	Value
Soil unit weight, γ	$20 kN/m^3$
Undrained shear strength, S_u	$40 kN/m^2$
Relation between strength and soil weight, $\frac{S_u}{\gamma H}$	0.20

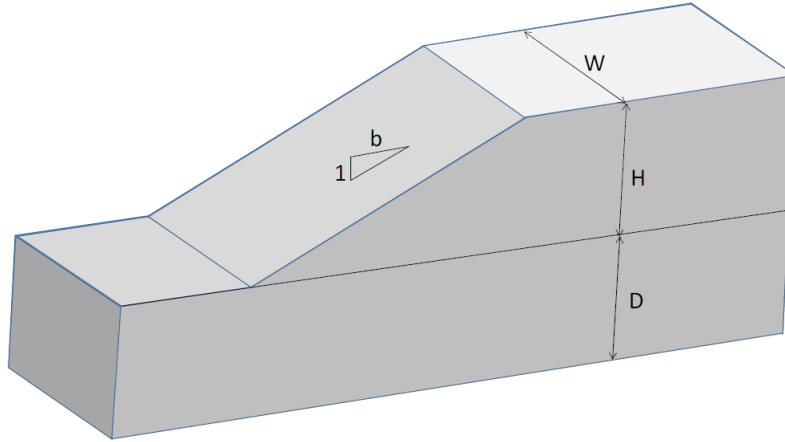


Figure 5.5: Defined 3D geometry, where W = slide width, H = slope height, D = depth from slope toe to bottom boundary and b = slope inclination, retrieved from (Jostad & Lacasse, 2015).

Since the study by Jostad and Lacasse (2015) is similar to the analysis of the present study, a more extensive comparison is conducted between the studies compared to the other validation examples. The study defined the safety factor as:

$$SF = F_{3D} N_0 \frac{S_u}{\gamma H} \quad (5.1)$$

where F_{3D} is the 3D-effect (ratio between 3D FEM and 2D LEM), N_0 is the stability number, S_u is the undrained shear strength, γ is the soil unit weight and H is the slope height. It is the same equation as defined in Janbu Direct Method with no loads, water or cracks, and with the 3D-effect included, see section 2.2. In the present study only an inclination $b = 2$ is used, and w that ranges from 1 to 4 in addition to $w = \infty$. The LE analyses are conducted in GS Stability, the same as in (Jostad & Lacasse, 2015). The present study obtained 2D LE safety factors of 1.19 and 1.60 for $d = 1$ and $d = 0$, respectively. Without other studies to compare the cases of Jostad and Lacasse (2015), it is assumed that the results are close to the correct solution.

Mesh Sensitivity

The safety factors obtained in the present study exceed the safety factors of Jostad and Lacasse (2015). Moreover, with a *Very fine* mesh the SF struggles with convergence and constantly increases with deformation in the safety analysis. Figure 5.6 and Figure 5.7 show the ΣMsf development for a *Very fine* mesh for $w = 4$ and $w = 1$, respectively, and a *Very fine* mesh with a

coarseness factor of 0.5. The refined mesh provides a better result with improved convergence. However, the refined mesh is too time consuming compared to the unrefined *Very fine* mesh. Therefore, a middle way is chosen. A *Very fine* mesh with coarseness factor 1.0 is used for the soil volume and coarseness factor 0.50 for the fully fixed side surface. The results with this mesh show a difference between the present study and the study of Jostad and Lacasse (2015). The difference is further discussed below.

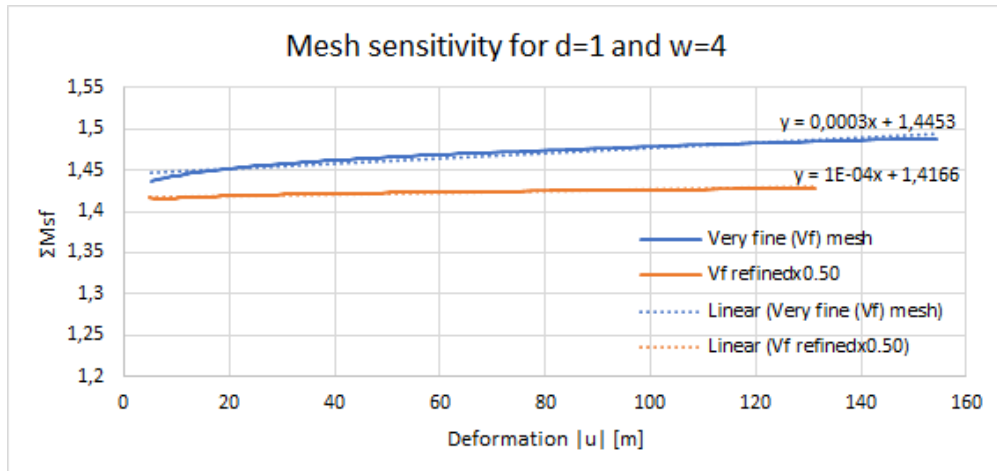


Figure 5.6: Results from a safety analysis conducted in PLAXIS 3D on Example 3 with $w = 4$. The *Very fine* mesh (highest) has a automatic coarseness factor of 1.0, while the *Very fine* refined mesh (lowest) has a coarseness factor of 0.50. A trend line (dotted line) has been adapted to each safety analysis with the corresponding trend equation.

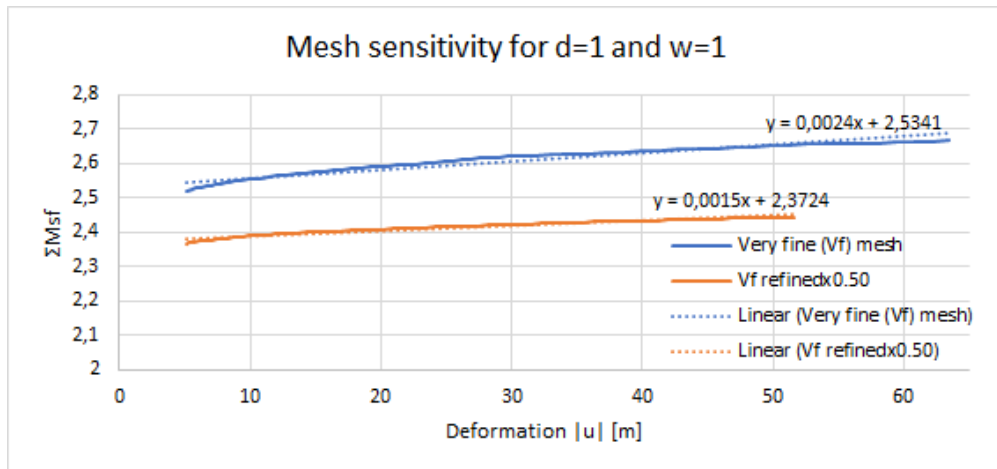


Figure 5.7: Results from a safety analysis conducted in PLAXIS 3D on Example 3 with $w = 1$. The *Very fine* mesh (highest) has a automatic coarseness factor of 1.0, while the *Very fine* refined mesh (lowest) has a coarseness factor of 0.50. A trend line (dotted line) has been adapted to each safety analysis with the corresponding trend equation.

Failure Mechanism

The comparison between the study by Jostad and Lacasse (2015) and the present study shows varying results. Figure 5.8 illustrates the incremental displacements for one of the cases analysed by Jostad and Lacasse (2015). The shear mechanism is similar to the one displayed in Figure 5.9 for the present study, where $b = 2$, $d = 1$ and $w = 4$. Figure 5.10 shows the shear mechanism for $w = 1$. It is observed that the slip surface does not 'reach' the bottom boundary, which is due to the rough restraints on the side surfaces. This changes the attempted $d = 1$ to a smaller value, which affects the stability number N_0 . The stability number should increase, which should lead to an increase in safety factor according to the stability chart by Janbu (1954), see Figure 2.12.

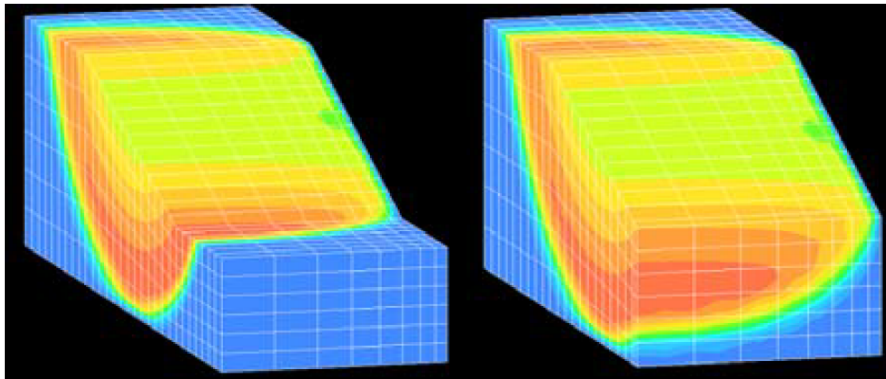


Figure 5.8: Shear mechanism for $b = 3$ and $d = 1$, retrieved from (Jostad & Lacasse, 2015).

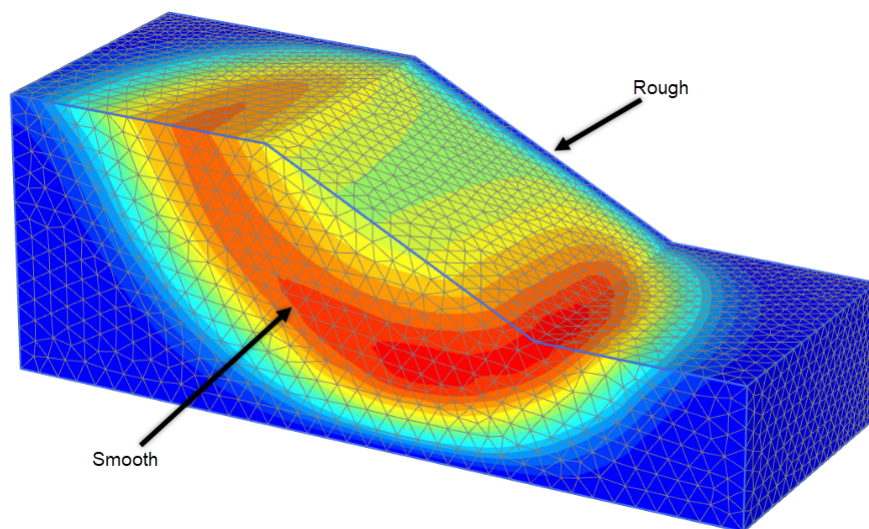


Figure 5.9: Half-model shear mechanism obtained in present study for $w = 4$ and $d = 1$.

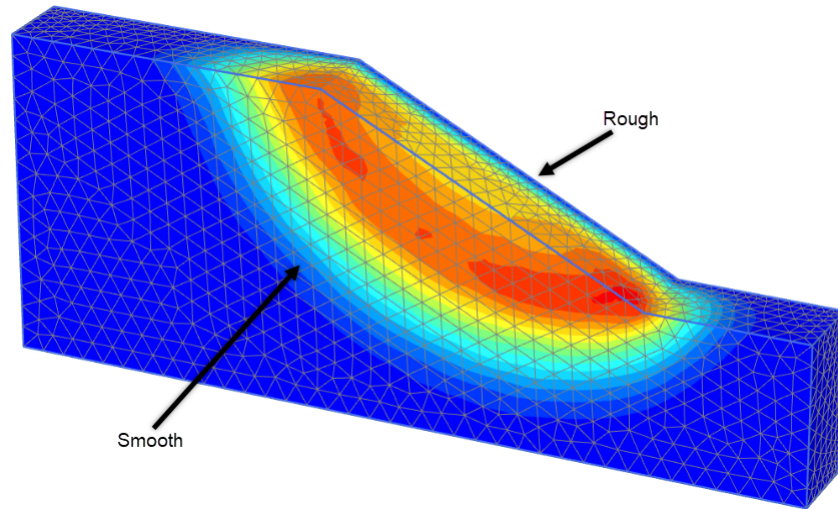


Figure 5.10: Half-model shear mechanism obtained in present study for $w = 1$ and $d = 1$.

Safety Factors and 3D-effects

Table 5.6: Comparison with Jostad and Lacasse (2015) for a slope with inclination $b = 2$ and $\frac{S_u}{\gamma H} = 0.20$. The 3D-effect F_{3D} is the ratio between the 3D FEM and the 2D LEM safety factor.

Case description			Jostad and Lacasse (2015)			Present study		
Inclination b	$d = D/H$	$w = W/H$	N_0	F_{3D}	SF	N_0	F_{3D}	SF
$b = 2$	$d = 1$	$w = 1$	5.90	1.92	2.27	5.94	2.07	2.46
$b = 2$	$d = 1$	$w = 2$	5.90	1.45	1.71	5.96	1.46	1.74
$b = 2$	$d = 1$	$w = 4$	5.90	1.19	1.40	5.97	1.19	1.42
$b = 2$	$d = 1$	$w = \infty$	5.90	1.00	1.18	5.95	1.00	1.19
$b = 2$	$d = 0$	$w = 1$	8.08	1.55	2.51	7.99	1.74	2.78
$b = 2$	$d = 0$	$w = 4$	8.08	1.11	1.79	8.01	1.23	1.97
$b = 2$	$d = 0$	$w = \infty$	8.08	1.00	1.62	7.98	1.04	1.66

Table 5.6 shows the comparison of safety factors (SF), stability numbers (N_0) and 3D-effects ($F_{3D} = SF_{3D}/SF_{2D}$) for the study by Jostad and Lacasse (2015) and the present study. For the simple infinitely wide slopes the numbers are similar. However, as the width decreases, the difference between the study results increases significantly. This is further illustrated in Figure 5.11, where the 3D-effects (F_{3D}) are plotted against the width-height ratios $w = W/H$. The large variation for lower values of w is possibly due to issues concerning unfavourable discretisation of

the present study models. Since the model width is narrowed, a greater part of the total nodes are restrained at the sides. Consequently, the discretisation errors are magnified with approximately the same mesh density. Therefore, a finer element distribution should be considered for the narrower fixed widths.

Figure 5.11 shows findings for $d = 0$ and $d = 1$ from the present study and the study by Jostad and Lacasse (2015). The 3D-effects (and safety factors) obtained for $d = 0$ vary more between the two mentioned studies compared to $d = 1$. The explanation from the previous paragraph regarding restraining of degrees of freedom (dofs) is still current. $d = 0$ gives a shallower slide than $d = 1$. The bottom restraints are elevated to the toe level, which further decrease the model volume and increase the relative number of restrained nodes. Consequently, the potential discretisation problems may increase for a shallower model, which may be remedied by a finer mesh. An extreme mesh refinement is tested for the smallest model, where $d = 0$ and $w = 1$. The element distribution is set as *Very fine* for a coarseness factor of 0.25 at the fixed side surface and 0.5 for the rest of the volume. This calculation provided approximately the same safety factor as obtained by Jostad and Lacasse (2015), which is assumed accurate.

The stability numbers and safety factors are larger for the cases with $d = 0$. However, the 3D-effects are lower for $d = 0$ than $d = 1$ as presented in Figure 5.11. The exception is for $w = 4$ in the present study, which is most likely due to too coarse element distribution that leads to an overshoot. The reason for lower 3D-effects for $d = 0$ may be that the slide depth and volume have decreased, and less side surface area is subjected to the end effects simulated by model restraints. There is less three-dimensional slip surface area, i.e. shear surface that is wider out from the deepest '2D shear surface', that contributes to the 3D-effects.

Griffiths and Marquez (2007) studied a similar case with undrained behaviour and fixed widths. The same $\frac{S_u}{\gamma H} = 0.20$ was used. However, the depth-height ratio was modelled as $d = 0.5$. Consequently, the findings are not completely comparable, but safety factors should be in close range. The result from Griffiths and Marquez (2007) should fit in between the results for $d = 0$ and $d = 1$ used in the present study and by Jostad and Lacasse (2015). As earlier presented in chapter 3 and Figure 3.3, Griffiths and Marquez (2007) obtained the following safety factors for varying w : $w = 1$ gave approximately $SF = 1.26$, $w = 2$ gave $SF = 1.73$ and $w = 4$ gave approximately $SF = 1.42$. The corresponding 3D-effects are included in Figure 5.11. The results fit well

between findings for $d = 0$ and $d = 1$ found by Jostad and Lacasse (2015), which is assumed to be accurate.

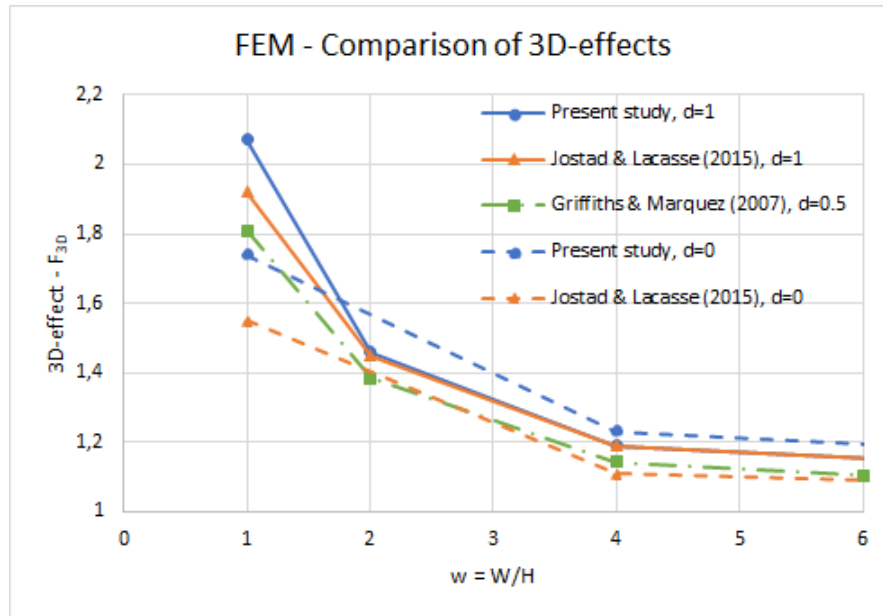


Figure 5.11: Comparison of 3D-effects between the present study, the study by Jostad and Lacasse (2015) and the study by Griffiths and Marquez (2007). Results include F_{3D} for $d = 0$ and $d = 1$ with varying $w = W/H$.

Safety factors of the present study with undrained strength are believed to be overestimated. As a consequence, this validation is not completely satisfied. Further mesh refinement may remedy the overshoot. However, the analyses are too time consuming for the present thesis. Fully fixed boundary conditions may be a significant factor that 'disturbs' the accuracy. Furthermore, use of two different material models Mohr-Coulomb and NGI-ADP may influence the variation. In addition, required element distribution may differ for various soil types, since the validations using drained strength provided adequate accuracy for a coarser mesh, unlike Example 3.

5.2 Mesh Sensitivity Analysis

The accuracy of three-dimensional finite element calculations depends significantly on the meshing and the element density. Therefore, a sensitivity analysis is conducted to assess and optimise the meshing options. Different geometrical properties are assessed, such as model depth and width. Moreover, a series of mesh densities are studied to evaluate their application in acquiring an accurate safety analysis. Default numerical settings were used for the calculation phases. 100 steps were used in the safety analysis, and the safety factor multiplier ΣMsf obtained in the last step is documented as the SF in the following tables as a simplification. Several safety analyses show a steady increase in safety factor (or ΣMsf) over deformation, and the last value of SF is possibly inaccurate.

Figure 5.12 shows the three-dimensional slope geometry in the PLAXIS defined coordinate system. b is the slope inclination, H is the slope height, W is the slope model width and D is the depth below toe level to the bottom (fixed) boundary. L is the horizontal length of the slope, LB is the model length behind the slope crest to and LF is the model length in front of the slope toe.

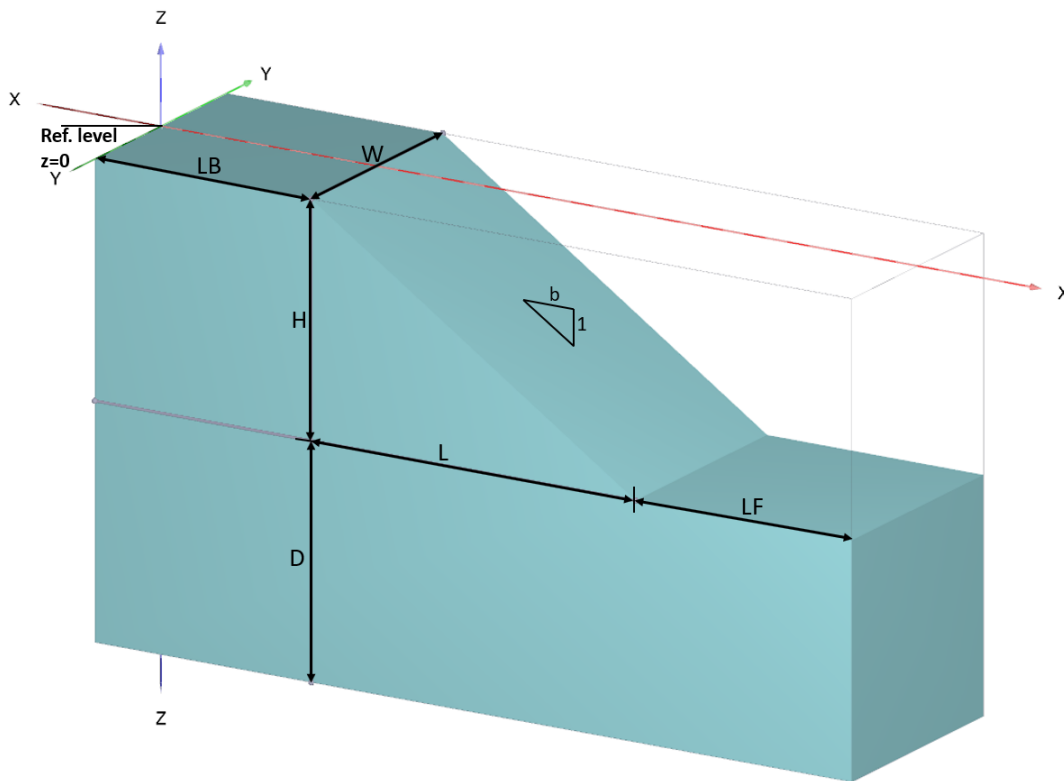


Figure 5.12: 3D slope geometry. See Table 5.7 for explanations.

Table 5.7 contains the various geometrical properties used in the sensitivity analysis. The values are varied for each attribute to study their influence on the safety factor and accuracy. The values are chosen on the basis of where it is believed that the slip surface will occur and how the slip surface may be affected by the boundaries. The width w is in this sensitivity analysis not a fixed width. It is the model width, i.e. the width modelled with elements in PLAXIS 3D. The side surface boundaries are automatically set as normally fixed, which implies that the slope is simulated infinitely wide in the y -direction (orthogonal to the slope sides). The exception is the fixed width sensitivity analysis in subsection 5.2.2, where the side surfaces are fully fixed.

Table 5.7: Defined geometrical attributes for a simple 3D slope, see Figure 5.12.

Geometrical attribute	Symbol	Value
Slope inclination	b	1.5
Slope height	H	10 m
Depth below slope toe	D	10 – 30 m
Length of surface behind the slope	LB	20 m
Length of surface in front of slope	LF	10 – 20 m
Horizontal length of slope	L	$H \cdot b$
Slope width	W	1 – 10 m

In subsection 5.2.2 a slope with curved surface is analysed. This is a simple convex curvature example. The model width is larger compared to the geometry just described. This sensitivity analysis focuses on the simple planar slope. However, the curved slope is added since it is an important part of the main analysis. To avoid repetition, the curvature model is explained in section 7.1.

5.2.1 Mesh Density

Various mesh configurations are available in PLAXIS 3D. The five automatic mesh settings are *Very coarse*, *Coarse*, *Medium*, *Fine* and *Very fine*, where the element density varies significantly inside the range. Figure 5.13 shows the results from three safety analyses using *Very coarse*, *Medium* and *Very fine* mesh. All analyses appear to obtain a flat curve, however, all have a slight tendency of increasing. The difference between the meshes are significant, but not extreme. The model is simple with a width of 10m and only normally restrained at the sides ('smooth'). Consequently, numerical issues or high inaccuracy is not of concern here. More restraints and

larger models may give a larger spread of safety factors between the different element distributions. Moreover, the variation between the results decreases as the mesh is refined, which means that a more accurate safety factor is approached. For a smaller model without fully fixed widths, the difference between the meshes would be less and potentially negligible.

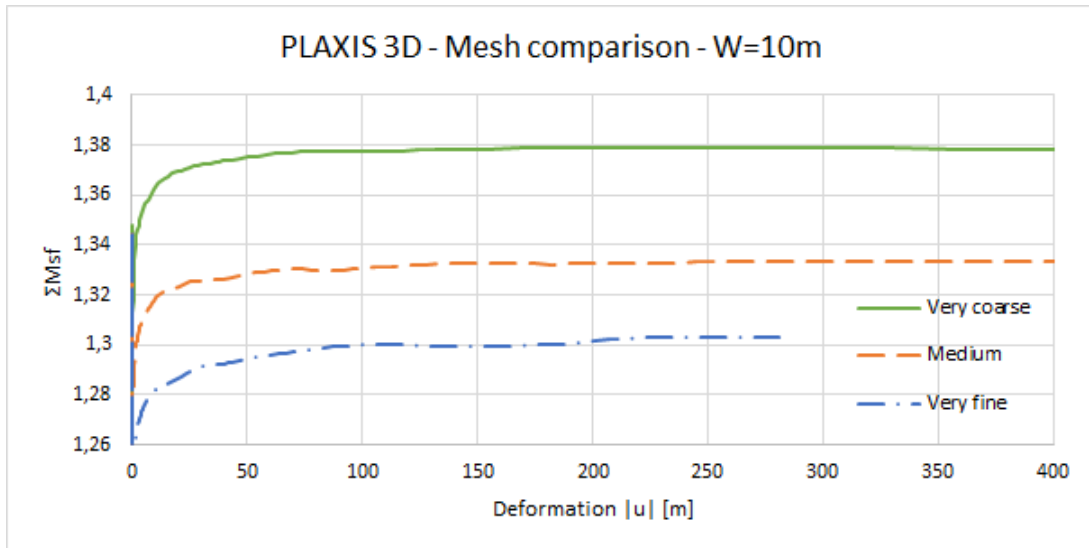


Figure 5.13: Comparison of safety analysis for three of the automatic element distributions available in PLAXIS 3D. The model used have a width of 10m with 'smooth' side surfaces. ΣMsf at failure defines the safety factor.

Width and Mesh Dependency

For simple models a *Very fine* mesh is used to obtain fairly accurate analyses, which are not too time consuming. It is possible to create a finer/denser mesh by reducing the coarseness factor for any model component, which opens for local refinement. This may enhance the accuracy for elements that are subjected to restraining conditions that complicate the discretisation. In the present study the coarseness factor (or reduction factor) is indicated by the \times -symbol and the value of reduction, e.g. no refining is $\times 1.0$ and by refining to approximately half the element size is noted $\times 0.50$.

Table 5.8 summarises the analyses for different widths and element distributions. Only widths W of 1 m, 5 m and 10 m are evaluated to save calculation time. The widths are not fully fixed and should simulate infinitely wide slopes. The safety factors (SF) in the table are simply the value obtained in the last step of the safety analysis of 100 steps. Coarseness factors of 1.0, 0.75 and 0.50 are used to assess the impact on safety factor and 'convergence' of the solution.

Further, Table 5.8 shows how the number of elements and nodes change, along with the average element size. The number of elements and nodes increase and the element size decreases as the mesh is refined, as expected. Furthermore, the average element size increases with the model width. The program adapts the element size differently depending on the model size. In addition, the difference in element size is greater between $W = 1 m$ and $W = 5 m$ than $W = 5 m$ and $W = 10 m$. This may be due to the relative narrowness of the width of $1 m$, where there is approximately only one element in the width.

Table 5.8: Evaluation of mesh and model width dependency for different (*Very fine*) element distributions for each depth below toe, with the corresponding last step safety factor. The depth D is set as $20m$.

Width W	element distribution	Nr. of elements	Nr. of nodes	Avg. elem. size	SF
$1m$	Very fine ($Vf \times 1.0$)	2893	6069	$1.439m$	1.250
$5m$	Very fine ($Vf \times 1.0$)	9827	16907	$1.930m$	1.291
$10m$	Very fine ($Vf \times 1.0$)	16821	26984	$2.015m$	1.302
$1m$	$Vf \times 0.75$	7479	15314	$1.178m$	1.239
$5m$	$Vf \times 0.75$	20406	33684	$1.501m$	1.275
$10m$	$Vf \times 0.75$	39234	60144	$1.517m$	1.289
$1m$	$Vf \times 0.50$	21142	40101	$0.8885m$	1.239
$5m$	$Vf \times 0.50$	66101	102386	$1.013m$	1.261
$10m$	$Vf \times 0.50$	125653	184705	$1.029m$	1.268

Figure 5.14 shows the plots with safety factor multiplier ΣMsf vs. total deformation $|u|$ from the various scenarios presented in Table 5.8. The non-dotted lines represent the *Very fine* $\times 1.0$ mesh, the dashed lines represent the *Very fine* $\times 0.75$ mesh and the small dotted lines represent the *Very fine* $\times 0.50$ mesh. The plots reveal a significant difference between the element distributions and the model widths. The finer and smaller models obtain a more accurate solution of the safety factor compared to the coarser and larger models. Further mesh refining is of less influence for the smaller models and finer meshes. The case of $W = 1 m$ shows how the influence of refinement reduces. Moreover, the curve has flattened out to an approximately horizontal line, and thus an unambiguous convergence of SF is obtained.

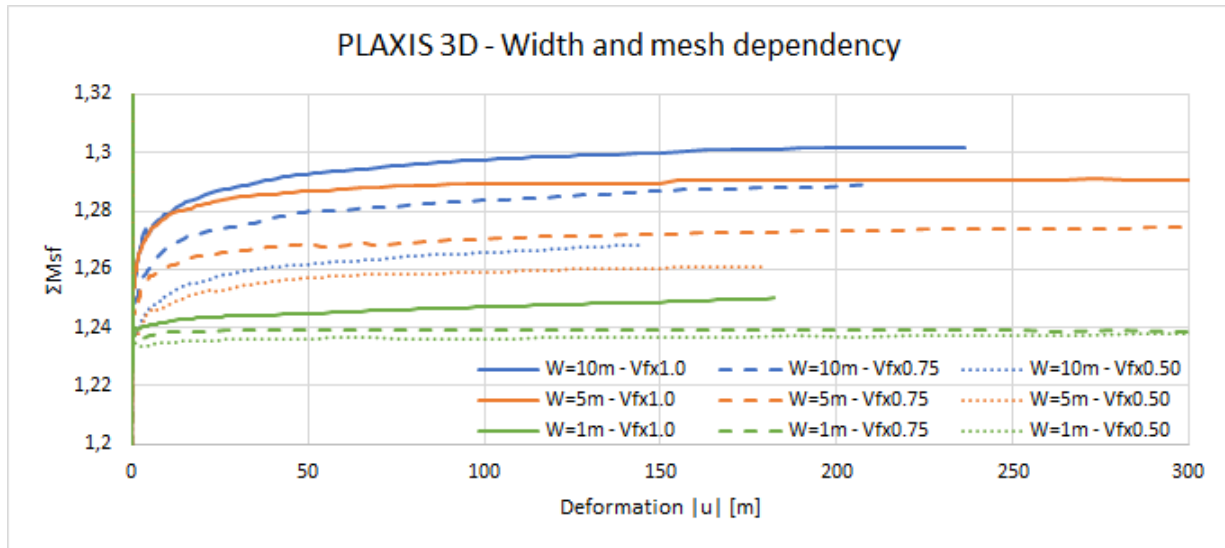


Figure 5.14: The plots show the effect of the model width and mesh coarseness on the safety factors.

Depth and Mesh Dependency

Favourable discretisation may depend on distance to model boundaries. Therefore, a brief sensitivity check is conducted for depths D equal 10 m , 20 m and 30 m for *Very fine* element distributions with coarseness factor 1.0 and 0.75. Table 5.9 summarises the data obtained for these cases. The difference in results is not significant. However, larger models (deeper) will use more CPU time and have greater average element size for the same element distribution. Consequently, the depth of 10 m is considered the optimal option.

Table 5.9: Evaluation of mesh and depth dependency for different (very fine) element distributions for each depth below toe, with the corresponding last step safety factor. The model used has a width of 1 m .

Depth D	Element distribution	Nr. of elements	Nr. of nodes	Avg. elem. size	SF
10 m	Very fine (Vf)	2893	6069	1.439 m	1.250
20 m	Very fine (Vf)	4315	8904	1.526 m	1.239
30 m	Very fine (Vf)	4984	10281	1.587 m	1.261
10 m	Vf \times 0.75	5286	10932	1.188 m	1.235
20 m	Vf \times 0.75	7479	15314	1.255 m	1.239
30 m	Vf \times 0.75	8967	18308	1.319 m	1.240

Furthermore, Figure 5.15 and Figure 5.16 display that there is a limit for element distribution

fineness needed to obtain reasonable safety factors independent of depth. For this specific model geometry the depth dependency becomes approximately negligible for a *Very fine* mesh with coarseness factor 0.75. Moreover, the plots in Figure 5.16 show better convergence of the safety factor multiplier ΣMsf .

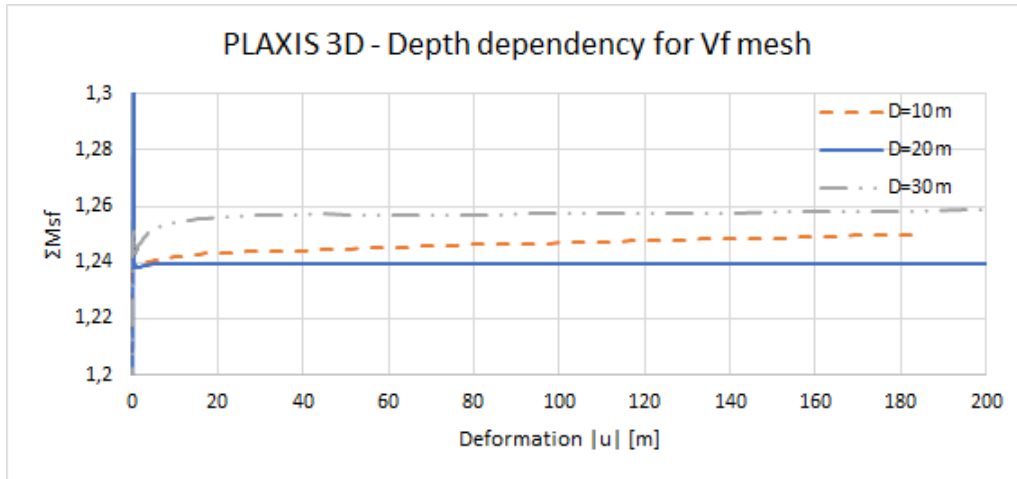


Figure 5.15: The plots show the effect of the model depth on the safety factors for a *very fine* element distribution.

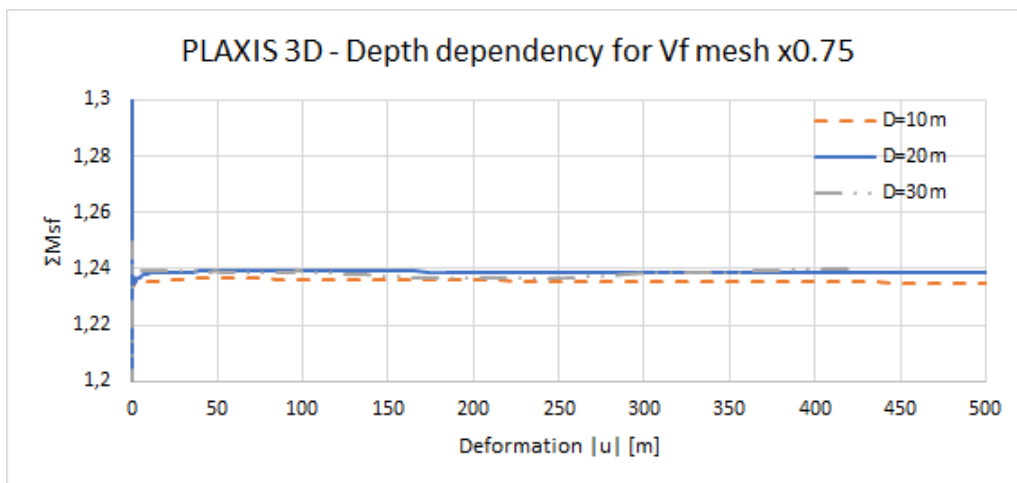


Figure 5.16: The plots show the effect of the model depth on the safety factors for a *very fine* mesh with a coarseness factor of 0.75.

Volume and Mesh Dependency

The calculations conducted in PLAXIS 2D used a depth below toe $D = 20\text{ m}$ and length behind crest LB and length in front of toe LF equal to 20 m . This 2D 'volume' is henceforth referred to as the regular volume. A new reduced volume is proposed as measure to streamline the calcula-

tions in PLAXIS 3D. The reduced volume has dimensions defined as: $LB = 20\text{ m}$, $LF = 10\text{ m}$ and $D = 10\text{ m}$. The width W of the analysed models is set as 5 m .

Table 5.10 summarises the results obtained for the two volumes with varying coarseness factors. The element size of the reduced volume is significantly lower compared to the regular volume, and consequently the reduced volume provides more elements and nodes. The denser mesh of the reduced volume gives lower safety factors compared to the regular volume, and the safety factors decrease as the coarseness factor is reduced.

Table 5.10: Evaluation of volume and depth dependency for different (very fine) element distributions, with the corresponding last step safety factor. The models used has a width of 5 m . The regular volume (reg. vol.) has back length of slope $LB = 20\text{ m}$, front length $LF = 20\text{ m}$ and depth $D = 20\text{ m}$. The reduced volume (red. vol.) has $LB = 20\text{ m}$, $LF = 10\text{ m}$ and $D = 10\text{ m}$.

Volume	element distribution	Nr. of elements	Nr. of nodes	Avg. elem. size	SF
Reg. vol.	Very fine (Vf)	9827	16907	1.930m	1.291
Red.vol.	Very fine (Vf)	10128	17255	1.533m	1.274
Reg. vol.	Vf×0.75	20406	33684	1.501m	1.275
Red. vol.	Vf×0.75	22095	35508	1.182m	1.266
Reg. vol.	Vf×0.50	66101	102386	1.013m	1.261
Red. vol.	Vf×0.50	72350	110009	0.79398m	1.252

Figure 5.17 shows the ΣMsf vs. deformation curves for the assessed cases. The plots representing the reduced volume develop at a lower safety factor and appear to be the most accurate solution. The incremental increase of ΣMsf over deformation is varying for the different cases. However, there is no alternative showing any apparent solution that converges with a flattening curve. Therefore, a volume option providing the lowest safety factor is considered the most optimal of those evaluated. A continuing search for the optimal volume may be completed.

The present study concluded that this is an adequate optimisation for this example. The necessary value of coarseness factor is difficult to predict. From this simple sensitivity analysis it seems advisable to use a coarseness factor lower than 1.0. However, a value of 0.50 may be inefficient. The following section presents a brief sensitivity analysis of the more complex slope geometries in the project to ensure accurate simulation of the failure mechanism.

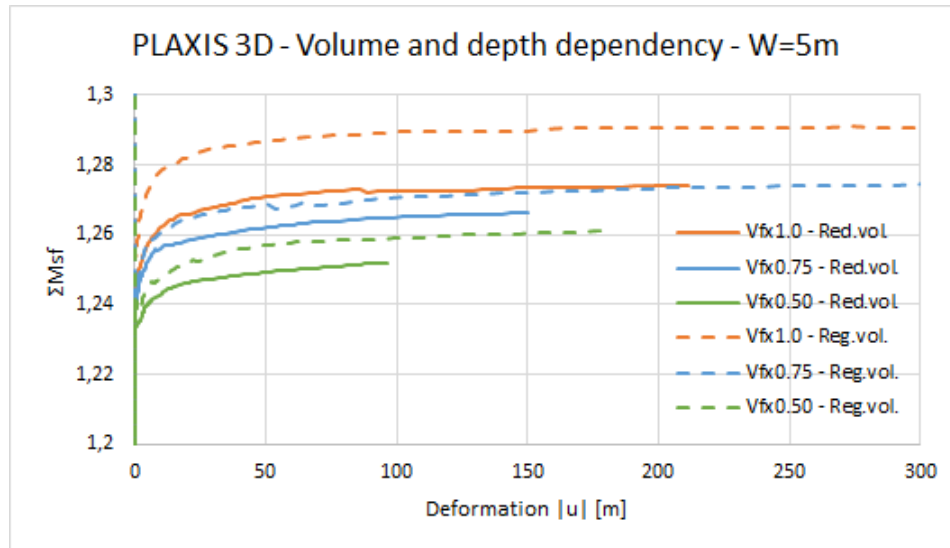


Figure 5.17: The plots show the effect of the model depth and volume on the safety factors for a different mesh coarseness factors. The model width is 5 m . The regular volume (reg. vol.) has back length of slope $LB = 20\text{ m}$, front length $LF = 20\text{ m}$ and depth $D = 20\text{ m}$. The reduced volume (red. vol.) has $LB = 20\text{ m}$, $LF = 10\text{ m}$ and $D = 10\text{ m}$.

5.2.2 Mesh Sensitivity for Fixed Width and Curved Geometry

The main focus of evaluation in the present study is analyses of fixed widths and curved geometries. Therefore, one example of both categories are analysed for two different mesh configurations. The model definitions with the smallest volume for each slope type is used to save time. Findings from subsection 5.2.1 are used as model basis, and continued on to optimise the main three-dimensional analyses.

Fixed Width - $w=1$

The fixed width model is defined similar to the reduced volume described in the previous subsection. The half-model width is 5 m , and $w = W/H$ is thus $10\text{ m}/10\text{ m} = 1$. For the half-model only one side surface needs fully fixed boundaries. Both cases of element distribution are defined as *Very fine*. The mesh configuration $Vfx0.50 - 1.0$ implies a coarseness factor of 1.0 for the soil volume and 0.5 at the side surface with zero displacement in all directions, see left slope in Figure 5.18. $Vfx0.25 - 0.50$ describes a mesh where the model volume has coarseness factor 0.50 and the side surface has 0.25, see right slope in Figure 5.18. The side surfaces are given a finer mesh, because the fully fixed boundaries leads to restrained nodes and fewer degrees of freedom. Therefore, more nodes are necessary to obtain a more accurate discretisation.

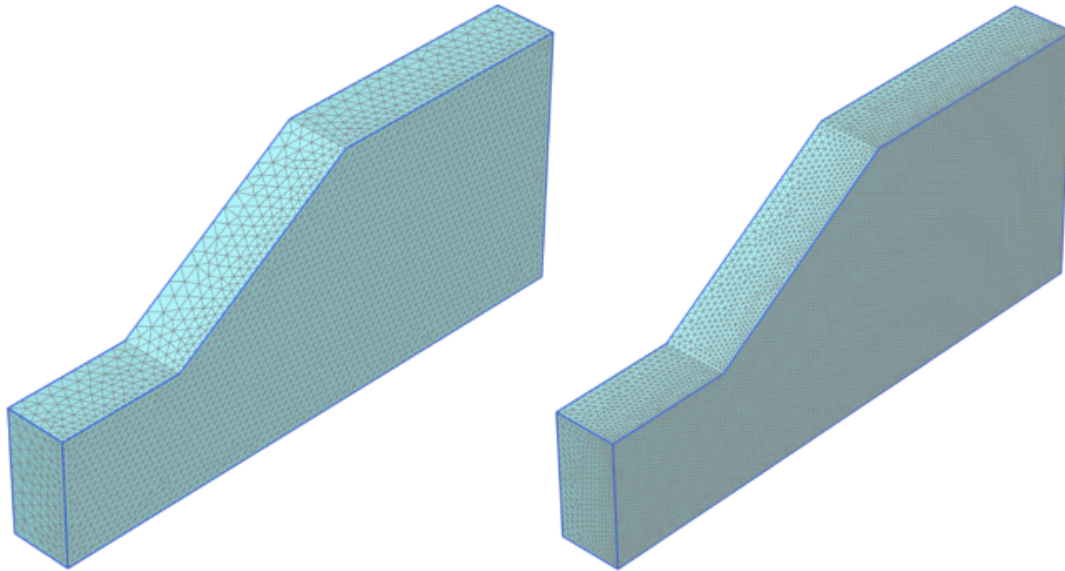


Figure 5.18: Mesh options $Vfx0.50 - 1.0$ (left) and $Vfx0.25 - 0.50$ (right) for $w = 1$

Figure 5.19 shows the significant difference between the two mesh configurations for $w = 1$. Approximately a value of 0.1 is dividing the two options. The accuracy of the two solutions is uncertain. Even though the refined solution for $Vfx0.25 - 0.50$ is more accurate, the calculation is too time consuming. Consequently, it is not an option for the limited time of the present project. Focus is rather directed at analysing different geometries and slope properties. Therefore, the element distribution used for the fixed width analyses is *Very fine* with a volume coarseness factor of 1.0 and side surface coarseness factor of 0.5.

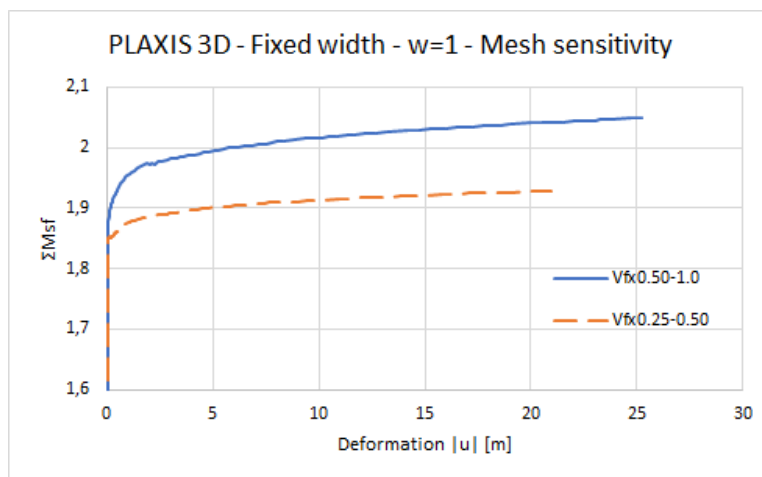


Figure 5.19: Safety analysis for fixed width $w = W/H = 1$ with mesh configuration $Vfx0.50 - 1.0$ and $Vfx0.25 - 0.50$ (dashed). Safety factor multiplier ΣMsf is plotted against deformation $|u|$.

Curvature - $r_u = 1$

The curved surface example model is a convex slope with radius-height ratio $r_u = R_u/H = 1$ and curvature angle $\alpha = 90^\circ$. Geometrical properties are further explained in section 7.1. All boundary conditions for the curved slope models are defined as only restrained normally on the surfaces, except for the fully fixed bottom boundary. Therefore, the model mesh is attempted refined near the location of the failure surface. Such local refinements are used, because the models and calculations become comprehensive and time consuming. Approximately the area from the slope toe to 10 m behind the slope crest is refined by half the coarseness factor of the remaining volume for this specific example. The same two mesh configurations are used as for the fixed width model. The left slope in Figure 5.20 has a coarseness factor 0.5 in the refined part of the volume, and 1.0 in the rest of the model. The right slope in Figure 5.20 has a refined part with coarseness factor 0.25, while the remaining model has 0.50.

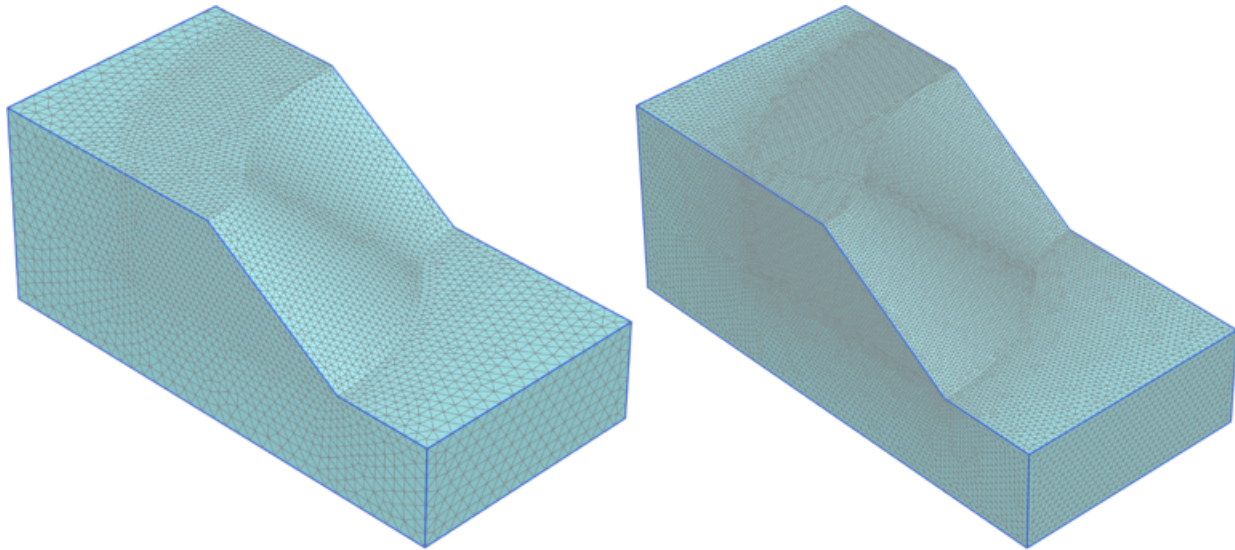


Figure 5.20: Mesh options $Vfx0.50 - 1.0$ (left) and $Vfx0.25 - 0.50$ (right) for $r_u = 1$

Figure 5.21 shows how the two mesh alternatives affect the safety analysis. This is the smallest curved slope model in the present study. The sensitivity may range significantly between the various slope models, since the variation in size makes it difficult to define comparable meshes. The difference between $Vfx0.50 - 1.0$ and $Vfx0.25 - 0.50$ for the slope example is small, which may indicate adequate accuracy. However, no conclusion can be made regarding the accuracy without a more extensive sensitivity analysis. Nonetheless, the refined option is considerably

more time consuming. Therefore, the *Very fine* option with coarseness factors 0.50 to 1.0 is selected for the main simulations of the present study.

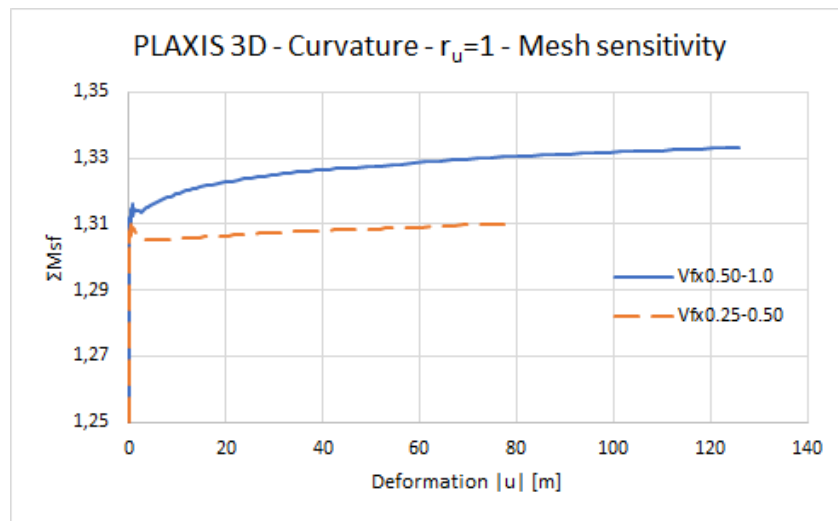


Figure 5.21: Safety analysis for convex slope surface where $r_u = R_u/H = 1$ and $\alpha = 90^\circ$ with mesh configurations $Vfx0.50 - 1.0$ and $Vfx0.25 - 0.50$ (dashed). Safety factor multiplier ΣMsf is plotted against deformation $|u|$.

5.2.3 Convergence in Safety Analysis

The $\Sigma Msf - |u|$ (safety factor multiplier - deformation) plot available as output in PLAXIS 3D is used to quality check the safety analysis. It provides the 'convergence' to the correct safety factor, i.e. the curve flattens towards a approximately horizontal line for increasing deformation. For the defined strength profile and soil model in this study, the 'convergence' of the safety factor is quite unambiguous in the PLAXIS 2D calculations, i.e. the curve flattens as it reaches the estimated safety factor, regardless of accuracy. However, for most PLAXIS 3D analyses using this strength and soil model the curve continues to increase steadily as the deformation increases.

An extreme mesh refinement or a very small model may act as a remedy to flatten the curve. However, it may be impractical and time consuming. Mesh refinement is of little use for several of the larger models in this study ($W > 10m$ or with curved surface). Therefore, to obtain a safety factor without an apparent 'convergence', a linear trend line is adapted to the part of the $\Sigma Msf - |u|$ curve that starts to exhibit an almost linearly increasing line. The constant term of the trend line equation is used as the documented safety factor. This procedure is a pragmatic method of acquiring the safety factor, and some uncertainty must be accounted for.

Chapter 6

3D Simulations - Finite Width Planar Slope

A simple evaluation of 3D-effects can be obtained by analysing planar slopes with varying fixed or finite widths. Several literature studies have used this procedure to assess and compare 3D slopes with traditional plane strain calculations. Such analyses can provide a useful indication of 3D-effects and their sensitivity to a change in geometry or material properties. Findings and limitations of the following analyses are discussed in the end of the chapter.

6.1 3D Modelling of Planar Slope with Finite Width

In the preliminary 2D analyses of the project, see chapter 4, the fixed widths were simulated using the side shear input in GeoSuite Stability. The three-dimensional simulations in the present section use the same width-height ratios as in the preliminary analysis to get a comparison of the two programs. PLAXIS 3D is the main three-dimensional software of the present study. FE modelling in PLAXIS 3D will be further described in the following subsection. Additionally, the LE program Slide3 is used to compare some finite widths.

The widths are fixed by fully restraining the side surfaces on the model in PLAXIS 3D, i.e. fully fixed at y_{min} and y_{max} . Width is defined in the y -direction. The actual modelled slope in PLAXIS 3D will only be half the width $W/2$ and only fully fixed on one side, because the model will become symmetrical around the side surface with only normally restrained displacement. A half-model reduces the number of elements and equations to be solved, which will decrease calculation time and discretisation errors. The accuracy becomes better for approximately the

same element density. The side surfaces with zero displacements in all directions are activated in phase 1 after initial phase (0) with gravity loading. Phase 2 is the safety analysis including the fixed slope sides. The calculation phases are provided in Appendix A. Moreover, default numerical settings are used.

6.1.1 Model Geometry

Figure 6.1 shows the defined geometry for a simple planar slope. The reference level at $z = 0$ is used to defined the undrained shear strength profile. z -axis is set as the vertical direction (positive upwards), and x - and y -axis are the horizontal directions. y is the width direction and x is the slope length direction. b is the slope inclination, H is the slope height, W is the slope model width and D is the depth below toe level to the bottom (fixed) boundary. L is the horizontal length of the slope, LB is the model length behind the slope crest and LF is the model length in front of the slope toe.

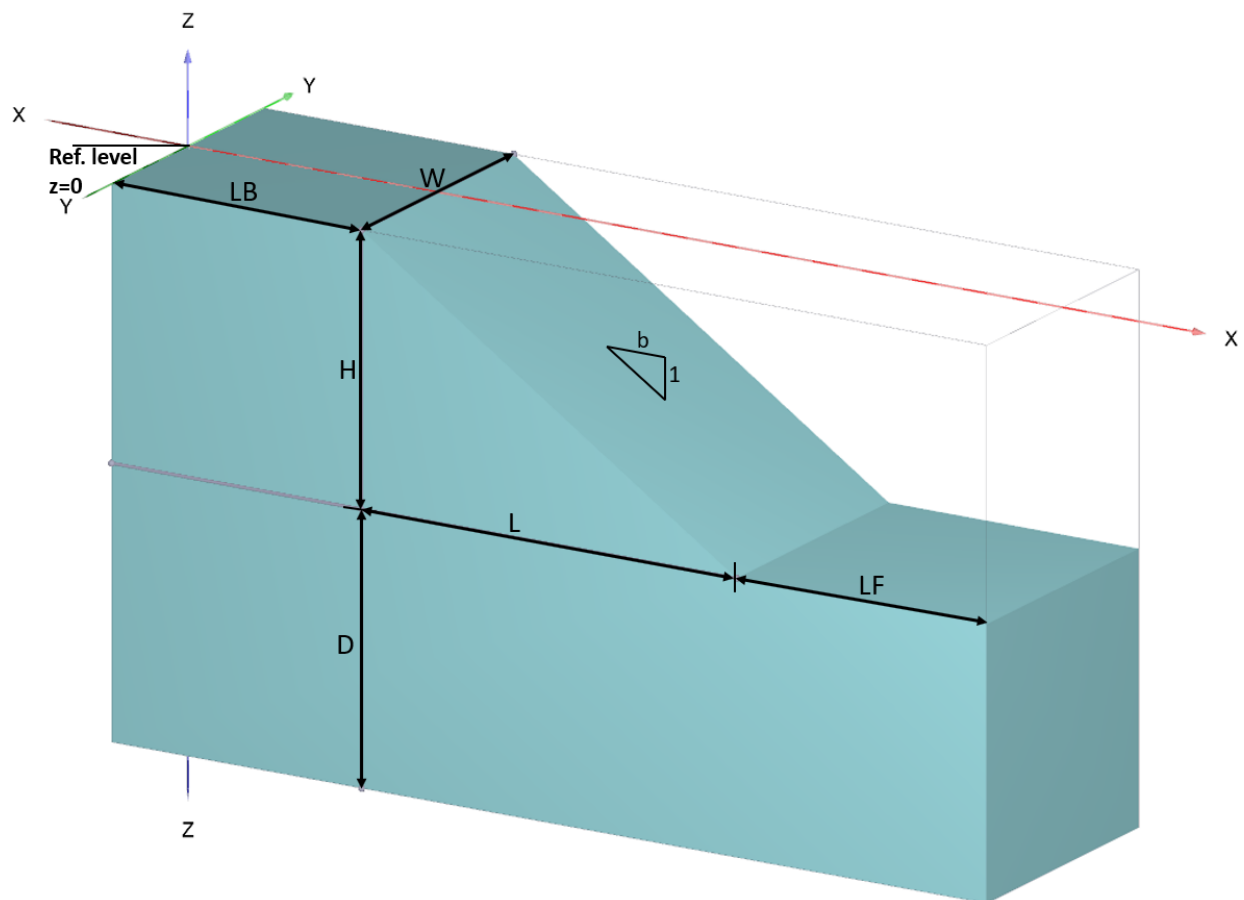


Figure 6.1: 3D geometry of finite width planar slope, with the PLAXIS 3D coordinate system.

Table 6.1 describes the geometrical attributes as explained in Figure 6.1. Lengths are chosen based on the mesh sensitivity analysis conducted in section 5.2. The model is optimised with respect to time and discretisation accuracy. A smaller model is less time consuming compared to a larger model. Moreover, the model should cover the failure surface in depth (z) and length direction (x), especially with regards to the bottom boundary. A depth $D = 10\text{ m}$ is found adequate since the slip surface is a toe failure, which will for this case be quite shallow. The front length is set as shorter than the back length since the slip surface will begin some meters behind the crest and exit at the toe, as found in the preliminary analysis (chapter 4).

Table 6.1: Defined geometrical properties for a simple 3D slope, see Figure 6.1.

Geometrical attribute	Symbol	Value
Slope inclination	b	1.5 (Case 1)
		2 (Case 2)
		3 (Case 3)
Slope height	H	10 m
Depth below slope toe	D	10 m
Length of surface behind the slope	LB	20 m
Length of surface in front of slope	LF	10 m
Horizontal length of slope	L	$H \cdot b$
Slope width	W	10, 20, 40 & 60 m

6.1.2 Soil Strength

The soil strength for the clay material is the same used in PLAXIS 2D and GS Stability in the preliminary analysis:

$$S_u = 20 + 2z \quad [kPa]$$

where z is the vertical depth in meters below reference level. Furthermore, the Mohr-Coulomb soil model with *Undrained B* is utilised in PLAXIS 3D. A toe failure mechanism is obtained, due to the increase in strength with depth. Furthermore, the soil unit weight is 19.0 kN/m^3 . The remaining material parameters are provided in Appendix A.

Since several studies in literature have stated that 3D-effects increase with cohesion, different strength profiles are tested in this analysis. The three cases of undrained soil strength defined

for the present analyses are:

$$S_u^1 = 20 + 2z \quad [kPa] \quad (6.1)$$

$$S_u^2 = 30 + 2z \quad [kPa] \quad (6.2)$$

$$S_u^3 = 40 + 2z \quad [kPa] \quad (6.3)$$

Only the first expression S_u^1 is used for all cases of slope inclination. The cohesion sensitivity analysis is carried out with a single value of inclination, which is $b = 1.5$, see subsection 6.2.3.

6.1.3 Mesh and Convergence

Several aspects influence the choice of mesh coarseness in finite element analysis, such as time, accuracy and discretisation errors. Computer and CPU capacity are important in the assessment of what is acceptable meshing, and several efficiency tests of PLAXIS 3D models are run to optimise the simulations. A more thorough mesh sensitivity analysis is presented in section 5.2.

For the analyses of a planar slope with fixed width in PLAXIS 3D, the automatic *Very fine* element distribution is selected. Furthermore, the soil volume of the half-model is given a default coarseness factor of 1.0, i.e. no further refinement from the *Very fine* mesh. The side surface with the fixed displacement field ('rough'), i.e. restraints in all directions, is given a coarseness factor of 0.5. Consequently, the mesh transfers from coarseness factor 0.5 at the fully fixed side to coarseness factor 1.0 at the symmetrical 'smooth' side of the model. The element density decreases from the 'rough' boundary to the 'smooth' boundary, see Figure 6.2. This is favourable for the element discretisation, since more nodes are available where the nodes are most restrained. The restraining of the nodes leads to fewer degrees of freedom (dofs). Therefore, the elements struggle more to accurately solve the numerical equations. A finer mesh results in more nodes (and dofs) to transfer the strains between the elements, and thus providing a better estimation of the displacements.

A brief explanation on how the safety analysis converge and how the documented safety factor is found is available in subsection 5.2.3. The data points from a $\Sigma Msf - |u|$ plot retrieved from PLAXIS 3D is copied to Excel, where the steps before the curve straightens are removed. The remaining points are fitted with a linear trend line, which provides a pragmatic value for the

safety factor. The curve normally straightens out around steps 30 to 40 for the 3D analyses in the present study. Each safety analysis calculation runs for 100 steps.

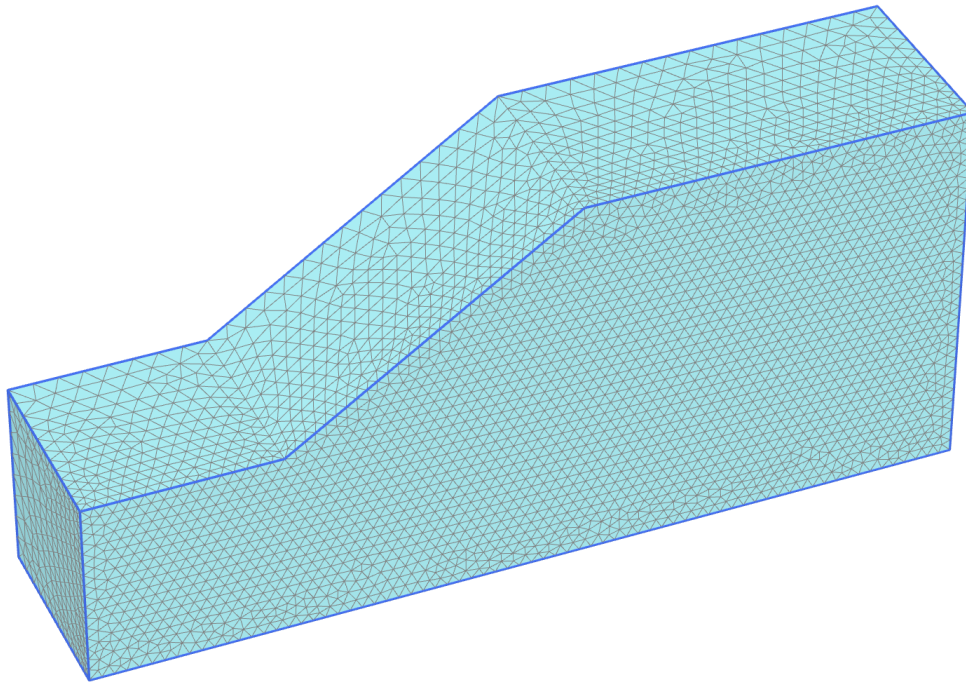


Figure 6.2: Planar slope connectivity plot from PLAXIS 3D with coarseness factor of 0.5 at the near side surface and 1.0 in the model volume.

6.1.4 Rocscience Slide3

The limit equilibrium software Slide3 from Rocscience is used to compare 3D LEM with 3D FEM. Only finite widths are modelled using Slide3. As explained in section 2.4, there are four different LE methods implemented in the program, Simplified Janbu, Simplified Bishop, Spencer and Morgenstern-Price. Morgenstern-Price with a half-sine intercolumn force function is regarded as the most advanced available method that satisfies force and moment equilibrium. Therefore, the safety factors used for comparison are those obtained with Morgenstern-Price, or GLE as called in the software.

Slide3 separates the Mohr-Coulomb model into a drained and an undrained part called Mohr-Coulomb and Undrained in the program, respectively. The Undrained material mode is selected for the shear strength profile $S_u = 20 + 2z$. Datum input is set as top of the slope, reference undrained shear strength as 20 kPa and strength gradient as 2. Consequently, the undrained strength profiles are equivalent for PLAXIS and Slide3. The soil unit weight is set as 19 kN/m^3 .

The slope model volume was created using the slope wizard function in Slide3. The same geometrical properties as given in subsection 6.1.1 were inserted. A constructed 2D profile was extruded to the desired model width W . The size of the slope volume automatically restricts the width of the resulting slide. Fully fixed side surface boundaries are required in PLAXIS 3D to force a finite width for a planar slope surface with homogeneous soil. Such boundary conditions are not available in Slide3, where columns are only mobilised within the defined model volume. Moreover, it is not possible to use a symmetrical half-model as in PLAXIS 3D, since the created volume controls which columns that are utilised. Therefore, the models that are run in Slide3 have the full width W , while only a model width of $W/2$ is constructed in PLAXIS 3D.

Various analysis options are offered in Slide3, for example regarding slip surface search and number of columns. The default settings are used for the present study analyses, with the exception that Spencer and Morgenstern-Price were included as calculations methods. Only Janbu and Bishop are set as default. The recommended default slip surface is the ellipsoidal shape, and the default search technique is the stochastic Cuckoo Search with Surface Altering Optimisation (SAO). The default number of columns is 50, which was considered sufficient for the narrow slopes defined for this thesis.

6.2 Results for Planar Slope with Fixed Width

The analysis findings for a planar slope with fixed/finite widths can be divided into three parts. The first part in subsection 6.2.1 uses the undrained shear strength profile $S_u^1 = 20 + 2z$ and the three inclination cases in PLAXIS 3D. The second part in subsection 6.2.2 has the same cases and is completed in Slide3. The third part in subsection 6.2.3 is a brief study of the effect of cohesion, with the three strength profiles as defined in subsection 6.1.2. However, only one inclination is implemented. In addition, a comparison of the results is presented in subsection 6.2.4.

6.2.1 PLAXIS 3D - Effect of Fixed Width and Inclination

PLAXIS 3D - Safety Factor

Table 6.2 presents the safety factors for four width-height ratios $w = W/H$ and the three slope inclinations. The undrained shear strength profile is defined by $S_u^1 = 20 + 2z$. The bottom three table rows include the 2D plane strain safety factors found in chapter 4. The middle row for $w = \infty$ (PLAXIS 3D, $W=1m$) is a 1 m wide 3D model with only normally fixed side surfaces, which is modelled to estimate near plane strain conditions. The 3D $w = \infty$ safety factors are close to the plane strain values. However, the 3D safety factor are slightly higher for all cases.

Table 6.2: Safety factor (SF) found in PLAXIS 3D for all cases with fixed width and shear strength S_u^1 . Additionally, plane strain solutions are included.

Width-height ratio (W/H)	Safety factor (SF)		
	Case 1: b = 1.5	Case 2: b = 2	Case 3: b = 3
$w = 1$	1.979	2.307	3.010
$w = 2$	1.557	1.764	2.179
$w = 4$	1.381	1.537	1.830
$w = 6$	1.336	1.476	1.730
$w = \infty$ (PLAXIS 3D, $W=1m$)	1.239	1.364	1.571
$w = \infty$ (PLAXIS 2D)	1.233	1.359	1.567
$w = \infty$ (GS Stability) - Ref. plane strain solution	1.232	1.357	1.570
$w = \infty$ (Hand calc. - Janbu Direct Method)	1.187	1.327	1.522

Figure 6.3 illustrates the results from Table 6.2, where the GS Stability plane strain solutions are included. As mentioned, the fixed widths defined by $w = W/H$ have a noticeable impact on the safety factors. The SF increases significantly for lower values of finite widths w . Moreover, the safety factor increase rate rises as w decreases. The smallest difference between a finite width and plane strain is approximately 8% for $b = 1.5$ and $w = 6$. The largest variation from plane strain solution is found for $b = 3$ and $w = 1$, where SF_{3D} is approximately 92% greater than $SF_{2D,GSS}$.

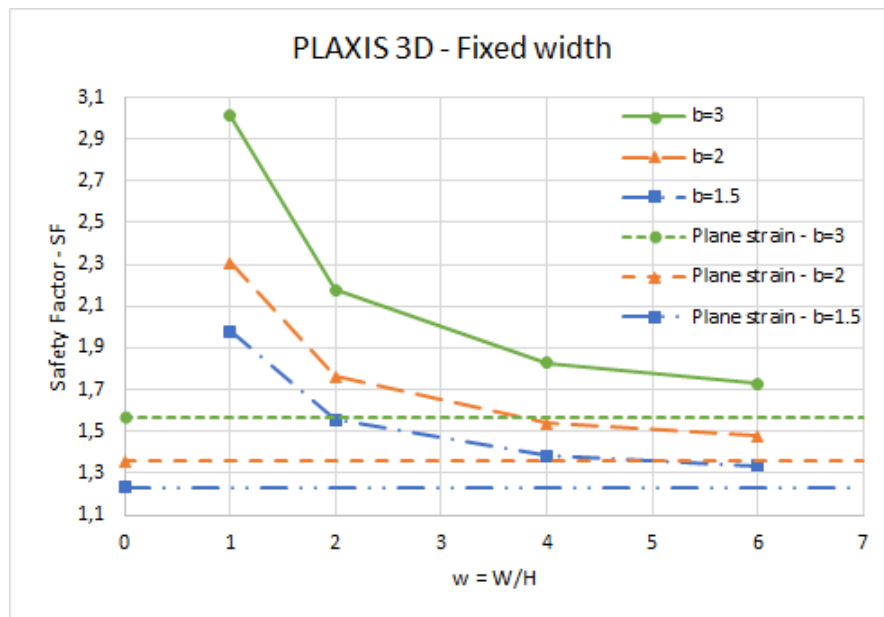


Figure 6.3: Comparison of safety factors obtained using PLAXIS 3D with fixed widths. Results from the three inclination cases. The plane strain solutions are retrieved from GS Stability.

Figure 6.4 shows the calculated 3D-effects using the plane strain solution from GS Stability as reference 2D safety factor. With accurate modelling and discretisation of the 3D-model in PLAXIS 3D, the 3D-effects should approach near $F_{3D} = 1$ for $w = \infty$. On this basis, the trend appears promising. At a slide width-height ratio $w = 6$, the 3D-effects are approximately 1.10 and similar for the three slope inclinations. As the width decreases, the effect gap between the cases increases. 3D-effects appear to increase as the slope flattens. Inclination $b = 1.5$ reaches a peak $F_{3D} = 1.61$ at $w = 0$, while $b = 3$ has a F_{3D} equal 1.92. 3D-effects from $w = 2$ to $w = 1$ have risen approximately 27%, 30% and 38% for $b = 1.5$, $b = 2$ and $b = 3$, respectively.

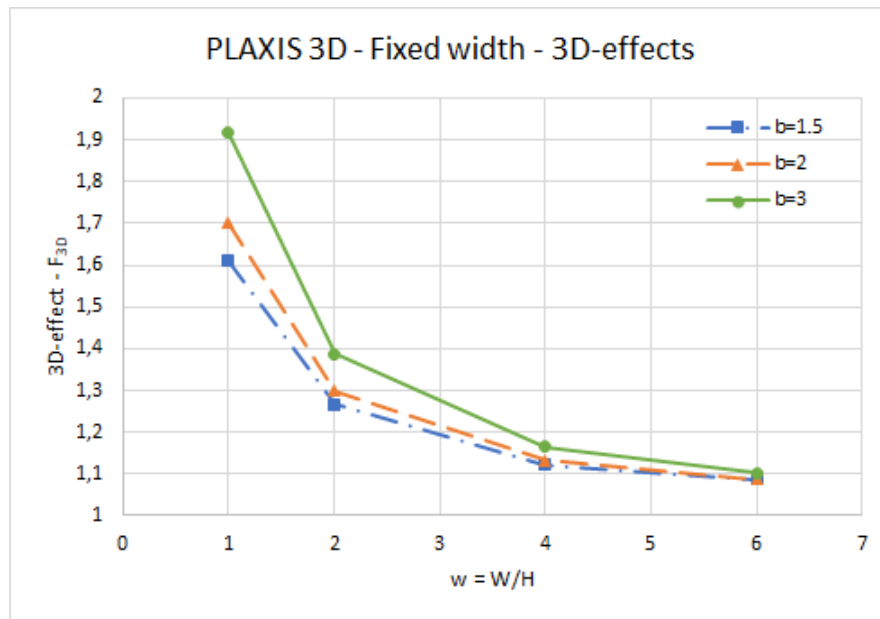


Figure 6.4: Comparison of the 3D-effects for the three cases with fixed widths. The 3D-effect is defined as the ratio between PLAXIS 3D SF and GS Stability (2D) SF.

PLAXIS 3D - Failure Mechanism

Incremental displacement plots are retrieved from PLAXIS 3D for each safety analysis to assess changes in slip surfaces. Four examples are included below, while the rest are available in Appendix D. All volumes have the same 2D profile for each slope inclination, with the back length $LB = 20\text{ m}$ and the front length $LF = 10\text{ m}$. The closest side surface has 'smooth' boundaries, i.e. the side is only fixed in the perpendicular direction. The farthest side is 'rough', i.e. fully fixed. This is illustrated by the increasing incremental displacement from near zero (dark blue) at the fully fixed side to a more widespread contour (red) at the 'smooth' side. All failure mechanisms are provided in Appendix D.

Figure 6.5 and Figure 6.6 show incremental displacements for $b = 1.5$ with $w = 1$ and $w = 6$, respectively. Both shear surfaces resemble an ellipsoidal shape and exit at the slope toe. The shear contours begin less than 10 m behind the slope crest for $w = 1$. For $w = 6$ the contours appear further behind, and more than 10 m behind the crest. This also implies a deeper slip surface for the wide slide compared to the narrow. Consequently, both the shear surface and the slide mass decrease when the slide narrows.

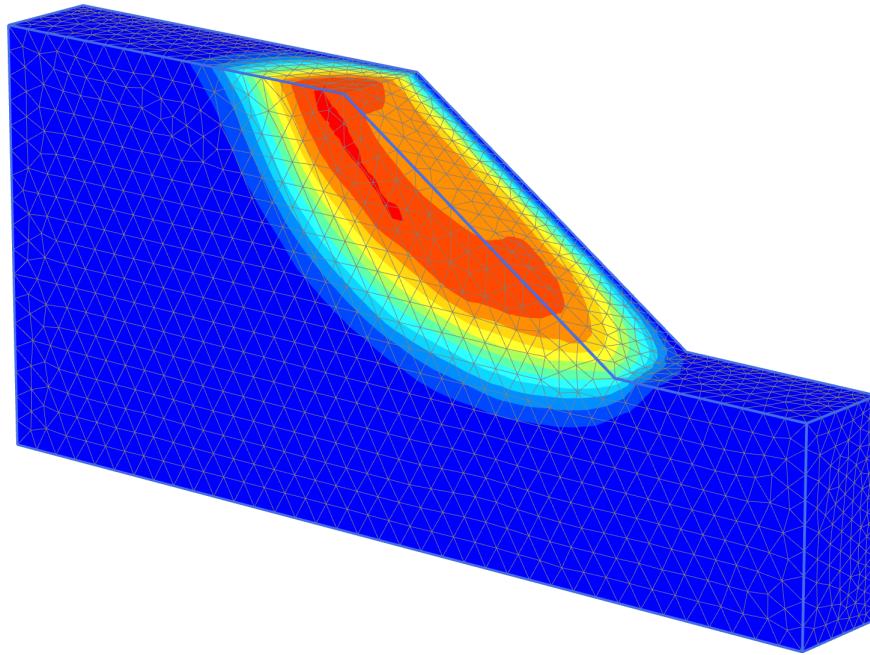


Figure 6.5: Half-model plot of incremental displacements for $w = 1$ and $b = 1.5$.

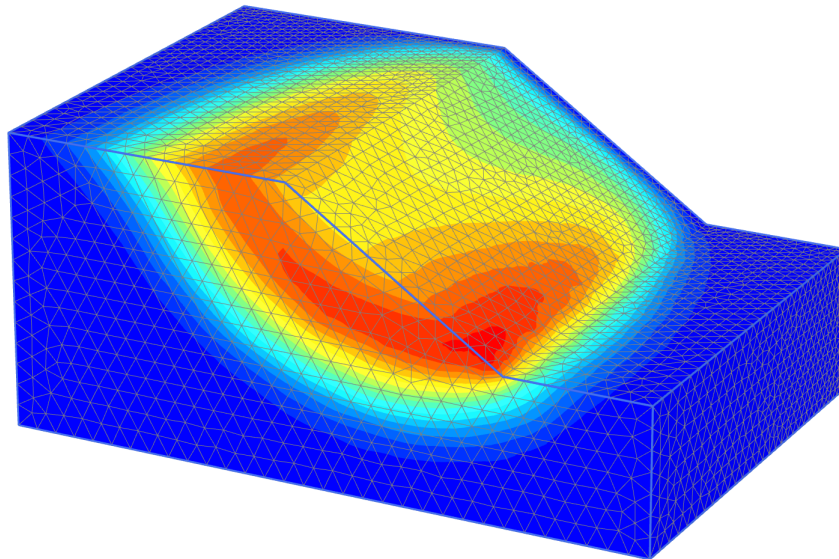


Figure 6.6: Half-model plot of incremental displacements for $w = 6$ and $b = 1.5$.

Figure 6.7 and Figure 6.8 show incremental displacements for $b = 3$ with $w = 1$ and $w = 6$, respectively. Similar mechanisms are observed as for $b = 1.5$. However, the change between the two widths appears more extensive. The depth and length of the $w = 6$ example is longer and deeper than $w = 1$. The failure surfaces for $b = 3$ are longer and deeper compared to $b = 1.5$, es-

pecially of for $w = 6$. Incremental displacements contours for $w = 1$ and $b = 3$ seem to stretch a longer distance, in addition to having a flatter (greater radius) circular surface than $w = 1$ and $b = 3$. This may indicate less mass to shear surface area compared to the steeper slope.

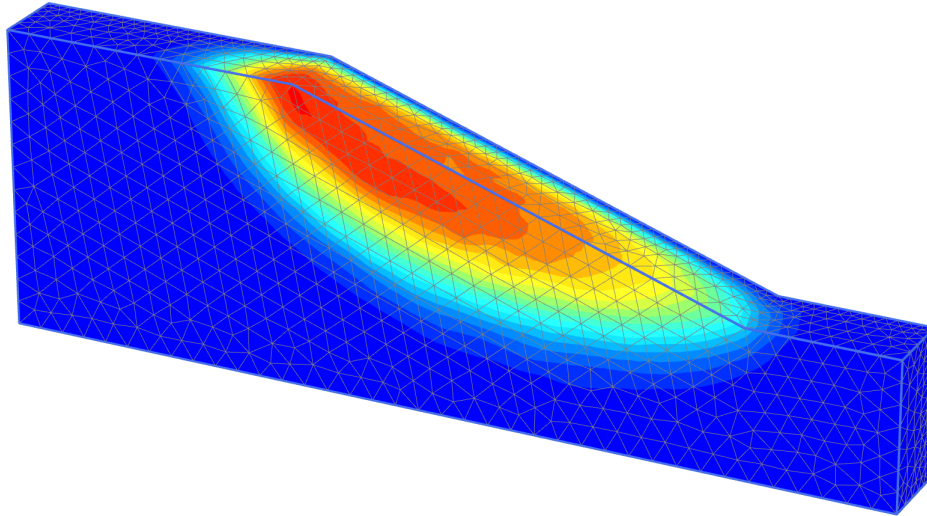


Figure 6.7: Half-model plot of incremental displacements for $w = 1$ and $b = 3$.

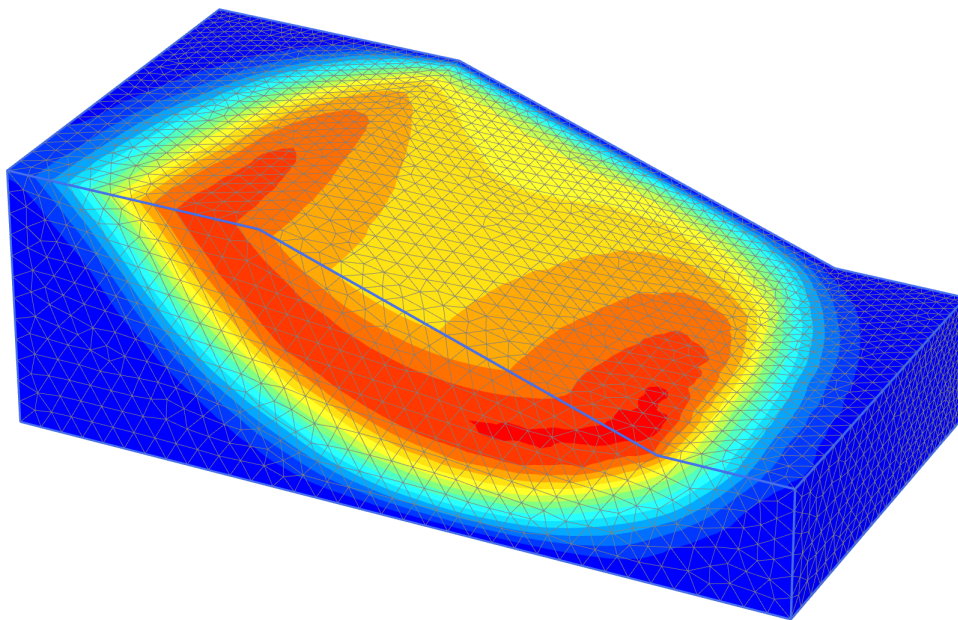


Figure 6.8: Half-model plot of incremental displacements for $w = 6$ and $b = 3$.

6.2.2 Slide3 - Effect of Fixed Width and Inclination

Slide3 - Safety Factor

3D limit equilibrium is compared to 3D finite element analysis by utilising Slide3. The same cases are analysed, and safety factors are provided in Table 6.3 for the Morgenstern-Price (M-P) method. The trend is similar to PLAXIS 3D, however, the safety factors are slightly lower. Figure 6.9 illustrates how the various methods in Slide3 differ from each other. The plot applies to inclination $b = 1.5$, but can represent the method variations for all cases. In general, Morgenstern-Price and Spencer provide similar safety factors for the defined slopes.

Table 6.3: Safety factor (SF) for all cases considered in the project analyses using Slide3. Only the Morgenstern-Price (M-P) results are tabulated from Slide3.

Width-height ratio (W/H)	Safety factor (SF)		
	Case 1: $b = 1.5$	Case 2: $b = 2$	Case 3: $b = 3$
$w = 1$	1.768	2.160	2.871
$w = 2$	1.474	1.708	2.102
$w = 4$	1.318	1.494	1.827
$w = 6$	1.256	1.408	1.712
$w = \infty$ (PLAXIS 2D)	1.233	1.359	1.567
$w = \infty$ (GS Stability) - Ref. plane strain solution	1.232	1.357	1.570
$w = \infty$ (Hand calc. - Janbu Direct Method)	1.187	1.327	1.522

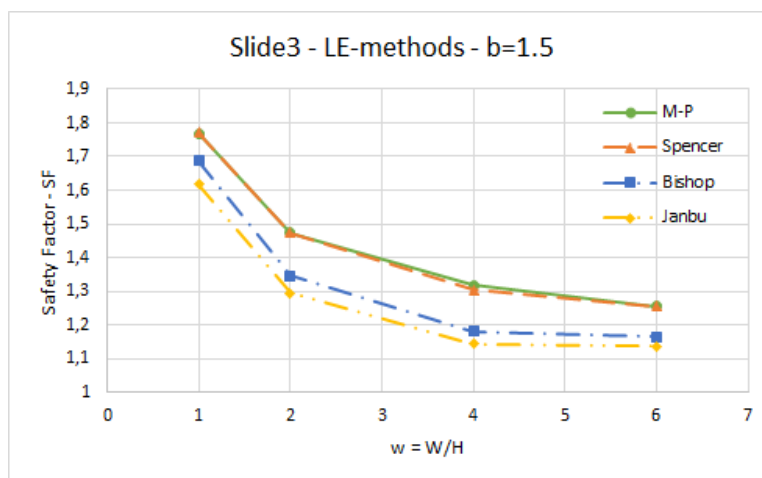


Figure 6.9: Safety factors for varying w and inclination $b = 1.5$, obtained by the Slide3 LE-methods: Morgenstern-Price (M-P) with half sine intercolumn force function, Spencer, Simplified Bishop and Simplified Janbu.

Figure 6.10 shows 3D-effects (F_{3D}) calculated using safety factors from Slide3 M-P and GS Stability (plane strain). The trend of rapidly increasing effect for low values of w is approximately the same as obtained with PLAXIS 3D. Further, the 3D-effects increase with slope inclination. Moreover, F_{3D} for $b = 1.5$ and $w = 6$ is close to 1, with a slight stabilising impact. The impact for $b = 3$ is significantly higher and close to 1.1.

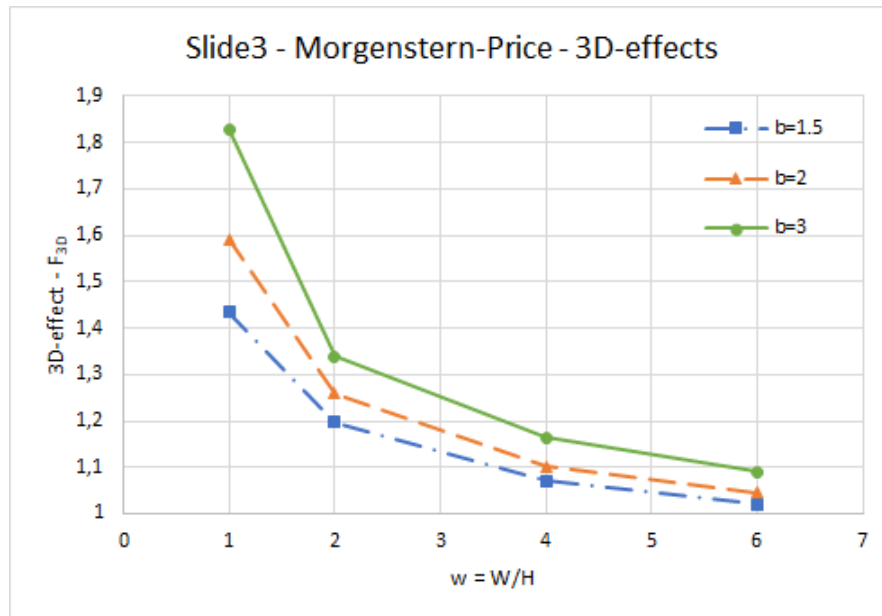


Figure 6.10: 3D-effects (F_{3D}) obtained in Slide3 for varying width-height ratio w and inclinations $b = 1.5$, $b = 2$ and $b = 3$. The Morgenstern-Price results are used as 3D SE. GS Stability is used to obtain the 2D plane strain results.

Slide3 - Failure Mechanism

Below are some critical slip surfaces found by Slide3 for the Morgenstern-Price method. These are defined as ellipsoidal shapes, and located using Cuckoo Search and Surface Altering Optimisation (SAO). The sharp corners observed on the surface along the slide edge are the result of vertical square columns. Figure 6.11 and Figure 6.12 show the failure mechanisms for slope inclination $b = 1.5$ with $w = 1$ and $w = 6$, respectively. Figure 6.13 and Figure 6.14 include the mechanisms for inclination $b = 3$ with $w = 1$ and $w = 6$, respectively. These models are equivalent to the PLAXIS 3D models presented in subsection 6.2.1. However, the models are not half-models as used in PLAXIS 3D, i.e. the figure models have the total width W . The remaining failure mechanisms from Slide3 analyses can be found in Appendix E.

The two slope examples for $b = 1.5$ illustrate a significant difference in slip surface. The wider

$w = 6$ slope shows a deeper shear surface than $w = 1$. Moreover, it stretches further back from the crest and slightly past the toe. The $w = 1$ slide exits slightly above the toe. Furthermore, the slide for $w = 1$ is developed for the whole model width at the surface. However, the $w = 6$ slide does not completely reach the model edges, i.e. the slide is not fully a $w = 6$ slide. This may be a result of too few columns. In addition, all failure mechanisms display a slightly uneven shear surface and not as circular (in cross-section) as was found in PLAXIS 3D. For example the bottom part of the shear surface for $w = 6$ and $b = 1.5$ deviates from a smoother circular surface.

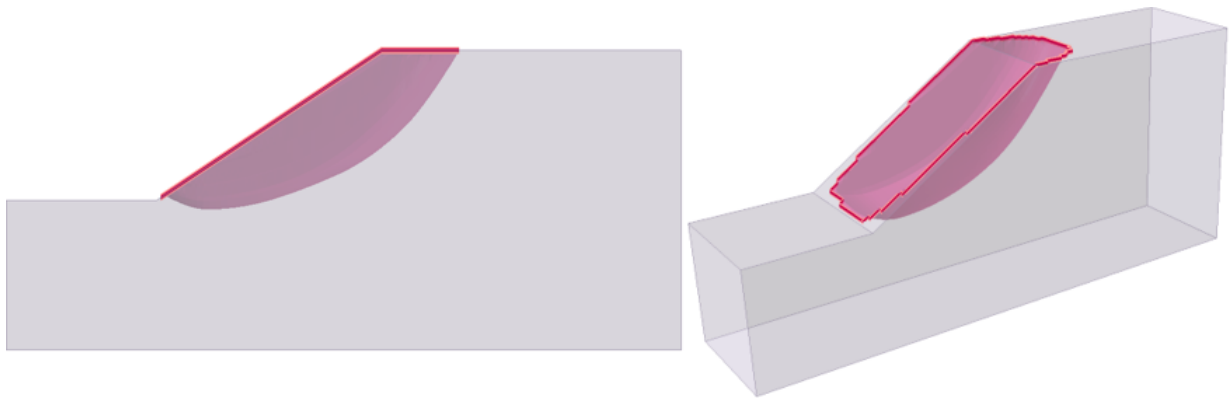


Figure 6.11: Slip surface obtained with Slide3 Morgenstern-Price for $b = 1.5$ and $w = 1$.

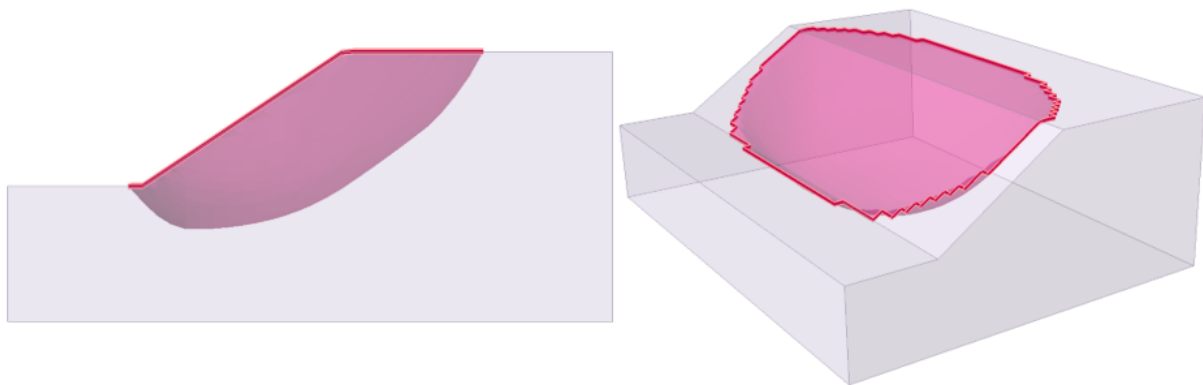


Figure 6.12: Slip surface obtained with Slide3 Morgenstern-Price for $b = 1.5$ and $w = 6$.

Two slope examples with inclination $b = 3$ are presented in Figure 6.13 and Figure 6.14 for $w = 1$ and $w = 6$, respectively. The slides display a more considerable difference in slip surface compared to $b = 1.5$. The $w = 1$ slide is a slope failure, which does not correspond to findings in PLAXIS 3D. Shear surface and slide mass have decreased significantly for the flatter slope. The slide still fills the entire model width. For $w = 6$, both the Slide3 slip surface and PLAXIS 3D sur-

face are similar, with a noticeably deeper shear surface compared to the three other examples. Moreover, the slide has extended to the entire model width, unlike the narrower slide for $b = 1.5$.

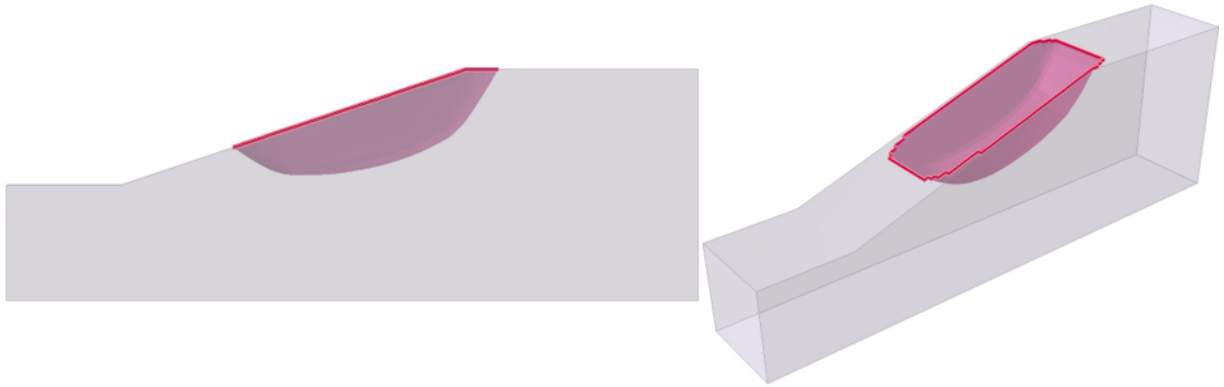


Figure 6.13: Slip surface obtained with Slide3 Morgenstern-Price for $b = 3$ and $w = 1$.

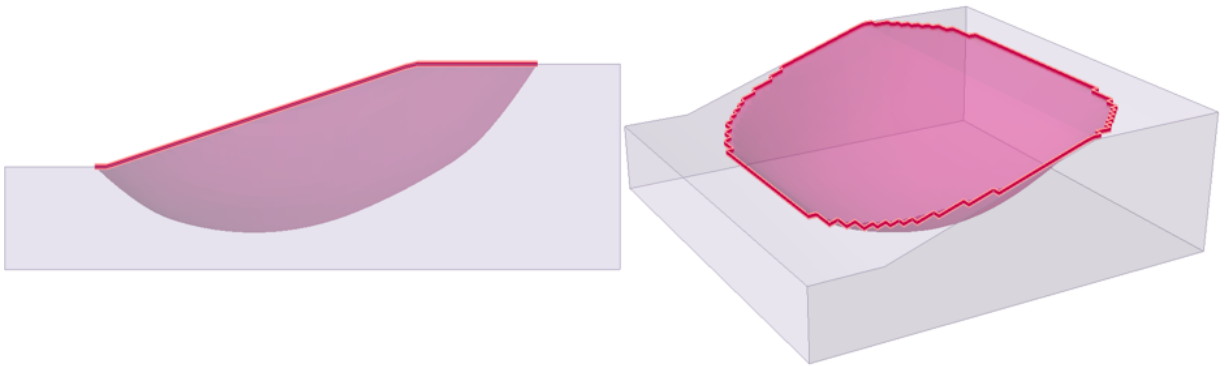


Figure 6.14: Slip surface obtained with Slide3 Morgenstern-Price for $b = 3$ and $w = 6$.

6.2.3 Effect of Fixed Width and Cohesion

Certain studies have stated that 3D-effects increase for cohesive soils, i.e. more cohesion results in greater effects. Most of these studies focused on drained conditions and materials with cohesive and frictional properties. Since the present study focuses on fully cohesive material and undrained behaviour, a brief analysis is conducted to evaluate the connection between cohesion and 3D-effects by varying S_u . Three previously defined strength profiles ((6.1), (6.2) and (6.3)) are used with Mohr-Coulomb *Undrained B* in PLAXIS 3D for various $w = W/H$. Table 6.4 summarises the PLAXIS 3D results along with the plane strain calculations from PLAXIS 2D, GS Stability and the Janbu Direct Method. Only slope inclination $b = 1.5$ (case 1) is considered.

Figure 6.15 shows the found 3D-effects for the three strength profiles. Little difference is ob-

served. For $w = 4$ and $w = 2$ analyses the strength provide an approximately identical impact. However, some variation is present for $w = 6$ and $w = 2$. At $w = 6$ the effects slightly decrease with increasing S_u , and the difference between S_u^3 and S_u^1 is approximately 1.5%. For $w = 1$, the effect is opposite, with an increased F_{3D} for increasing undrained strength. Here, S_u^3 gives a 3D-effect approximately 3.2% greater than S_u^1 .

Table 6.4: Safety factors (SF) for undrained strength profiles S_u^1 , S_u^2 and S_u^3 . The slope inclination is set as $b = 1.5$.

Width-height ratio (W/H)	Safety factor (SF)		
	$S_u^1 = 20 + 2z$	$S_u^2 = 30 + 2z$	$S_u^3 = 40 + 2z$
$w = 1$	1.979	2.563	3.161
$w = 2$	1.557	1.992	2.421
$w = 4$	1.381	1.752	2.117
$w = 6$	1.336	1.688	2.032
$w = \infty$ (PLAXIS 2D)	1.233	1.567	1.892
$w = \infty$ (GS Stability) - Ref. plane strain solution	1.232	1.570	1.906
$w = \infty$ (Hand calc. - Janbu Direct Method)	1.187	1.521	1.856

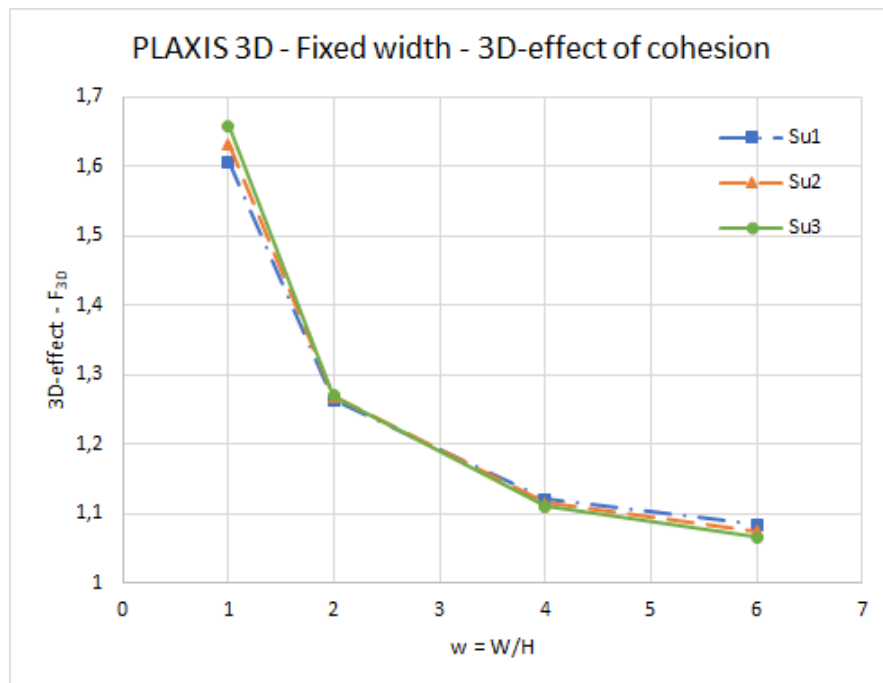


Figure 6.15: 3D-effects F_{3D} for strength profiles S_u^1 , S_u^2 and S_u^3 for varying width-height ratio w . Reference plane strain solutions are retrieved from GS Stability.

6.2.4 Comparison of Solutions for Fixed Width

Three different programs have been used to analyse stability of slopes, where the effect of finite widths $w = W/H$ has been evaluated. Both GeoSuite Stability and Slide3 are based on limit equilibrium considerations, while PLAXIS 3D uses the finite element method. Moreover, GS Stability is a 2D software, where finite widths can be simulated by including a side shear input. Clearly, the programs solve stability issues in different ways with different assumptions.

Below is a comparison of the 3D-effects for each slope inclination, where all have used the same plane strain reference safety factor from GS Stability. Figure 6.16, Figure 6.17 and Figure 6.18 show effects for cases $b = 1.5$, $b = 2$ and $b = 3$, respectively. In all plots GS Stability gives the greatest 3D-effects (or SF), Slide3 M-P the lowest and PLAXIS 3D in-between values. The exception is for $b = 3$ and $w = 1$, where GS Stability and PLAXIS 3D results are practically identical. Further, all approaches obtain a similar tendency of increased stabilising for lower values of w . Moreover, flatter slopes have increased positive effect for all cases.

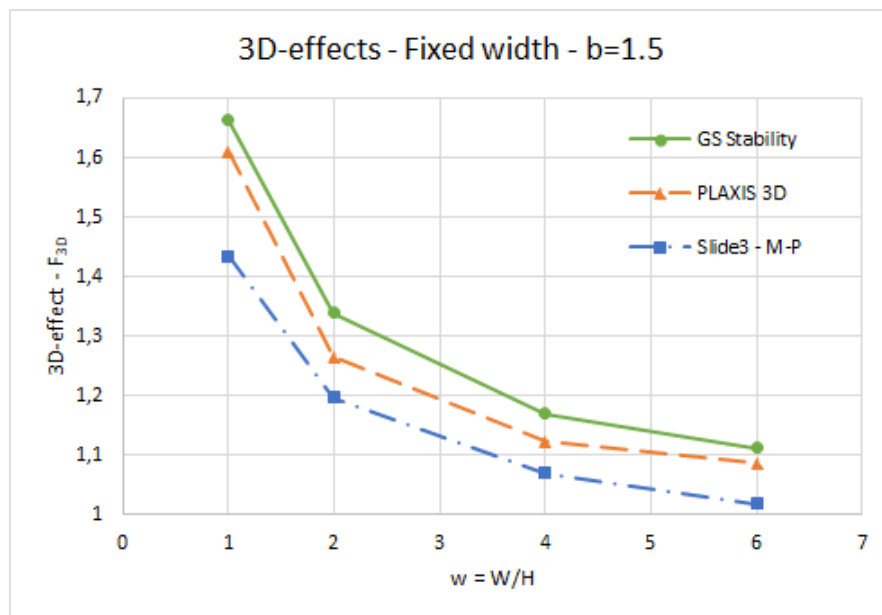


Figure 6.16: 3D-effects (F_{3D}) for varying width-height ratio w and inclination $b = 1.5$ using GS Stability, PLAXIS 3D and Slide3 Morgenstern-Price. Reference plane strain ($w = \infty$) solutions are retrieved from GS Stability.

The position of the plots relative to each other changes for each case. Solutions from GS Stability and Slide3 approach each other as the inclination increases. Furthermore, the PLAXIS 3D SF closes in on the GS Stability safety factor for $w = 1$ as the slope flattens. However, PLAXIS

3D seems to behave opposite as the width-height ratio increase, and is approximately equal to Slide3 for $w = 4$ and $w = 6$. Both GS Stability and Slide3 increase their effects more compared to PLAXIS 3D, especially from $b = 2$ to $b = 3$.

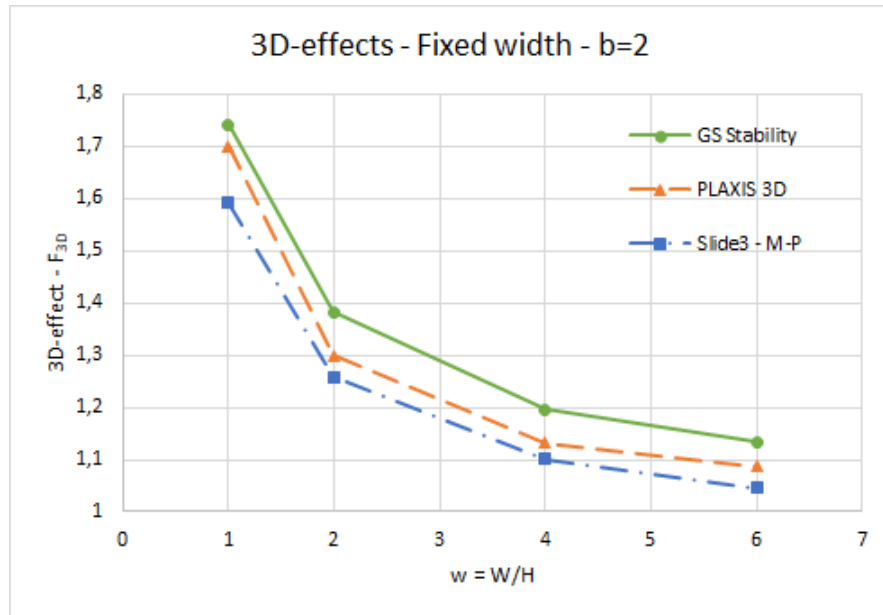


Figure 6.17: 3D-effects (F_{3D}) for varying width-height ratio w and inclination $b = 2$ using GS Stability, PLAXIS 3D and Slide3 Morgenstern-Price. Reference plane strain ($w = \infty$) solutions are retrieved from GS Stability.

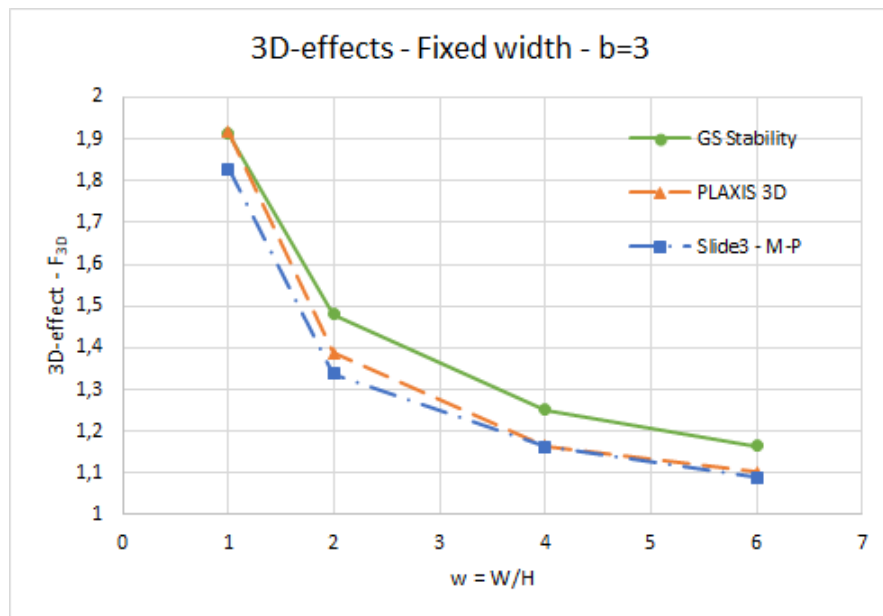


Figure 6.18: 3D-effects (F_{3D}) for varying width-height ratio w and inclination $b = 3$ using GS Stability, PLAXIS 3D and Slide3 Morgenstern-Price. Reference plane strain ($w = \infty$) solutions are retrieved from GS Stability.

6.3 Discussion on Effect of Finite Width

The completed analyses of finite width planar slopes have provided an indication on how three-dimensional fixed widths affect stability. Moreover, how sensitive 3D-effects are to slope inclination and cohesion. Furthermore, it is found that choice of software and calculation methods may impact the findings. However, the analyses are conducted using idealised models that may be unrealistic and/or uncommon.

Accuracy

The plane strain safety factor from GeoSuite Stability was used as the reference 2D SF to calculate 3D-effects F_{3D} . This is done to assess the difference between the traditional 2D limit equilibrium method and the more advanced 3D finite element method. However, for this ratio to be generally applicable, both the 3D SF and 2D SF should be accurate. The plane strain solution obtained with GS Stability and the BEAST method is similar to what is obtained with PLAXIS 2D, which is an indication of sufficient accuracy.

The accuracy of the PLAXIS 3D solution depends on sufficiently fine element distribution. Based on the validation and mesh sensitivity analysis in chapter 5, some overshoot of safety factors may be expected. Consequently, the calculated 3D-effects may be too high. However, noticeable positive effects should still be present. Overestimated safety factors should especially be considered for the smaller fixed widths, since significant difference was found in the comparison with Jostad and Lacasse (2015) in section 5.1. This problem may be due to fixed nodes at the model side surfaces, which requires finer discretisation to remedy the lost degrees of freedom in a narrow model. As stated by Jostad and Lacasse (2015), hexahedral 20-noded element may be more effective for a simple planar slope analysis compared to the tetrahedral 10-noded elements in PLAXIS 3D. This can decrease the need for finer discretisation to avoid overshoot and shear locking.

Effect of Fixed Width

The simulations have shown a significant influence of fixed widths defined by w . As the width decreases the resisting forces increase. The reason is that the driving mass decreases more relative to the resisting shear contact area. For an infinitely wide slope the shear surface will run

infinitely along the width of the slide. However, a finite slide has a shear surface that runs sideways along the bottom and up on the sides to the ground surface. Moreover, the slide mass is not infinitely wide, and will therefore decrease at the same time. The addition of side resistance together with diminished slide mass results in an increased ratio between shear resistance and driving forces, i.e. increased stability. When the slide width decreases, the side resistance remains to a certain degree and the bottom shear surface is narrowed. Simultaneously, the slide mass volume decreases. For the slope to become more stable, the negative change in volume must be relatively greater than the negative change of shear surface area.

In addition to an increase of safety factor for decreased fixed width, it is observed that the SF increases more rapidly for narrower widths. The fixed side boundaries force the slide to a narrower mechanism, which may alter the slip surface shape in the 2D profile, i.e. how the slide would develop in a 2D analysis. This is observed in the incremental displacement plots for the considered cases. The shape and depth of the toe failure change for the smallest widths, especially for $w = 1$. Depth decreases and the slip surface curvature flattens, which implies an increased radius of an assumed circular rotational failure surface. This phenomenon will further decrease the driving masses. Consequently, increased stability.

Similar results are found for the present study and literature for a planar slope with finite width. The trend of rapidly increasing 3D-effects for narrower slopes repeats for several studies. However, the magnitude of effects varies considerable. Finite element analyses of the finite planar slope show reasonable findings when compared with each other and the present project. Moreover, a comparison of results reveals how different geometrical and geotechnical properties affect the safety factor, assuming accurate solutions. Further, the present study is limited by a toe failure mechanism, and the effect of varying depth is not considered as in certain earlier studies in literature. Deeper slides (greater value of d) reduce the stability. However, the 3D-effects are observed to increase with increased d , since 3D increase of shear surface is greater relative to the mass volume.

Effect of Inclination

Varying slope inclinations have revealed a considerably influence on three-dimensional stability. The 3D-effects are more sensitive to a decrease in width for flatter slopes. In a 2D analysis the slip surface would be more prolonged and deeper for a flatter slope, which is also the case

for a 3D analysis. However, in 3D the influence of the finite width and side shear contributions are increased more compared to a steeper slope, due to the larger extent of the slip surface. The 3D-effect mechanism explained in the two previous paragraphs is intensified when the slope flattens.

Slide3

The findings of LE software Slide3 differed slightly from the PLAXIS 3D results. The magnitude of variation depends on the selected limit equilibrium method. The considered cases obtained the highest safety factors with the most advanced procedures, which are assumed the most accurate. Using less accurate methods may therefore provide overconservative safety factors. 3D-effects obtained with Slide3 Morgenstern-Price are lower compared to PLAXIS 3D. The reason may be a slight overshoot by PLAXIS or some inherent conservatism in the limit equilibrium approach or assumptions. Therefore, Slide3 may be a safer tool for design values.

Furthermore, the difference between the programs is decreased for flatter slopes, which may be explained by the different procedures of finding the slip surface. The search method used in Slide3 may be more sensitive to a change in inclination compared to PLAXIS 3D. This is supported by the change in the failure mechanism from a toe failure for $w = 1$ and $b = 1.5$ to a slope failure for $w = 1$ and $b = 3$. Moreover, the slip surfaces from Slide3 appear to have more uneven and slightly unnatural shapes. On the other hand, PLAXIS obtains less irregular and smoother surfaces, which is expected for a homogeneous soil. Additionally, the variation may be slightly random, which for instance is caused by inaccuracy due to too few columns in Slide3.

Effect of Cohesion

A slight influence of cohesion was observed when varying finite widths. The difference between the three undrained shear strength profiles was not significant, and close to negligible. PLAXIS 3D gave results that indicated a small increase of effect for $w = 1$ and higher strength. Moreover, an opposite impact was found for $w = 6$. A wider range of shear strength values should be tested to confirm if the trend is real or due to inaccurate analysis or processing of data. However, the S_u profiles are reasonable for materials that resemble a Norwegian clay. A change in strength profiles may alter the failure mechanism, and thus the 3D-effects. For instance, a comparison of strength profiles with varying strength gradients in depth may reveal greater variations, due

to a different distribution of inclined shear strength over the shear surface.

Applicability of GeoSuite Stability

The comparison between PLAXIS 3D, Slide3 and GS Stability showed that GS Stability gives the largest 3D-effects. These are not real 3D-effects, since GS Stability is a 2D program. Nonetheless, the difference from PLAXIS 3D is not extreme. The same width definition is used in GS Stability as PLAXIS and Slide3, i.e. the width from each outermost point of the slide surface. This will give an overestimated shear resistance in GS Stability, due to the assumption of vertical slide sides where the input resistance is added. All points on this vertical side will be the outermost point of the width. Therefore, the shear surface area simulated in GS Stability will be greater than the ellipsoidal side shear surface in 3D analysis. Consequently, a more stable slope with simulated finite width. The width used for the side shear input in GS Stability should therefore be reduced to avoid overestimated safety factors.

Chapter 7

3D Simulations - Slope with Curvature

A planar slope with fully fixed side boundaries are rarely encountered, especially in nature. Certain structural elements, such as walls or geotextiles, may have significant restraining impact. However, near fully fixed boundary conditions are seldom encountered in untouched soils. The level of restraints in soil may vary significantly. A possible phenomenon that can provide some restraints is a soil transfer to a stronger material, i.e. a non-homogeneous soil. Moreover, slopes with curvature may force a finite slide.

Curved slope surfaces are a common sight both in natural environments and in man-made structures. Examples are natural arching ridges or valleys, and constructed cornered embankments or excavations. Curved geometries can be divided into convex and concave shapes, with various curvatures such as corners or arches. Furthermore, the curvature can be quantified by radius and/or angle. Several literature studies in chapter 3 present analyses of various three-dimensional curved surface slopes.

Many examples of natural slopes contain a geometry that differs from an infinitely wide slope. A range of slopes encountered in nature display a geometry that may intuitively result in a critical slide with a finite width, e.g. a valley. On the other side, convex curved slope such as a ridge may at first sight seem less stable than a planar slope. How these can affect the safety factors and failure mechanisms is briefly analysed in the present study. Findings and limitations are discussed in the end of the chapter.

7.1 3D Modelling of Slope with Curvature

PLAXIS 3D is the three-dimensional program used for the present simulations of curved slopes. The more flexible shape of tetrahedral elements is more suitable for modelling complex geometries compared to hexahedral (brick) elements. Moreover, all sides are only normally fixed, except the fully fixed bottom boundary. This should reduce numerical issues related to restrained nodes and potentially improve accuracy.

Idealised slopes that resemble natural curvatures are modelled. Often arched slopes are analysed with a model of a single arch. The curvature is assumed continuing symmetrical from the arch side surfaces, or the sides are fully fixed. A natural slope may have a range of ridges/valleys, e.g. along a mountain side. This analysis focuses on curved geometries along the same plane, by constructing smooth transitions from the side surfaces. Furthermore, many studies in literature of complex geometries use drained strength. Few have considered curved slopes with undrained material, such as clay. Therefore, the use of undrained shear strength is continued.

7.1.1 Model Geometry

A similar 2D reference profile is used as for the x-z-plane in subsection 6.1.1 for a planar slope. The same height $H = 10\text{ m}$ and model depth $D = 10\text{ m}$ are used. Only slope inclinations $b = 1.5$ and $b = 3$ are analysed, due to limited time. Some length values vary throughout the model, since the slope surface is arched. The minimum length behind slope crest (for concave only) is varying between 15 m and 20 m and the minimum length in front of slope toe (for convex only) is approximately $10\text{ m} \pm 1\text{ m}$ for all models. The geometrical properties differ from convex to concave. Both LB and LF as defined in Figure 7.1 are 10 m , and are used to define the revolved geometry. The actual model may span further along the x-axis, see Figure 7.2 and Figure 7.3. Geometrical attributes are summarised in Table 7.1.

The left drawing in Figure 7.1 defines the curvature of a convex slope in the x-y-plane. Convex slopes have concave transition arches on each side. The middle part defined by the curvature angle α is the main arch, i.e. the convex one. Vertical (z-direction) rotation axis for the main arch is at the top of the corner defined by α . Further, $R2 = R_u + L + LF$, where R_u is the convex radius from slope crest to rotation axis, $L = H \cdot b$ is the horizontal length of the slope surface and $LF = 10\text{ m}$ is the length outwards from the slope toe. Angle $\theta = (180^\circ - \alpha)$ is used in $R2 \cdot \sin(\theta)$

and $R2 \cdot \cos(\theta)$ to find the x- and y-values of the rotation axis for the concave transition arches.

The right drawing in Figure 7.1 describes the concave curved slope in the x-y-plane. Concave slopes have convex transition arches on each side. The middle part defined by the curvature angle α is the main arch, i.e. the concave one. Vertical rotation axis for the main arch is at the bottom of the corner defined by α . Further, $R2 = R_l + L + LB$, where R_l is the concave radius from slope toe to rotation axis, L is the horizontal length of the slope surface and $LB = 10\text{ m}$ is the length outwards from the slope crest. Angle $\theta = (180^\circ - \alpha)$ is used in $R2 \cdot \sin(\theta)$ and $R2 \cdot \cos(\theta)$ to find the x- and y-values of the rotation axis for the convex transition arches.

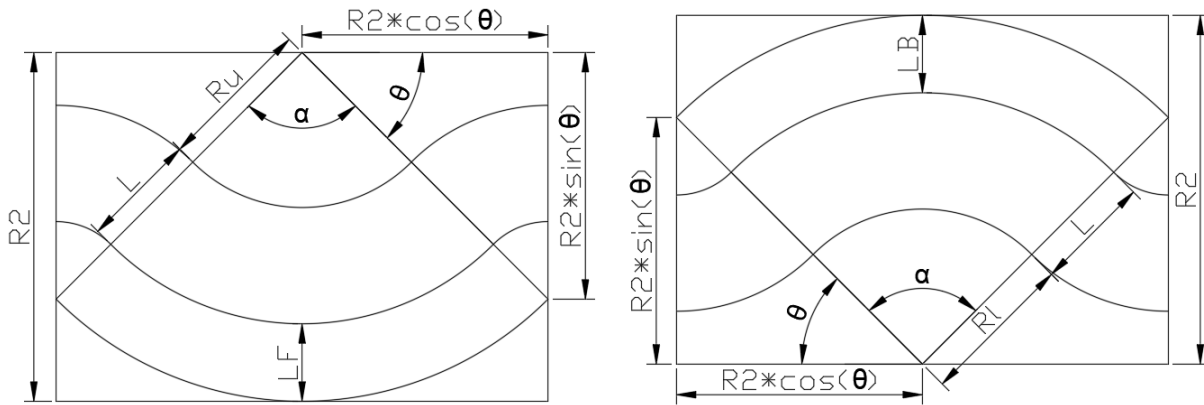


Figure 7.1: Top view of x-y-plane with geometrical properties for convex (left) and concave (right) curvature.

Table 7.1: Defined geometrical properties for curved 3D slope, see Figure 6.1 and Figure 7.1.

Geometrical attribute	Symbol	Value
Slope inclination	b	1.5 (Case 1) 3 (Case 2)
Slope height	H	10 m
Depth below slope toe	D	10 m
Length of surface in front of slope (convex)	LF	10 m
Length of surface behind the slope (concave)	LB	10 m
Horizontal length of slope	L	$H \cdot b$
Convex radius from slope crest to axis of rotation	R_u	10 – 60 m
Concave radius from slope toe to axis of rotation	R_l	10 – 60 m
Angle of curvature	α	90° 180°

Degree of curvature is described using rotation radius R and curvature angle α . Radius-height ratios $r = R/H$ are used to decrease the slope height dependency, similar to the width-height ratio $w = W/H$. The radius definition is the same as defined for the axisymmetric model in subsection 4.2.1. The models are separated using $r_u = R_u/H$ for convex and $r_l = R_l/H$ for concave. The angle of which the main arch is rotated around the z-axis is denoted α . Two curvature angles are included in the analyses, which are $\alpha = 90^\circ$ and $\alpha = 180^\circ$. Figure 7.2 and Figure 7.3 shows convex (left) and concave (right) curvatures for $\alpha = 90^\circ$ and $\alpha = 180^\circ$, respectively.

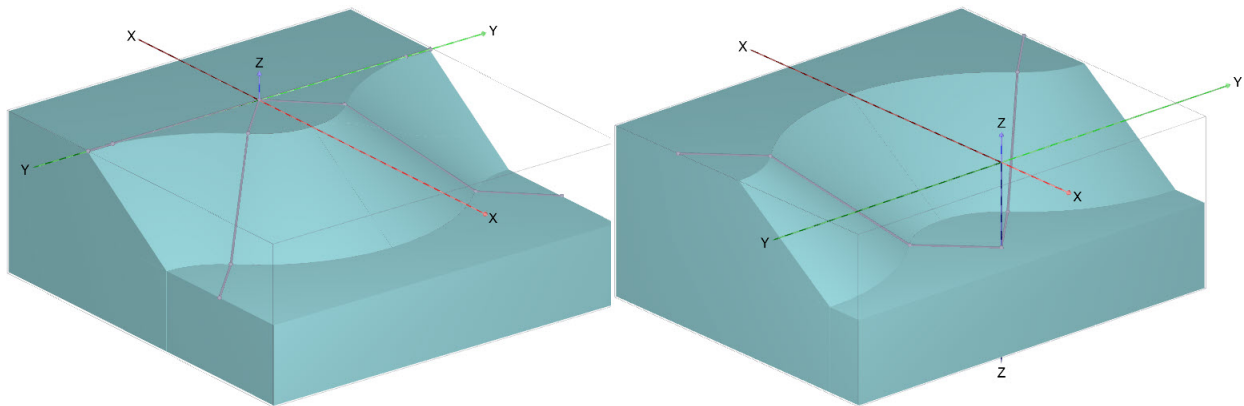


Figure 7.2: PLAXIS 3D models of a convex (left) and a concave (right) curved slope surface with a curvature angle of 90° within the grey lines. The radius-height ratios are defined as $r_u = r_l = R_u/H = R_l/H = 1$ in the figures.

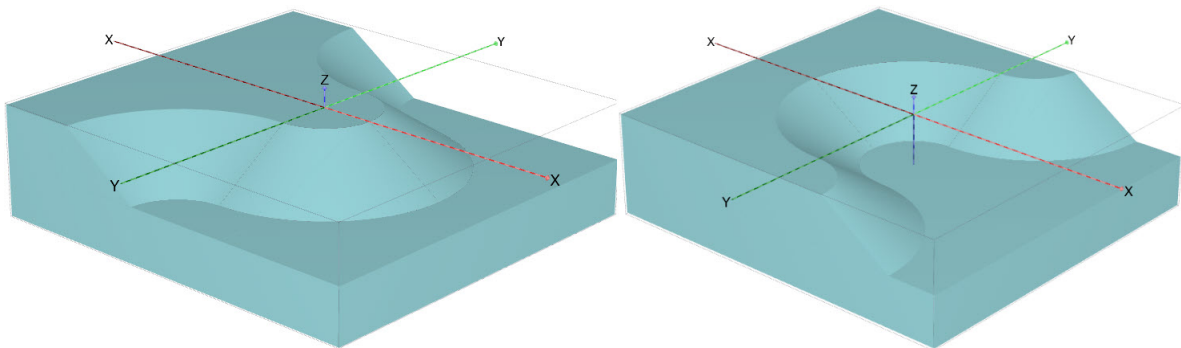


Figure 7.3: PLAXIS 3D models of a convex (left) and a concave (right) curved slope surface with a curvature angle of 180° . The radius-height ratios are defined as $r_u = r_l = R_u/H = R_l/H = 1$ in the figures.

The finite element method assume symmetrical conditions outside the boundary, when the side surface boundary conditions only are fixed normally. As for the planar slope with fixed width, a half-model of each slope in Figure 7.2 and Figure 7.3 is created to increase accuracy and decrease CPU time. The model is split along the x-axis. Due to the symmetry at both side surfaces,

the various curvatures are repeated frequently and infinitely along the y-axis. Therefore, the simulated neighbouring arch outside the model may affect the analysis of the main arch.

Several ridges or valleys are possible to encounter after each other in reality. However, cases with more widespread curved surfaces along a slope may be of interest. To test this, planar extensions are inserted at the sides of the arch extensions. Due to limited time and to avoid too comprehensive models, an extension of only 10 m is included as supplementary analyses, i.e. a 20 m planar gap between the curvatures. Further, the calculation phases are simply initial phase (0) with gravity loading followed by a safety analysis with 100 steps, since no fully fixed side boundaries are activated, see Appendix A. Default numerical settings are used.

Construction

The curved slope surfaces as defined above are constructed in PLAXIS 3D by revolving a 2D profile around the z-axis at $(x=0, y=0)$. This 2D cross section is constructed along the x-axis with a set radius from the origin of revolution. Then it is revolved 45° or 90° to each side around the z-axis to create a curvature angle of 90° or 180° . Further, each side surface of the created volume is revolved the opposite direction around a rotation axis located using the formulas in Figure 7.1. The resulting outer side surfaces are now parallel to the x-axis. Lastly, planar surfaces are extruded to fill the void in front and behind the revolved volume and to create a sufficiently large model with only rectangular sides. For the analyses with 10 m extension, the outer side surface is extruded parallel to the y-axis.

7.1.2 Soil Strength

The clay material is unaltered from the previous analyses of the thesis. The material model is Mohr-Coulomb with drainage type *Undrained B*. Strength is defined by the undrained shear strength profile:

$$S_u = 20 + 2z \quad [kPa]$$

where z is the depth from reference elevation, which is set at $z = 0$ in PLAXIS 3D. Only one strength profile is used in the 3D simulations of curved slopes. Remaining Mohr-Coulomb material parameters are also unchanged, e.g. unit weight $\gamma = 19 \text{ kN/m}^3$, and are provided in Appendix A.

7.1.3 Mesh and Convergence

Findings from the mesh sensitivity analysis in section 5.2 has been used to define minimum geometrical properties, such as depth and horizontal extent. Moreover, an indication of required minimum mesh density is obtained. The basis of mesh configuration and safety multiplier convergence is similar as in subsection 6.1.3. A difference from the fixed width planar slopes is that the side boundaries are not fully fixed. Additionally, the models become significantly larger for the arching slopes, especially with $\alpha = 180^\circ$.

Local mesh refining is completed, due to the volume-consuming curvature as illustrated in Figure 7.2 and Figure 7.3, and previous knowledge of the approximate extent of a regular planar slope. The slide is expected to develop somewhere between the slope toe and approximately $10\text{ m} \pm 5\text{ m}$ behind the crest, and to a depth slightly lower than the toe level. Therefore, a significantly lower coarseness factor is given for a volume approximately defined by this area. The small coarseness factors range from 0.50 for the smaller models to 0.30 for the larger models. Rest of the volume is given a coarseness factor ranging from 1.0 to 0.80, depending on the model size. The *Very fine* element distribution is selected for all slopes.

A single sensitivity test was conducted in subsection 5.2.2 for the smallest slope volume. The convex curvature was defined with $\alpha = 90^\circ$ and $r_u = 1$. The *Very fine* element distribution was used with two sets of coarseness factors. One had a general coarseness factor of 1.0 and a refined part near the expected slide with coarseness factor 0.50. The other finer mesh had half the coarseness factors as the coarser mesh. A small deviation was found between the two. Moreover, the finer mesh consumed considerable more time. Consequently, the increase in accuracy was not considered worth the increase in time.

The curve of safety factor multiplier versus total deformation increase steadily after some steps, as explained in subsection 5.2.3 in the mesh sensitivity analysis. Therefore, the pragmatic way of fitting a linear trend to the data points is used for the flatter part of the curve with a steady rise. As for a planar slope with fixed width, the trend line is fitted for the steps after approximately 30 to 40 steps of a total of 100 steps.

7.2 Results for Slope with Curvature

The findings from the three-dimensional analysis of slopes with curvature are presented as safety factors in tables with corresponding plots for illustration. Moreover, certain incremental displacement figures are shown to compare failure mechanisms. Two-dimensional results for $w = \infty$ using PLAXIS 2D, GS Stability and Janbu Direct Method are included in the safety factor tables for comparison. Furthermore, the result from GS Stability is used as the reference plane strain solution for calculation of 3D-effects. The effects can be formulated as $F_{3D} = SF_{3D}/SF_{2D,GSS}$, where SF_{3D} is found with PLAXIS 3D and $SF_{2D,GSS}$ is the plane strain reference solution. Additionally, the symbol for curvature angle α is simplified to the Latin letter a in plots.

This section is divided into six parts. The first two parts are for convex and concave curvatures without planar extension for $b = 1.5$ and $b = 3$, see subsection 7.2.1 and subsection 7.2.2. The next two are for convex and concave curvatures with extension, where only one slope inclination is analysed, see subsection 7.2.3 and subsection 7.2.4. The fifth part in subsection 7.2.5 presents how different geometrical properties affect the stability. Lastly, a comparison of effects between the curvature analyses conducted using PLAXIS 2D Axisymmetric model and PLAXIS 3D is included in subsection 7.2.6. All failure mechanisms are provided in Appendix F.

7.2.1 Convex Curvature

Slopes with a convex idealised shape are analysed to simulate a natural ridge or similar consisting of homogeneous soil. Due to the model symmetry on both side surfaces, the curvature is virtually continuing outside the model along the same plane. Consequently, the non-visible neighbouring curvature may affect the stability. Nonetheless, the results are defined using the main convex arch geometry via α and $r_u = R_u/H$.

Safety Factor

Table 7.2 summarises the safety factors obtained for inclinations $b = 1.5$ and $b = 3$. The two-dimensional results for width-height ratio $w = \infty$ are included to compare with the a planar infinitely wide slope. All solutions from PLAXIS 3D are greater than the 2D solutions. Furthermore, the safety factors decrease from low to high value of r_u . In addition, curvature angle $\alpha = 180^\circ$ provides greater safety factors compared to $\alpha = 90^\circ$.

Table 7.2: Safety factors obtained by varying convex radius-height ratios $r_u = R_u/H$ for curvature angle $\alpha = 90^\circ$ and $\alpha = 180^\circ$ and slope inclinations $b = 1.5$ and $b = 3$.

Convex radius-height ratio	Safety factor (SF)			
	$b = 1.5$		$b = 3$	
	$\alpha = 90^\circ$	$\alpha = 180^\circ$	$\alpha = 90^\circ$	$\alpha = 180^\circ$
$r_u = R_u/H$				
$r_u = 1$	1.321	1.381	1.686	1.785
$r_u = 2$	1.317	1.355	1.686	1.760
$r_u = 4$	1.307	1.329	1.681	1.726
$r_u = 6$	1.300	1.320	1.675	1.708
$w = \infty$ (PLAXIS 2D)	1.233		1.567	
$w = \infty$ (GS Stability) - Ref. plane strain solution	1.232		1.570	
$w = \infty$ (Hand calc. - Janbu Direct Method)	1.187		1.522	

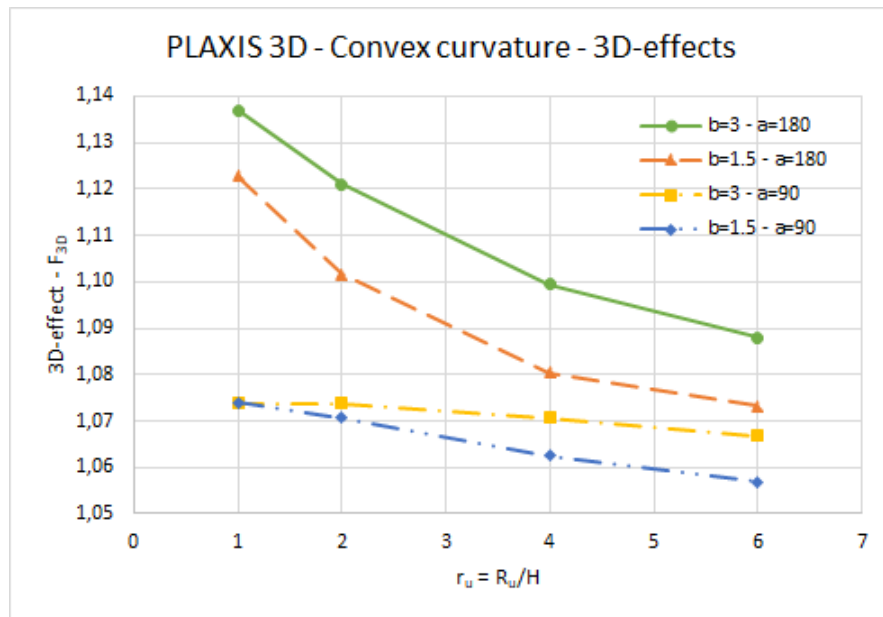


Figure 7.4: 3D-effects for convex curvature defined by $r_u = R_u/H$ and curvature angles 90° and 180° , with inclinations $b = 1.5$ and $b = 3$.

3D-effects for convex slopes are calculated and plotted in Figure 7.4. The obtained effect is positive for all convex cases, where it is almost 1.14 for $b = 3$ and $\alpha = 180^\circ$. The lowest F_{3D} is calculated to slightly below 1.06 for $b = 1.5$ and $\alpha = 90^\circ$. Effects for slope inclination $b = 3$ are approximately 1% to 2% higher than for $b = 1.5$ when the curvature angle is 180° . This variation

is quite steady for all values of r_u . Furthermore, there is a trend of significant destabilising as the radius increases for $\alpha = 180^\circ$.

Effects found for $\alpha = 90^\circ$ are quite steady over the change of r_u and lower than all obtained with $\alpha = 180^\circ$. Moreover, curves for $b = 1.5$ and $b = 3$ with $\alpha = 90^\circ$ are approximately equal at $r_u = 1$. However, the $b = 1.5$ curve decrease more rapidly than $b = 3$ from $r_u = 1$ to $r_u = 6$. The larger curvature of $\alpha = 180^\circ$ appears to be more stable and more sensitive to a change in r_u compared to $\alpha = 90^\circ$.

Failure Mechanism

The following figures present incremental displacement plots retrieved from PLAXIS 3D for convex curvature. Since these are half-models of the main arch, the entire main geometry can be visualised by mirroring the model at the closest slope side surface, see Figure 7.2 and Figure 7.3. Two different radii are included for each slope inclination b and curvature angle α , which are $r_u = 1$ and $r_u = 6$. This is to compare the most prominent or 'sharpest' curvature with the least 'sharp' and more extensive curvature.

Figure 7.5 illustrates the failure mechanisms for $b = 1.5$ and $\alpha = 90^\circ$, where the left slope has $r_u = 1$ and the right has $r_u = 6$. The left slide develops at the side of the main convex arch. The most distinguished contour (red) is found near the toe of the concave extension arch. Mass movement may be directed from the convex arch crest to the toe of the concave arch. Unlike the $r_u = 1$ slope, the right $r_u = 6$ slope have the most critical part at the middle of the convex arch. Moreover, the incremental displacements nearly vanish at the concave extension arch.

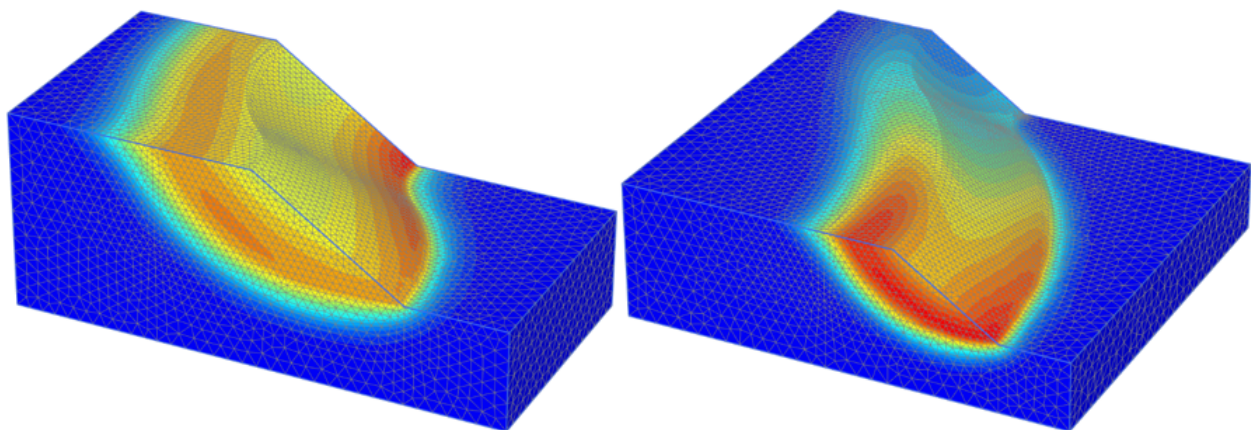


Figure 7.5: Incremental displacements for $b = 1.5$ and $\alpha = 90^\circ$ with $r_u = 1$ (left) and $r_u = 6$ (right).

Figure 7.6 shows the failure mechanism for $r_u = 1$ (left) and $r_u = 6$ (right). The inclination is $b = 1.5$ and curvature angle is $\alpha = 180^\circ$. The left $r_u = 1$ slope displays a small concentration of incremental displacements at the crest middle of the convex main arch. It appears that the slide occurs down the side of the convex arch at the transition between the convex and the concave curvature. Further, approximately no movements are observed in the middle of the concave transition arch. The $r_u = 6$ model to the right shows how the critical slip surface has moved from the side to the middle of the convex arch, similar as for $\alpha = 90^\circ$. Moreover, no incremental displacements are present at the concave arch, i.e. the slide is finite.

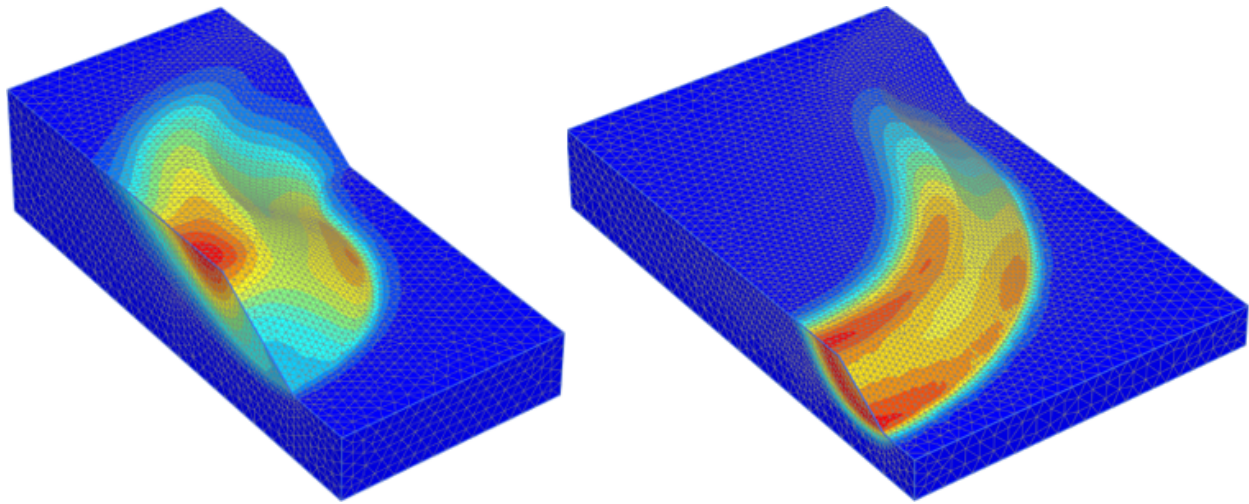


Figure 7.6: Incremental displacements for $b = 1.5$ and $\alpha = 180^\circ$ with $r_u = 1$ (left) and $r_u = 6$ (right).

Figure 7.7 contains the incremental displacement plots of $r_u = 1$ (left) and $r_u = 6$ (right) for $b = 3$ and $\alpha = 90^\circ$. The left figure of $r_u = 1$ is similar to the equivalent slope with $b = 1.5$. However, the slip surface is deeper and stretches further back behind the crest. The incremental displacements seem to follow the curvature at the top of the slope. Further, the movements appear to concentrate at the toe of the concave extension arch. This critical concentration is moved to the convex main arch middle for the right $r_u = 6$ slope. The incremental displacements diminishes further away from the middle towards the concave extension. Also the $r_u = 6$ case is similar for both $b = 1.5$ and $b = 3$ with 90° curvature, except the increase in shear surface depth for the flatter slope.

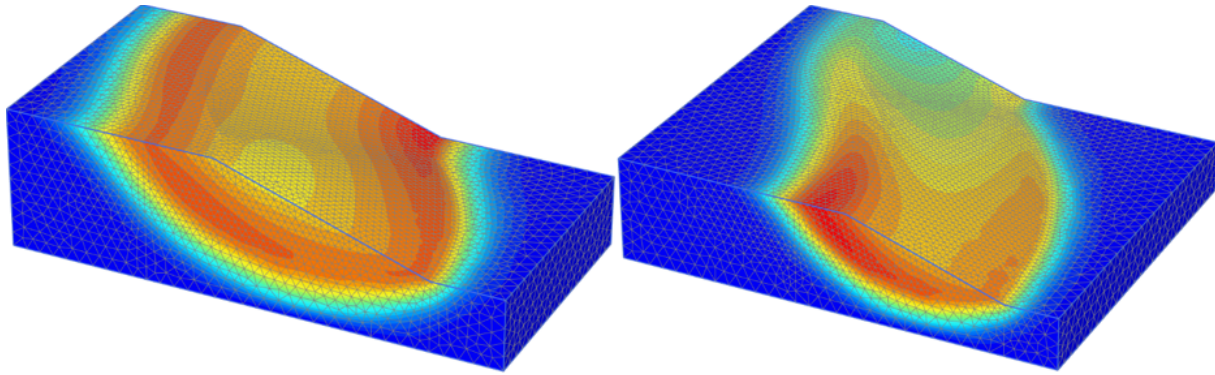


Figure 7.7: Incremental displacements for $b = 3$ and $\alpha = 90^\circ$ with $r_u = 1$ (left) and $r_u = 6$ (right).

Figure 7.8 presents slopes with $b = 3$ and $\alpha = 180^\circ$, where the $r_u = 1$ example is to the left and the $r_u = 6$ example is to the right. The $r_u = 1$ model shows a similar failure mechanism as obtained for the equivalent curvature with $b = 1.5$. A concentration of mass on the top of the convex curvature is set in movement to each side of the prominent curvature, and exits near the transition between the main arch and the concave extension arch. Furthermore, the failure mechanism for $r_u = 6$ curvature has altered from the equivalent $b = 1.5$ slope. Instead of developing a critical slide at the convex arch middle, the most intensive incremental displacements are observed at the side of the convex arch close to the transition to the concave arch. However, the slide appears quite wide, since the contours continue around the main arch. The slide stops near the middle of the concave extension arch.

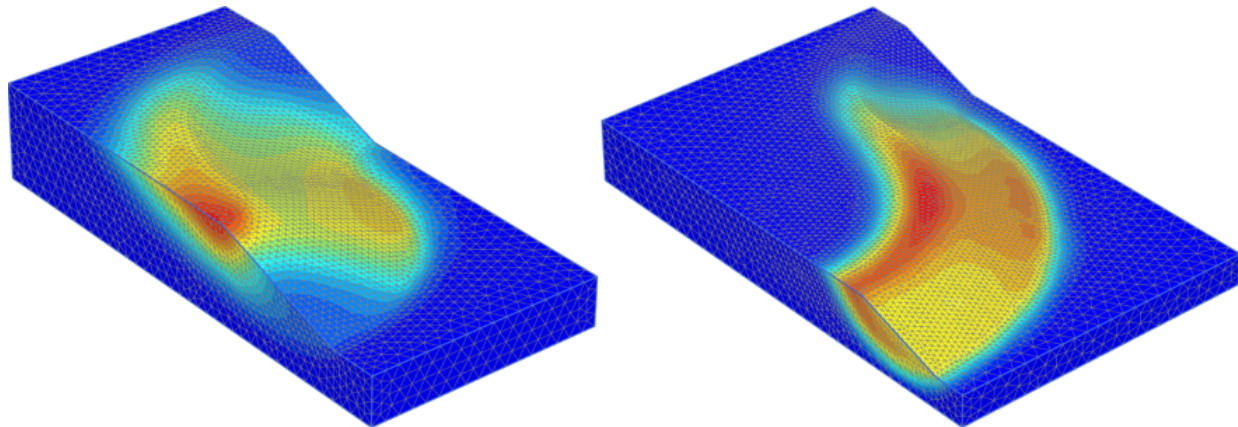


Figure 7.8: Incremental displacements for $b = 3$ and $\alpha = 180^\circ$ with $r_u = 1$ (left) and $r_u = 6$ (right).

7.2.2 Concave Curvature

Concave idealised slopes are analysed to simulate a natural valley or similar containing homogeneous soil. The curvature is virtually continuing outside the model along the same plane as for the convex case, due to the inherent symmetry in FEM. Consequently, the simulated neighbouring curvature may affect the stability. Nonetheless, the results are defined using the main concave arch geometry through α and $r_l = R_l/H$.

Safety Factor

Table 7.3 provides the safety factors for inclinations $b = 1.5$ and $b = 3$. The two-dimensional results for width-height ratio $w = \infty$ are included to compare with a planar infinitely wide slope. All safety factors from PLAXIS 3D are greater than the two-dimensional solutions. Further, the safety factors decrease when r_u increases. In addition, curvature angle $\alpha = 180^\circ$ provides greater safety factors compared to $\alpha = 90^\circ$.

Table 7.3: Safety factors obtained by varying concave radius-height ratios $r_l = R_l/H$ for curvature angle $\alpha = 90^\circ$ and $\alpha = 180^\circ$ and slope inclinations $b = 1.5$ and $b = 3$.

Concave radius-height ratio	Safety factor (SF)			
	$b = 1.5$		$b = 3$	
	$\alpha = 90^\circ$	$\alpha = 180^\circ$	$\alpha = 90^\circ$	$\alpha = 180^\circ$
$r_l = R_l/H$				
$r_l = 1$	1.320	1.381	1.685	1.784
$r_l = 2$	1.316	1.366	1.685	1.757
$r_l = 4$	1.313	1.352	1.680	1.736
$r_l = 6$	1.311	1.348	1.677	1.727
$w = \infty$ (PLAXIS 2D)	1.233		1.567	
$w = \infty$ (GS Stability)	1.232		1.570	
$w = \infty$ (Hand calc. - Janbu Direct Method)	1.187		1.522	

Calculated 3D-effects are plotted in Figure 7.9. The obtained effect is positive for all convex cases, where it is almost 1.14 for $b = 3$ and $\alpha = 180^\circ$. The lowest F_{3D} is calculated to slightly below 1.07 for $b = 1.5$ and $\alpha = 90^\circ$. Effects for slope inclination $b = 3$ are approximately 0.3% to 1% greater compared to $b = 1.5$ when the curvature angle is 180° . This variation is quite steady for all values of r_l . Furthermore, there is a trend of significant destabilising as the radius

increases for $\alpha = 180$. However, the effect loss rate is decreasing for increasing r_l .

The effects found for $\alpha = 90^\circ$ have steady magnitude over the change of r_l . F_{3D} for $\alpha = 90^\circ$ is lower compared to $\alpha = 180^\circ$ with a minimum difference of approximately 2.5% at $r_l = 6$. Moreover, curves for $b = 1.5$ and $b = 3$ with $\alpha = 90^\circ$ are approximately equal at $r_u = 1$. However, the $b = 1.5$ curve decrease slightly going from $r_l = 1$ to $r_l = 2$ and the two curves run nearly parallel to each other to $r_l = 6$. Similar to convex slopes, the more prominent curvature of $\alpha = 180^\circ$ appears more stable and more sensitive to a change in r_u compared to $\alpha = 90^\circ$.

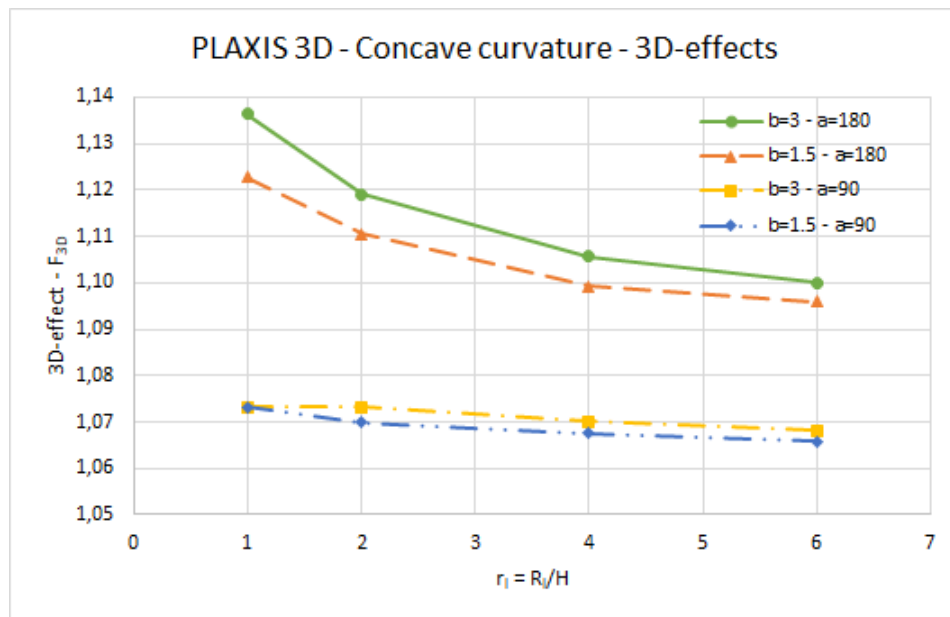


Figure 7.9: 3D-effects for concave curvature defined by $r_l = R_l/H$ and curvature angles 90° and 180° , with inclinations $b = 1.5$ and $b = 3$.

Failure Mechanism

The following figures present incremental displacement plots retrieved from PLAXIS 3D for concave curvature. Since these are half-models of the main arch, the entire main geometry can be visualised by mirroring the model at the closest slope side surface, see Figure 7.2 and Figure 7.3. Two different radii are included for each slope inclination b and curvature angle α , which are $r_l = 1$ and $r_l = 6$. This is to compare the most prominent or 'sharpest' curvature with the least 'sharp' and more extensive curvature.

Figure 7.10 illustrates the failure mechanisms for $b = 1.5$ and $\alpha = 90^\circ$, where the left slope has $r_l = 1$ and the right has $r_l = 6$. The failure mechanism of $r_u = 1$ is essentially the same as for the

convex equivalent, since the concave and convex parts of this slope have almost identical geometry. The most concentrated incremental displacements are found at the toe of the concave main arch. The upper mass of the convex extension arch moves towards the toe of the concave arch. $r_l = 6$ to the right has a critical part at the side of the convex extension arch, where mass is concentrated near the convex crest and slides down the side. The displacements decrease towards the concave arch middle.

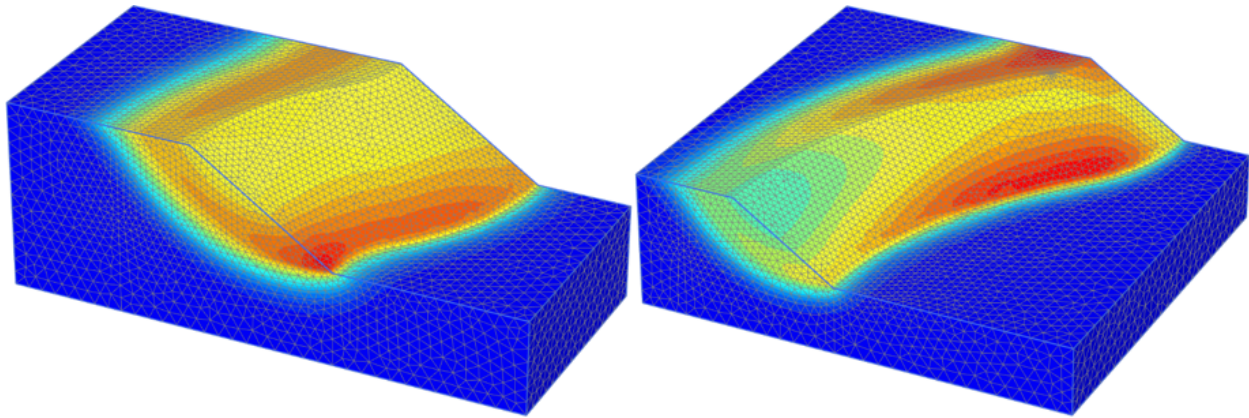


Figure 7.10: Incremental displacements for $b = 1.5$ and $\alpha = 90^\circ$ with $r_l = 1$ (left) and $r_l = 6$ (right).

Figure 7.11 shows the failure mechanism for $r_l = 1$ (left) and $r_l = 6$ (right). The inclination is $b = 1.5$ and curvature angle is $\alpha = 180^\circ$. The left $r_l = 1$ slope displays a small concentration of incremental displacements at the crest middle of the convex extension arch, practically identical to the equivalent in the previous subsection. The slide occurs down on the side of the convex arch at the transition between the main concave and the convex curvature. Further, approximately no movements are observed in the middle of the concave arch. The $r_l = 6$ model to the right have as similar mechanism, but wider. The incremental displacements are greatest at the side of the concave arch near the transition to the convex arch, and are decreasing towards the middle of the concave curvature.

Figure 7.12 contains the incremental displacement plots of $r_l = 1$ (left) and $r_l = 6$ (right) for $b = 3$ and $\alpha = 90^\circ$. The left figure of $r_l = 1$ is practically identical to the convex equivalent with the same characteristics. The mass runs towards the concave arch toe and concentrates there. This critical concentration is similar for the right $r_l = 6$ slope. However, the slide has widened inside the concave arch and diminishes at the convex extension arch. The mass concentrates at the crest near the convex arch and moves towards the less 'sharp' and more extensive con-

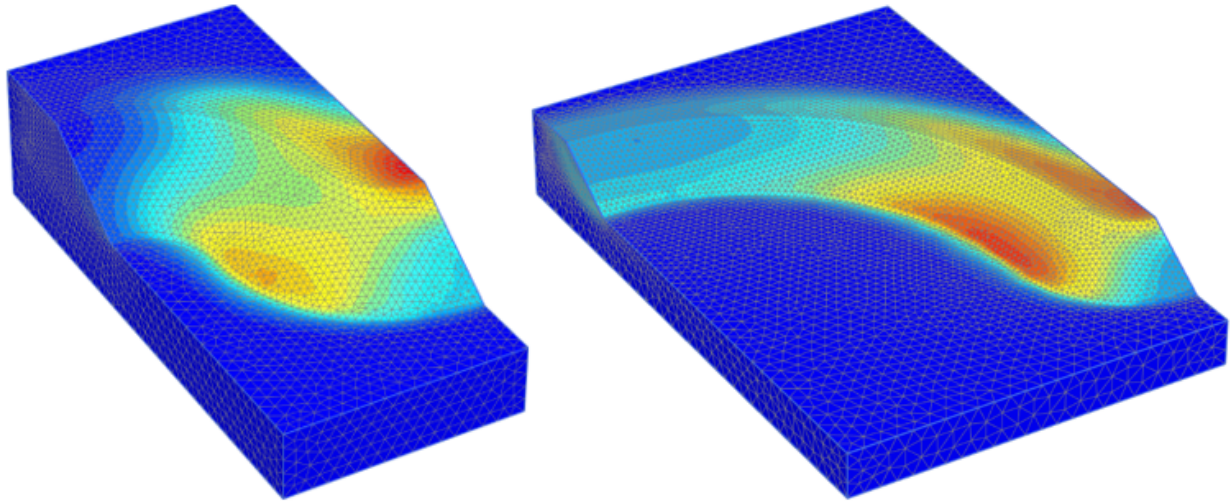


Figure 7.11: Incremental displacements for $b = 1.5$ and $\alpha = 180^\circ$ with $r_l = 1$ (left) and $r_l = 6$ (right).

cave curvature. Compared to the $b = 1.5$ equivalent the mechanism is similar, but it appears slightly shifted towards the concave middle. Moreover, the critical shear surface appears more distributed along the concave curvature toe.

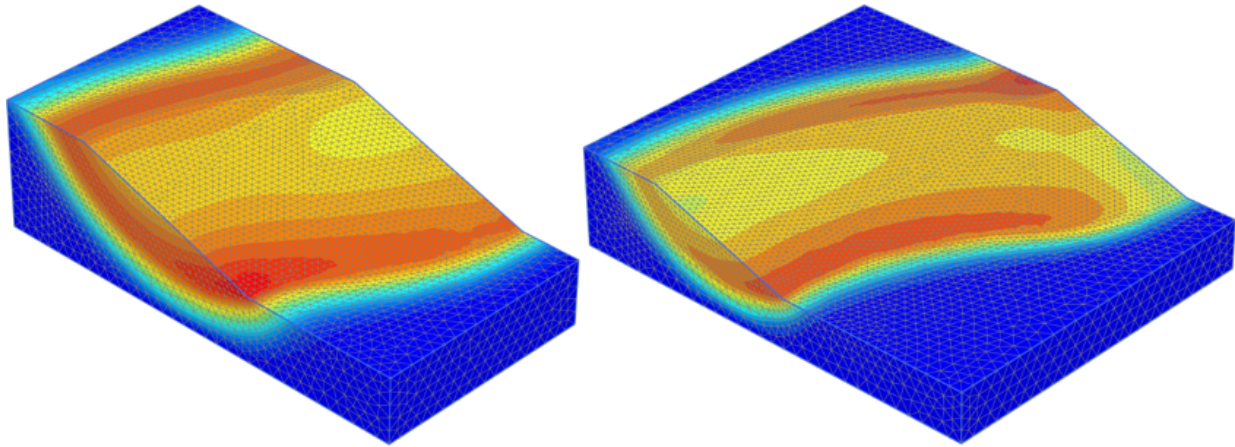


Figure 7.12: Incremental displacements for $b = 3$ and $\alpha = 90^\circ$ with $r_l = 1$ (left) and $r_l = 6$ (right).

Figure 7.13 presents slopes with $b = 3$ and $\alpha = 180$, where the $r_l = 1$ example is to the left and the $r_l = 6$ example is to the right. The $r_l = 1$ model shows an identical failure mechanism to the equivalent convex curvature. A concentration of mass on the top of the convex extension arch is set in motion towards the less curved transition side inside the concave main arch. Furthermore, the failure mechanism for $r_l = 6$ curvature is similar to the equivalent $b = 1.5$ slope, with a slight alteration. The critical area of incremental displacements at the slope top is moved back-

wards from the convex tip. Just inside of the transition to the convex extension arch is the most developed shear surface. This is the area with least curvature, as a result of the concave curvature with a large radius. Additionally, the rate of displacement decreases towards the middle of the concave main arch.

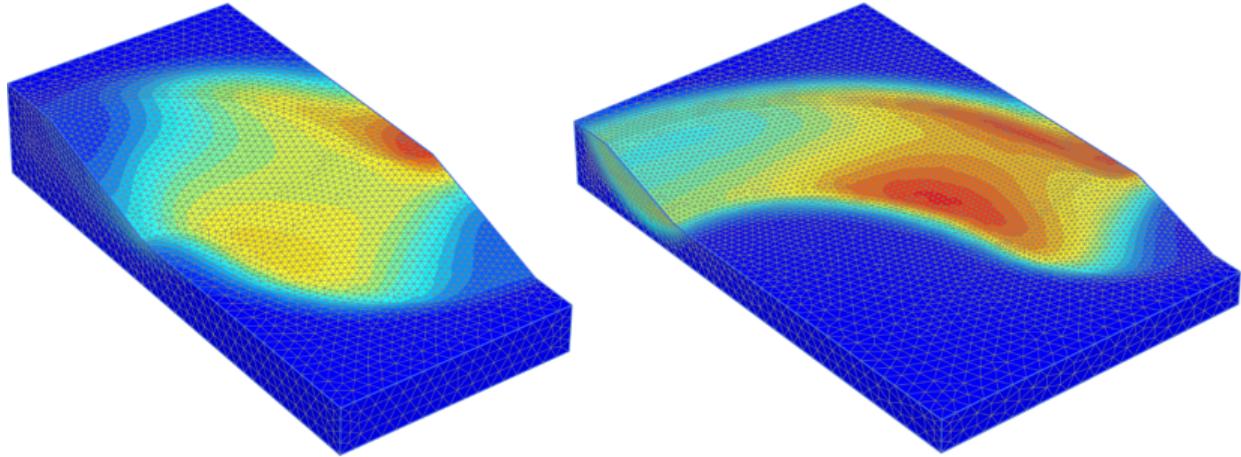


Figure 7.13: Incremental displacements for $b = 3$ and $\alpha = 180^\circ$ with $r_l = 1$ (left) and $r_l = 6$ (right).

7.2.3 Convex Curvature with 10 m Planar Extension

To study the effect of neighbouring curvatures, a 10 m planar slope extension is added to the concave side extension arch of the idealised convex slope. A virtual gap of 20 m is now present as a result of model symmetry. The curvature remains defined by the main arch geometry via α and $r_u = R_u/H$, such that a comparison between 0 and 10 m extension can be obtained.

Safety Factor

Table 7.4 summarises the safety factors obtained for slopes with inclination $b = 1.5$. Both slopes with and without a 10 m extension are included for comparison. The two-dimensional results for width-height ratio $w = \infty$ are included to compare with the a planar infinitely wide slope. All solutions from PLAXIS 3D are greater than the 2D solutions. Furthermore, the safety factors decrease from low to high value of r_u , except from $r_u = 1$ to $r_u = 2$ for $\alpha = 90$ and 10 m extension. In addition, curvature angle $\alpha = 180^\circ$ provides greater safety factors compared to $\alpha = 90^\circ$.

Table 7.4: Safety factors obtained by varying convex radius-height ratios $r_u = R_u/H$ for curvature angle $\alpha = 90^\circ$ and $\alpha = 180^\circ$ and slope inclination $b = 1.5$. The extended slope has a 10 m planar extension on the side.

Convex radius-height ratio	Safety factor (SF)			
	0 extension		10 m extension	
	$\alpha = 90^\circ$	$\alpha = 180^\circ$	$\alpha = 90^\circ$	$\alpha = 180^\circ$
$r_u = R_u/H$				
$r_u = 1$	1.321	1.381	1.302	1.376
$r_u = 2$	1.317	1.355	1.305	1.356
$r_u = 4$	1.307	1.329	1.305	1.329
$r_u = 6$	1.300	1.320	1.298	1.314
$w = \infty$ (PLAXIS 2D)			1.233	
$w = \infty$ (GS Stability)			1.232	
$w = \infty$ (Hand calc. - Janbu Direct Method)			1.187	

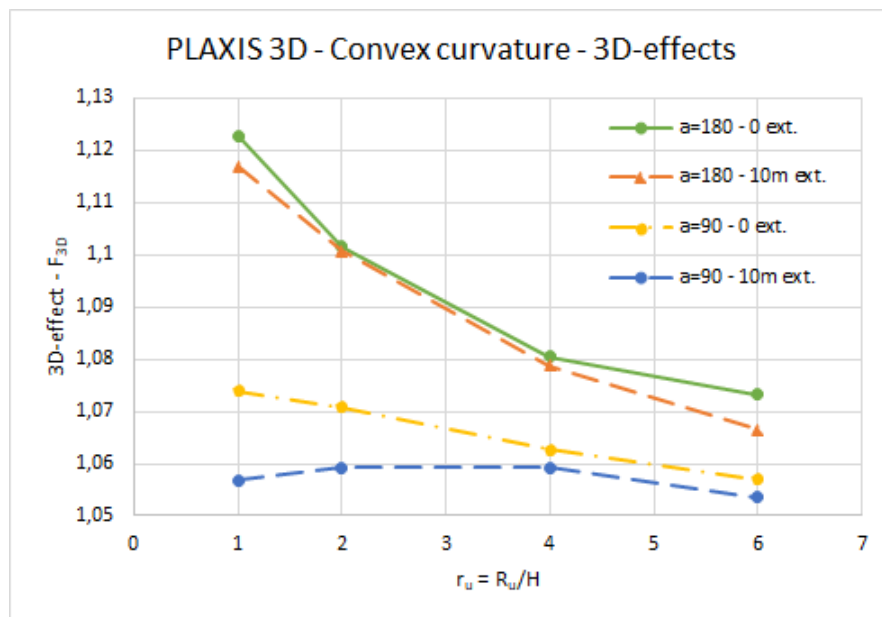


Figure 7.14: 3D-effects for convex curvature defined by $r_u = R_u/H$ and curvature angles 90° and 180° with inclination $b = 1.5$, including a 10 m planar extension.

3D-effects for convex slopes with and without planar extension are plotted in Figure 7.14 for inclination $b = 1.5$. The obtained effects are positive for all convex cases. Moreover, all slopes with extension give a smaller effect compared to those with no planar extension. The lowest F_{3D} is slightly higher than 1.06 for 10 m extension and $\alpha = 90^\circ$. The variation of 3D-effects for

$\alpha = 180^\circ$ is small, where 10 *m* extensions lead to less than a 1% lower value than no extension. Both $\alpha = 180^\circ$ cases show a significant decrease of F_{3D} for increasing r_u . The decrease rate is slightly flattened for increased radius-height ratio.

Curves for $\alpha = 90^\circ$ show a different trend from $\alpha = 180^\circ$. The zero extension slopes have a steady decrease of effect over r_u . Effects of the extended slope first increase between $r_u = 1$ and $r_u = 2$, and then flatten out towards $r_u = 4$. Lastly, F_{3D} decreases with a similar gradient to the zero extension slope. The effect of planar extension appears to have impacted the $\alpha = 90^\circ$ slopes more than the $\alpha = 180^\circ$ slopes.

Failure Mechanism

The following figures present incremental displacement plots retrieved from PLAXIS 3D for convex curvature with a 10 *m* planar slope extension attached on the concave arch extension. Since these are half-models of the main arch, the entire main geometry can be visualised by mirroring the model at the closest slope side surface, see Figure 7.2 and Figure 7.3. The planar extensions are used to assess the effect of mixed planar and curved slope surface. Two different radii are included for each slope inclination b and curvature angle α , which are $r_u = 1$ and $r_u = 6$.

Figure 7.15 illustrates the failure mechanisms for 10 *m* extended slopes with $b = 1.5$ and $\alpha = 90^\circ$, where the left has $r_u = 1$ and the right has $r_u = 6$. The left slide seem to have the most critical development at the planar extension, where the most distinguished contour (red) is found at the extension toe. Some mass may be directed from the curved slope crest towards the planar toe. The observed failure mechanism for $r_u = 6$ at the left is not significantly altered from the non-extended slope, with the most severe displacements at the convex arch middle.

Figure 7.16 shows the failure mechanism for $r_u = 1$ (left) and $r_u = 6$ (right) slopes with planar extension. Slope inclination is $b = 1.5$ and curvature angle is $\alpha = 180^\circ$. The left $r_u = 1$ slope displays large displacements from the convex crest middle and down the side near the arch transition, similar to the non-extended equivalent. However, activity is also observed at the planar part. The slide has become more widespread. The $r_u = 6$ model to the right shows a similar critical slide mechanism as for the slope with no extension, where the slide is primarily located along the convex main arch.

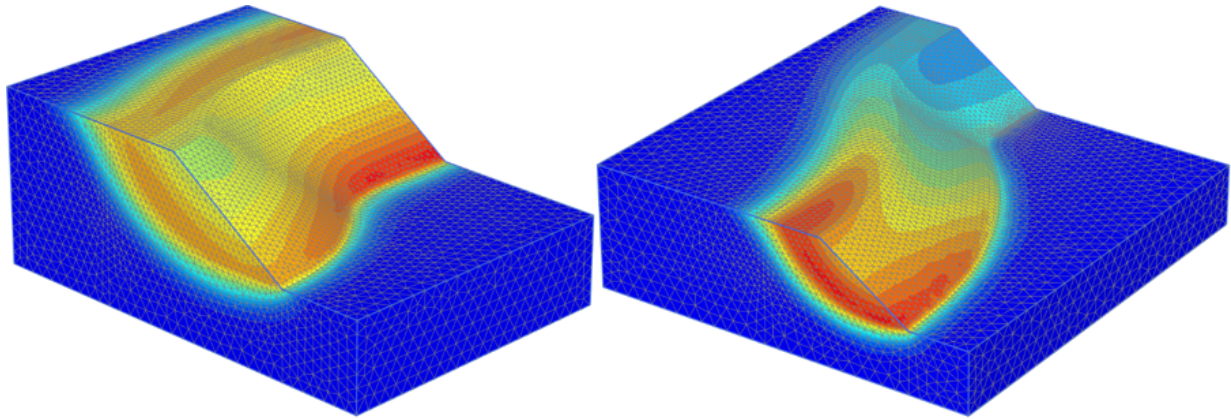


Figure 7.15: Incremental displacements for slopes with 10 *m* planar extension, where $b = 1.5$ and $\alpha = 90^\circ$ with $r_u = 1$ (left) and $r_u = 6$ (right).

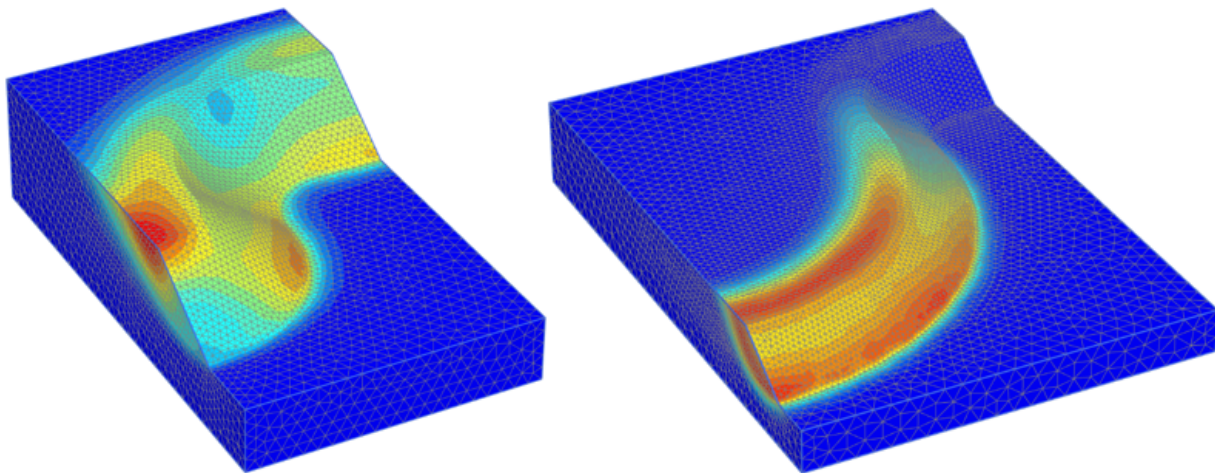


Figure 7.16: Incremental displacements for slopes with 10 *m* planar extension, where $b = 1.5$ and $\alpha = 180^\circ$ with $r_u = 1$ (left) and $r_u = 6$ (right).

7.2.4 Concave Curvature with 10 m Planar Extension

To study the effect of neighbouring curvatures, a 10 *m* planar slope extension is added to the convex side extension arch of the idealised concave slope. A virtual gap of 20 *m* is the result of finite element model symmetry. The curvature remains defined by the main arch geometry through α and $r_l = R_l/H$, such that findings for 0 and 10 *m* extension can be compared.

Safety Factor

Table 7.5 summarises the safety factors for concave slopes with $b = 1.5$. Both slopes with and without a 10 *m* extension are included for comparison. The two-dimensional results for width-

height ratio $w = \infty$ are included to compare with planar infinitely wide slopes. All safety factors found with PLAXIS 3D are greater than the 2D solutions. Moreover, the safety factors decrease from low to high value of r_l , except from $r_l = 1$ to $r_l = 2$ for $\alpha = 90$ and 10 m extension. In addition, curvature angle $\alpha = 180^\circ$ provides greater safety factors compared to $\alpha = 90^\circ$.

Table 7.5: Safety factors obtained by varying concave radius-height ratios $r_l = R_l/H$ for curvature angle $\alpha = 90^\circ$ and $\alpha = 180^\circ$ and slope inclination $b = 1.5$. The extended slope has a 10 m planar extension on the side.

Concave radius-height ratio	Safety factor (SF)			
	0 extension		10 m extension	
	$\alpha = 90^\circ$	$\alpha = 180^\circ$	$\alpha = 90^\circ$	$\alpha = 180^\circ$
$r_l = R_l/H$				
$r_l = 1$	1.320	1.381	1.301	1.344
$r_l = 2$	1.316	1.366	1.303	1.341
$r_l = 4$	1.313	1.352	1.301	1.336
$r_l = 6$	1.311	1.348	1.293	1.329
$w = \infty$ (PLAXIS 2D)		1.233		
$w = \infty$ (GS Stability)		1.232		
$w = \infty$ (Hand calc. - Janbu Direct Method)		1.187		

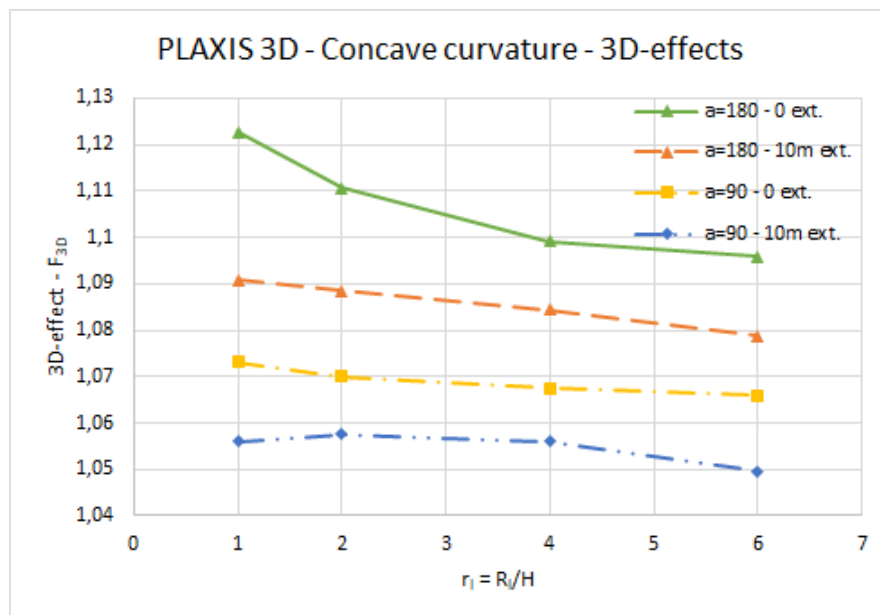


Figure 7.17: 3D-effects for convex curvature defined by $r_l = R_l/H$ and curvature angles 90° and 180° with inclination $b = 1.5$, including a 10 m planar extension.

3D-effects for concave slopes with and without planar extension are presented in Figure 7.17 for inclination $b = 1.5$. The stabilising effects are positive for all concave cases. Moreover, all slopes with extension lead to a diminished effect compared to those without planar extension. The lowest F_{3D} is approximately 1.05 for 10 m extension and $\alpha = 90^\circ$. All included concave cases are showing a noticeable variation from each other, with the least difference of approximately 1%.

The trends vary slightly between the concave slopes. The $\alpha = 180^\circ$ case with no extension illustrates a decreasing effect gradient for higher values of r_u . Further, the slopes with $\alpha = 180^\circ$ and 10 m extension provide a more steady decrease of effects. Similar for the trend of $\alpha = 90^\circ$ and no extension. Observations of the extended slope with $\alpha = 90^\circ$ are similar as for the convex curvature. First a slight increase of stability between $r_u = 1$ and $r_u = 2$, then a flatter stretch and lastly a slight decrease. It seems that concavity has had a similar impact on destabilising for both 90° and 180° slopes with planar extension.

Failure Mechanism

The following figures present incremental displacement plots retrieved from PLAXIS 3D for concave curvature with a 10 m planar slope extension attached on the convex arch extension. Since these are half-models of the main arch, the entire main geometry can be visualised by mirroring the model at the closest slope side surface, see Figure 7.2 and Figure 7.3. The planar extensions are used to assess the effect of mixed planar and curved slope surface. Two different radii are included for each slope inclination b and curvature angle α , which are $r_l = 1$ and $r_l = 6$.

Figure 7.18 illustrates the failure mechanisms of 10 m extended slopes for $b = 1.5$ and $\alpha = 90^\circ$, where the left slope has $r_l = 1$ and the right has $r_l = 6$. The most critical incremental displacements has moved from the concave arch middle with $r_u = 1$ to the planar extension, i.e. the planar extension is less stable. A similar impact has occurred for the left $r_u = 6$ slope, where the most intensive movements have relocated from the arch transition to the planar part.

Figure 7.19 shows the failure mechanism for $r_l = 1$ (left) and $r_l = 6$ (right) with a 10 m extension. The inclination is $b = 1.5$ and curvature angle is $\alpha = 180^\circ$. The left $r_l = 1$ slope displays a small concentration of incremental displacements at the crest middle of the convex extension arch, which is similar to the non-extended equivalent. However, instead of progressing down on the side by the arch transition, the most critical slide exits at the planar extension toe. Moreover,

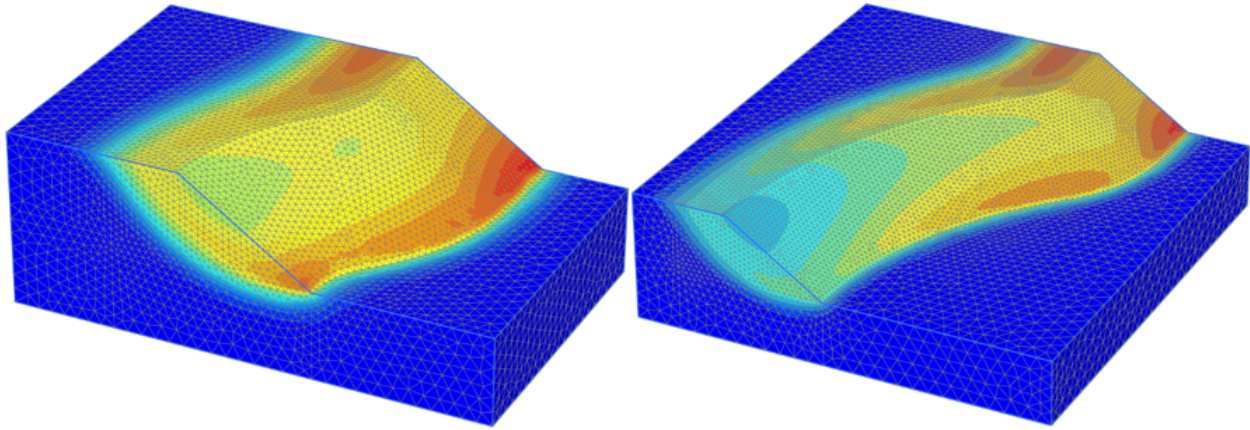


Figure 7.18: Incremental displacements for slopes with 10 m planar extension, where $b = 1.5$ and $\alpha = 90^\circ$ with $r_l = 1$ (left) and $r_l = 6$ (right).

approximately no movements are observed in the middle of the concave arch. The $r_l = 6$ model to the right have as similar mechanism. However, the most prominent displacements are still present on the curvature transition side. The slide is distributed on the side on the concave main arch and the planar extension.

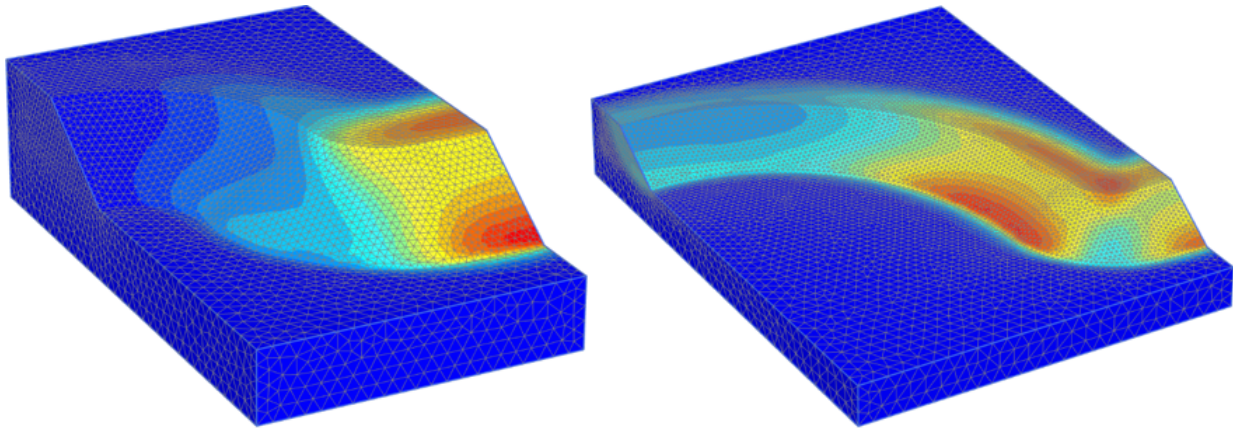


Figure 7.19: Incremental displacements for slopes with 10 m planar extension, where $b = 1.5$ and $\alpha = 180^\circ$ with $r_l = 1$ (left) and $r_l = 6$ (right).

7.2.5 Comparison of Results for Curved Slopes

Convex vs. Concave Curvature

The three-dimensional simulations of varying curvature have revealed a potentially significant impact of convex and concave slopes. Figure 7.20 and Figure 7.21 compare the convex and concave curvatures without any planar extension. The more comprehensive curved slope of $\alpha = 180^\circ$ is more stable compared to the $\alpha = 90^\circ$ slopes for smaller relative radii. Furthermore, convex and concave slopes provide approximately the same effect for $r = 1$. The reason is that the main arch has approximately the same curvature as the extension arch on the side. Consequently, a similar failure mechanism is obtained for both convex and concave main arch.

The difference between convex and concave slope increases with radius for slope inclination $b = 1.5$, as illustrated in Figure 7.20. The two types of curvature starts of as similar 3D slopes. The difference between them increases as the main arch radius increases, since the two curvatures are opposite of each other. Increasing radius and curvature size reveal that the concave shape is more stabilising compared to convex. This effect is more prominent for larger curvature angle α , because the difference between convex and concave has decreased from $\alpha = 180^\circ$ to $\alpha = 90^\circ$.

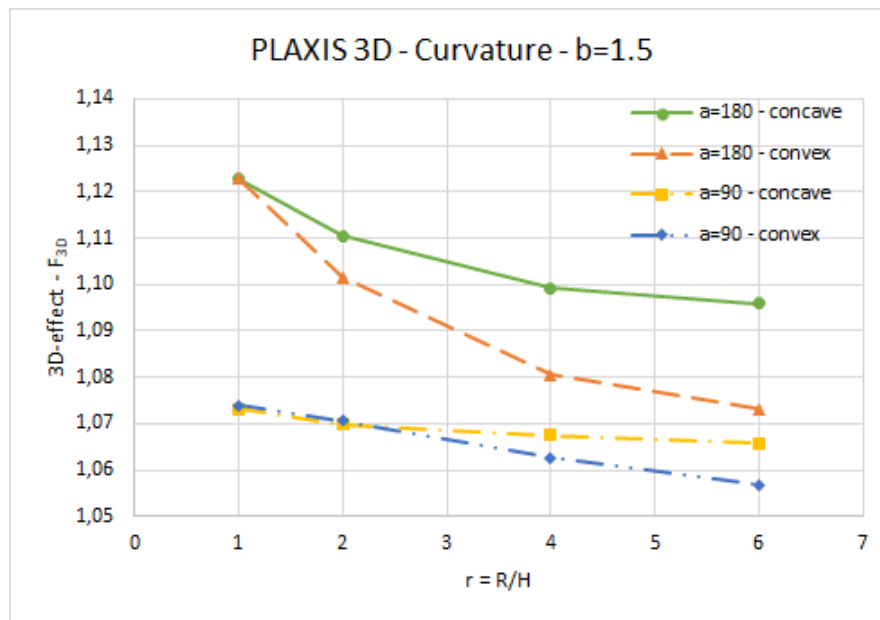


Figure 7.20: 3D-effects for curvature defined by $r = R/H$ and curvature angles 90° and 180° , with inclination $b = 1.5$. $r_u = r_l = r = R/H$ for comparison.

Figure 7.21 shows the difference between convex and concave curvatures for $b = 3$, i.e. a flat-

ter slope. Similar trends are observed as for $b = 1.5$, where the variation between convex and concave increase with radius. However, the difference is significantly diminished. The two curvature types have approximately the same 3D-effect for $r = 1$ and $r = 2$. Further, the stabilising effect of the convex slope decreases more rapidly than of the concave for the 180° curvature angle. For curvature angle $\alpha = 90^\circ$ there is nearly no difference between convex and concave. Moreover, only has a slight decrease with rising radius is observed for both.

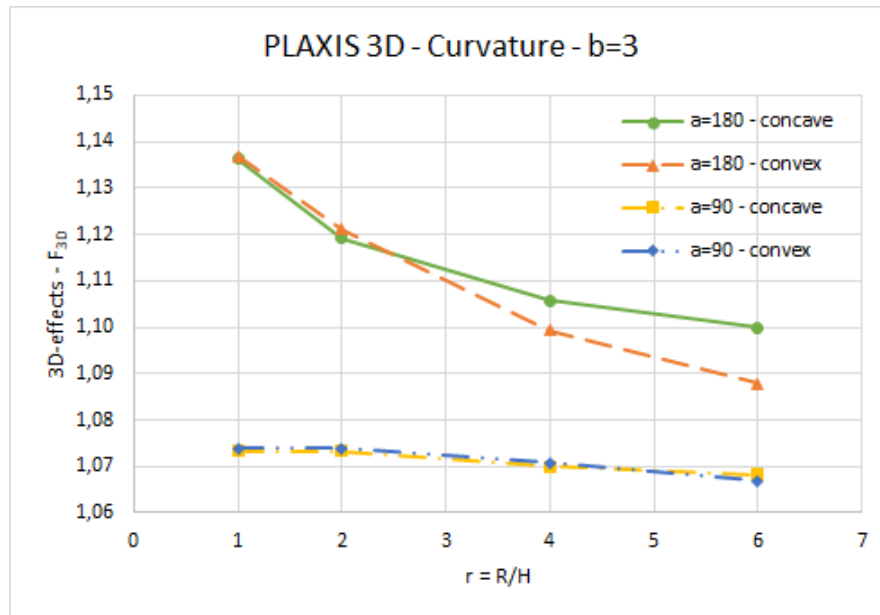


Figure 7.21: 3D-effects for curvature defined by $r = R/H$ and curvature angles 90° and 180° , with inclination $b = 1.5$. $r_u = r_l = r = R/H$ for comparison.

Effect of Inclination on Curvature

Figure 7.22 presents all curvature analyses with no planar extension. Most simulations with slope inclination $b = 3$ gave more prominent 3D-effects compared to its equivalent curvature with inclination $b = 1.5$, i.e. the same α and curvature type. Moreover, the flatter slopes are more influenced by the change from $\alpha = 90^\circ$ to $\alpha = 180^\circ$ compared to $b = 1.5$. The 3D-effects rise more for $b = 3$ than $b = 1.5$ when the curvature extent is enlarged. However, the sensitivity to a change in curvature radius is greater for $b = 1.5$ than $b = 3$. The difference in F_{3D} between concave and convex becomes more distinct for $b = 1.5$ than $b = 3$ as the radius increases.

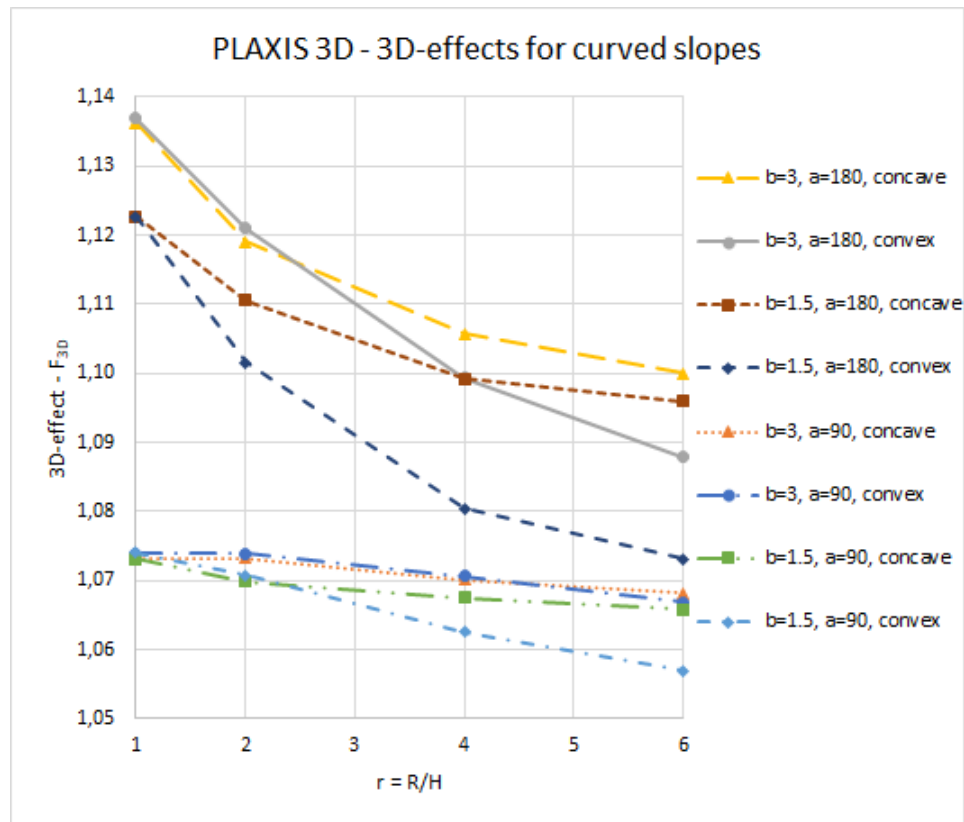


Figure 7.22: 3D-effects for convex and concave curvature defined by $r = R/H$ and curvature angles 90° and 180° , with inclination $b = 1.5$ and $b = 3$ and no planar extension. $r_u = r_l = r = R/H$ for comparison.

Effect of More Widespread Curvature

Figure 7.23 shows the 3D-effects calculated for curved slopes with and without a 10 m planar extension. The slope inclination is limited to $b = 1.5$. The effects are generally higher for zero extension compared to the equivalent geometry defined by α and curvature type. Furthermore, the extended slopes provide a different trend compared to the non-extended. The curves for a convex slope with $\alpha = 180^\circ$ are similar, where both have a rapid rate that is slowly reducing. However, the extended concave slopes with $\alpha = 180^\circ$ show significantly less effects and a lower rate of decrease over r compared to the equivalent (top curve). Moreover, the concave effects are less than the convex for $r_u = 2$ and especially $r_u = 1$. Whereas F_{3D} for other slope pairs with the same curvature angle and model extent is approximately equal for $r_u = 1$. Additionally, a different trend is observed for the 10 m extended slopes with $\alpha = 90^\circ$. Instead of slightly decreasing for increasing r , the effects first rise, then flattens, and lastly decrease. Both convex and concave slopes with extension exhibit the same behaviour.

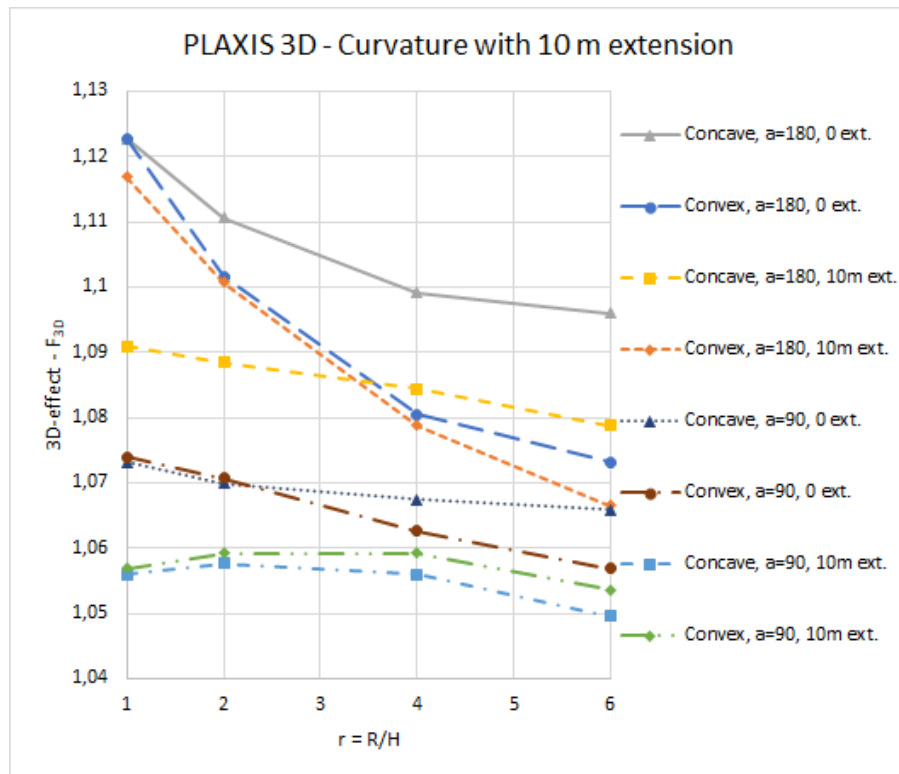


Figure 7.23: 3D-effects for convex and concave curvature defined by $r = R/H$ and curvature angles 90° and 180° . Models with and without 10 m planar extension are included for $b = 1.5$. $r_u = r_l = r = R/H$ for comparison.

7.2.6 PLAXIS 2D Axisymmetric vs. PLAXIS 3D

A brief comparison of the axisymmetric analysis conducted in section 4.2 (chapter 4) and the present 3D analysis is presented. These are not directly comparable, since the 3D models have a defined curvature angle of 90° or 180° with arch extensions, while the 2D axisymmetric model is a simulated curvature 360° around the reference axis. However, the radius for convex and concave slopes are defined equally.

Figure 7.24 shows the comparison of plots for inclination $b = 1.5$. The highest value of F_{3D} is observed for axisymmetric concave simulations. However, the decrease of effects is considerably steeper for the axisymmetric model than for 3D. Moreover, the axisymmetric 3D-effects approach each other for increasing radius, while the PLAXIS 3D convex and concave effects separate from each other for the r values considered here. Nonetheless, for the radius interval defined in the plot, the 3D-effects are quite similar between the two models types considering the different curvature definitions.

3D-effects from axisymmetric and three-dimensional analyses of slopes with inclination $b = 3$ are presented in Figure 7.25. The curves are similar to those for $b = 1.5$. However, all convex-concave slope pairs are closer together, i.e. the variation between convex and concave curvature is decreased. A noticeable gap remains for axisymmetric analyses, however, it is slightly narrowed. Furthermore, the effects have increased for all cases from $b = 1.5$. Moreover, the values of F_{3D} are still approximately in the same range for the two types of analysis.

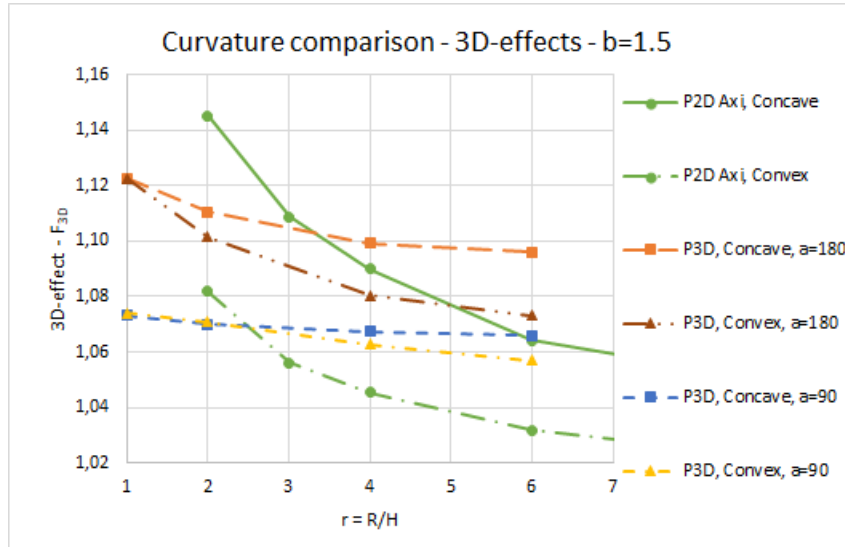


Figure 7.24: Comparison of curvature effects for PLAXIS 2D Axisymmetric (P2D Axi) and PLAXIS 3D (P3D), where $b = 1.5$. Convex and concave slopes are included, defined by $r = R/H \approx r_u \approx r_l$ and curvature angles 90° and 180° .

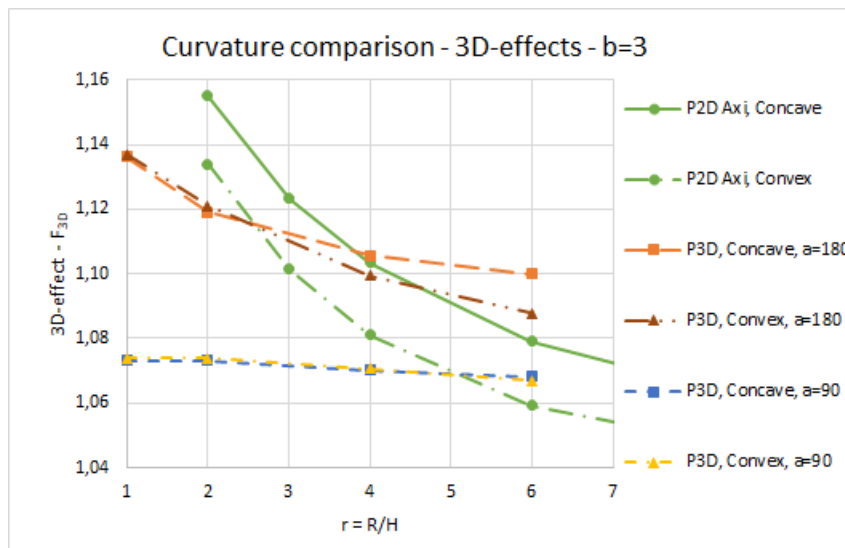


Figure 7.25: Comparison of curvature effects for PLAXIS 2D Axisymmetric (P2D Axi) and PLAXIS 3D (P3D), where $b = 3$. Convex and concave slopes are included, defined by $r = R/H \approx r_u \approx r_l$ and curvature angles 90° and 180° .

7.3 Case - Sørkjosen Slide 2015

The Sørkjosen slide 10th of May 2015 is proposed as a real slide scenario to assess 3D-effects in practice. Sørkjosen is a village in Nordreisa Municipality in Troms and Finnmark, Norway. Roadworks along the E6 and extension of the breakwater had been completed in the previous years. The slide area extend from the breakwater and northwards along the road and seafront to Jubelen as illustrated in Figure 7.26. (Nordal et al., 2016)

A report was compiled to assess the slide and determine potential triggering factors. The findings of the report is briefly described in the following paragraphs, and for more information see (Nordal et al., 2016). Amongst the work in the report, two-dimensional slope stability analyses were conducted to study the area stability before the slide incident. The present study attempts to complete a three-dimensional analysis of the slide area to check for potential 3D-effects.

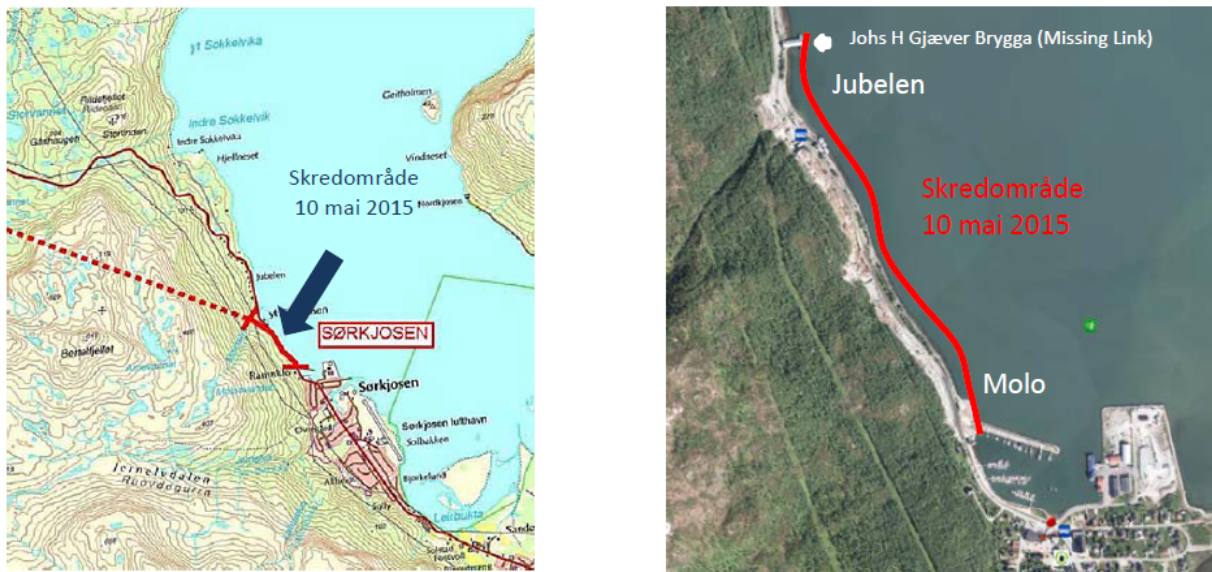


Figure 7.26: Map of Sørkjosen and the surrounding area (left) and bird's eye view photo of the slide area (right), retrieved from (Nordal et al., 2016). The slide stretches from the breakwater (molo) to Jubelen.

7.3.1 Causal Factors and Conclusion

The report findings and conclusion are based on witness observations, hydrometeorological data, interpretation of ground investigations, bathymetri, orthophoto and 2D stability calculations. Several triggering elements and construction events were assessed in search of the cause of incident. The report concluded that the slide was a consequence of the filling in the sea by the

breakwater. The filling was completed in November 2014 and led to low stability. Heavy rainfall and snowmelt 10th of May 2015 provided additional load, which initiated the slide.

The study suggested that the breakwater was filled with water from the heavy rainfall and snowmelt. Consequently, the fill became heavier and the soil below obtained increased pore pressure. Low stability and over-pressure led to a initial slide of approximately $250000 m^3$. The upper part of the soil below the filling consisted of loose to medium dense sand and silt, where parts had a porosity of more than 45%. These layers are part of the river delta from the river Reisa. If sat in motion, such masses may slide rapidly on a flat seabed. A clay layer was located beneath the sand and silt layer. One borehole showed sensitive and quick clay. It was believed that the clay layer is approximately continuous in the area by the breakwater.

The initial slide obtained significant velocity outwards in the fjord, due to altitude difference and steep slope inclination. As a consequence, the slide of disturbed masses moved towards Jubelen along the seabed and slope toes downwards from the E6 seafront. The disturbance and erosion led to subsequent secondary slides that were believed to be progressive and quick.

7.3.2 Bathymetry Analysis and Area Description

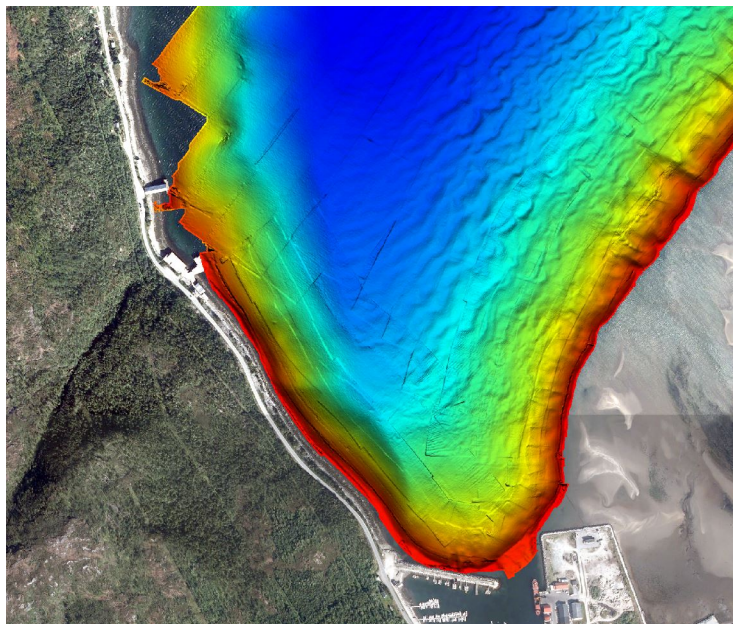


Figure 7.27: Bathymetry before the slide, retrieved from (Nordal et al., 2016). The breakwater is found near the image bottom, while Jubelen is seen further up slightly to the left.

A bathymetry analysis of the area was completed to find the slide extent and failure mechanism. Images of the seabed before and after the incident were analysed, which resulted in a proposed slide development. Figure 7.27 shows the seabed before the slide for the relevant area. The breakwater is pictured near the image bottom. Figure 7.28 illustrates the slide order and directions based on after-images of the seabed. The left figure shows the initial slide (1), which developed from the breakwater. It was suggested in (Nordal et al., 2016) that this slide initiated several secondary slides along the seafront northwards to Jubelen, which are shown on the left image. The numbers in the figure refer to the order of slides. The full analysis is available in (Nordal et al., 2016) and its attachments.

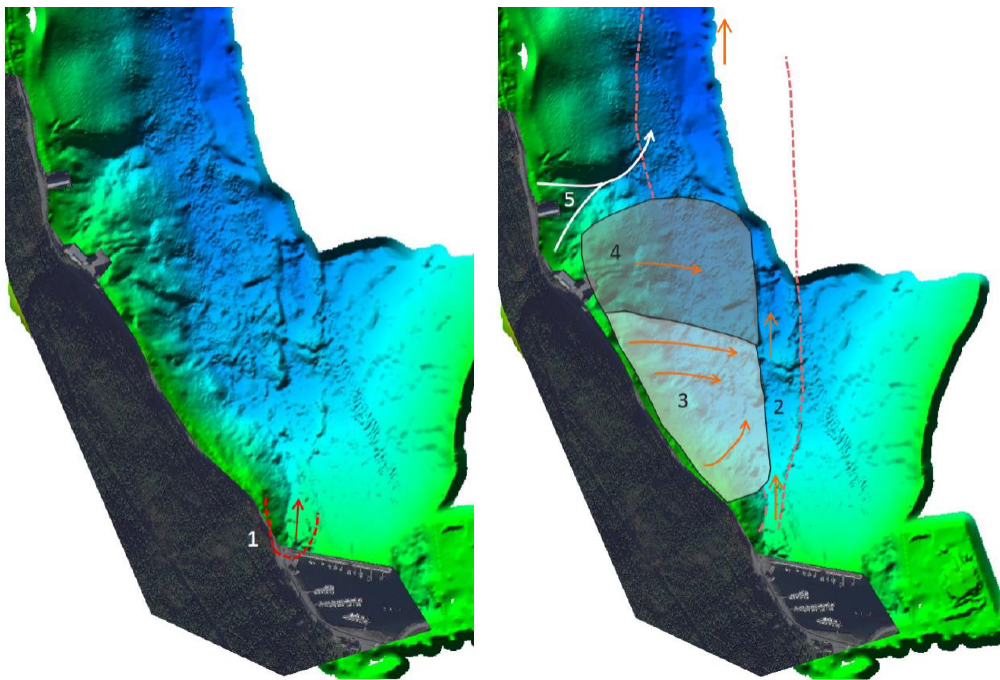


Figure 7.28: Illustration of slide stages from the breakwater to Jubelen, where 1 is the initial slide, retrieved from (Nordal et al., 2016). The stages were found from the bathymetric analysis.

Area Description

As found in the bathymetri analysis, the initial slide happened by the breakwater. The question of potential 3D-effects has come up, due to the narrowness of the slide and a underwater slope surface with some curvature. The generated report by Nordal et al. (2016) only included two-dimensional analyses using GeoSuite Stability and PLAXIS 2D. A proposed profile through the suggested initial slide gives a slope at the verge of collapse, i.e. a safety factor around 1.

The bathymetry image in Figure 7.27 reveals potentially significant curvatures and variations in slope inclination inside the bay. These may provide some 3D-effects, of which the magnitude is unknown. The slope surface is concavely curved at the inner part of the breakwater, approximately where the initial slide propagated. The slope north of the breakwater is steeper with a slight convex shape.

Figure 7.29 shows orthophotos of the breakwater over several years. It was constructed in 1977, and the breakwater parking near E6 has been extended in several stages. The last extension was the 2014 fill. The last image shows the breakwater after the slide in 2015, where the parking and part of the narrower breakwater have vanished into the sea.



Figure 7.29: Pictures of the breakwater construction stages from 1994 to 2014, and the post-slide image from 2015 where the breakwater has collapsed, retrieved from (Nordal et al., 2016).

An overview of field investigations, interpretation of soil stratification and geotechnical parameters are included in (Nordal et al., 2016). The history of the Sørkjosen area and the river delta of Reisa, together with field investigations form the basis of the ground conditions. The stratification of the area can roughly be divided into three layers. The upper layer (Layer 1) consists of loose to medium dense sand/silt. Layer 2 is clay/silty clay, which is quick in certain locations. The bottom layer (Layer 3) is assumed moraine or bedrock. Layer thickness and depth vary considerable over the area.

Available quality field investigations are only completed in the area near the breakwater and near Jubelen. There is a extensive area where no investigations are conducted. Consequently, there is a considerable degree of uncertainty regarding ground conditions in parts of the area between the two locations. Therefore, several assumptions must be made to construct a three-dimensional model of the area with soil layering.

7.3.3 Two-dimensional Stability Analysis

Report 2D Analysis

Two-dimensional stability analyses are included in the report by Nordal et al. (2016), where Geo-Suite Stability and PLAXIS 2D are used. Based on field investigations a set of geotechnical parameters are found for each area, the Breakwater and Jubelen. Only the soil properties found for the breakwater area are included, since the initial slide is considered here. The long term (drained) parameters are given in Table 7.6, while the short term (undrained) parameters for the clay layer are provided in Table 7.7.

The analysis phases were split into several construction stages. These were the 1994, the 2006 and the last 2014 filling. The clay beneath the two first stages is assumed consolidated, and is therefore given an additional undrained shear strength of 7 kPa . The last extension had approximately half a year to consolidate, and is thus given a shear strength increase of 2 kPa . Additionally, strength reductions of 5% (case 1) and 10% (case 2) are used for the clay, due to time effects (rate). Moreover, unit weight of sand is tested for values of 19 kN/m^3 and 19.5 kN/m^3 .

Table 7.6: Relevant soil parameters for materials with drained behaviour.

Parameter description	Breakwater/fill	Sand/silt	Bedrock
Material model	Mohr-Coulomb	Mohr-Coulomb	Linear elastic
Material behaviour	Drained	Drained	Drained
Soil unit weight, $\gamma_{sat} = \gamma_{unsat}$	20 kN/m^3	$19/19.5 \text{ kN/m}^3$	27 kN/m^3
Young's modulus, E	10000 kN/m^2	10000 kN/m^2	$1.0E + 8 \text{ kN/m}^2$
Poisson's ratio, ν	0.33	0.33	0.2
Cohesion, c	20 kN/m^2	0	-
Friction angle, ϕ	40°	33°	-
Dilatancy angle, ψ	0	0	-

Table 7.7: Relevant soil parameters for clay.

Parameter description	Clay
Material model	NGI-ADP
Material behaviour	Undrained (C)
Soil unit weight, $\gamma_{sat} = \gamma_{unsat}$	19 kN/m^3
Shear modulus over active undrained shear strength, G_{ur}/S_u^A	500
Shear strain at failure for triaxial compression, γ_f^C	2%
Shear strain at failure for triaxial extension, γ_f^E	4%
Shear strain at failure for direct simple shear, $\gamma_f^D SS$	3%
Active undrained shear strength, S_u^A	$25 + 1.5z \text{ kN/m}^2$
Passive over active undrained shear strength, S_u^P/S_u^A	0.35
Direct simple shear over active undrained shear strength, S_u^{DSS}/S_u^A	0.65

The report presented stability analyses of profile 31, as illustrated from a top view in Figure 7.30, which was deemed most critical. It stretches from behind the breakwater parking to around 185 – 190 m out into the sea. Figure 7.31 shows the cross-section of profile 31, with the layering consisting of sand (top), clay (middle) and bedrock (bottom). The breakwater parking extent was divided into the years 1994, 2006 and 2015 for the 2D analyses.

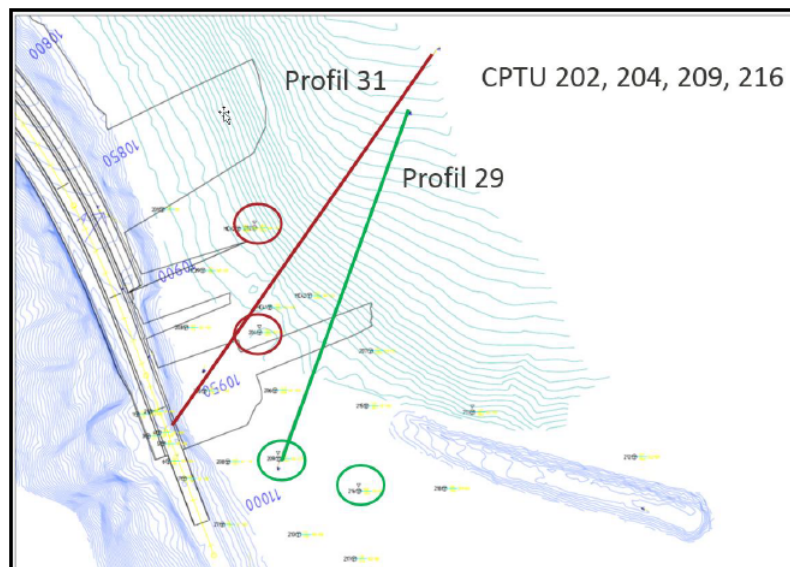


Figure 7.30: Considered profiles through the initial slide, retrieved from (Nordal et al., 2016).

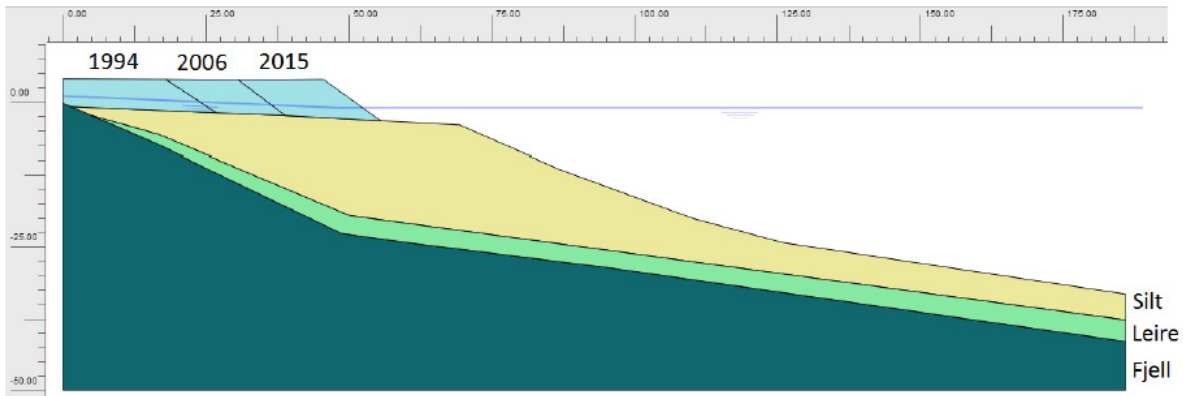


Figure 7.31: Profile 31 showing the parking extent in 1994, 2006 and 2015, retrieved from (Nordal et al., 2016). The three layers beneath the breakwater are included.

The slide occurred at low tide with a water level of -0.4 m . Elevation 0 is approximately where the bedrock is in the back of the breakwater in profile 31, see Figure 7.31. To simulate an assumed over-pressure in the filling, a groundwater level of $+1\text{ m}$ at the back of the breakwater is used. A water level of -1 m is assumed in the sea and at the outer end of the breakwater parking. The 2D analyses revealed that the slope was unstable. Half a year after the breakwater extension in 2014, the safety factor obtained in GS Stability was 1.00 with active S_u reduction of 10% and $\gamma_{sand} = 19.0\text{ kN/m}^3$, i.e. on the verge of collapse in 2015. The PLAXIS 2D analyses using the parameters in Table 7.6 and Table 7.7 provided similar findings. In 2015 the safety factor was 1.00 for $\gamma_{sand} = 19.0\text{ kN/m}^3$ and case 1 ($0.95 \cdot S_u^A$). The soil collapsed when the sand unit weight increased to 19.5 kN/m^3 . The same happened for case 2 with the 10% reduction of active undrained shear strength, for both sand unit weights. The failure mechanism obtained in PLAXIS 2D for case 1 is shown in Figure 7.32.

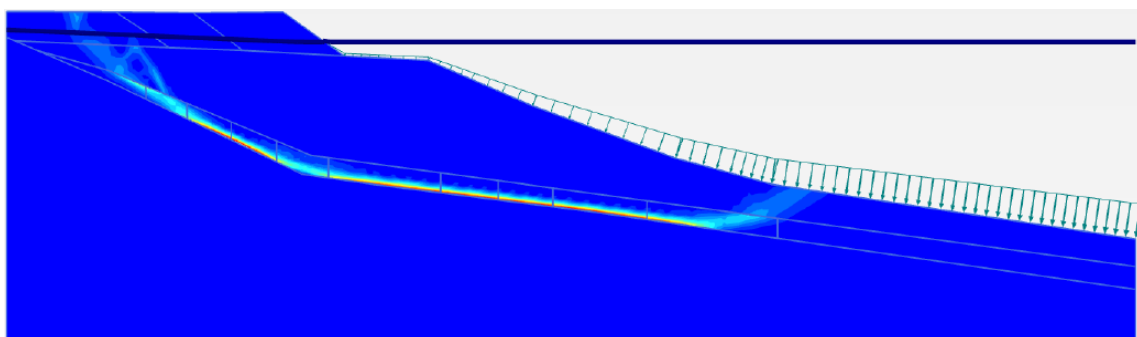


Figure 7.32: Failure mechanism obtained for case 1 in PLAXIS 2D, retrieved from (Nordal et al., 2016).

Present Study 2D Analysis

To validate the 2D analysis in the report, an approximate replication of profile 31 is modelled in PLAXIS 2D in the present study. The cross-section is not an exact replica. Nonetheless, similar results should be obtained. Material models and geotechnical properties are the same as summarised in Table 7.6 and Table 7.7. The clay layer is divided into several soil polygons with different strength profile reference elevations z_0 , since the $S_u^A (= 25 + 1.5z)$ profile starts from the original seabed that is inclined. Additional strength from consolidation beneath the breakwater is included. The material for each soil polygon is defined with a reference S_u^A elevation that coincides approximately with the average seabed elevation at that position.

The safety factors obtained in the present study using PLAXIS 2D are similar to those of the report. Both sand unit weights of 19.0 kN/m^3 and 19.5 kN/m^3 are analysed. However, only the undrained shear strength profile with a 5% reduction is evaluated. The model is shifted 4 m in negative vertical (z) direction, i.e. elevation 0 in the report corresponds to elevation -4 m in the present study analysis. The water level is set as elevation -3 m at the back of the breakwater and a -5 m in the sea at the front of the breakwater parking. This is the same as used in the report to account for a slight over-pressure. The model is shown in Figure 7.33.

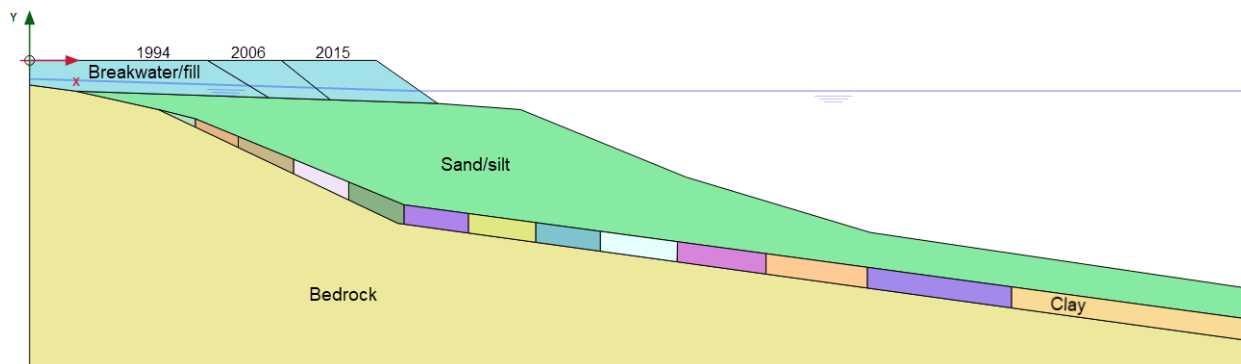


Figure 7.33: Approximated replica of profile 31 based on the report model. The material layers are labelled, where the clay layer is divided into several clay materials.

The analysis in PLAXIS 2D provided a safety factor of approximately 1.01 with $\gamma = 19.0 \text{ kN/m}^3$, i.e. practically equal to the report analyses. A $\gamma = 19.5 \text{ kN/m}^3$ gave collapse, i.e. $SF < 1$. Moreover, the failure mechanism as presented in Figure 7.34 in incremental shear strains is similar to the one included in the report. Therefore, the 2D model of profile 31 should be sufficiently

accurate to be used as the 2D reference model that is imported into PLAXIS 3D and revolved to an idealised curvature.

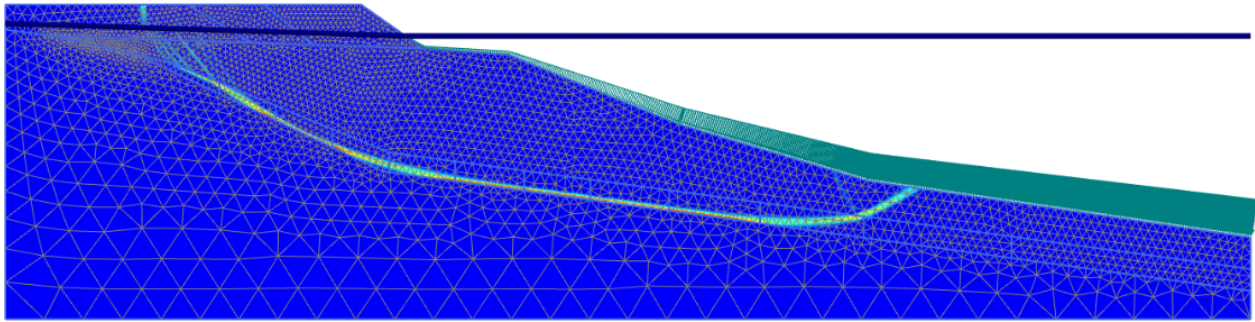


Figure 7.34: Failure mechanism for profile 31, shown by incremental shear strains.

7.3.4 Three-dimensional Stability Analysis

Three-dimensional simulations of the initial slide are attempted to evaluate potential 3D-effects. As mentioned in the area description in subsection 7.3.2, there are some variations in bathymetry and curvatures in the area of the initial slide. These curvatures may provide 3D-effects, which could lead to a change in the safety factor obtained in 2D analysis. A 3D analysis may quantify the potential effects.

Two different procedures are used to assess the potential 3D-effects. The first approach is an idealised curvature with layering equal to profile 31, where the cross-section is revolved around an axis. This creates a simple concave curvature with a certain radius based on approximate measures of the bathymetry curvature. The second is based on using bathymetry data to create a realistic seabed surface. The layering must be assumed based on profile 31 and the available field investigations. The 2D result for profile 31 is used as the reference plane strain solution to calculate the 3D-effects.

Idealised Surface

An idealised model with curvature is proposed to quantify the 3D-effects of a slope composition as in profile 31. The cross-section replica with the various layers, including several clays, is imported to PLAXIS 3D. Figure 7.35 illustrates the suggested concave curvature of the slide area. The breakwater is approximately located slightly outside the middle of the arch. An arch with curvature angle 90° is adapted to the bathymetry. The radius is estimated to approximately

185 m from the slope crest in front of the 2014 filling to the rotation axis. This covers a slope length slightly further than profile 31. This idealised curve is not realistic, since local differences and the steeper seabed to the left in Figure 7.35 are excluded. Moreover, the side surfaces are only perpendicularly fixed, and thus the model is symmetric. Ideally, a convex transition arch should be added at the left steep side.

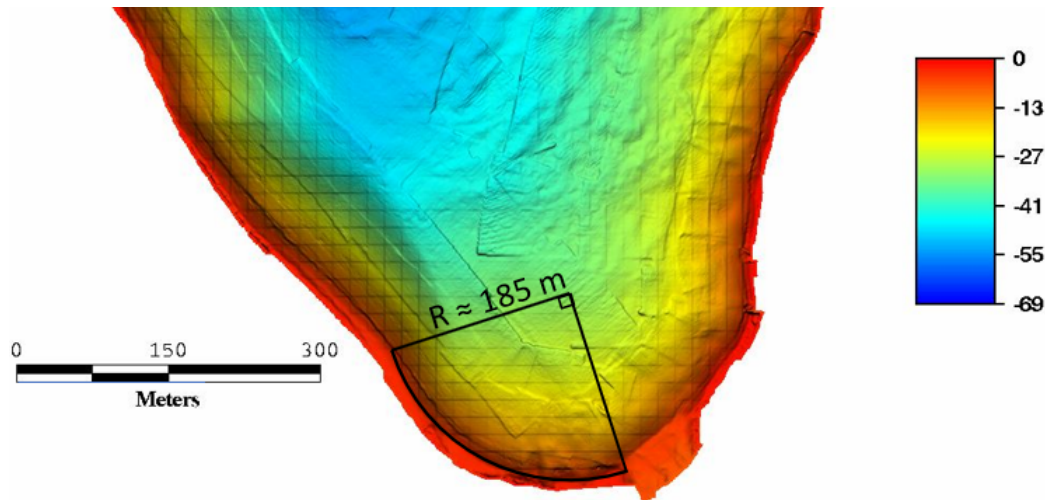


Figure 7.35: Proposed approximate radius and curvature angle for an idealised model.

Two different idealised curvatures are created to evaluate the effect of a concentrated load from the fillings at the breakwater parking. In one model all material clusters are revolved around the same axis. The other model has all clusters revolved except the fillings from 2006 and 2014. The two last constructions are simply extruded to a length that intercepts with the revolved original breakwater. These models are not suitable to obtain a realistic safety factor. Nonetheless, approximated potential 3D-effects may be revealed.

Figure 7.36 shows the model where the entire 2D profile 31 is revolved a curvature angle of 90° with a radius from crest to rotation axis of approximately 185 m. The water level is similar to the one used in 2D. Three profiles of water level points are created, where each profile has three points, same as for profile 31. One profile is positioned at the middle and one at each model side. However, it is assumed higher over-pressure near the mountain where the rainfall gathered compared to further east. Therefore, a 1 m lower water level is created at the easternmost side, which is the nearest side in Figure 7.36. Additionally, the bedrock material is used to fill out the model behind the breakwater, as a simplification.

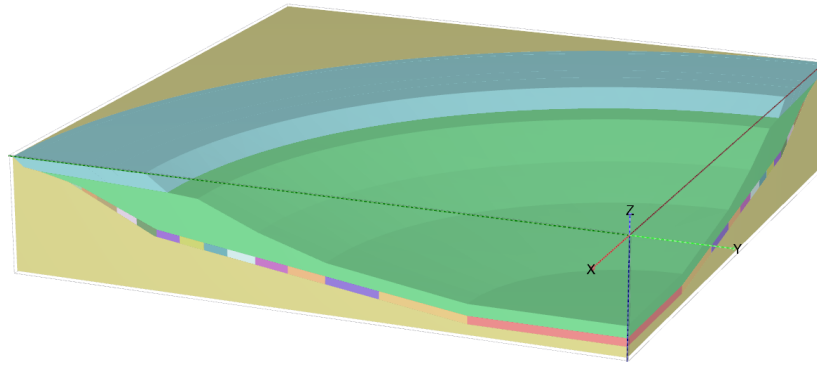


Figure 7.36: Fully revolved model of profile 31. All fillings are included.

The analysis consisted of a gravity loading (initial phase) of the fillings up until 2006, then a plastic loading of the 2014 filling followed by a safety analysis of the 2015 situation before the slide. Default numerical settings were used and the mesh *Very fine* with soil coarseness factors ranging from 0.20 to 0.30. The safety factor for $\gamma_{sand} = 19.0 \text{ kN/m}^3$ was found as approximately 1.20, by using the pragmatic method of finding the safety factor as described in subsection 5.2.3. This implies a 3D-effect of approximately 1.20, i.e. a 20% increase of stability.

Figure 7.37 presents the failure mechanism. The '2D' slip surface is similar to the one obtained in the 2D analysis. The most critical part is located where there is most over-pressure from higher water level. Moreover, the displacements follow the curvature and decrease eastwards. It appears that curvature and variation in water pressure have a restraining effect.

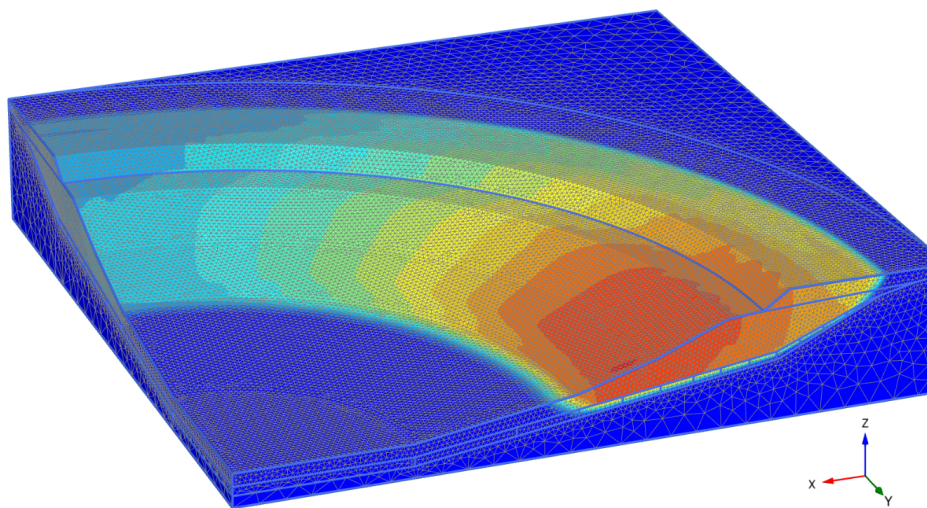


Figure 7.37: Incremental displacements for the fully revolved model of profile 31. All fillings are included and water loads are hidden.

Figure 7.38 shows the other revolved and extruded idealised option. Profile 31 is revolved as in Figure 7.37, except the fillings constructed in 2006 and 2014. These are extruded sideways from the middle until intercepting with the curved breakwater. This is an simplified attempt of simulating the projecting extensions of the breakwater parking, which creates local loads. The model is still considerably simplified, however, the local load is more realistic compared to the fully revolved structure. The concentration of local loading may be slightly inaccurate and the safety factor can be overestimated.

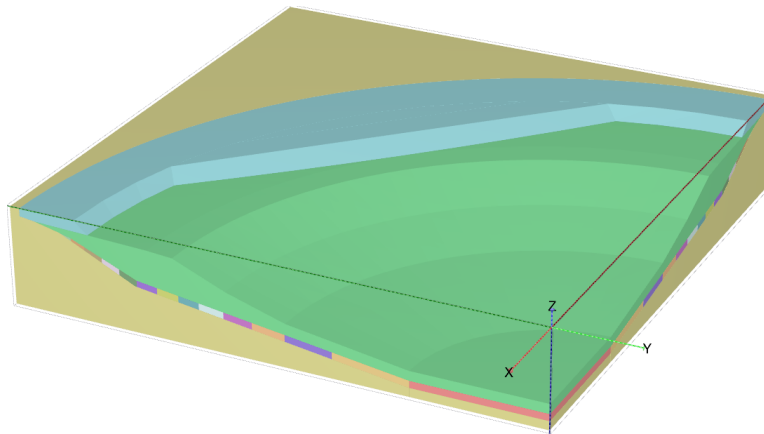


Figure 7.38: 3D model of profile 31 where fillings from 2006 and 2014 are not revolved, but extruded at the middle of the curvature. All fillings are included and water loads are hidden.

The same analysis phases are run as for the fully revolved slope. The 2014 filling is constructed after the gravity loading and a safety analysis of the 2015 pre-slide situation is calculated. Default numerical settings are used and a *Very fine* mesh with soil coarseness factor between 0.15 and 0.25. Sand unit weight of 19.0 kN/m^3 provided an estimated safety factor of approximately 1.27. Thus the slope is slightly more stable than the more conservative fully revolved model, due to less loading near the slope crest. The corresponding 3D-effects are approximately 1.27, which is a significant impact.

The case with a local load at the time of slide in 2015 results in the failure mechanism shown in Figure 7.39. The incremental displacements follow the curvature and are concentrated at the location of the latest breakwater fillings in the middle of the model. The local loading leads to a finite slide width of more than 200 m. Figure 7.40 shows a cross-section with incremental displacements at the middle of the 3D model that corresponds to profile 31. The contours are

similar to the mechanism obtained in 2D.

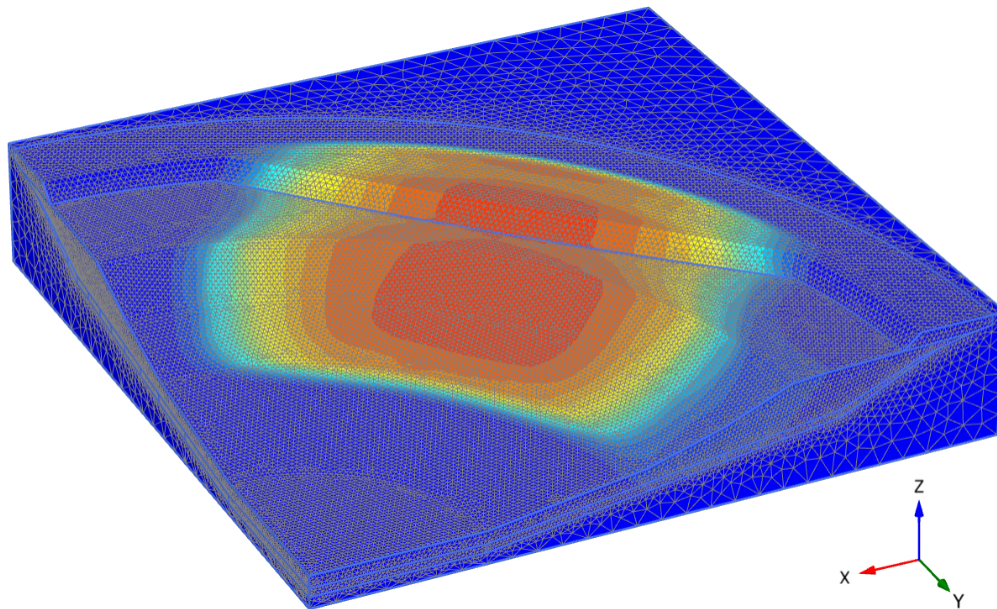


Figure 7.39: Incremental displacements of revolved profile 31, except fillings from 2006 and 2014 that are extruded. All fillings are included and water loads are hidden.

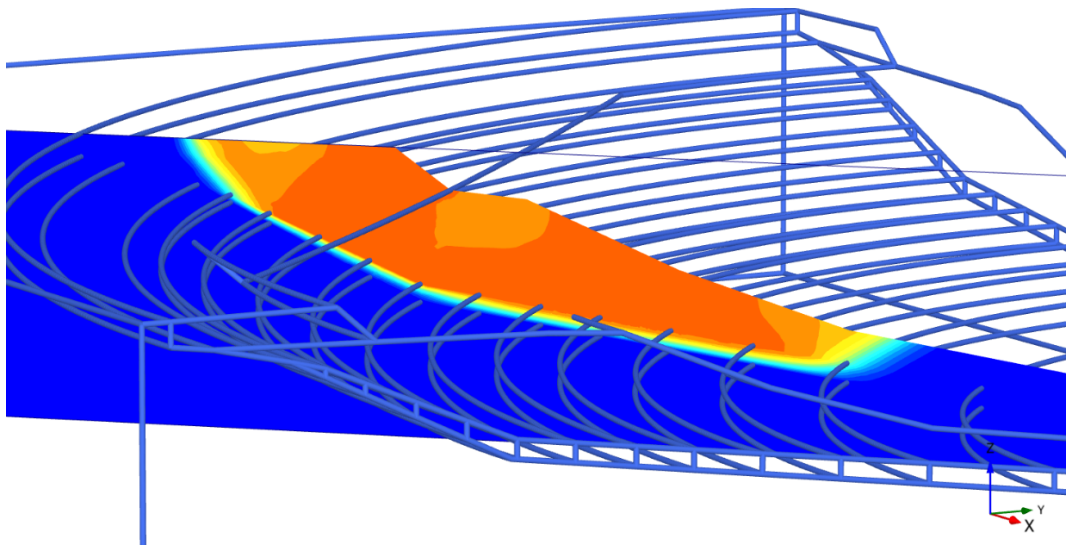


Figure 7.40: Incremental displacements of the profile 31 cross-section in the middle of the 3D-model in Figure 7.39.

Realistic Surface

Bathymetry data from NGU (Geological Survey of Norway) is used to create a three-dimensional surface of the area before the slide, as shown in Figure 7.27. A point cloud is imported to

Rhinoceros 6, a 3D computer graphics and CAD software, where a mesh of the seabed surface is constructed. Further, the surface is imported to PLAXIS 3D. In PLAXIS 3D boreholes are placed around in the imported bathymetry area to create the layering beneath the seabed surface. The layer thicknesses are based on CPTUs, total soundings, soil samples and ground descriptions in the report and its attachments. Figure 7.41 shows a large model created in PLAXIS 3D. The model size is reduced for actual calculations.

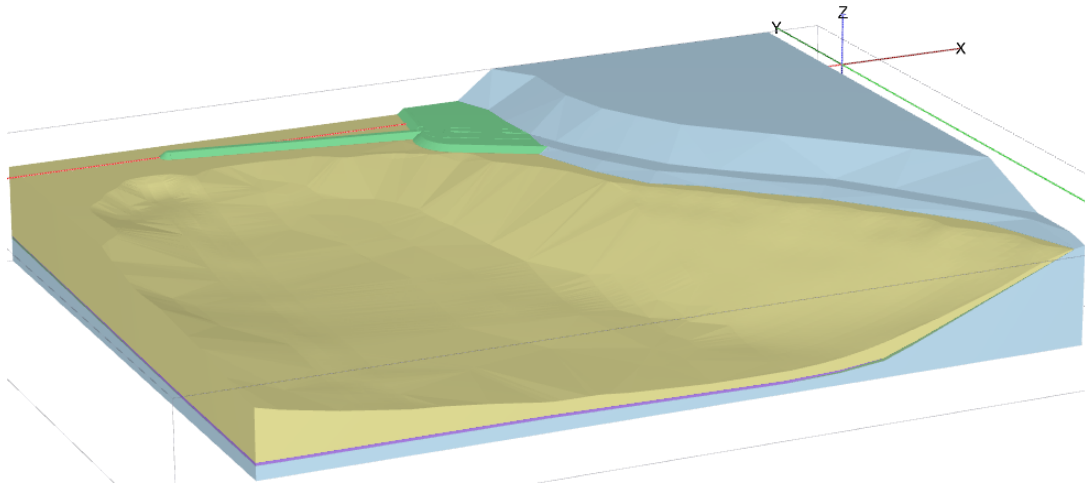


Figure 7.41: Large 3D model of a simplified breakwater and a realistic seabed. The model area in the horizontal plane is approximately $600\text{ m} \times 480\text{ m}$.

The modelled stratification is highly inaccurate, due to few ground investigations relative to the area extent. Soundings and sampling are only done close to the seafront, and no adequate data is available at the steepest part of the slope between the breakwater and Jubelen. It is attempted to replicate the layering of profile 31, since the corresponding analysis is used as 3D reference plane strain solution. However, the seabed surface is considerably varying over the area, and the depth to bedrock varies significantly. The bedrock is inclined outwards into the sea from the mountain side by the road.

The soil layers are created by boreholes instead of constructed volumes. The bathymetry and depth to bedrock varies in the relevant slide area. Consequently, it is unrealistic to simply insert profile 31 at its location and revolve and/or extrude the cross-section. Nonetheless, with care and time it could be possible to use the revolve and extrude tools to insert the correct layering and clay materials at the right place. The clay layer is divided into several clay materials with different undrained shear strength reference levels in the PLAXIS 2D analysis. Moreover, some

clays have additional strength due to consolidation from the breakwater, as defined in subsection 7.3.3. Strength from consolidation and reduction due to time effect is neglected here, because of an already existing uncertainty in the inaccurate model.

Too many clay layers defined by boreholes in PLAXIS 3D led to problems with parametric intersections and meshing. Therefore, one layer set was created with only one constant undrained shear strength in the clay layer, which is inaccurate. Another set layer was defined with three different clay materials in the clay layer, see Figure 7.42. The materials differ by having different undrained shear strength reference elevations. This last set is based in the stratification in profile 31. The ground surface under and in front of the breakwater are roughly at the same level, and then a steep inclination before it flattens slightly. The three sections are given a clay material each as a rough approximation.

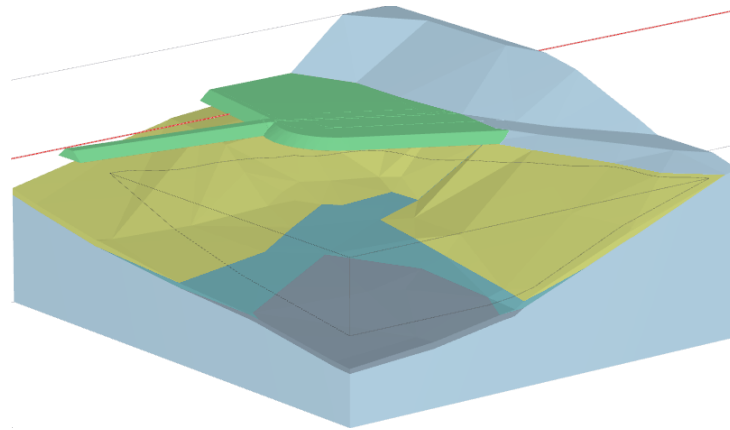


Figure 7.42: Small model showing the assumed contours of the three clays. The sand layer is hidden.

The same calculation procedure was used as for the idealised models. After gravity loading, the 2014 filling was placed and loaded plastically, followed by a safety analysis. Default numerical settings were used, except the steps in the safety analysis were increased to 500. The element distribution was *Very fine* and the clay and sand coarseness factors were set as 0.1. The water level was assumed based on the description in the report.

No clear and unambiguous safety factor convergence was obtained over many calculation attempts. If the plastic loading of the 2015 case was completed, the *c/phi reduction* would at first develop a slide at the breakwater parking. The mechanism was similar as found in the 2D analysis and in the bathymetry after the slide. However, as the safety analysis continues, the safety

factor multiplier increases and the shear surface moves towards the steep part slightly to the north of the breakwater and forms a small concentrated spot of incremental displacements only in the sand material, see Figure 7.43. Consequently, no safety factor is found with this model.

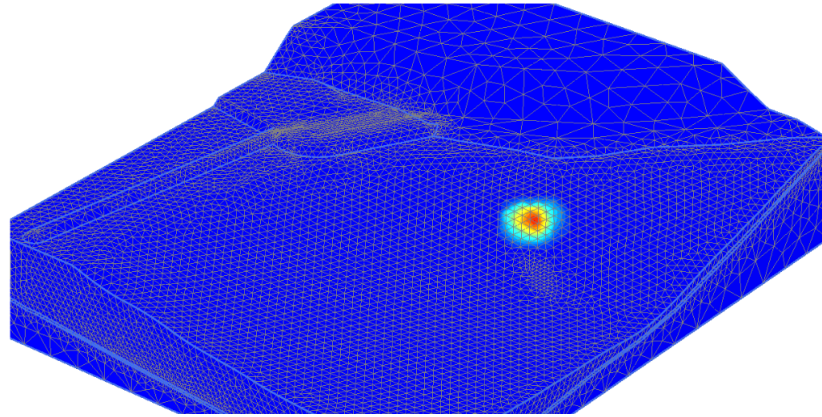


Figure 7.43: Illustration of the incremental displacement concentration spot in the sand, developed in the safety analysis.

Due to problems with the safety factor convergence, several material sets are tested to obtain a collapse near non-collapse in the plastic loading of the 2015 situation. These materials and the incremental displacements may give an indication of the three-dimensional stability and restraining geometry factors. Collapse near loading completion was obtained with a clay layer beneath the breakwater with reference elevation of 0, i.e. corresponding to the ground surface under the breakwater. Outside the breakwater where the depth increases, the clay is given as reference elevation of -15 m , which is near the average of the steeper part in profile 31. Further out into the sea where the seabed flattens, the clay is given a reference elevation of -30 m . This is reasonable for the area where the slide occurs. However, the clay with an elevation of -30 m is slightly over-conservative, since the seabed is closer to a depth between 20 m and 25 m where the slide ends. This is a potential indication of 3D-effects, however, with uncertainty.

The simulations using a single constant clay layer collapsed with a $S_u = 40$. Collapse was avoided with $S_u = 45$. This interval is reasonable, because an average undrained shear strength along the slip surface obtained for profile 31 was approximated to a value in this range. The assumption of a constant strength is highly erroneous and is only usable as a simple validation.

Figure 7.44 shows the incremental displacements when the case with three clay materials col-

lapses in the plastic loading. The length extent and shape resembles the slip surface found in the 2D analysis. Moreover, the width extent is similar to the actual slide, where the breakwater parking and parts of the thinner breakwater slides out into the sea. For materials that does not cause collapse, Figure 7.45 illustrates the failure mechanism that develops in the beginning of the safety analysis before it moves to the small sand spot. The right model in Figure 7.45 has the sand layer hidden and displays the movements in the clay layer. It appears that the variations in surface geometry and layering restrict the slip surface to a finite slide. Notice that the depths to the clay and sand thickness are assumed and a considerable uncertainty.

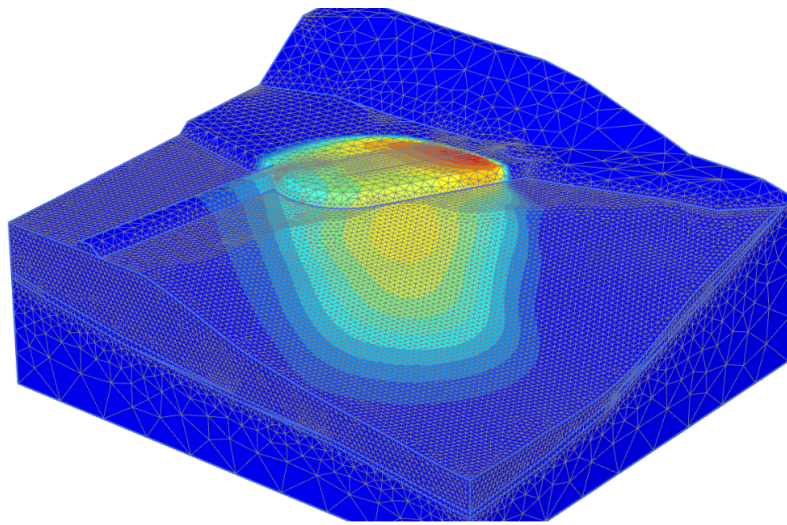


Figure 7.44: Reduced model showing incremental displacements at collapse with three defined clays with reference elevations 0, -15 m and -30 m .

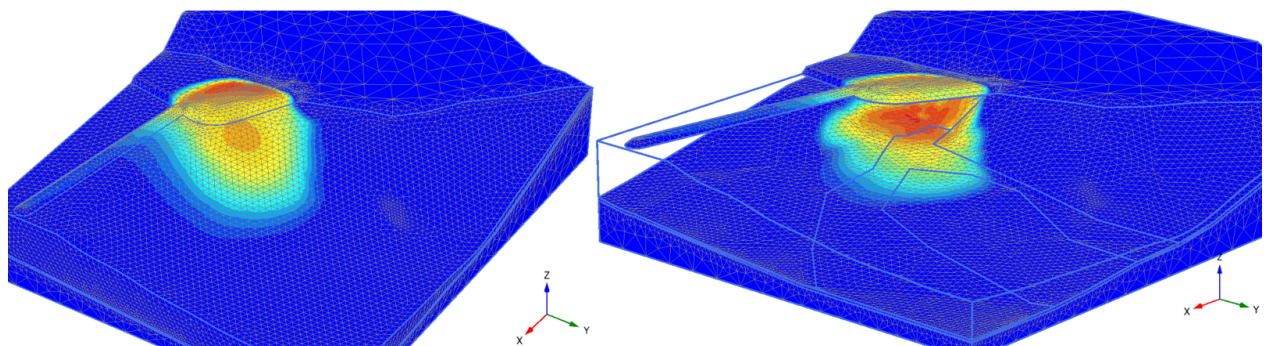


Figure 7.45: Failure mechanism at the beginning of the safety analysis for slightly stronger clay than was used at collapse in Figure 7.44. The top layer of sand is included at the left and the sand is hidden at the right.

7.4 Discussion on Effect of Curvature

The aim of analysing curved slopes was to assess what effects are present and how curvature impacts stability. The 3D-effects were not as large as certain fixed width results. Nonetheless, the effects were significant and restraining mechanisms were observed. It was attempted to model realistic natural curved slopes. However, the findings are still limited by idealised geometries and homogeneous soil.

Accuracy and Numerical Limitations

As discussed for planar slopes with fixed width in section 6.3, the 3D-effects should be sufficiently accurate to be of practical use. Similar assumptions regarding accuracy of GS Stability and PLAXIS 3D are applicable. The main differences regard model size and boundary conditions. The analysed curved slope models are mostly larger than the finite width models, and increase significantly in extent for certain geometries. This emphasises the need of local mesh refining. The assumption of approximate slide occurrence was adequate and covered most of the incremental displacements. It is difficult to define an element distribution that creates equally dense meshes for all cases. Consequently, slight variations in accuracy between the geometries may be present.

The defined model mesh probably provides a slight overshoot of safety factor. However, the change in safety factor was near insignificant when the coarseness factor was halved in the mesh sensitivity analysis in section 5.2. The impact from the same mesh refining in the fixed width slope was considerable greater. This may indicate a sufficient mesh configuration for the curvature models. Still, some overestimated 3D-effects should be accounted for. The difference in mesh sensitivity between the planar fixed width slopes and the curved slopes may be due to absence of fully fixed side surfaces. Since the boundaries on the sides of the slope only are normally fixed, less nodes are restrained and more degrees of freedom are available.

Effect of Curvature

Certain curvatures provided significant stabilising effects. However, the impact varied considerable, depending on curvature angle, radius, inclination and whether the shape was convex or concave. Intuitively, it may seem a bit strange that a convex structure is more stable than a

planar slope. The explanation is that there is less mass near and at the slope crest, due to the inclined arching surface that narrows the area behind the crest. Consequently, less driving mass is available, while the shear surface area is less altered.

The effect of concave curvature is for most cases greater compared to convex. The reason is that much of the slide mass is removed due to the concave valley shape, while the slip surface extends beneath and slightly around the curvature. Consequently, the shear surface area extends and the driving mass is reduced. Moreover, the arching effect and inclination narrow the width of the driving mass from the crest towards the toe, where it concentrates at the middle of the concave arch. This contributes to opposite forces that support the slope.

It was observed an increasing gap between convex and concave 3D-effects as the radius increased. As a result of the arching curvature definitions and the symmetric boundaries in PLAXIS 3D, there were practically no difference between the convex and concave results with $r_u = 1$ for the same curvature angle and slope inclination. The difference between the main arch and the extension arches increases when the main arch radius increases. The reason is that the main curvature becomes larger and more governing relative to the extension arches. This reveals the variation of resisting effects between convex and concave curved slopes. Furthermore, the decline of 3D-effects for increased r is due to less prominent curvature, which will cause less restraining impact and the slide may develop wider in extent.

Effect of Curvature Angle

The extent of the curvature angle proved to be of significant influence. The curvature angle $\alpha = 180^\circ$ gave higher safety factors compared to $\alpha = 90^\circ$. $\alpha = 90^\circ$ permits the slide to develop laterally to include the extensions, since the curve is not large enough. $\alpha = 180^\circ$ provides a sufficiently comprehensive curved surface to limit most of the slide to the main arch. A greater curvature angle makes it more difficult for the slide to propagate towards a neighbouring curvature. Moreover, the concentrated slide mass near the crest of a 180° curve may need to distribute over a larger area, due to larger α . While the slide near the crest of $\alpha = 90^\circ$ may be less concentrated and have less total curved surface area with restraining effect.

Additionally, the curvature angle affects how sensitive the safety factors are to a change in radius. $\alpha = 180^\circ$ displays a significantly more varied trend over r than $\alpha = 90^\circ$. Observations of

the incremental displacement plots may reveal why. The radius of the $\alpha = 180^\circ$ slope affect the slide extent more, since most of the movements are happening at the main arch. However, for $\alpha = 90^\circ$, the curvature is not large enough for the slide to only develop at the main arch, even for greater radii. As a consequence the slide is distributed wider than the main arch towards the neighbouring curvature. The larger curvature angle force the slide to split more. If one slide is split into several slides, the shear surface area is considerably enlarged. Consequently, the more extensive curvature will more significantly vary from a planar slope and the radius will have a greater impact.

Effect of Inclination

Similar to findings from the simulations of a planar slope width fixed width, the 3D-effects rose for flatter slopes. Furthermore, it is observed that steep slopes are more sensitive to a change in curvature type, i.e. convex or concave, compared to flatter slopes. The explanation may be that the flatter slope surface reduces the relative curvature between the radius at the crest and radius at the toe. This makes the curvature appear less prominent compared to the steeper slope. Less prominent curvature leads to less difference between convex and concave shapes, since these are opposite curvature types. According to the incremental displacement plots, the failure mechanism is slightly extended in the width for the flatter slopes, which may decrease the difference between the various values of r . This further contributes to practically no difference between convex and concave for $b = 3$ and $\alpha = 90^\circ$, since the 90° curved slopes already have developed slides that extend past the transition arches for $b = 1.5$.

Effect of Planar Extension

The addition of a 10 m planar extension to assess the impact of neighbouring curvature leads to reduced stability, which is expected. The 10 m planar extension creates a 20 m planar gap to the next curvature. Therefore, the restraining effect of neighbouring curvature diminishes. The critical slide may move from the arch curvature to the planar extension, since the planar part provides less stability compared to the curved part. Some cases alter the entire displacement mechanism from the arch to the planar part. Others partly change the mechanism and the slip surface may be distributed both at the planar and the curved part of the slope. The degree of reduced stability is dependent on curvature type, inclination, curvature angle and radius. The

variations observed from the planar extension analyses make it difficult to obtain a clear connection between curvature and the magnitude of 3D-effects. Nonetheless, all cases considered here imply reduced 3D-effects when planar parts are included.

Use of Axisymmetric Model

The findings of PLAXIS 2D axisymmetric analysis and PLAXIS 3D analysis are not directly comparable due to different curvature definitions. The convex and concave radii are defined similar. However, the axisymmetric model does not have side transition arches, only a single arch that extends symmetric around the reference axis. Some values of F_{3D} are similar to those obtained with PLAXIS 3D. However, the effects vary significantly over the varying radius-height ratio. Consequently, the effects obtained with PLAXIS 2D axisymmetric model may be misleading. Nonetheless, the model can be used as an indication of potential 3D-effects. Use of PLAXIS 2D as a replacement to 3D-modelling should be practised with caution.

The Sørkjosen Slide

The case of the Sørkjosen slide from 2015 has revealed how difficult and time consuming it can be to construct an accurate 3D model. The slide area was comprehensive with field investigations only conducted certain places near shore. A realistic seabed surface is possible to model if bathymetry data is available. However, modelling an accurate representation of soil layers in an extensive area with considerable variations in surface altitudes and inclinations is demanding. With sufficient time and modelling experience it may be possible to obtain realistic conditions. However, the model could be too detailed with respect to geometry and material division that the finite element program may struggle with e.g. parametric intersecting and meshing. Moreover, numerical issues may easier occur. Additionally, proper element distribution is essential, and the comprehensiveness and complexity may exacerbate the discretisation process. Consequently, lack of unambiguous convergence and potential overshoot of safety factor.

Most of the model stratification had to be assumed, due to lack of sufficient ground data. This is not uncommon in geotechnics. However, it prevents an accurate solution, which is necessary to quantify the 3D-effects. Nonetheless, an indication of critical failure mechanism may be found, even if the safety factor is not trustworthy. However, the location of critical failure mechanism can be significantly wrong if soil conditions are assumed incorrect. If similar depths and layering

as profile 31 are assumed around the entire bay, the failure will occur at the steeper slope slightly further north from the actual initial slide.

Construction of idealised models to simulate slope characteristics may provide an indication of 3D-effects. An accurate basis of comparison can be achieved by simply extruding and/or revolving the 2D reference profile to estimate features that may give stabilising effects, such as a concave curvature. This allows for accurate replication of the critical profile layers, and may reveal the sensitivity of soil properties for a change in geometry. As found in literature, soil properties may impact the 3D-effects. However, idealised models may not be accurate enough to find a critical safety factor, only an indication of potential 3D-effects. In addition, the extensiveness and complexity may give a considerable overshoot if inadequately discretised in FEM.

The 3D-effects found using the idealised slopes for the Sørkjosen case are noticeably greater compared to the curvatures analysed in the two previous sections. The Sørkjosen soil consists of a mixture of clay and sand/silt, i.e. both undrained and drained behaviour. As mentioned and as found in literature, various soil properties may affect 3D stability differently. Furthermore, drained material under water is dominant, which may impact the 3D-effects differently compared to a fully undrained analysis. Moreover, the 3D distribution of water level to account for over-pressure and low tide may be assumed wrongly. Water-pressure can significantly affect the stability, and is therefore essential to model correctly. Additionally, sub-sea slides may act and develop differently than what is found in PLAXIS 3D. For instance the failure may develop progressive, and the slide mass could be more disturbed and thus flows more effortless.

The definition of curvature is different compared to the previously analysed curved slopes, with no side arch extensions. This simplification is tolerable for the eastern part of the curvature, i.e. toward the end of the breakwater. However, at the north-western side there should be a slightly convex arch. Moreover, there could be a transition to a steeper slope, as observed from the bathymetry. Nonetheless, the slide did not occur at the steep part, which may indicate a more stable stratification. Therefore, the assumption of constant layers and inclination may be conservative. Further, the safety factor from the two breakwater geometries differ noticeably. The fully revolved model is a conservative option, since significantly more load is placed at the slope crest compared to the real situation. The alternative with a more concentrated load from the two last fillings should be more realistic, but still simplified.

Chapter 8

Method and Model Limitations

8.1 Accuracy and Numerical Limitations

Obtaining sufficient accuracy is more than a discussion of 2D vs. 3D, it is also about method of solution. Both limit equilibrium and finite element method have been used in the thesis, with emphasis on FEM using PLAXIS. The simple 2D cases showed insignificant difference in safety factors between PLAXIS 2D and GeoSuite Stability with the custom method BEAST. However, this is obtained by forcing BEAST to develop a toe failure, which was found using PLAXIS 2D. PLAXIS and FEM has the inherent capability of locating a realistic slip surface, which is favourable. The calculation time is slightly longer with FEM, however, not significantly longer in 2D.

Modelling errors, CPU time and variations in results may increase in 3D, due to increased complexity. As for two-dimensional analysis, the finite element considerations in PLAXIS 3D locates a realistic failure mechanism. The LE program Slide3 finds reasonable shear surfaces that are similar to PLAXIS. However, the mechanisms are not as accurate and may deviate slightly. Moreover, the safety factors may depend significantly on which LE method that is used. The calculation time for 3D limit equilibrium analysis may be significant, and depend on the number of columns. This is similar to the element distribution effect in PLAXIS. More columns or elements lead to increased time consumption, and potentially enhanced accuracy. It is difficult to conclude if 3D FEM or LEM is more accurate without a more thorough accuracy analysis.

The comparison between Slide3 and PLAXIS 3D revealed greater safety factors for PLAXIS 3D.

Moreover, an overshoot was observed in the mesh sensitivity analysis for too coarse element densities. The overshoot appeared higher for narrower slopes with fully fixed side boundary conditions. This may be due to lack of sufficient nodes, and thus degrees of freedom, to accurately calculate displacements. Furthermore, this contributes to a false stiffness present in elasto-plastic finite element analysis.

Nordal and Antonsen (1985) described how elasto-plastic collapse loads may overshoot, due to the false elastic stiffness, see subsection 2.5.2. The elasto-plastic material model cannot obtain a purely plastic deformation at failure using FEM. Moreover, the ability to model pure elastic collapse depends on the type of finite element and mesh density, i.e. number of integration points and nodes. Therefore, the relation between the number of degrees of freedom and equations (constraints) to be solved should be evaluated. Overweight of constraints may lock the system and reduce the possibility of pure plastic failure. Finer discretisation may remedy the problem, i.e. more nodes. Jostad and Lacasse (2015) stated that 20-noded hexahedral elements were suitable for modelling undrained behaviour in a planar slope with fixed sides, with little shear locking. Therefore, 20-noded hexahedral element may provide less false stiffness, and thus reduced overshoot for the fixed width planar slopes. 10-noded tetrahedral elements as used in PLAXIS 3D may be more suitable for complex geometries, dependent of sufficiently fine discretisation.

8.2 Realistic Conditions

The models considered are simplified and idealised. The single inclined undrained shear strength profile and a single height value limit the application. Nonetheless, the defined material is reasonable for Norwegian clays. Furthermore, the assumption of a single reference elevation of the strength profile and horizontally constant values rarely describes the soil conditions in natural slopes. The strength may follow the slope inclination. This is a limitation with most models in PLAXIS 3D. The SHANSEP-MC model may be an option with correctly adapted parameters, since it is based on current stresses and thus follows the slope.

Local soil, water or load conditions may affect the three-dimensional stability. Often there is a mixture of drained and undrained materials, instead of purely undrained soil. The groundwater will be of importance in drained soil, which again may impact an undrained layer by additional loading. The groundwater may significantly influence curved slopes. For a convex curvature,

the groundwater path will take the shortest way down the slope and thus run further below the convex surface. Consequently, a considerable part of the protruding ridge remains dry. However, a concave surface may intercept the shortest groundwater path. The water may even be higher up on the concave sides and a destabilising over-pressure may occur. Moreover, water may naturally run over the surface along the concave slope, e.g. as a river. This may significantly erode the soil. In addition, local surface loading like the breakwater in Sørkjosen, may affect the 3D stability differently than in 2D.

8.3 Method Assumptions

In addition to finite element analyses, limit equilibrium and limit analysis studies were included in the literature study. These are limited by the assumptions regarding the critical slip surface. Especially the LAM study restricted the slip surface to a toe failure, which is unlikely in a constant homogeneous undrained soil, unless the bottom boundary conditions are at a specific location. The studies using 3D LEM also assume the slip surface shape, however, optimisation procedures allow for accurate search of a critical failure mechanism. Nonetheless, these may deviate from a more natural circular slip surface, e.g. uneven and irregular surfaces as observed in Slide3.

The studies of a translational slide with drained conditions showed how important a correct earth pressure coefficient is. The coefficient is used to simulate side resistance using the Mohr-Coulomb failure criterion. A similar assumption is used in GS Stability when side shear resistance is activated. At-rest earth pressure coefficient K_0 may overestimate the safety factor, while active coefficient K_A may underestimate. Therefore, an initial evaluation of soil behaviour may be necessary. Moreover, finite element and finite difference analyses can be used as lower and upper bounds, respectively.

Chapter 9

Summary and Recommendations for Further Work

9.1 Summary

This master thesis consisted of a literature study, two-dimensional and three-dimensional numerical analyses. Earlier literature was used to locate and evaluate factors that impact the 3D-effects. The 2D simulations were used to find plane strain solutions and to study applicability of the side shear input in GeoSuite Stability. Moreover, brief 2D axisymmetric analyses were completed to simulate simple axisymmetric curvatures. Three-dimensional analyses were used to quantify and evaluate potential 3D-effects due to finite slope widths and curvatures.

Literature on 3D-effects and three-dimensional stability analysis have uncovered potentially significant effects. Several papers emphasised the importance of 3D analysis when the slope has three-dimensional characteristics that deviates from the plane strain assumption. Including 3D-effects may save construction costs and time, and an overestimated shear strength may be avoided in back-analysis. Finite slides may be a result of man-made structures, a transition between different soil properties or curvatures.

By fixing a planar slope to develop a finite width, the effect of narrower failure mechanisms can be found. Both undrained and drained analyses were reviewed in the literature studies, which revealed considerable 3D-effects reaching as high as 2.3 for lower values of the width-height ratio $w = W/H$. Flatter slopes provided increased stabilising effect, which further increased

more rapidly for narrower slides. Additionally, larger 3D-effects were observed for deeper slides. Earlier literature studied 3D slopes with various curvatures, such as turning corners or arches. Mostly positive effects were observed, especially for concave slopes. Certain convex curvatures had a negative impact, e.g for a vertical inclination. By varying arch radius, a trend of increased 3D-effect for reduced radius was observed. Moreover, sharper corner angles were more stable. In addition, 3D-effects appeared to be influenced by the drained strength parameters.

The 2D plane strain analyses conducted in this master project illustrated the functionality of the side shear input in GeoSuite Stability. The 3D-effects for a simulated finite width were significant and had a similar trend as found in literature. The plane strain FE calculations conducted in PLAXIS 2D proved useful in obtaining a realistic 2D slip surface, which could be transferred to LE software GS Stability.

PLAXIS 2D with an axisymmetric model was used to simulate simple convex and concave curvatures. Slightly greater stability was observed for the concave slopes. However, the 3D-effects increased more rapidly for the convex cases when the slope flattened. The 3D-effects for both curvature types ranged between approximately 1.04 and 1.16 when the relative radius $r = R/H$ was below 5. The safety factors approached the plane strain solutions as the radius increased.

3D simulations of a planar slope with fixed width were completed to evaluate the potential magnitude of 3D-effects. Significant effects were found, similar to findings in literature and with GS Stability. Safety factors from PLAXIS 3D gave 3D-effects that ranged from approximately 1.08 for $w = W/H = 6$ to 1.92 for $w = 1$. Safety factors increased more rapidly for decreased width, and greater 3D-effects were obtained for flatter slopes. In addition, a brief cohesion sensitivity analysis provided little influence.

3D-effects found in GS Stability with the BEAST method were slightly higher than the PLAXIS 3D findings. The optional side shear input in GS Stability is assumed acting on vertical sides, which overestimates the safety factor when compared with the more accurate curved or ellipsoidal end surfaces in PLAXIS 3D and Slide3. A slightly reduced input is therefore recommended.

The 3D LE program Slide3 with Morgenstern-Price is used to compare with 3D FEM. The method gives lower 3D-effects than PLAXIS 3D. Therefore, Slide3 may be useful in design with slightly conservative results. Moreover, the failure mechanisms differ slightly from PLAXIS, which may

be caused by LE assumptions or FE overshoot. The left plots in Figure 9.1 show the range of effects using PLAXIS 3D, GS Stability and Slide3 for $b = 1.5$ and $b = 3$.

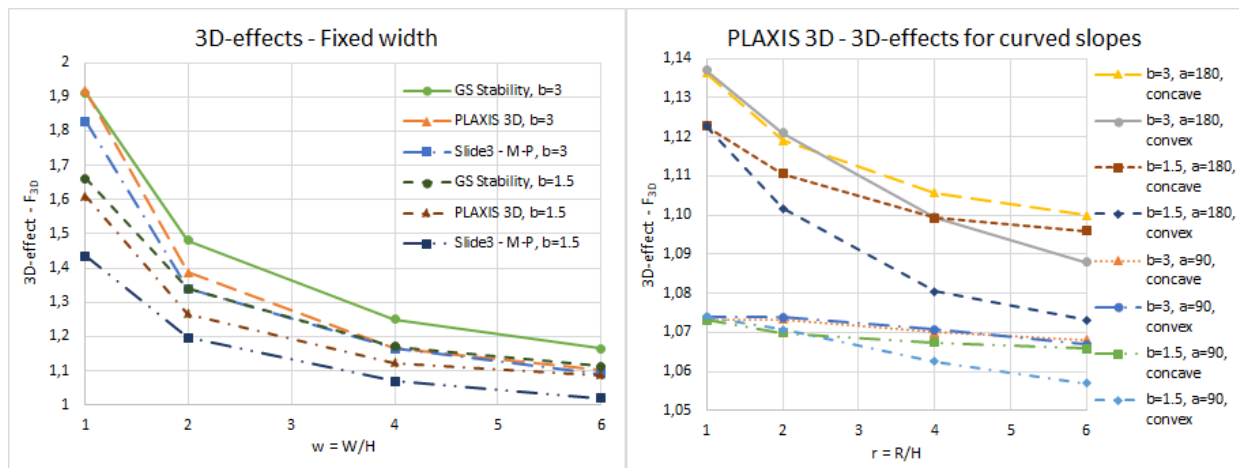


Figure 9.1: Selected plots illustrating potential 3D-effects for finite planar width (left) and curved slopes (right).

The three-dimensional simulations of curved slopes are completed to evaluate the influence of curvature. The slopes are modelled to simulate a ridge (convex) or valley (concave) along a more extensive slope system. All considered cases gave positive 3D-effects, and concave slopes were more stable than convex. Further, the difference between convex and concave curvatures increased for steeper inclination. However, the 3D-effects were greater for flatter slopes. Additionally, neighbouring curvature may have a restraining effect.

The defined curvature angle has a considerable impact on stability, with a similar trend as the axisymmetric analyses. A revolved arch of 180° was more sensitive to r and almost doubled the effects compared to 90° for some cases. More prominent, sharper and extensive curvatures provide increased stability. The plots to the right in Figure 9.1 illustrate the effect and sensitivity of curvature. The 3D-effects for $\alpha = 180^\circ$ ranged from approximately 1.07 to 1.14, while $\alpha = 90^\circ$ gave values ranging from just below 1.06 to just above 1.07.

The Sørkjosen slide from 2015 was evaluated considering potential 3D-effects. Idealised concave curvature was used to estimate the influence by simply revolving the 2D reference profile. The analyses suggested significant curvature effect, with $F_{3D} = 1.20$ for a fully revolved model. In addition to the idealised curvature, a full scale model was constructed using bathymetry. The large extent of the area and limited ground data diminished the model accuracy, and quantifica-

tion of 3D-effects was unreliable. Nonetheless, the finite failure mechanism indicated potential restraining effects.

Adequate accuracy in finite element analysis requires sufficiently fine discretisation. The safety factor may overshoot, which is exacerbated when boundary conditions are fixed. Moreover, the 3D safety analysis may struggle with convergence. An inherent false stiffness in elasto-plastic finite element analysis may prevent the soil from collapsing fully plastic.

The thesis analyses cover limited cases. As found in literature and the present study, 3D-effects can vary considerably depending on geometry and soil properties. Consequently, limitations include simulations using only undrained shear strength and only arch type curvature.

9.2 Conclusion

Literature and three-dimensional finite element simulations have revealed potentially significant 3D-effects. These are dependent and highly sensitive to various geometrical and geotechnical properties. All considered finite width and curved slope cases with undrained behaviour in the present thesis have shown stabilising effects. However, as found in literature on 3D-effects, convex curvature may be less stable than a planar or 2D slope. Moreover, 3D FE analyses may give erroneous results, such as an overshoot of safety factor.

The main objective of this master thesis was to evaluate and quantify the relationship between 2D and 3D slope stability analyses. Moreover, explore the possibility of simulating 3D-effects in 2D LE software GeoSuite Stability. Further, study how three-dimensional curvature and boundary conditions affect slope stability. The project research questions were defined as:

1. *What is the magnitude of 3D-effects for different slopes and curvatures in stability analysis?*

3D-effects F_{3D} are potentially significant, but can vary considerably. Planar slopes with a fixed width have shown that the safety factor may be doubled if the slide is narrow enough. Such restraints are rare, and the effects are reduced rapidly for increased width. Simulations of curved slopes may provide significant 3D-effects, especially for concave slopes with prominent curvature. The effects are less compared to the fixed width slope and can be negligible. The effects cannot be exactly quantified. However a minimum of 5% increase in stability may be considered in many cases for both curved and fixed width planar slopes.

If the attributes and characteristics of the slope indicate a possibility of a quite narrow finite slide, the 3D-effects may be considerable and a 3D analysis should be considered.

2. *How do geometric slope properties influence the 3D-effects and the failure mechanism?*

How geometric properties affect the 3D stability is dependent on the relation between the mobilised shear surface area and the driving slide mass. Increased stability is obtained if the geometric attribute reduces the sliding mass weight relatively more than the total shear surface area. A decrease in slope width w increases the 3D-effect, since the side shear area remains. Increased 3D-effects are obtained for flatter slopes, since the side shear surface area increases. A larger value of slide depth to slope height ratio d prolongs the shear surface, and thus increase the 3D side shear area. Moreover, the F_{3D} increase is more rapid for a flatter slope as the slide width decreases.

The degree of curvature is influential, and can be defined by relative radius r and angle of revolution α . Concave slopes have an arching effect that gives opposite forces and a restraining effect. Moderately inclined convex slopes have less driving mass near the crest. Decreased r leads to increased 3D-effect, since the mentioned convex and concave characteristics are enhanced. Greater α leads to a more prominent and extensive curvature that denies the slide of propagating wider.

3. *How can the side shear input in GeoSuite Stability be used to simulate the 3D slope stability problem in practice?*

The safety factors found with GS Stability using the side shear input as a function of slide width w were slightly too high compared to PLAXIS 3D. If the side shear factor is reduced it could be useful as a simple evaluation of the 3D safety factor. However, an estimate of the assumed slide width is required to quantify the side shear input, which may be difficult to obtain. The input should be used with great caution, especially for large values of the side shear factor.

The difference in 3D-effects between the curved slopes and the fixed widths is too large to see a connection. Moreover, it is hard to predict the finite slide widths due to curvature. Consequently, no apparent connection between curvature and the side shear input in GS Stability is observed.

9.3 Recommendations for Further Work

The analyses should extend to a broader set of soil cases. Drained conditions should undergo the same simulations to seek for any major differences in effect. Furthermore, various materials with different cohesiveness should be studied, since literature have suggested this as an affecting factor. Drained conditions and influence of groundwater should be properly investigated. Effect of natural groundwater should especially be assessed for concave and convex slopes, since the curvature may affect the water path.

As for the case study, the soil may be a mixture of various materials and drainage types. Knowledge about how complex layering may influence the 3D-effects can be important in geotechnical practice. How curvatures, such as turning corners or arches, affect complex stratification could be of significance. A material transfer within the slope could provide additional 3D restraining effect.

References

- Akhtar, K., & Stark, T. D. (2017). Importance of side resistance in a 3D stability analysis [Book Section]. In *Geotechnical frontiers 2017* (p. 285-293). Retrieved from <https://ascelibrary.org/doi/abs/10.1061/9780784480458.028> doi: 10.1061/9780784480458.028
- Arellano, D., & Stark, T. D. (2000). Importance of three-dimensional slope stability analyses in practice [Book Section]. In *Slope stability 2000* (p. 18-32). Retrieved from <https://ascelibrary.org/doi/abs/10.1061/40512%28289%292> doi: doi:10.1061/40512(289)2
- Brinkgreve, R. B. J., Kumarswamy, S., & Swolfs, W. M. (2018, 10). PLAXIS 3D 2018 [Computer software manual]. Delft, the Netherlands.
- Brinkgreve, R. B. J., Kumarswamy, S., Swolfs, W. M., Zampich, L., & Ragi Manoj, N. (2019, 10). PLAXIS 2D 2019 [Computer software manual]. Delft, the Netherlands.
- Cai, F., & Ugai, K. (2000). Numerical analysis of the stability of a slope reinforced with piles. *Soils and Foundations*. doi: 10.3208/sandf.40.73
- Cavounidis, S. (1987). On the ratio of factors of safety in slope stability analyses [Journal Article]. *Géotechnique*, 37(2), 207-210. Retrieved from <https://www.icevirtuallibrary.com/doi/abs/10.1680/geot.1987.37.2.207> doi: 10.1680/geot.1987.37.2.207
- Chaudhary, K., Domingos, V., Gitirana, G., Fredlund, M., & Lu, H. (2016). *Three-Dimensional Slope Stability: Geometry Effects*.
- Chen, Z., Mi, H., Zhang, F., & Wang, X. (2003). A simplified method for 3D slope stability analysis. *Canadian Geotechnical Journal*. doi: 10.1139/t03-002
- Chen, Z., Wang, X., Haberfield, C., Yin, J. H., & Wang, Y. (2001). A three-dimensional slope stability analysis method using the upper bound theorem Part I: Theory and methods. *International Journal of Rock Mechanics and Mining Sciences*. doi: 10.1016/S1365-1609(01)00012-0
- Cheng, Y. M., & Yip, C. J. (2007). Three dimensional asymmetrical slope stability analysis extension of Bishop's, Janbu's, and Morgenstern-Price's Techniques. *Journal of Geotechnical and Geoenvironmental Engineering*. doi: 10.1061/(ASCE)1090-0241(2007)133:12(1544)
- Damians, I. P., Bathurst, R., Josa, A., & Lloret, A. (2013). Comparison of finite element and finite difference modelling results with measured performance of a reinforced soil wall. In *Proceedings of géomontréal 2013. 66th*

canadian geotechnical conference.

- Duncan, J. M. (1996). State of the art: Limit equilibrium and finite-element analysis of slopes [Journal Article]. *Journal of Geotechnical Engineering*, 122(7), 577-596. Retrieved from [https://doi.org/10.1061/\(ASCE\)0733-9410\(1996\)122:7\(577\)](https://doi.org/10.1061/(ASCE)0733-9410(1996)122:7(577)) doi: 10.1061/(ASCE)0733-9410(1996)122:7(577)
- Duncan, J. M., Wright, S. G., & Brandon, T. L. (2014). *Soil strength and slope stability* (Second. ed.) [Book].
- Fredlund, D. G., & Krahn, J. (1977). COMPARISON OF SLOPE STABILITY METHODS OF ANALYSIS. *Canadian Geotechnical Journal*. doi: 10.1139/t77-045
- Fredlund, D. G., Krahn, J., & Pufahl, D. E. (1981). The relationship between limit equilibrium slope stability methods. *Soil mechanics and foundation engineering. Proc. 10th international conference, Stockholm, June 1981. Vol. 3, (A.A.Balkema)*. doi: 10.1016/0148-9062(84)91799-6
- Gens, A., Hutchinson, J. N., & Cavounidis, S. (1988). Three-dimensional analysis of slides in cohesive soils. *Geotechnique*. doi: 10.1680/geot.1988.38.1.1
- Griffiths, D., & Lane, P. A. (1999). Slope stability analysis by finite elements. *geotechnique*, 49(3): 387-403 [Journal Article]. *Geotechnique*, 49, 387-403. doi: 10.1680/geot.1999.49.3.387
- Griffiths, D., & Marquez, R. (2007). Three-dimensional slope stability analysis by elasto-plastic finite elements [Journal Article]. *Geotechnique*, 57(6), 537-546.
- Grimstad, G., Andresen, L., & Jostad, H. P. (2011). NGI-ADP: Anisotropic shear strength model for clay. *International Journal for Numerical and Analytical Methods in Geomechanics*. doi: 10.1002/nag.1016
- Huang, C. C., Tsai, C. C., & Chen, Y. H. (2002). Generalized method for three-dimensional slope stability analysis. *Journal of Geotechnical and Geoenvironmental Engineering*. doi: 10.1061/(ASCE)1090-0241(2002)128:10(836)
- ITASCA. (2008). FLAC - fast lagrangian analysis of continua, user's guide [Computer software manual]. Minneapolis, USA.
- Janbu, N. (1954). *Stability analysis of slopes with dimensionless parameters*. Cambridge MA: Harvard University Press.
- Jostad, H., & Lacasse, S. (2015). 3D effects in undrained slope stability analysis of clays [Book Section]. In *Geotechnical engineering for infrastructure and development* (p. 1573-1578). Retrieved from <https://www.icevirtuallibrary.com/doi/abs/10.1680/ecsmge.60678.vol14.231> doi: 10.1680/ecsmge.60678.vol14.231
- Kalatehjari, R., & Ali, N. (2013). A review of three-dimensional slope stability analyses based on limit equilibrium method [Journal Article]. *EJGE*, 18, 119-134.
- Kelesoglu, M. K. (2015). The evaluation of three-dimensional effects on slope stability by the strength reduction method [Journal Article]. *KSCE Journal of Civil Engineering*, 20(1), 229-242. Retrieved from <https://doi.org/10.1007/s12205-015-0686-4> doi: 10.1007/s12205-015-0686-4
- Lam, L., & Fredlund, D. G. (1993). A general limit equilibrium model for three-dimensional slope stability analysis. *Canadian Geotechnical Journal*. doi: 10.1139/t93-089

- Leshchinsky, D. O. V., & Baker, R. (1986). Three-dimensional slope stability : End effects [Journal Article]. *SOILS AND FOUNDATIONS*, 26(4), 98-110. doi: 10.3208/sandf1972.26.4_98
- Michalowski, R. L., & Drescher, A. (2009). Three-dimensional stability of slopes and excavations. *Geotechnique*. doi: 10.1680/geot.8.P.136
- Morgenstern, N. R., & Price, V. E. (1965). The analysis of the stability of general slip surfaces. *Geotechnique*. doi: 10.1680/geot.1965.15.1.79
- Nian, T. K., Huang, R. Q., Wan, S. S., & Chen, G. Q. (2012). Three-dimensional strength-reduction finite element analysis of slopes: geometric effects [Journal Article]. *Canadian Geotechnical Journal*, 49(5), 574-588. Retrieved from <https://doi.org/10.1139/t2012-014> doi: 10.1139/t2012-014
- Nordal, S., & Antonsen, P. (1985). Plastic collapse loads by the finite element method [Conference Proceedings]. In *International conference on soil mechanics and foundation engineering*. 11 (pp. 603–606). A.A.Balkema.
- Nordal, S., L'Heureux, J., Skotheim, A., Emdal, A., Lyche, E., & Christensen, S. (2016). *Skredet i Sørkjosen 10. mai 2015* (Rapport No. 01).
- NVE. (2014). *Sikkerhet mot kvikkleireskred* (Veileder No. 7- 2014). Retrieved from http://publikasjoner.nve.no/veileder/2014/veileder2014_07.pdf
- Rocscience. (2017). Slide3 - 3D limit equilibrium slope stability overview [Computer software manual]. Toronto, Canada. Retrieved from https://www.rocscience.com/help/slide3/pdf_files/theory/3D_Limit_Equilibrium_Slope_Stability.pdf
- Rocscience. (2019, 2). Surface search in Slide3 - principles and practices [Computer software manual]. Toronto, Canada. Retrieved from [https://www.rocscience.com/help/slide3/pdf_files/Surface_Search_in_Slide3_\(principles_and_practices\).pdf](https://www.rocscience.com/help/slide3/pdf_files/Surface_Search_in_Slide3_(principles_and_practices).pdf)
- Solli, V. A. (2019). *Evaluation of 3D-effects in slope stability analysis - use of side shear input in GeoSuite Stability*. Norwegian University of Science and Technology, Trondheim. (Project thesis)
- Stark, T. D., & Eid, H. T. (1998). Performance of three-dimensional slope stability methods in practice [Journal Article]. *Journal of Geotechnical and Geoenvironmental Engineering*, 124(11), 1049-1060. Retrieved from [https://doi.org/10.1061/\(ASCE\)1090-0241\(1998\)124:11\(1049\)](https://doi.org/10.1061/(ASCE)1090-0241(1998)124:11(1049)) doi: 10.1061/(ASCE)1090-0241(1998)124:11(1049)
- Sun, C., Chai, J., Xu, Z., & Qin, Y. (2017). 3D stability charts for convex and concave slopes in plan view with homogeneous soil based on the strength-reduction method [Journal Article]. *International Journal of Geomechanics*, 17(5), 06016034. Retrieved from [https://doi.org/10.1061/\(ASCE\)GM.1943-5622.0000809](https://doi.org/10.1061/(ASCE)GM.1943-5622.0000809) doi: 10.1061/(ASCE)GM.1943-5622.0000809
- Trimble. (2018, 1). Novapoint GeoSuite toolbox stability help [Computer software manual]. Stockholm, Sweden.
- Tschuchnigg, F., Schweiger, H. F., Sloan, S. W., Lyamin, A. V., & Raissakis, I. (2015). Comparison of finite-element limit analysis and strength reduction techniques. *Geotechnique*. doi: 10.1680/geot.14.P.022
- Wei, W. B., & Cheng, Y. M. (2009). Strength reduction analysis for slope reinforced with one row of piles. *Computers and Geotechnics*. doi: 10.1016/j.compgeo.2009.05.004

- Wei, W. B., Cheng, Y. M., & Li, L. (2009). Three-dimensional slope failure analysis by the strength reduction and limit equilibrium methods [Journal Article]. *Computers and Geotechnics*, 36(1), 70-80. Retrieved from <http://www.sciencedirect.com/science/article/pii/S0266352X08000384> doi: <https://doi.org/10.1016/j.compgeo.2008.03.003>
- Won, J., You, K., Jeong, S., & Kim, S. (2005). Coupled effects in stability analysis of pile-slope systems. *Computers and Geotechnics*. doi: 10.1016/j.compgeo.2005.02.006
- Xing, Z. (1988). Three-dimensional stability analysis of concave slopes in plan view. *Journal of Geotechnical Engineering*. doi: 10.1061/(ASCE)0733-9410(1988)114:6(658)
- Yu, H. S., Salgado, R., Sloan, S. W., & Kim, J. M. (1998). Limit analysis versus limit equilibrium for slope stability. *Journal of Geotechnical and Geoenvironmental Engineering*. doi: 10.1061/(ASCE)1090-0241(1998)124:1(1)
- Zhang, L. L., Fredlund, M. D., Fredlund, D. G., Lu, H., & Wilson, G. W. (2015). The influence of the unsaturated soil zone on 2-D and 3-D slope stability analyses [Journal Article]. *Engineering Geology*, 193, 374-383. Retrieved from <http://www.sciencedirect.com/science/article/pii/S0013795215001659> doi: <https://doi.org/10.1016/j.enggeo.2015.05.011>
- Zhang, Y., Chen, G., Zheng, L., Li, Y., & Zhuang, X. (2013). Effects of geometries on three-dimensional slope stability [Journal Article]. *Canadian Geotechnical Journal*, 50(3), 233-249. Retrieved from <https://doi.org/10.1139/cgj-2012-0279> doi: 10.1139/cgj-2012-0279

Appendix A

Model and Parameter Definition

A.1 PLAXIS Model and Calculation Definition

Table A.1: PLAXIS model definitions.

Model type	Plane strain	Axisymmetric	3D
Program	PLAXIS 2D	PLAXIS 2D	PLAXIS 3D
Element type	Triangular 15-noded	Triangular 15-noded	Tetrahedral 10-noded

Calculation Phases for PLAXIS 2D Simulations

ID	Calculation t...	Loading type...	Pore pressur...	Time interval	Estimated en...	Ignore undr....	Reset displa...	Updated me...	Max steps (D)	First step	Last step
Gravity loading [InitialPhase]	Gravity loading	Staged construction	0 day	0 day	<input checked="" type="checkbox"/>	<input type="checkbox"/>	<input type="checkbox"/>	<input type="checkbox"/>	1000	0	3
Safety analysis [Phase_1]	Safety	Incremental multipli	0 day	0 day	<input type="checkbox"/>	<input checked="" type="checkbox"/>	<input type="checkbox"/>	<input type="checkbox"/>	100	4	103

Figure A.1: Phases run in PLAXIS 2D to obtain failure mechanism and SF.

Calculation Phases for PLAXIS 3D Simulations

ID	Calculation t...	Loading type...	Pore pressur...	Time interval	Estimated en...	Ignore undr....	Reset displa...	Updated me...	Max steps (D)	First step	Last step	
Gravity loading [InitialPhase]				0,000 day	0,000 day	<input checked="" type="checkbox"/>	<input type="checkbox"/>	<input type="checkbox"/>		1000	101	104
Restrain side surface [Phase_1]				0,000 day	0,000 day	<input type="checkbox"/>	<input checked="" type="checkbox"/>	<input type="checkbox"/>		1000	105	109
Safety analysis [Phase_2]				0,000 day	0,000 day	<input type="checkbox"/>	<input type="checkbox"/>	<input type="checkbox"/>		100	0	99

Figure A.2: Phases run in PLAXIS 3D to obtain failure mechanism and SF for a planar slope with fixed width.

ID	Calculation t...	Loading type...	Pore pressur...	Time interval	Estimated en...	Ignore undr...	Reset displa...	Updated me...	Max steps (D)	First step	Last step
Gravity loading [InitialPhase]				0,000 day	0,000 day	<input checked="" type="checkbox"/>	<input type="checkbox"/>	<input type="checkbox"/>	1000	0	3
Safety analysis [Phase_1]				0,000 day	0,000 day	<input type="checkbox"/>	<input checked="" type="checkbox"/>	<input type="checkbox"/>	100	4	103

Figure A.3: Phases run in PLAXIS 3D to obtain failure mechanism and SF for a curved slope.

A.2 PLAXIS 2D/3D Parameters

Table A.2: Relevant soil parameters in the Mohr-Coulomb model with *Undrained B*.

Parameter description	Value
Soil unit weight, $\gamma_{sat} = \gamma_{unsat}$	19 kN/m ³
Young's modulus, E	10000 kN/m ²
Poisson's ratio, ν	0.3
Reference undrained shear strength, $S_{u,ref}$	20 kN/m ²
Inclination of undrained shear strength, $S_{u,inc}$	2 kN/m ² /m
Reference elevation for S_u -profile, y_{ref}	0 m

A.3 GeoSuite Stability Parameters

Table A.3: Relevant soil parameters for undrained analysis in GS Stability.

Parameter description	Value
Soil unit weight, ρ	19 kN/m ³
Submerged soil unit weight, ρ'	9 kN/m ³
Undrained analysis, with cohesion $c = S_u$	20 + 2z kN/m ²
Reference point for c -profile	(x = 0, z = 0)

A.4 Slide3 Parameters

Table A.4: Relevant soil parameters for undrained analysis in Slide3.

Parameter description	Value
Soil unit weight, γ	19 kN/m ³
Undrained strength profile, $c = S_u$	20 + 2z kN/m ²

Appendix B

PLAXIS 2D Results

B.1 Safety Analysis

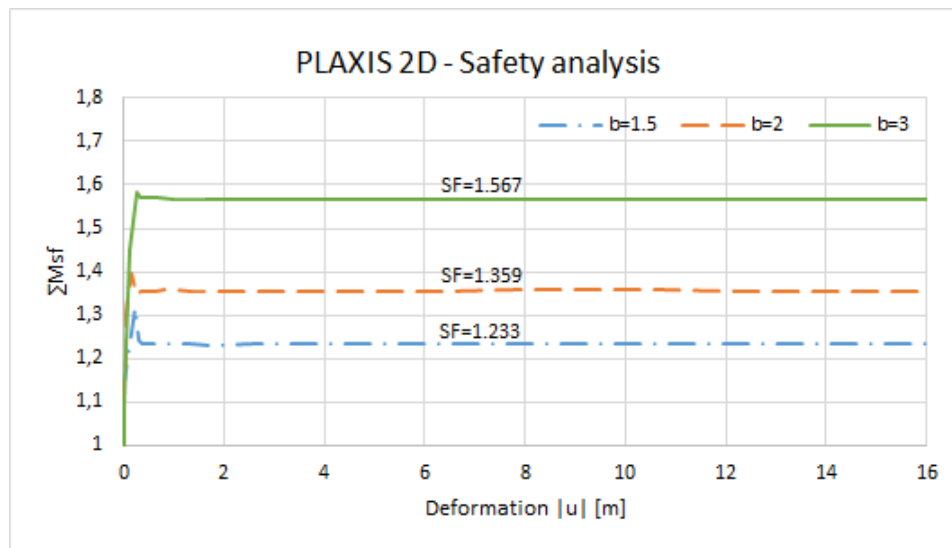
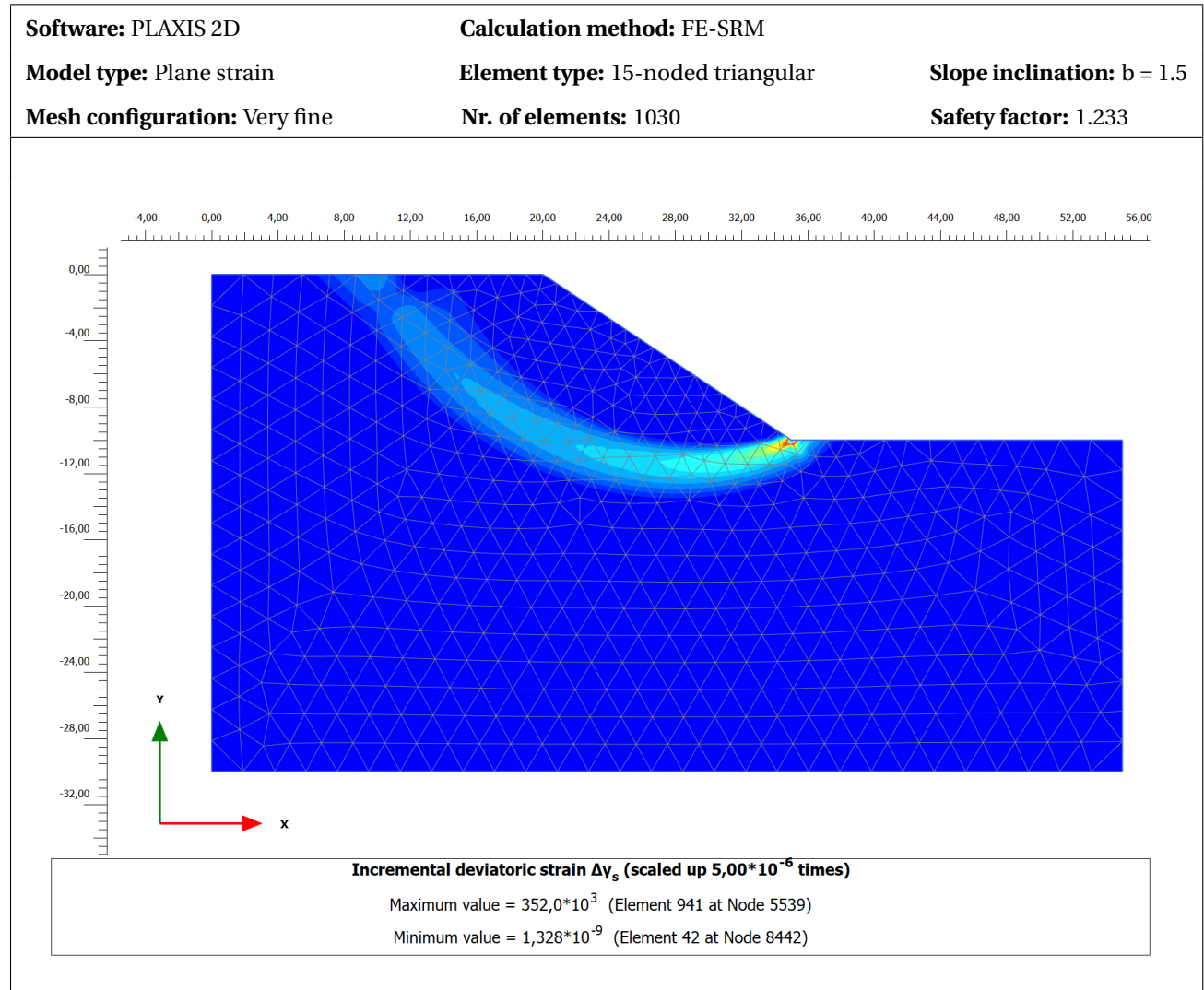


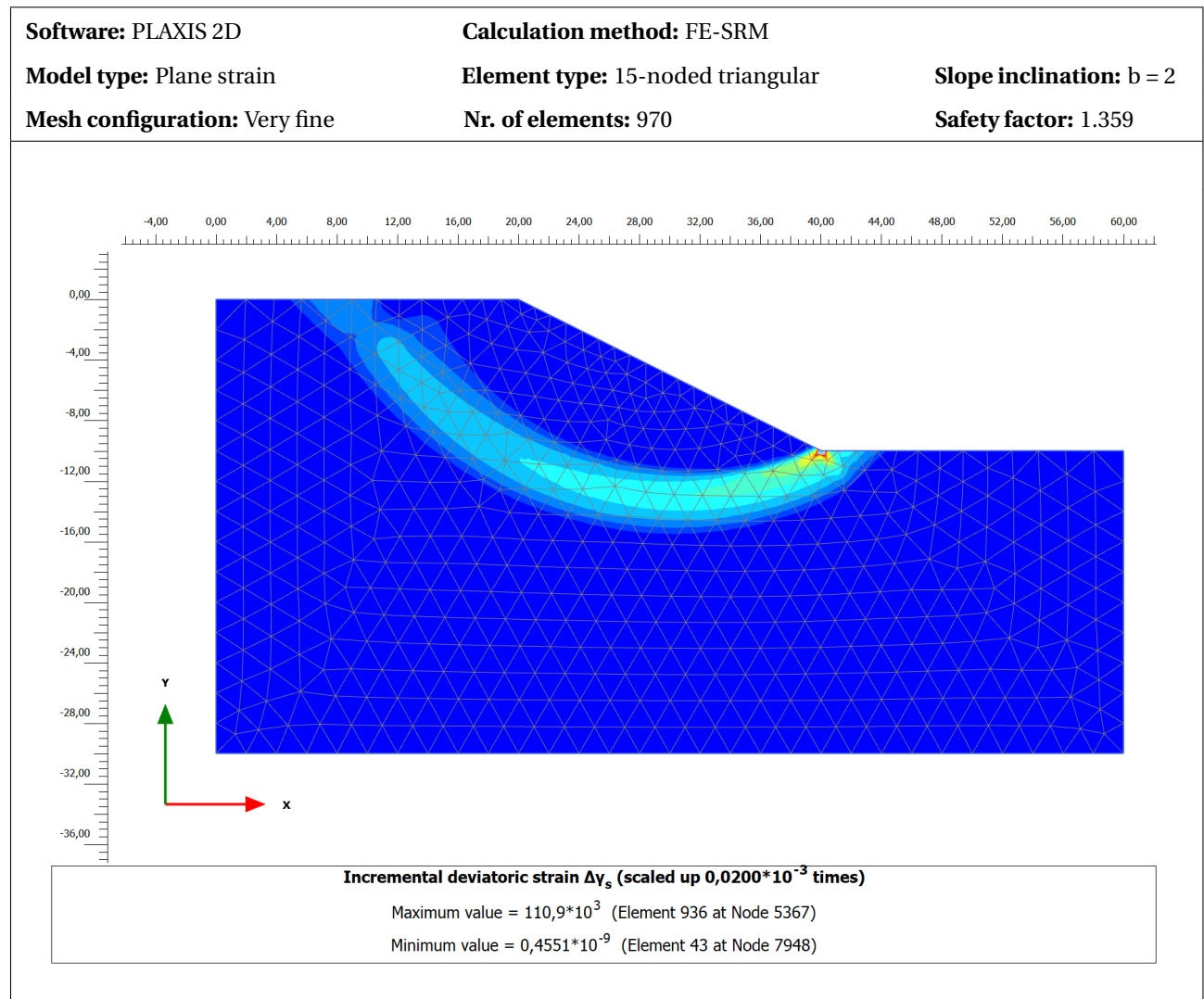
Figure B.1: Result from safety analysis conducted in PLAXIS 2D.

B.2 Failure Mechanism

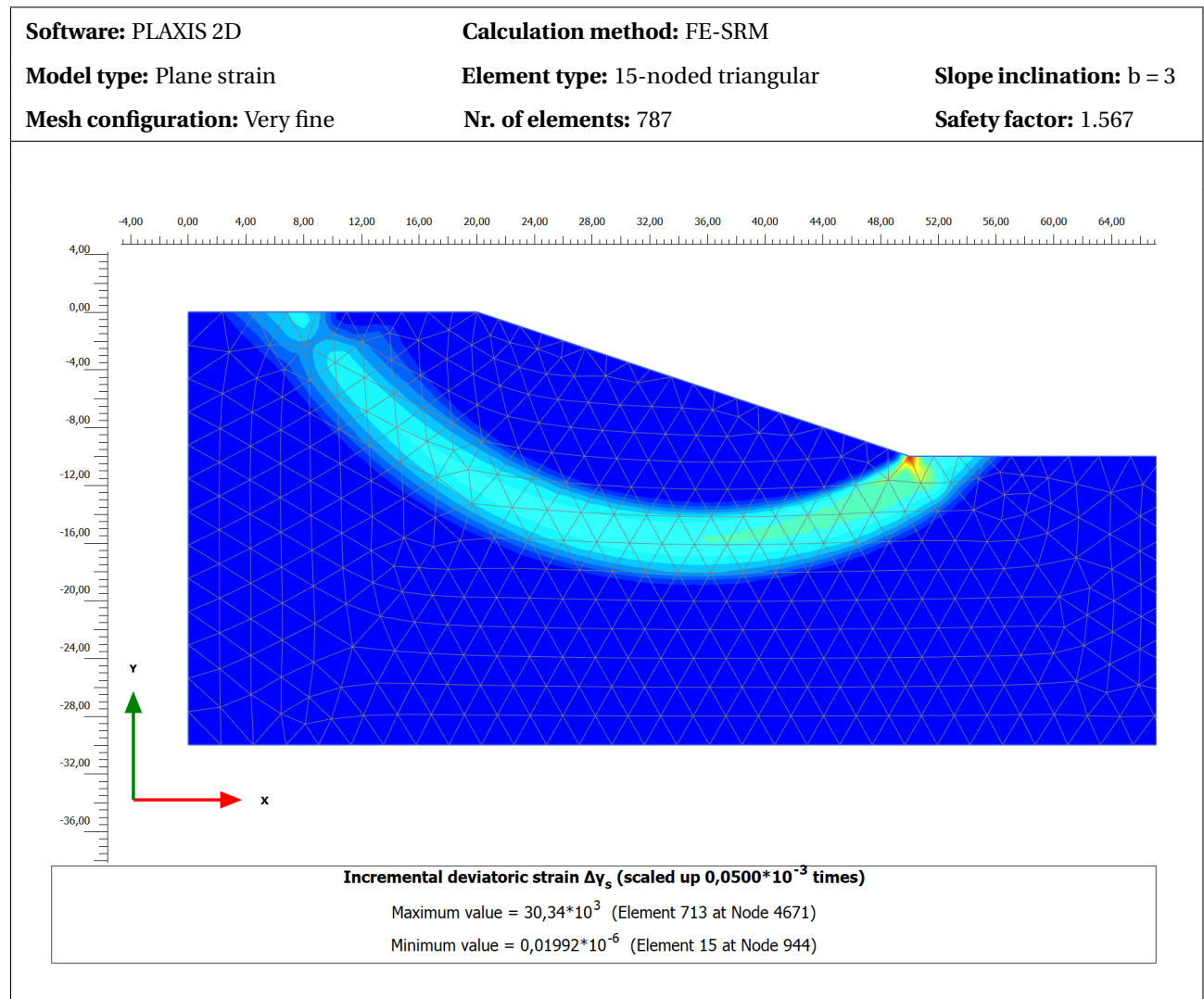
Inclination $b=1.5$



Inclination b=2



Inclination b=3

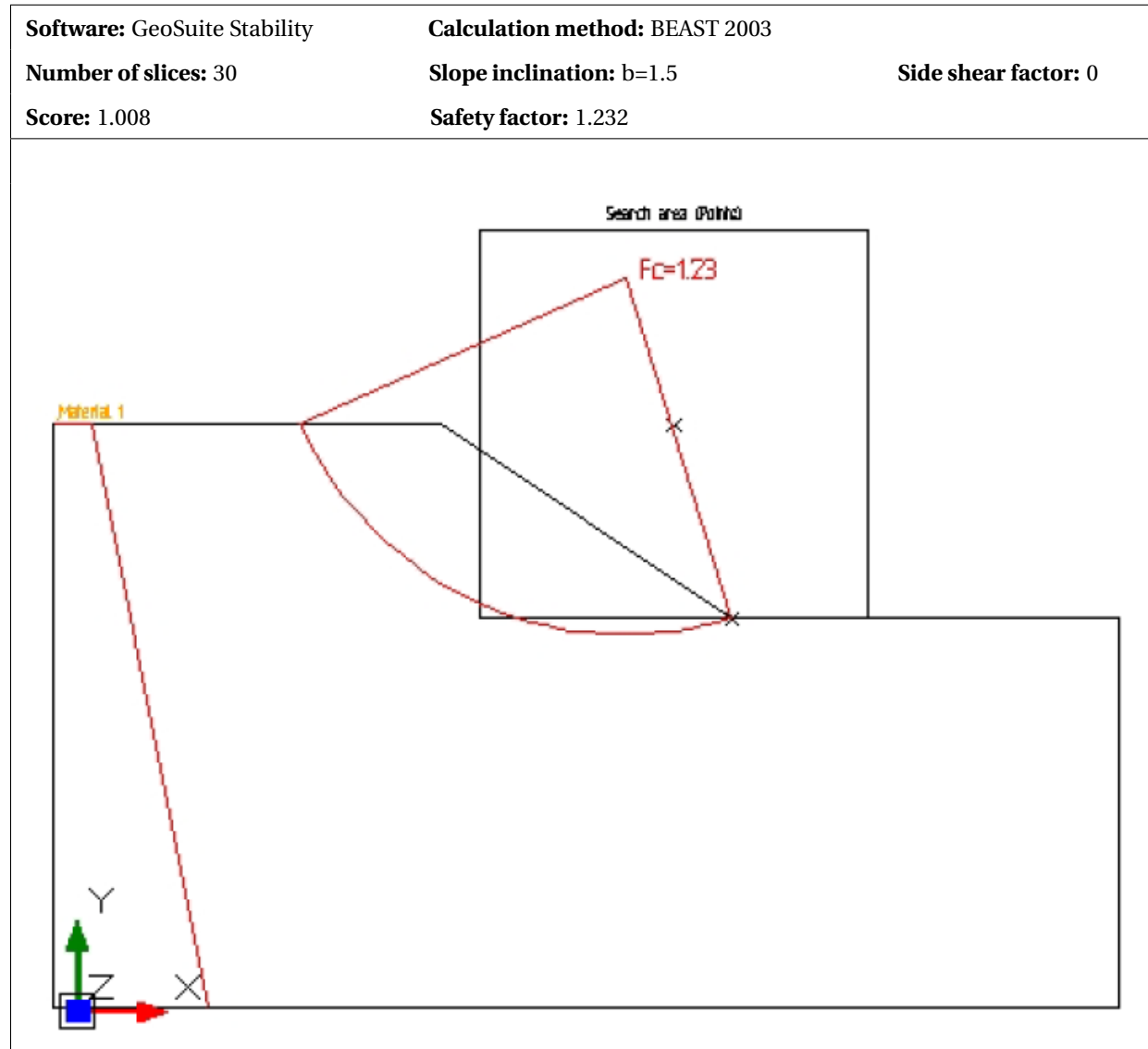


Appendix C

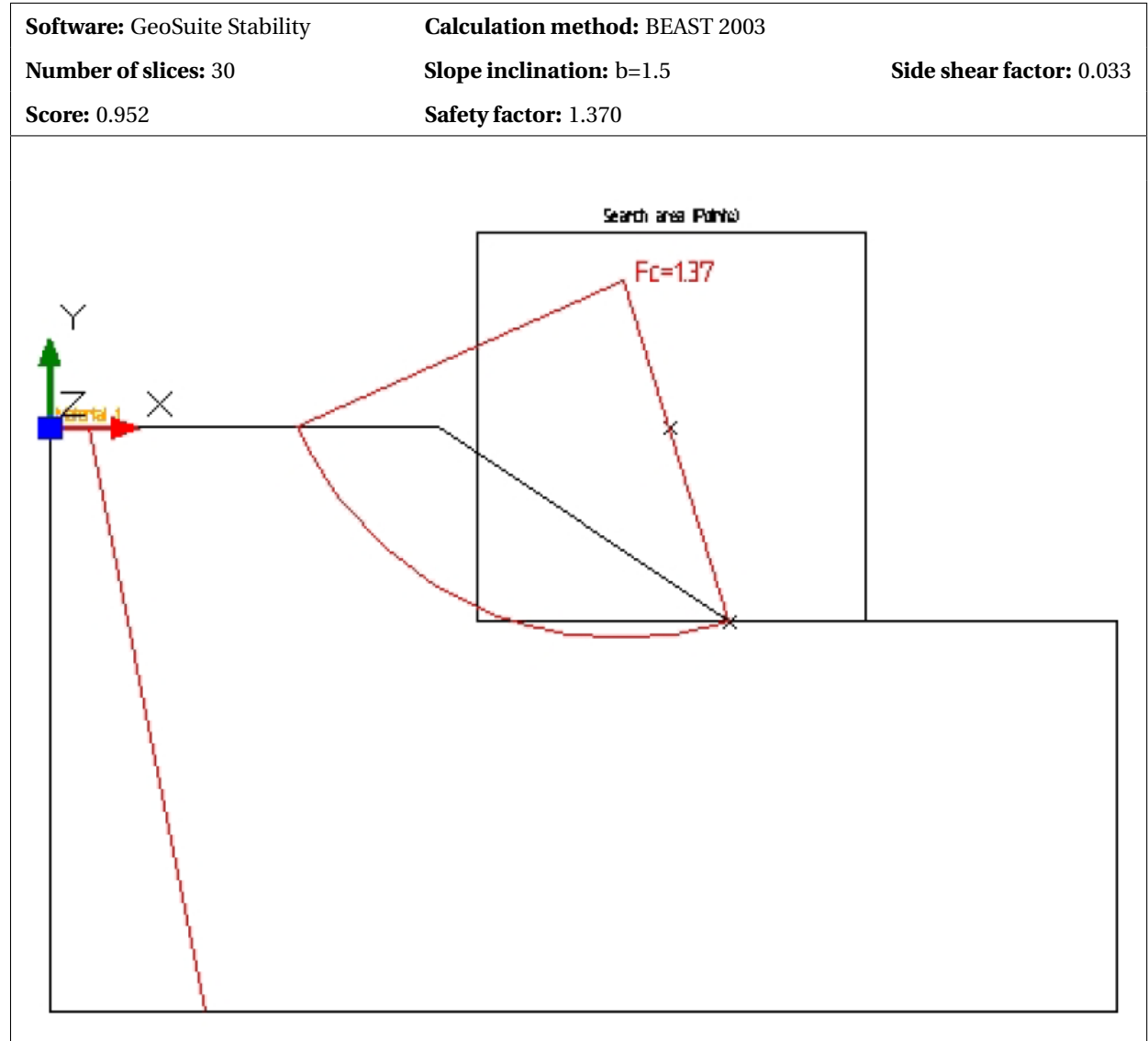
GeoSuite Stability Failure Mechanism

C.1 Case 1 - b=1.5

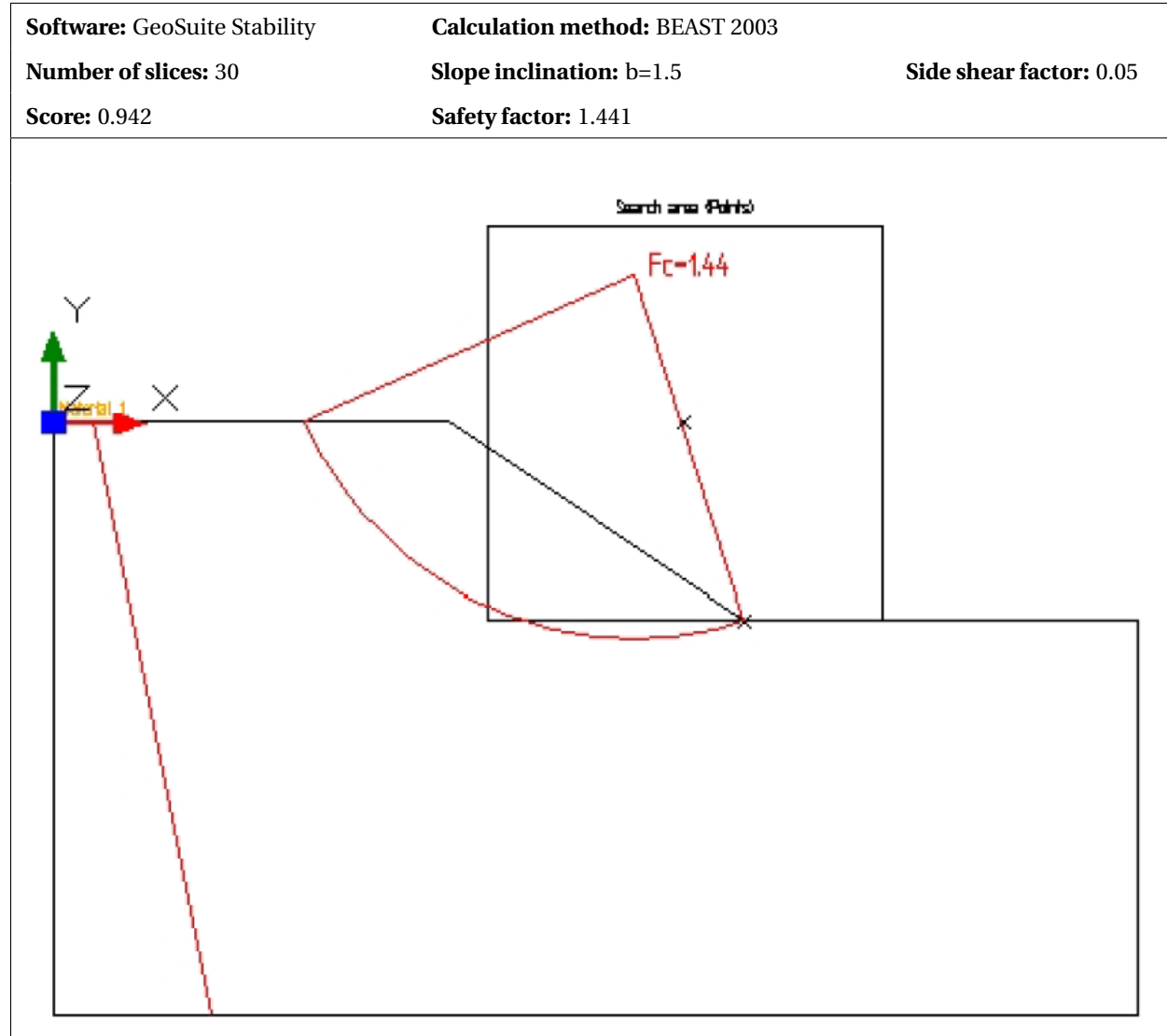
Infinite Slope Width



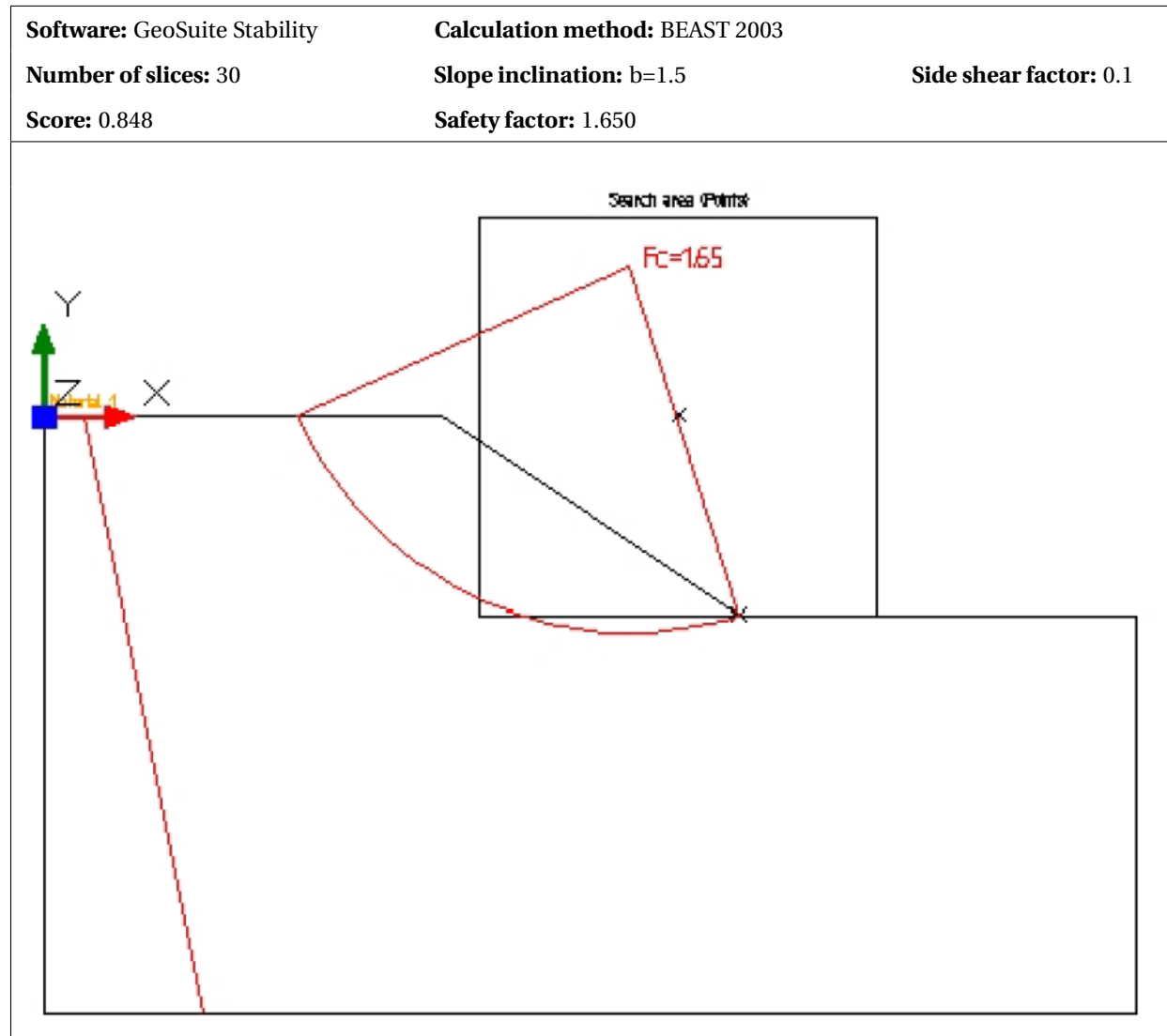
Simulation of $w=6$



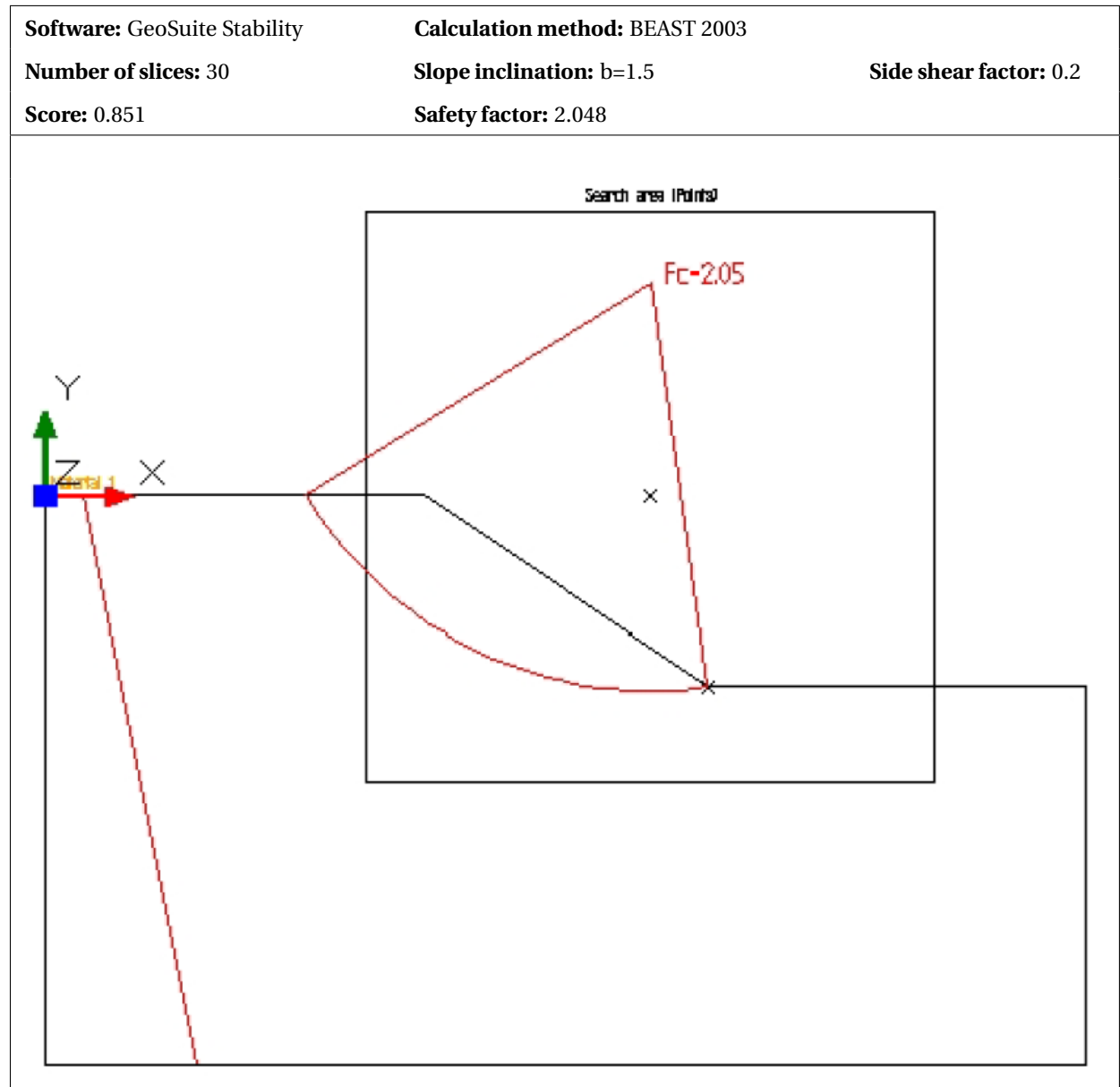
Simulation of $w=4$



Simulation of $w=2$

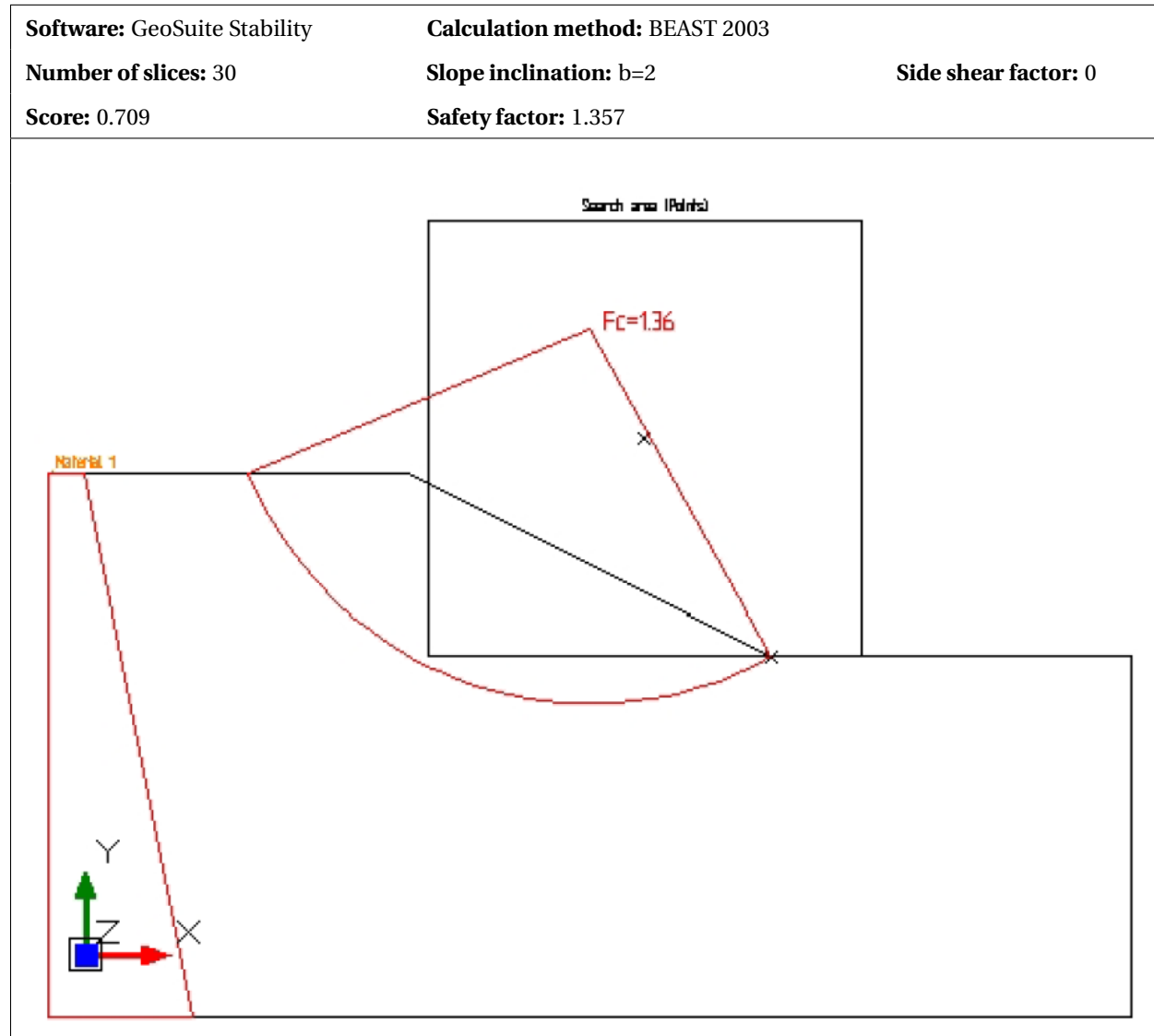


Simulation of $w=1$

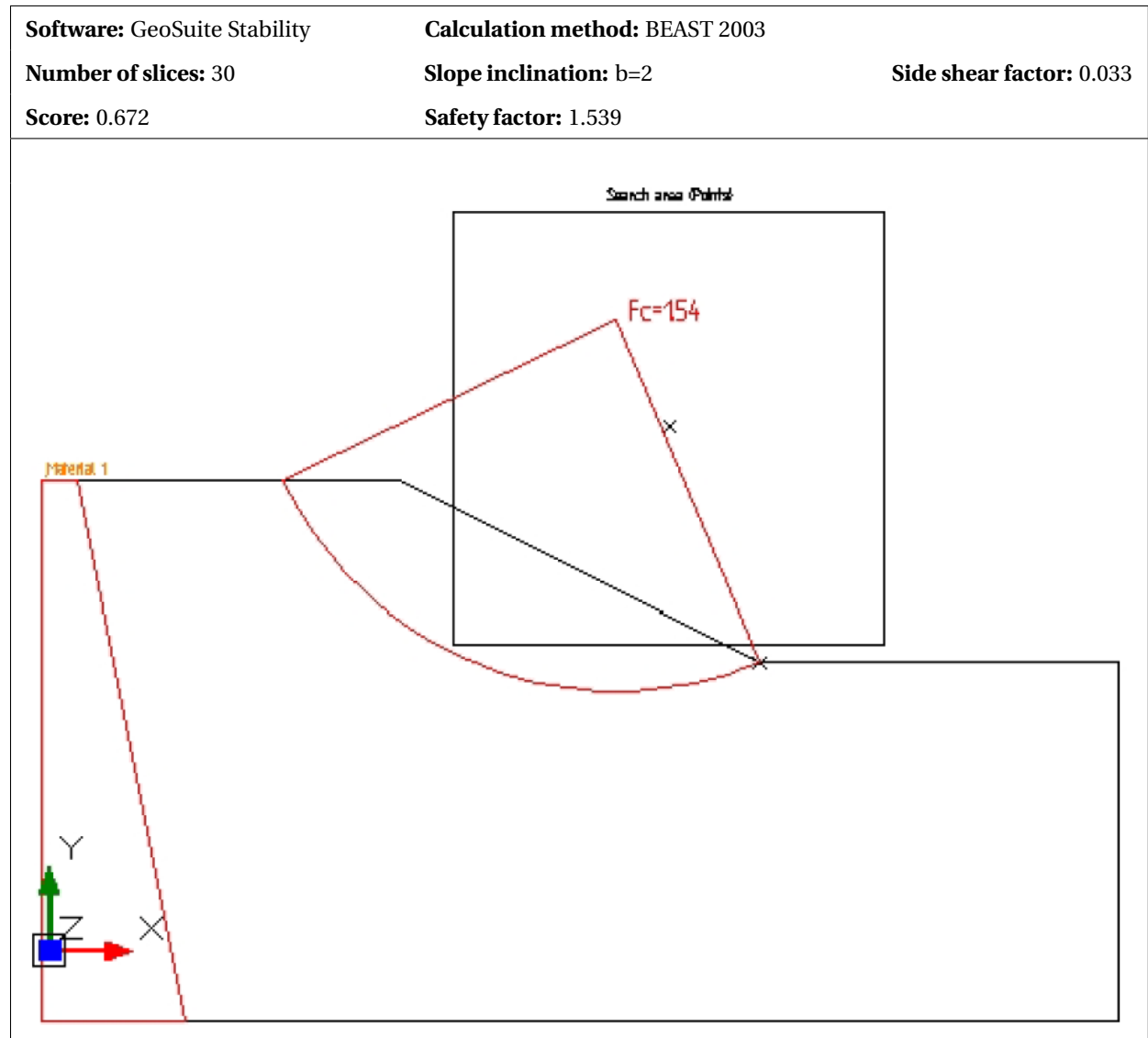


C.2 Case 2 - b=2

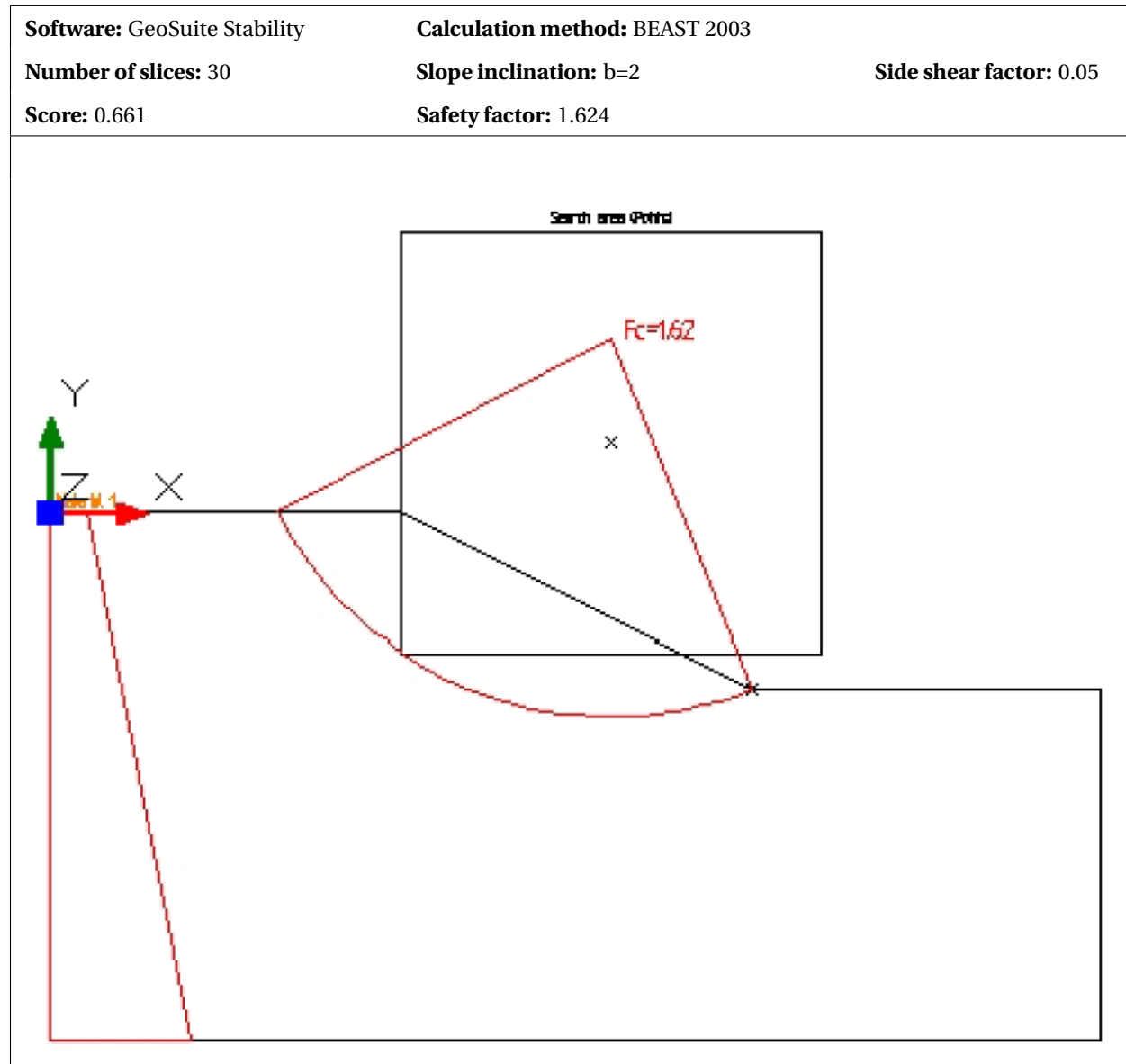
Infinite Slope Width



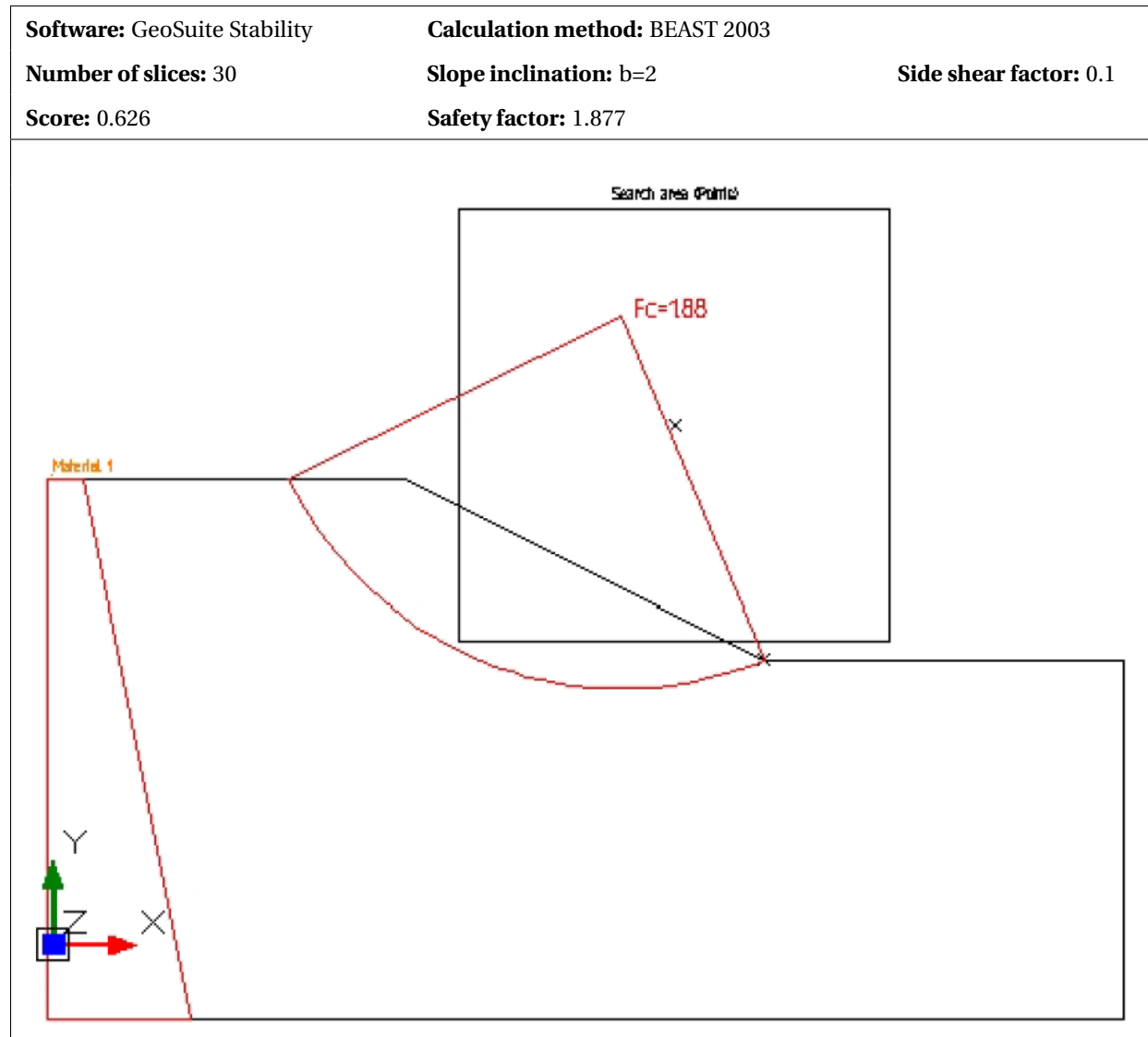
Simulation of w=6



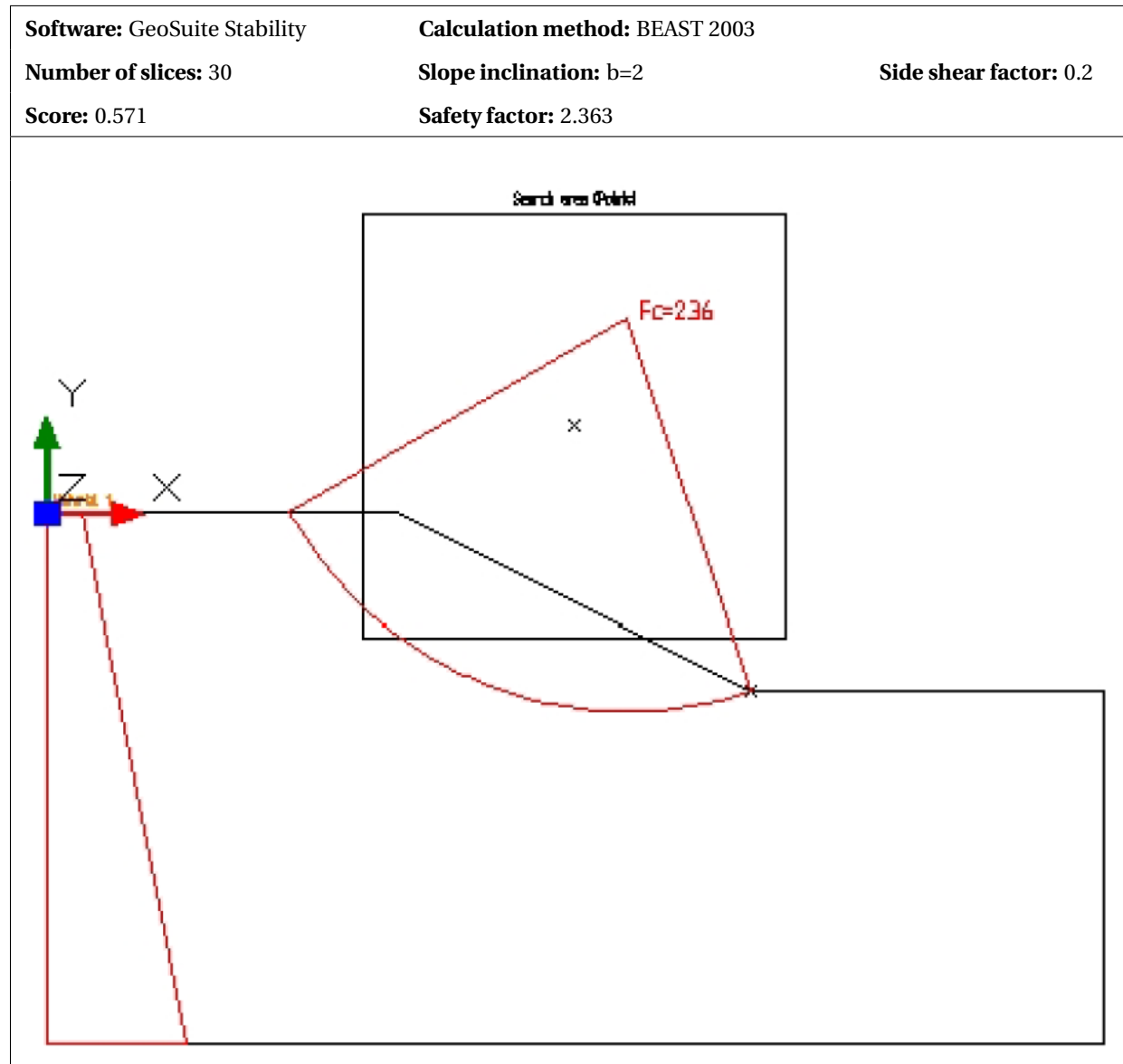
Simulation of $w=4$



Simulation of $w=2$

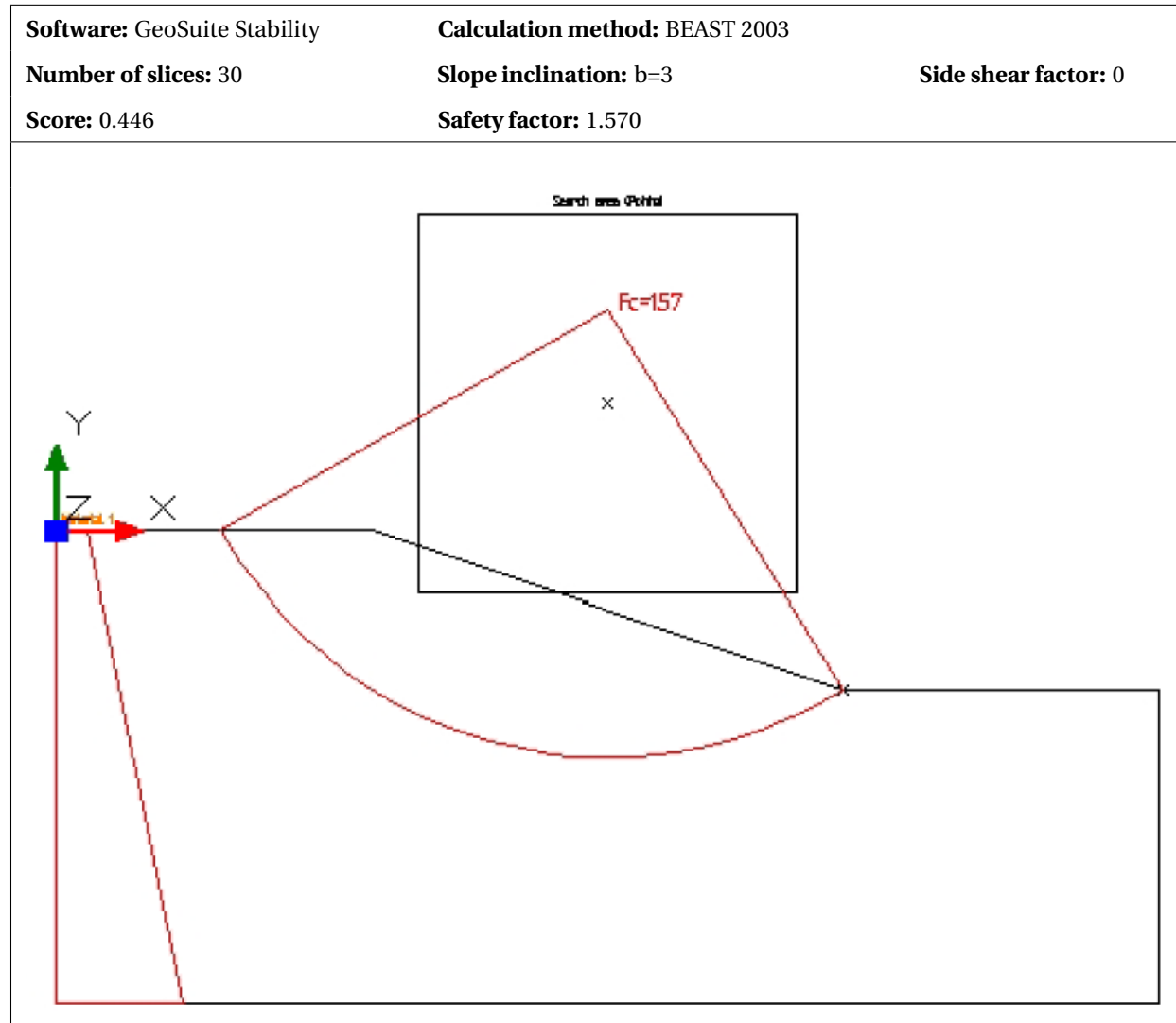


Simulation of $w=1$

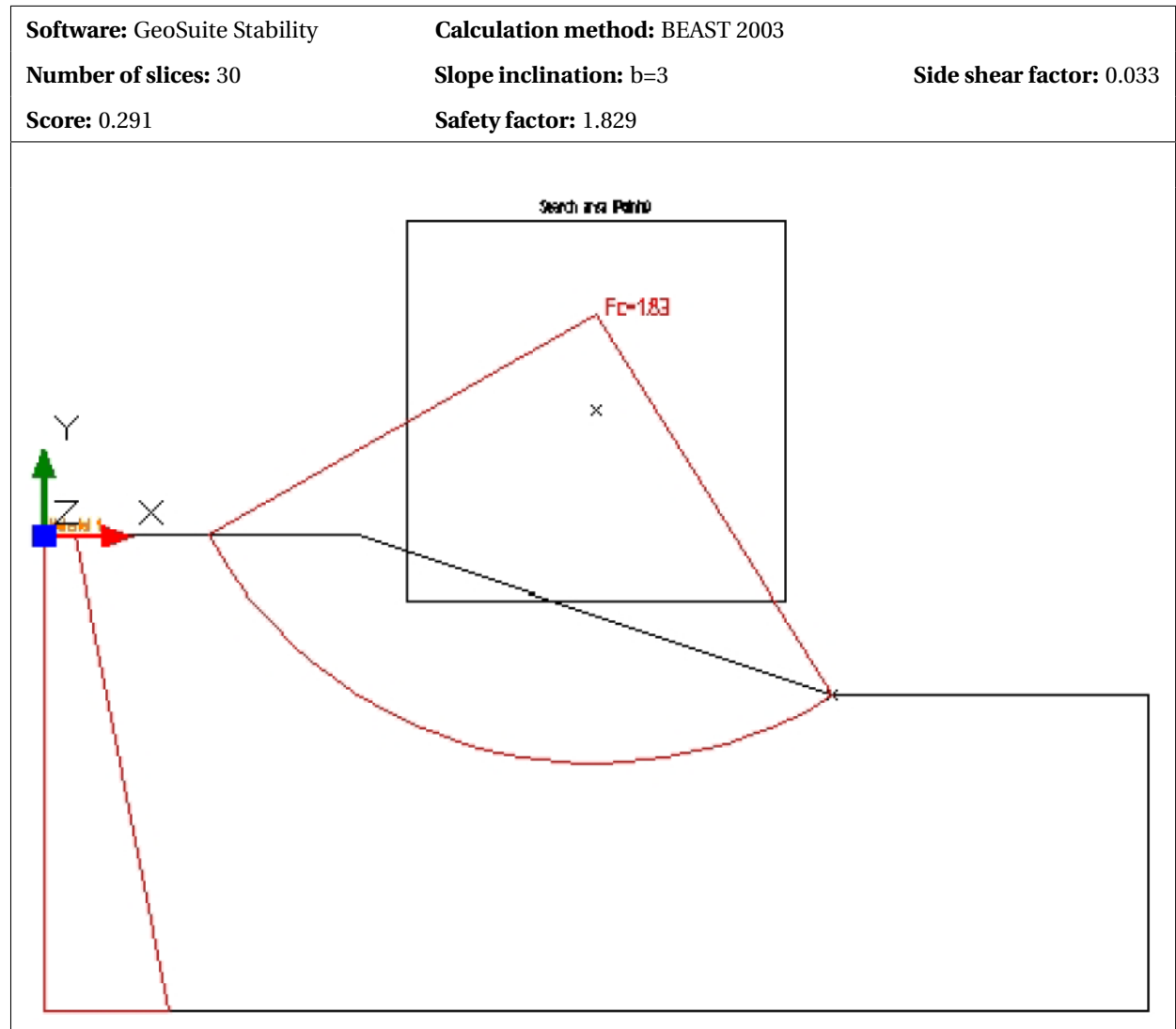


C.3 Case 3 - b=3

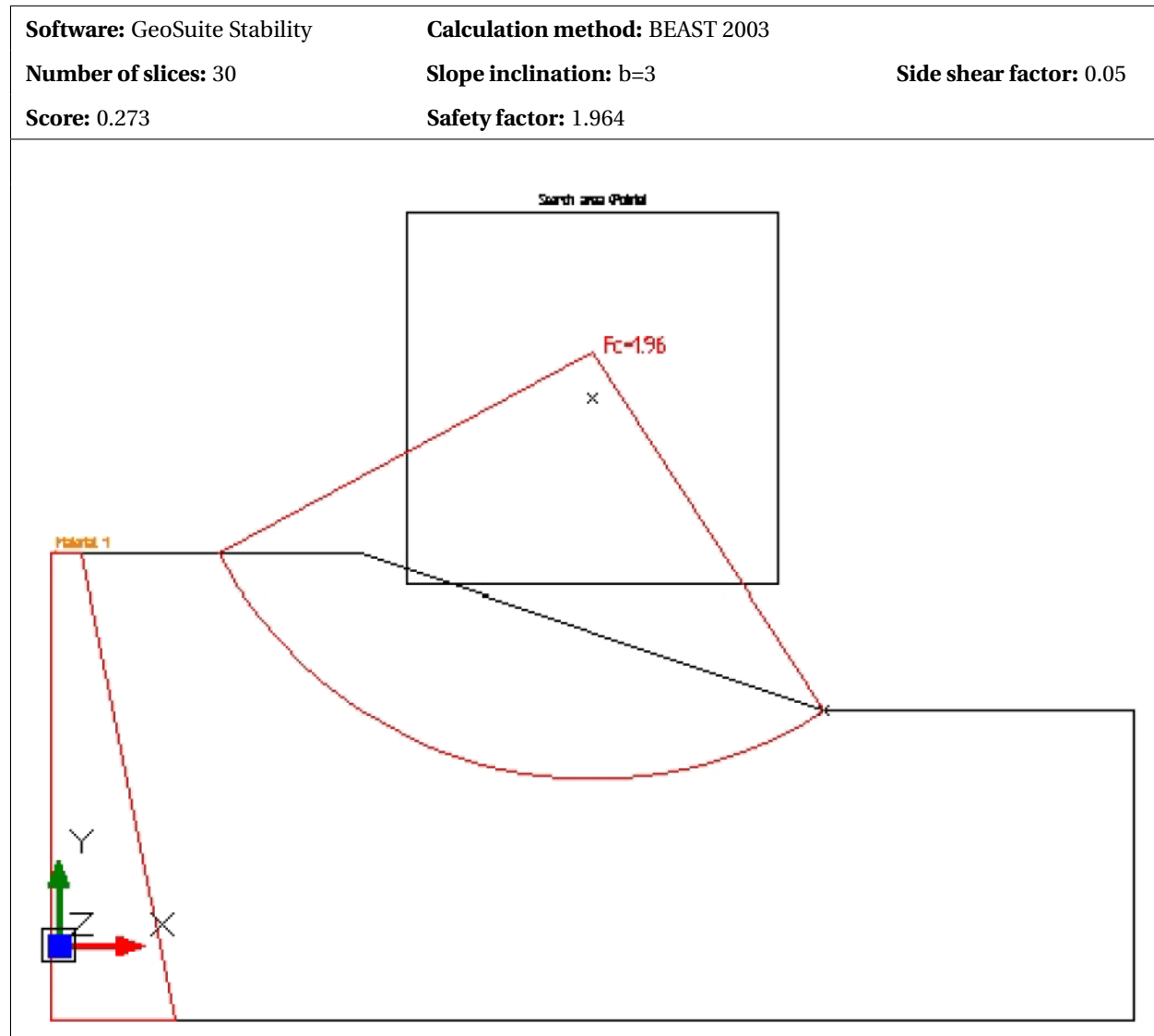
Infinite Slope Width



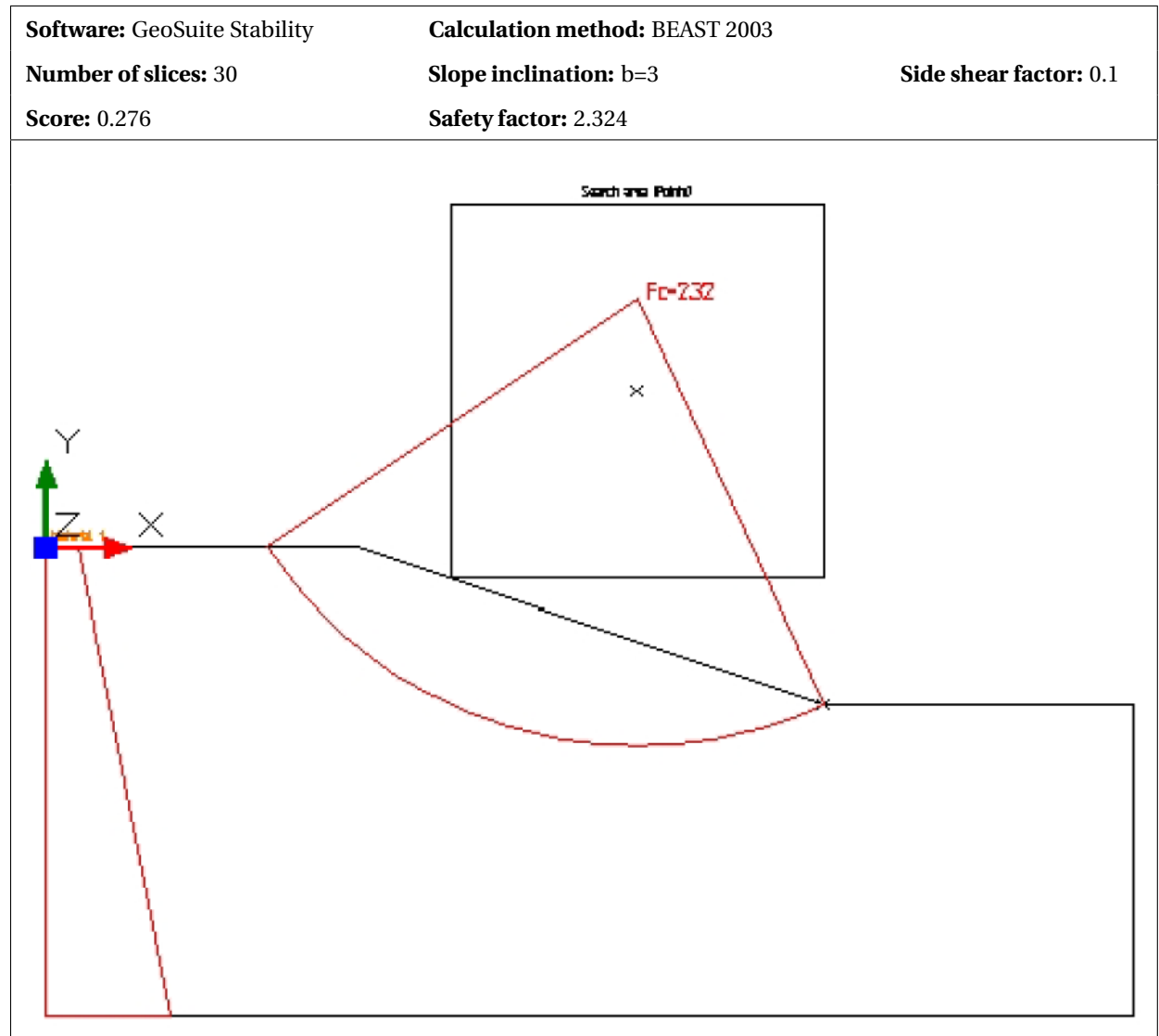
Simulation of $w=6$



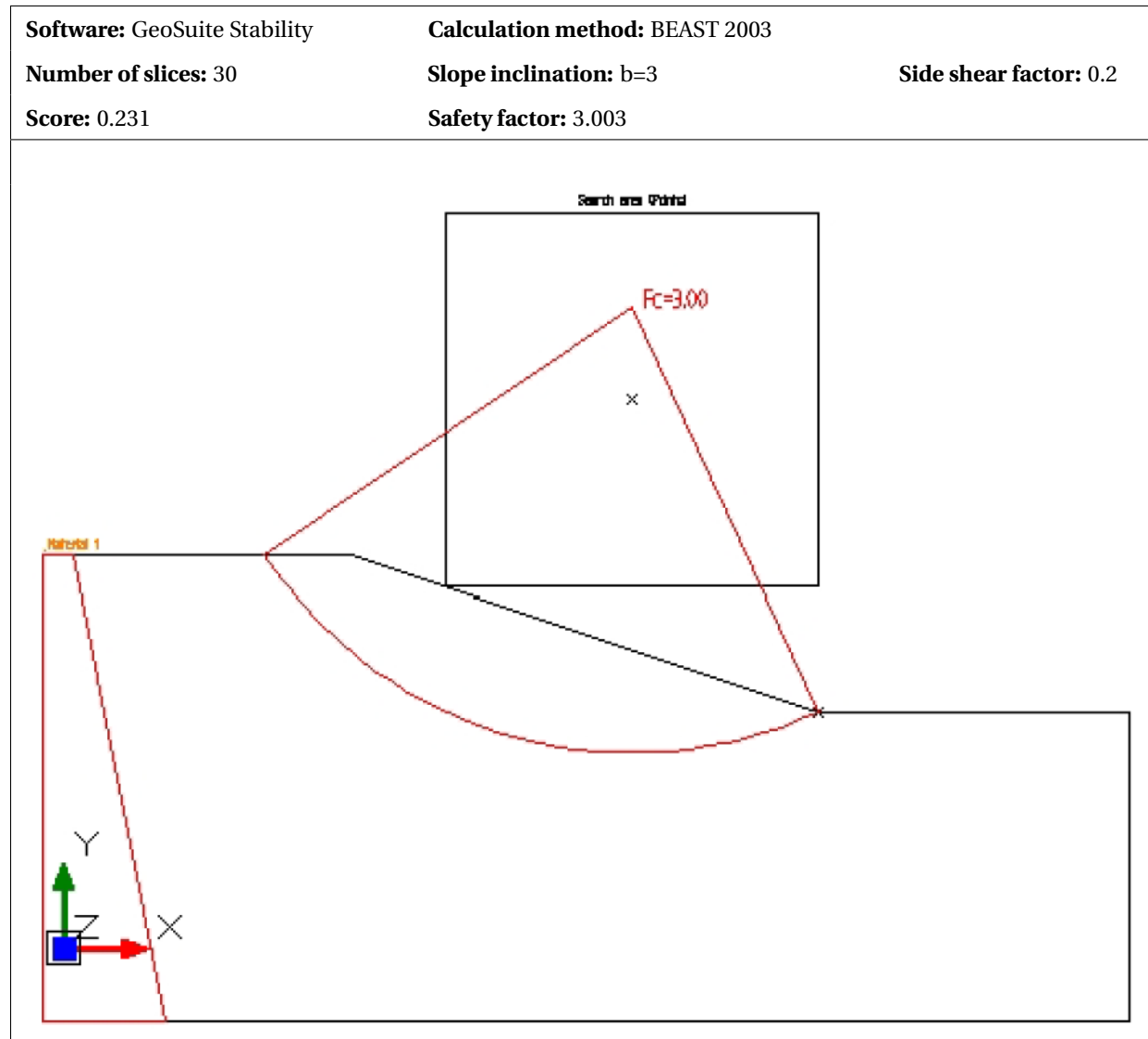
Simulation of $w=4$



Simulation of $w=2$



Simulation of $w=1$



Appendix D

PLAXIS 3D Failure Mechanism - Planar Slope with Finite Width

D.1 Case 1 - $b=1.5$

$w=1$ & $b=1.5$

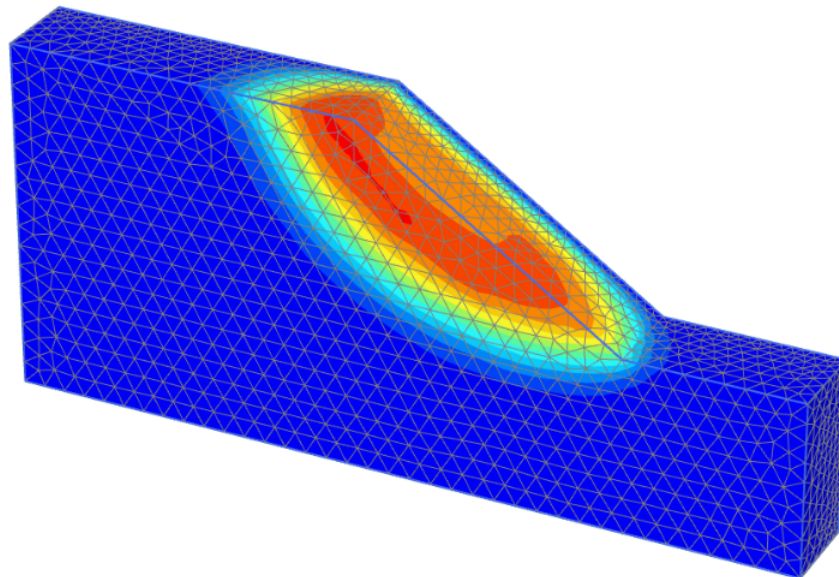


Figure D.1: Incremental displacements from PLAXIS 3D for a fixed width planar slope with slope inclination $b = 1.5$ and relative width $w = W/H = 1$.

w=2 & b=1.5

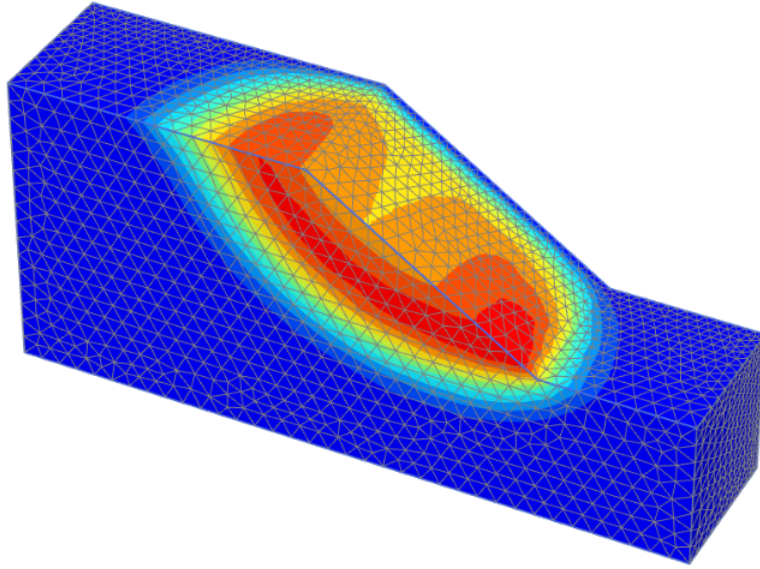


Figure D.2: Incremental displacements from PLAXIS 3D for a fixed width planar slope with slope inclination $b = 1.5$ and relative width $w = W/H = 2$.

w=4 & b=1.5

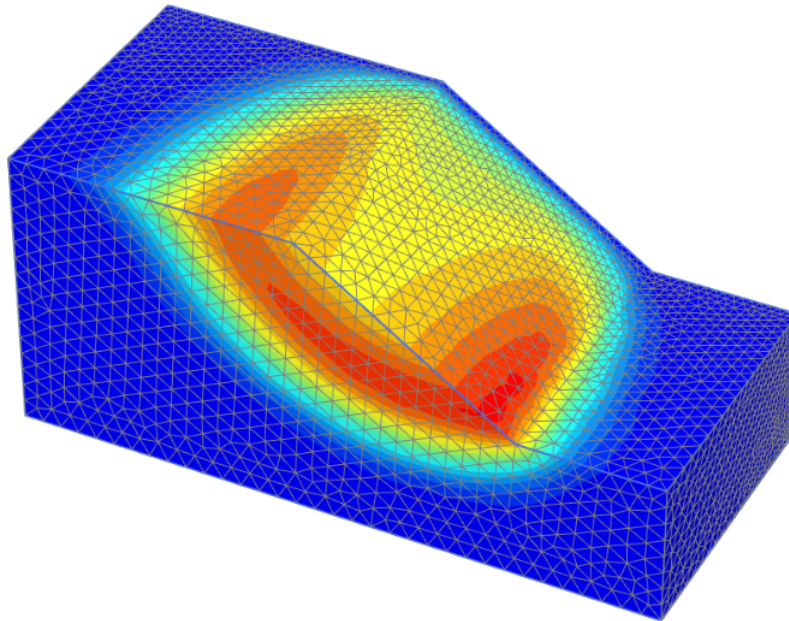


Figure D.3: Incremental displacements from PLAXIS 3D for a fixed width planar slope with slope inclination $b = 1.5$ and relative width $w = W/H = 4$.

w=6 & b=1.5

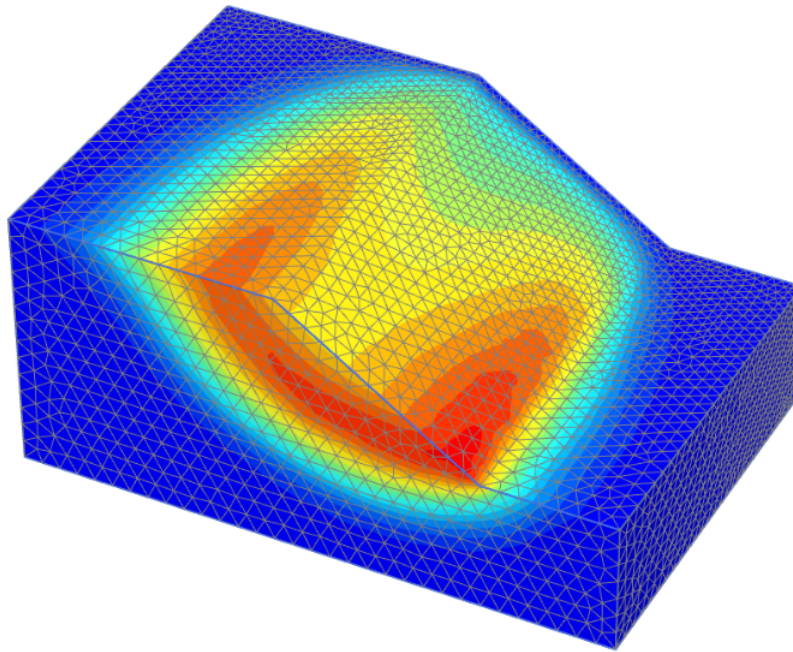


Figure D.4: Incremental displacements from PLAXIS 3D for a fixed width planar slope with slope inclination $b = 1.5$ and relative width $w = W/H = 6$.

D.2 Case 2 - b=2

w=1 & b=2

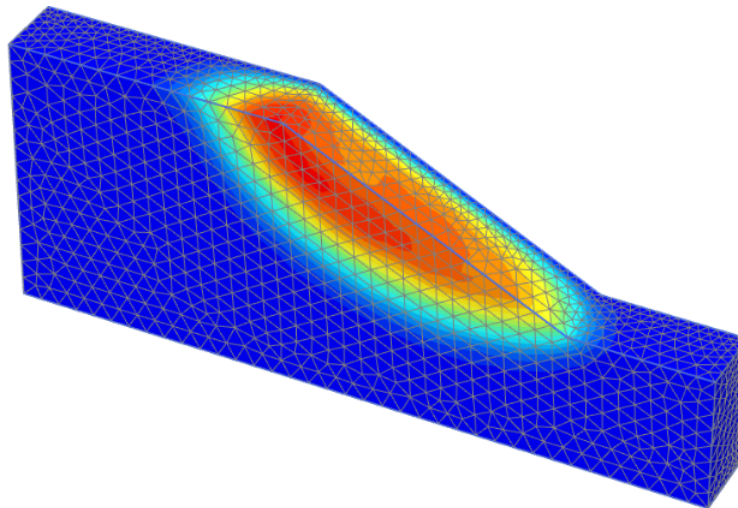


Figure D.5: Incremental displacements from PLAXIS 3D for a fixed width planar slope with slope inclination $b = 2$ and relative width $w = W/H = 1$.

w=2 & b=2

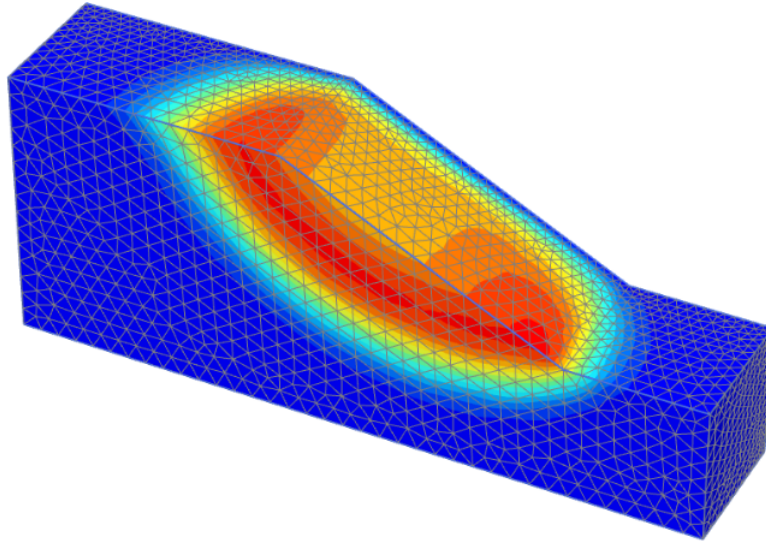


Figure D.6: Incremental displacements from PLAXIS 3D for a fixed width planar slope with slope inclination $b = 2$ and relative width $w = W/H = 2$.

w=4 & b=2

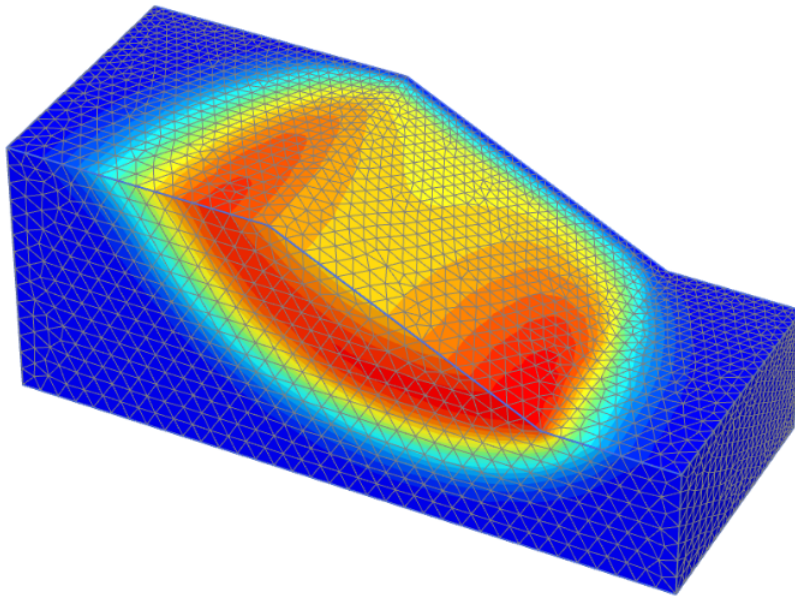


Figure D.7: Incremental displacements from PLAXIS 3D for a fixed width planar slope with slope inclination $b = 2$ and relative width $w = W/H = 4$.

w=6 & b=2

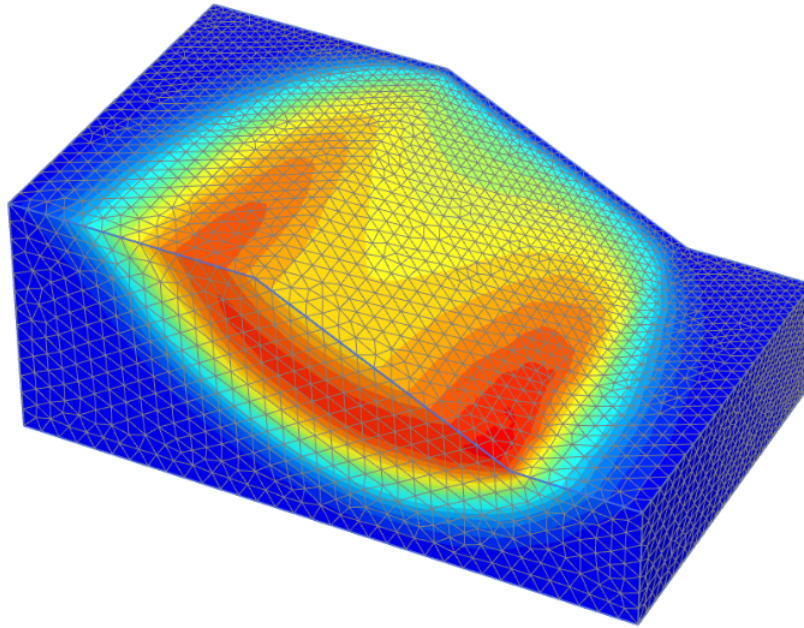


Figure D.8: Incremental displacements from PLAXIS 3D for a fixed width planar slope with slope inclination $b = 2$ and relative width $w = W/H = 6$.

D.3 Case 3 - b=3

w=1 & b=3

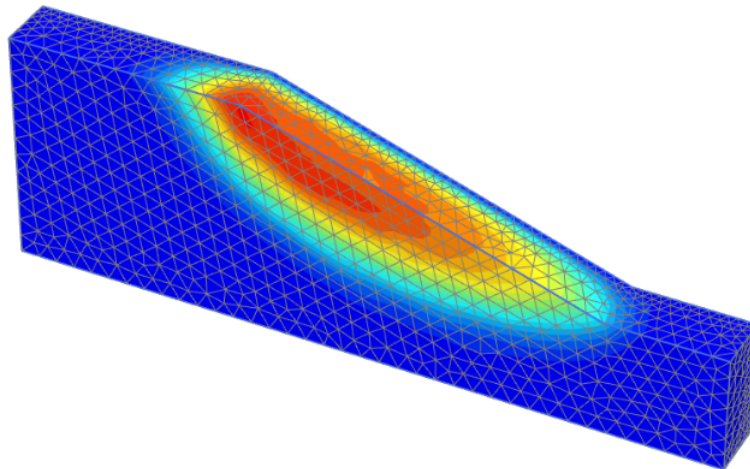


Figure D.9: Incremental displacements from PLAXIS 3D for a fixed width planar slope with slope inclination $b = 3$ and relative width $w = W/H = 1$.

w=2 & b=3

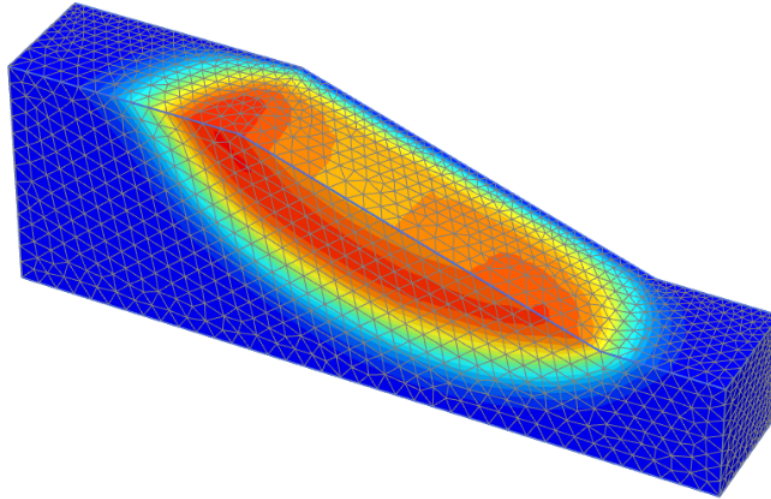


Figure D.10: Incremental displacements from PLAXIS 3D for a fixed width planar slope with slope inclination $b = 3$ and relative width $w = W/H = 2$.

w=4 & b=3

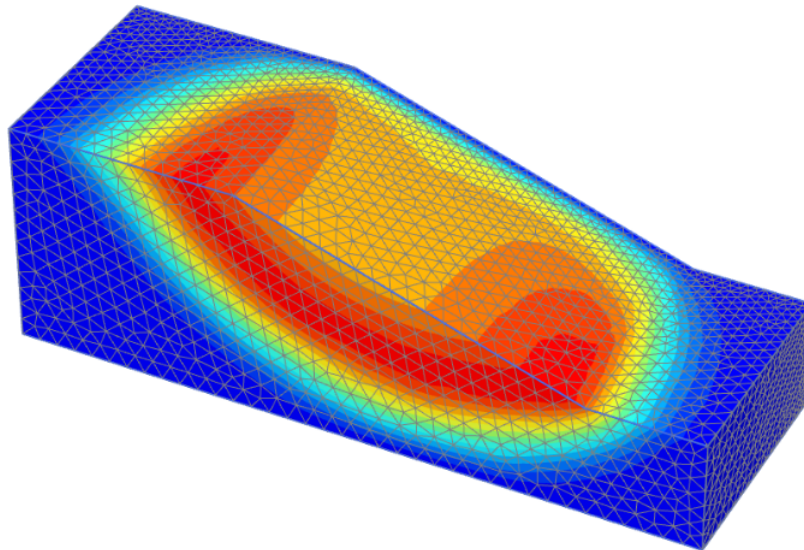


Figure D.11: Incremental displacements from PLAXIS 3D for a fixed width planar slope with slope inclination $b = 3$ and relative width $w = W/H = 4$.

w=6 & b=3

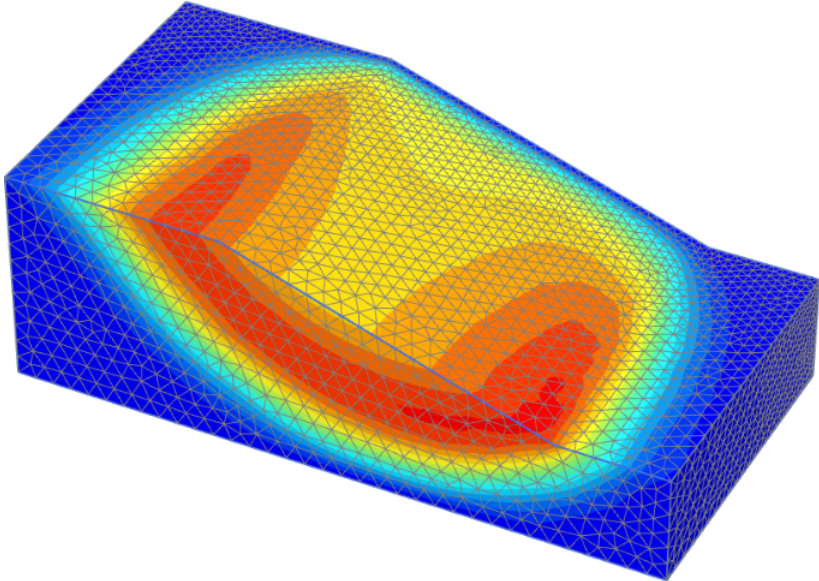


Figure D.12: Incremental displacements from PLAXIS 3D for a fixed width planar slope with slope inclination $b = 3$ and relative width $w = W/H = 6$.

Appendix E

Slide3 Failure Mechanism - Planar Slope with Finite Width

E.1 Case 1 - $b=1.5$

Slide3 - $w=1$ & $b=1.5$

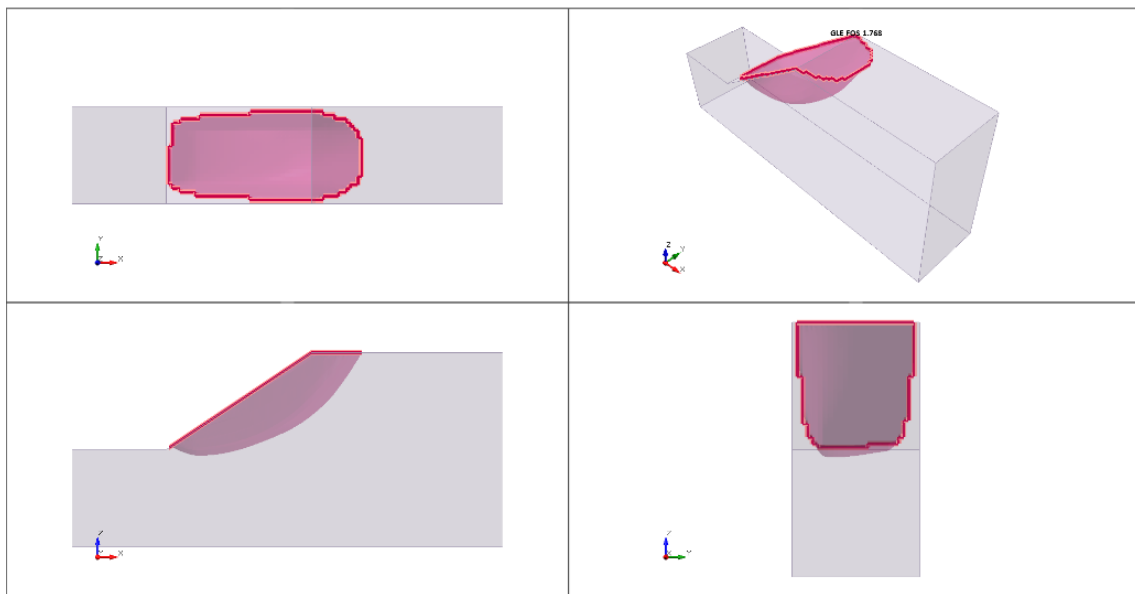


Figure E.1: Slip surface from Slide3 using Morgenstern-Price (GLE) with half-sine intercolumn force function for a fixed width planar slope where $b = 1.5$ and $w = 1$.

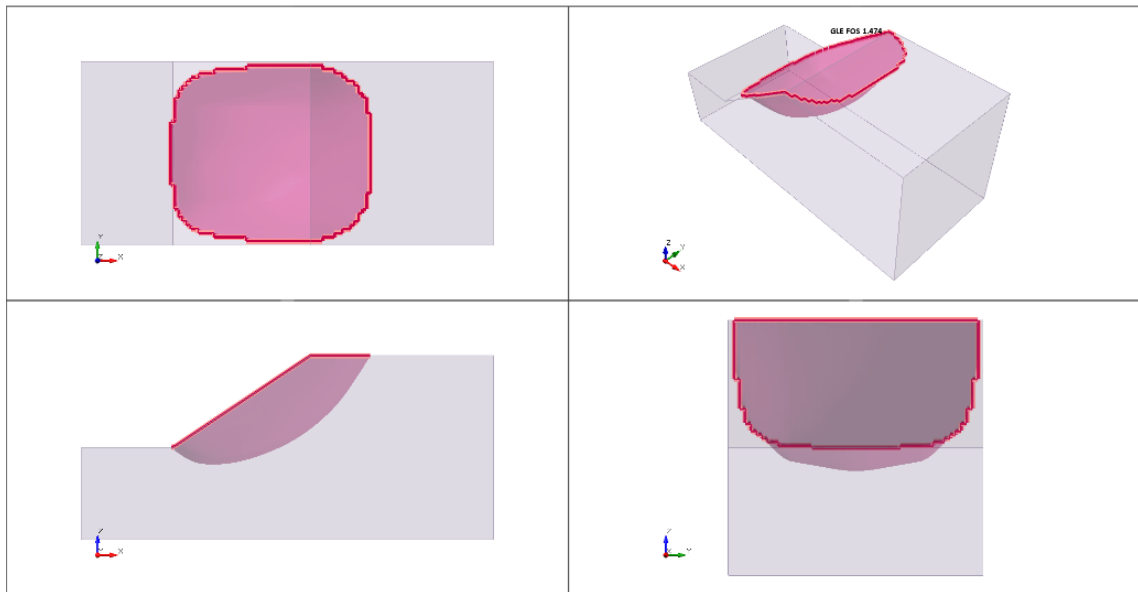
Slide3 - $w=2$ & $b=1.5$ 

Figure E.2: Slip surface from Slide3 using Morgenstern-Price (GLE) with half-sine intercolumn force function for a fixed width planar slope where $b = 1.5$ and $w = 2$.

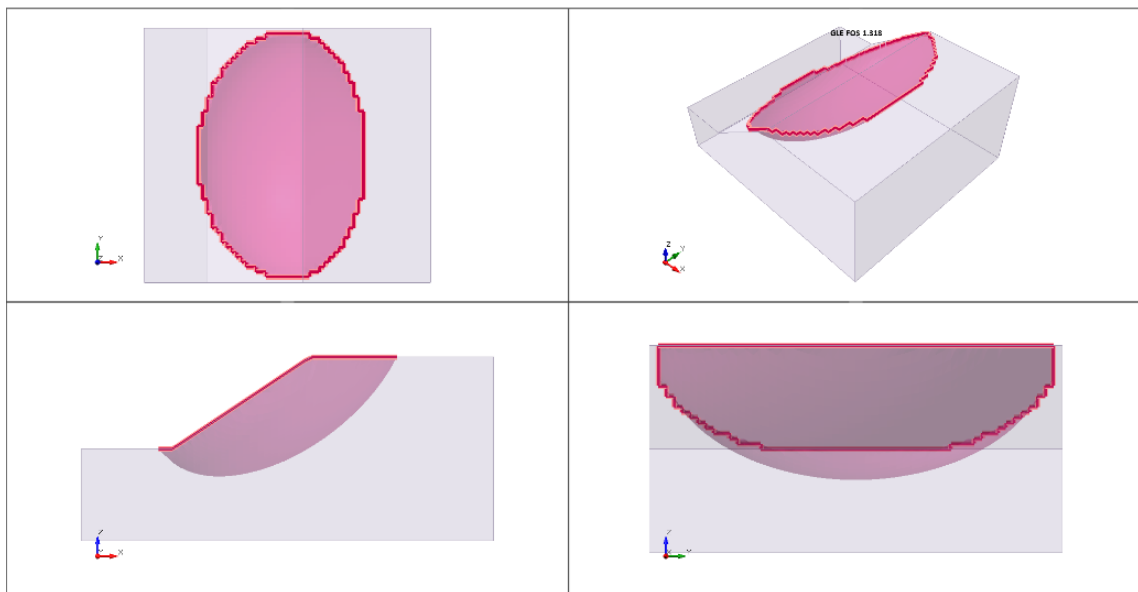
Slide3 - $w=4$ & $b=1.5$ 

Figure E.3: Slip surface from Slide3 using Morgenstern-Price (GLE) with half-sine intercolumn force function for a fixed width planar slope where $b = 1.5$ and $w = 4$.

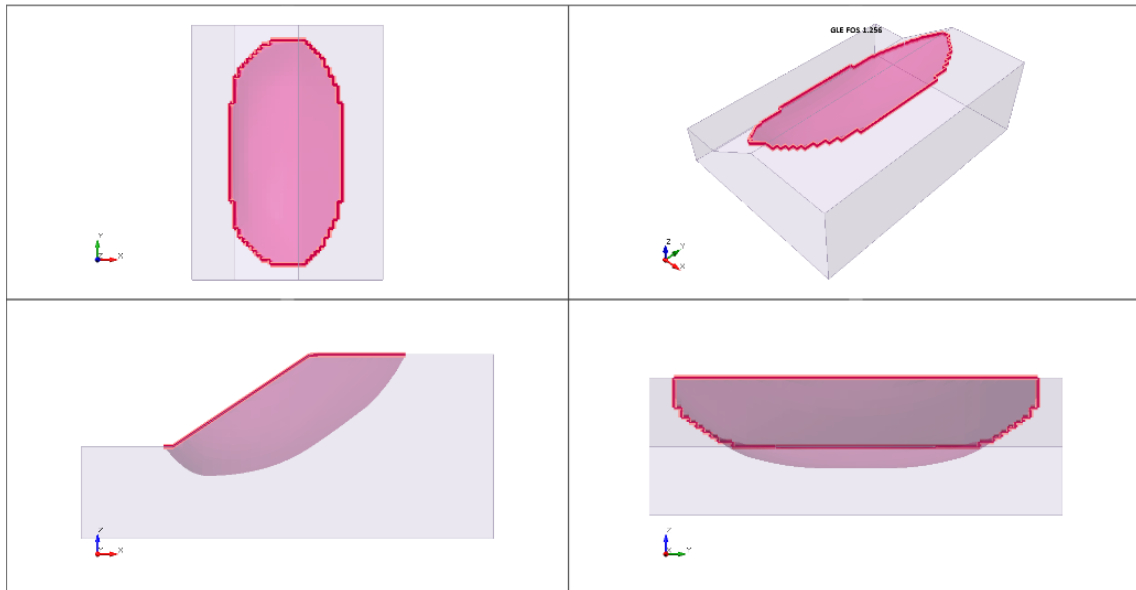
Slide3 - $w=6$ & $b=1.5$ 

Figure E.4: Slip surface from Slide3 using Morgenstern-Price (GLE) with half-sine intercolumn force function for a fixed width planar slope where $b = 1.5$ and $w = 6$.

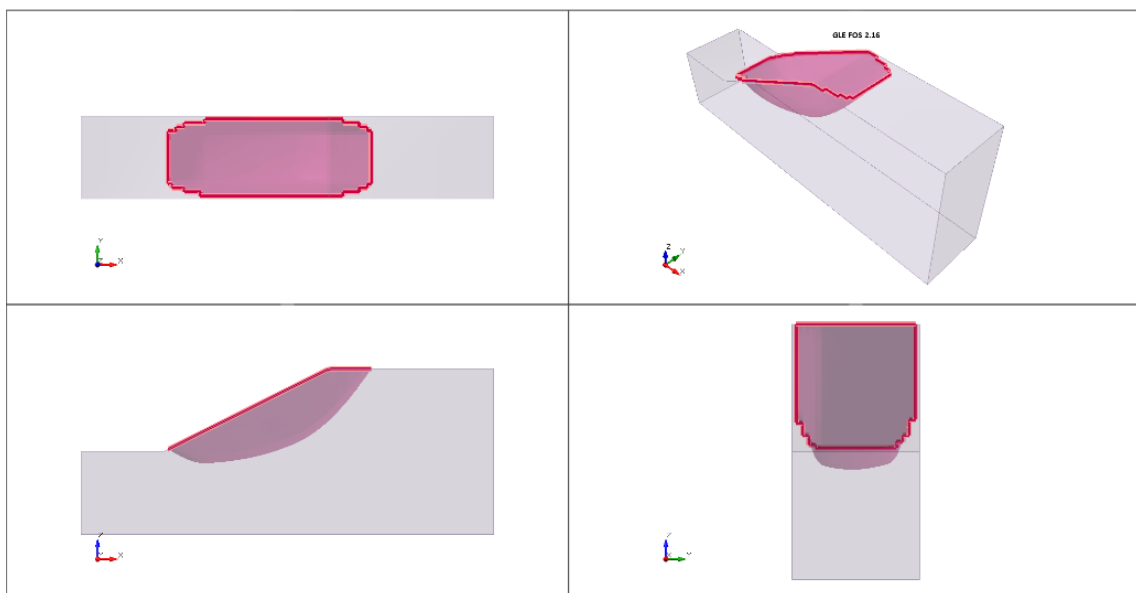
E.2 Case 2 - $b=2$ **Slide3 - $w=1$ & $b=2$** 

Figure E.5: Slip surface from Slide3 using Morgenstern-Price (GLE) with half-sine intercolumn force function for a fixed width planar slope where $b = 2$ and $w = 1$.

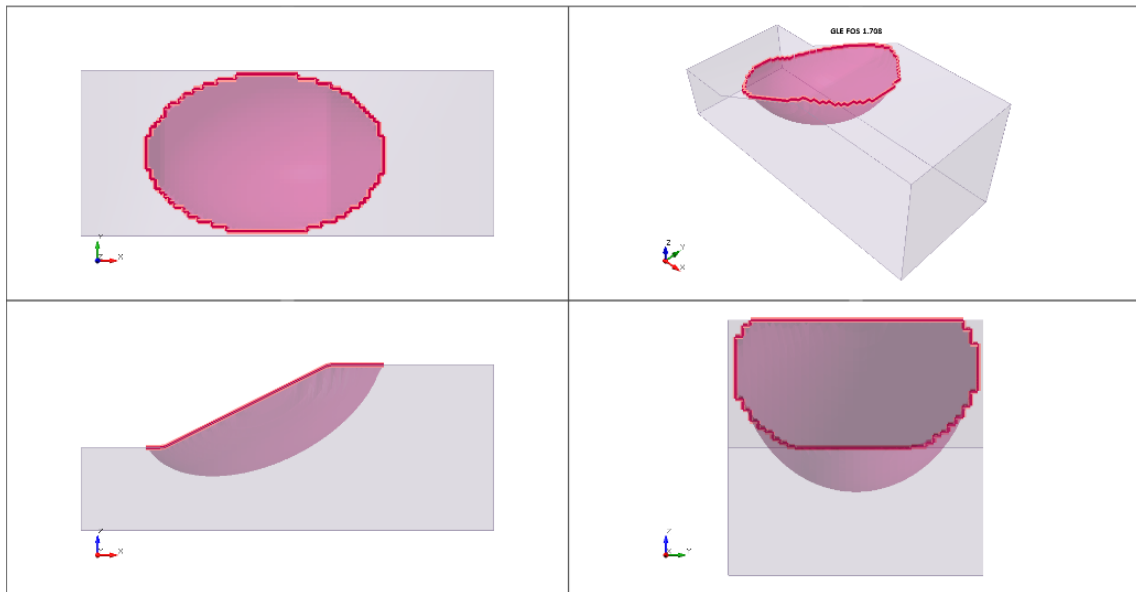
Slide3 - w=2 & b=2

Figure E.6: Slip surface from Slide3 using Morgenstern-Price (GLE) with half-sine intercolumn force function for a fixed width planar slope where $b = 2$ and $w = 2$.

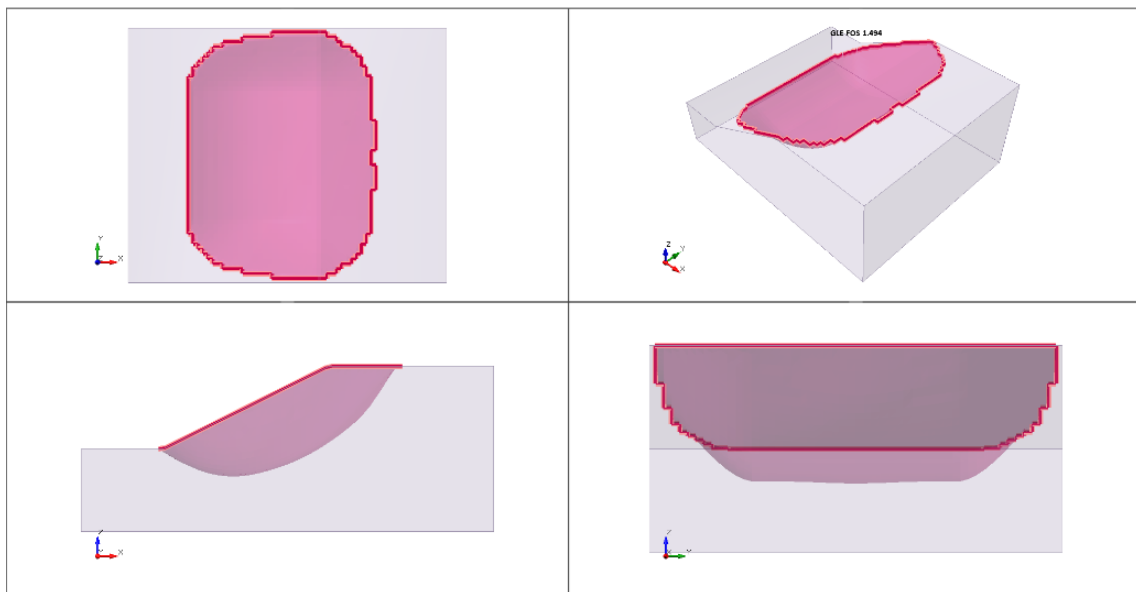
Slide3 - w=4 & b=2

Figure E.7: Slip surface from Slide3 using Morgenstern-Price (GLE) with half-sine intercolumn force function for a fixed width planar slope where $b = 2$ and $w = 4$.

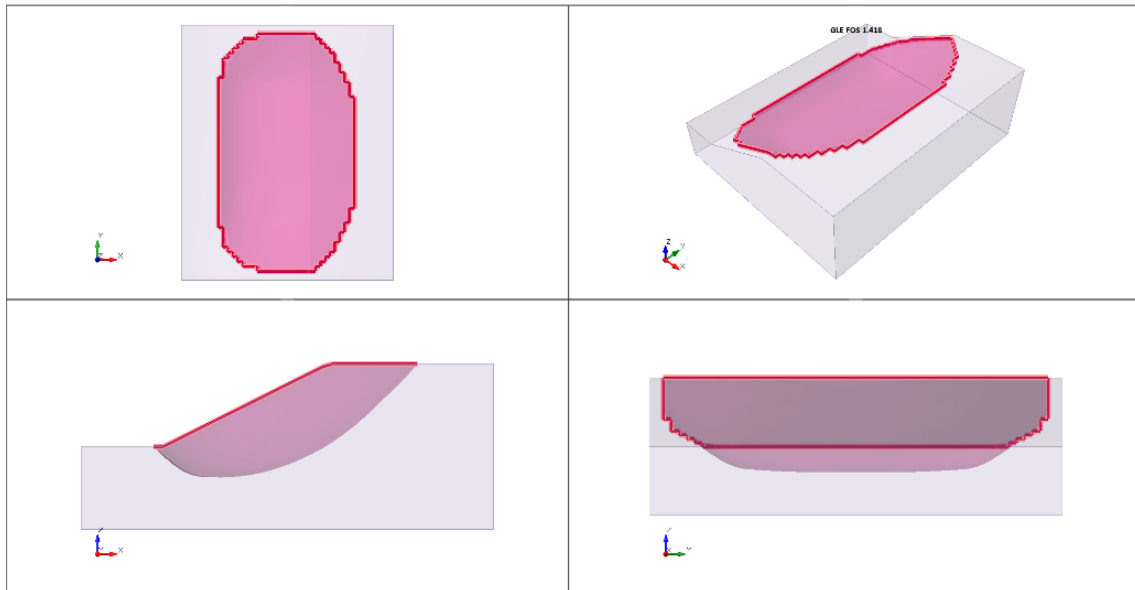
Slide3 - w=6 & b=2

Figure E.8: Slip surface from Slide3 using Morgenstern-Price (GLE) with half-sine intercolumn force function for a fixed width planar slope where $b = 2$ and $w = 6$.

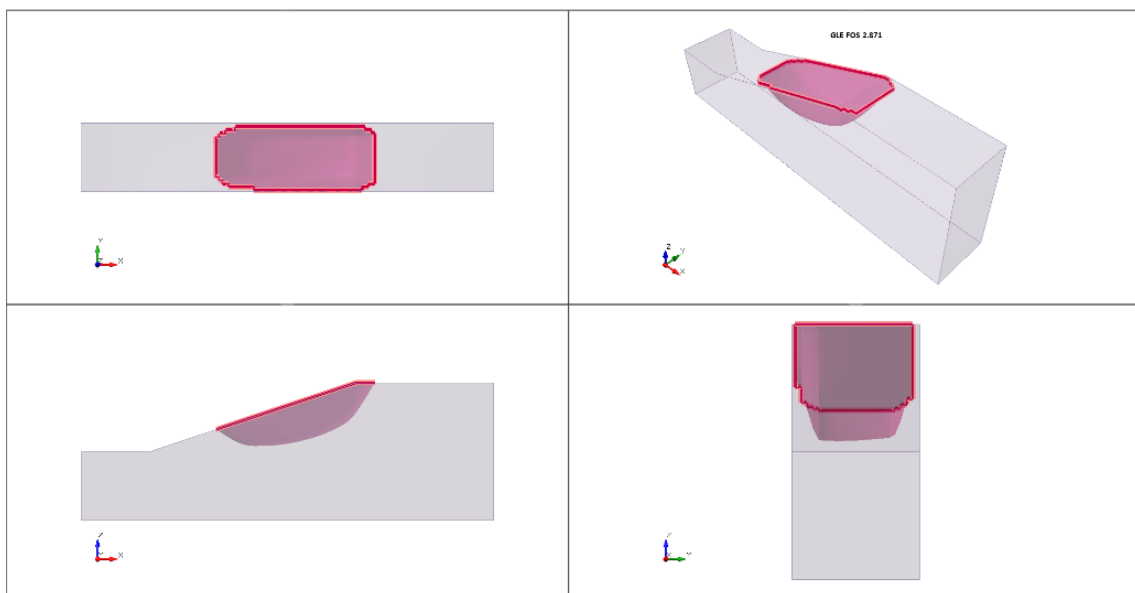
E.3 Case 3 - b=3**Slide3 - w=1 & b=3**

Figure E.9: Slip surface from Slide3 using Morgenstern-Price (GLE) with half-sine intercolumn force function for a fixed width planar slope where $b = 3$ and $w = 1$.

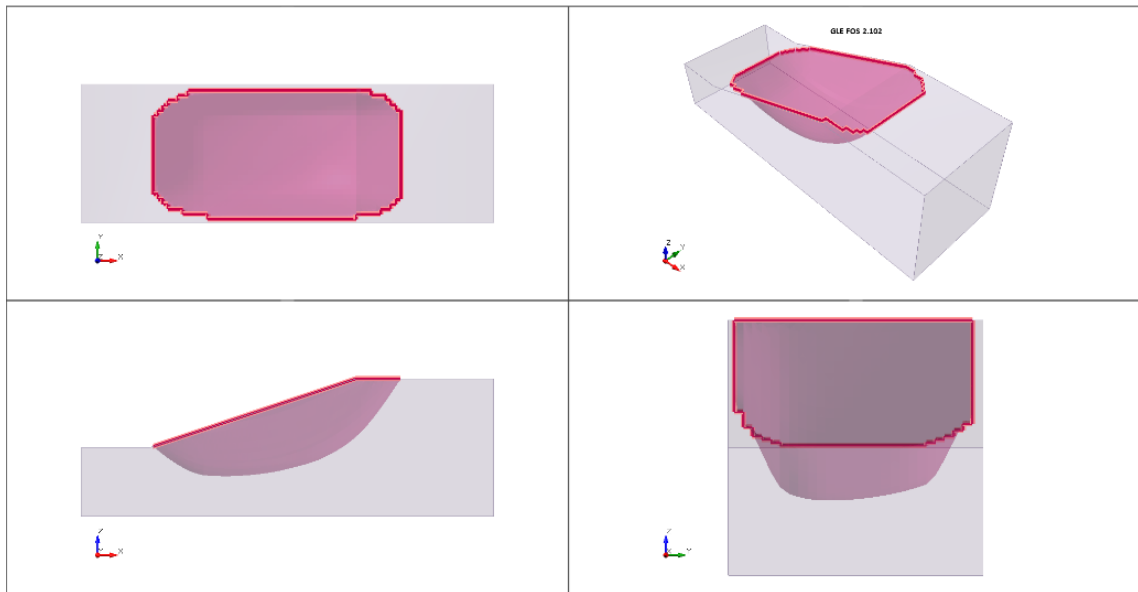
Slide3 - w=2 & b=3

Figure E.10: Slip surface from Slide3 using Morgenstern-Price (GLE) with half-sine intercolumn force function for a fixed width planar slope where $b = 3$ and $w = 2$.

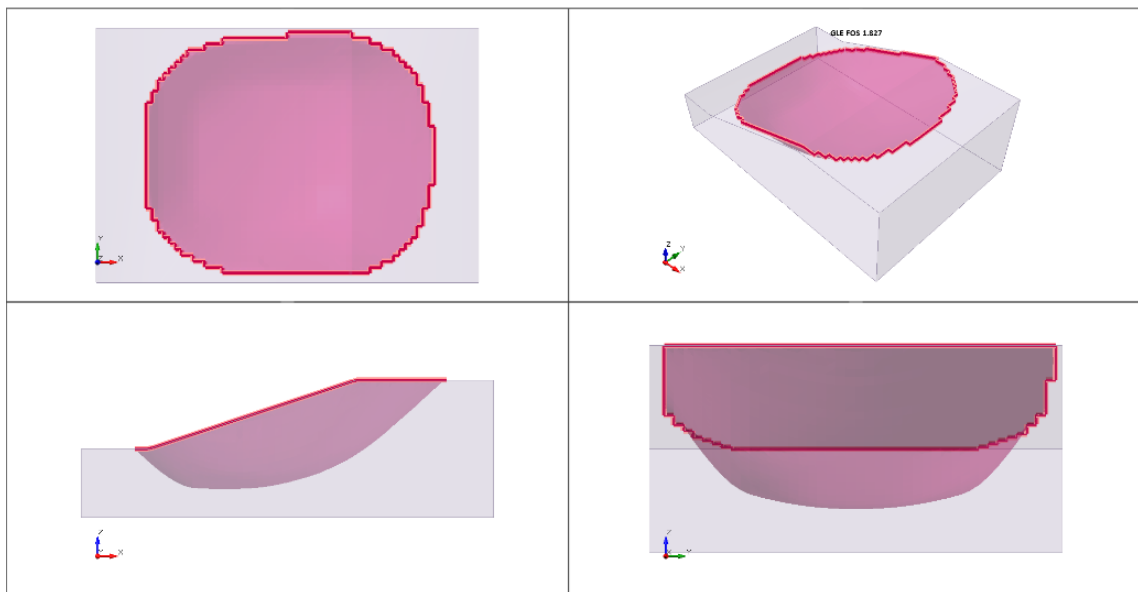
Slide3 - w=4 & b=3

Figure E.11: Slip surface from Slide3 using Morgenstern-Price (GLE) with half-sine intercolumn force function for a fixed width planar slope where $b = 3$ and $w = 4$.

Slide3 - w=6 & b=3

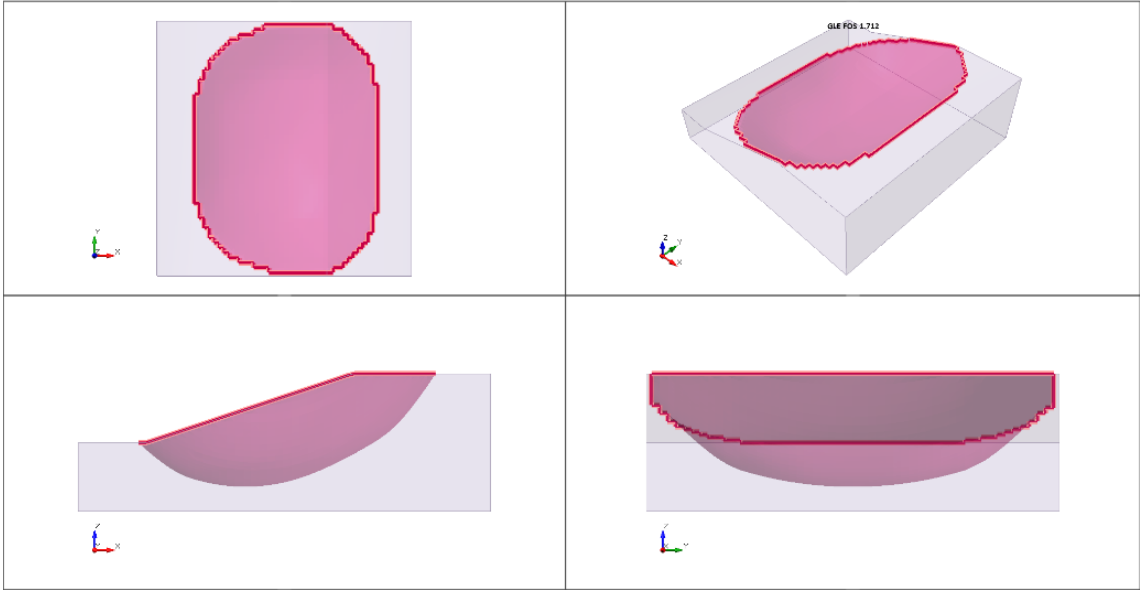


Figure E.12: Slip surface from Slide3 using Morgenstern-Price (GLE) with half-sine intercolumn force function for a fixed width planar slope where $b = 3$ and $w = 6$.

Appendix F

PLAXIS 3D Failure Mechanism - Slope with Curvature

F1 Convex - $b=1.5$

$r_u = 1, b=1.5$ & $\alpha = 90^\circ$

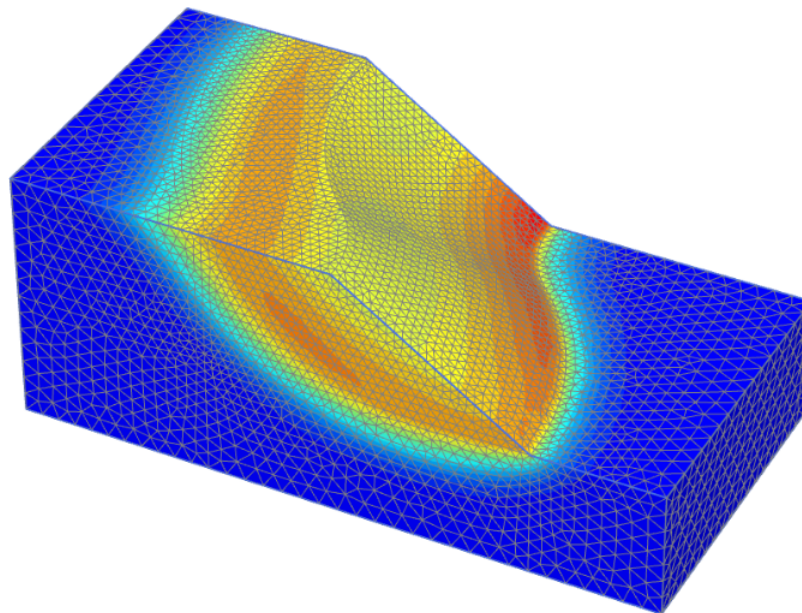


Figure F1: Incremental displacements from PLAXIS 3D for a convex slope with inclination $b = 1.5$, curvature angle $\alpha = 90^\circ$ and relative radius $r_u = R_u/H = 1$. No planar extension.

$r_u = 2, b=1.5$ & $\alpha = 90^\circ$

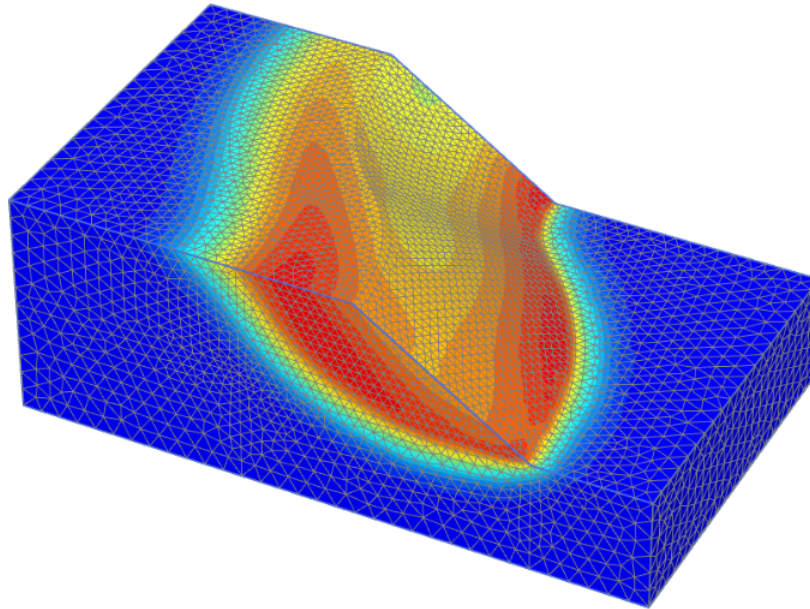


Figure E2: Incremental displacements from PLAXIS 3D for a convex slope with inclination $b = 1.5$, curvature angle $\alpha = 90^\circ$ and relative radius $r_u = R_u/H = 2$. No planar extension.

$r_u = 4, b=1.5$ & $\alpha = 90^\circ$

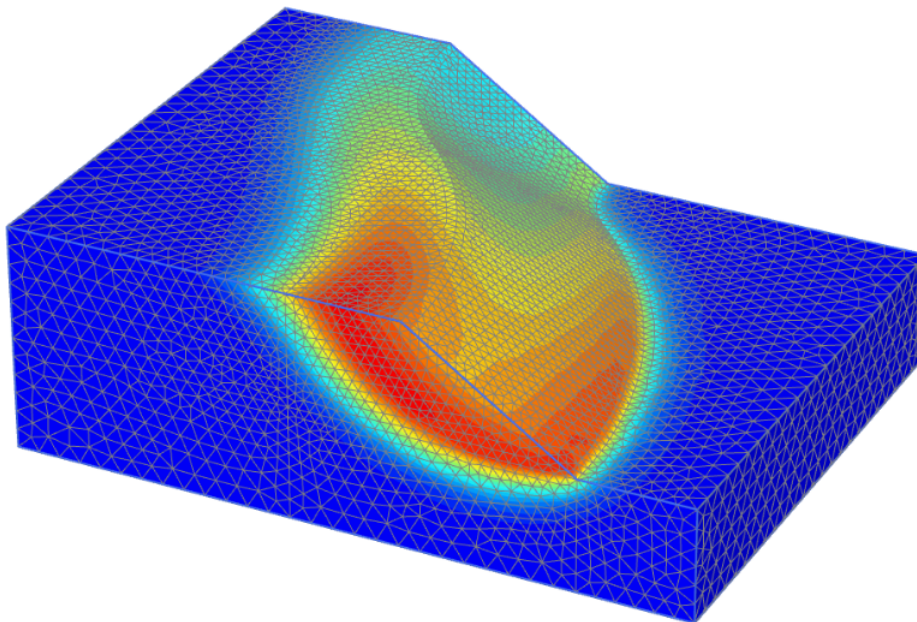


Figure E3: Incremental displacements from PLAXIS 3D for a convex slope with inclination $b = 1.5$, curvature angle $\alpha = 90^\circ$ and relative radius $r_u = R_u/H = 4$. No planar extension.

$r_u = 6, b=1.5$ & $\alpha = 90^\circ$

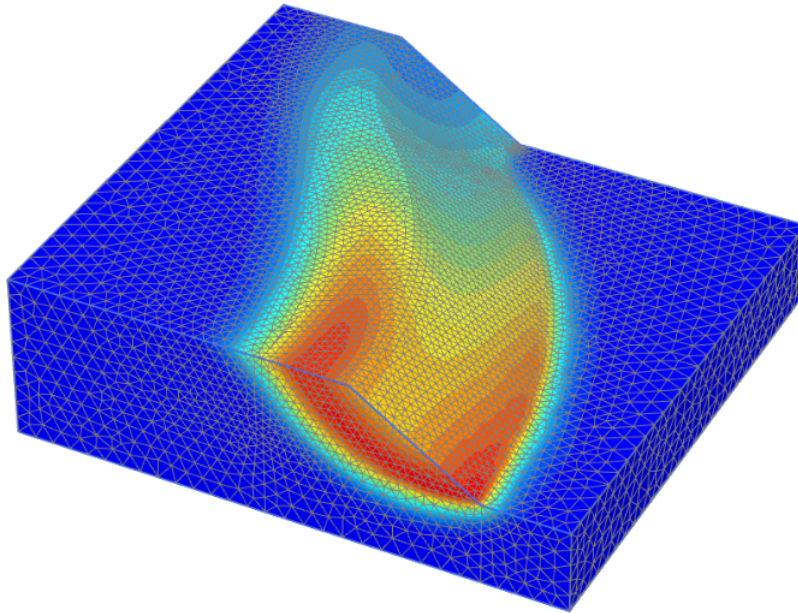


Figure F4: Incremental displacements from PLAXIS 3D for a convex slope with inclination $b = 1.5$, curvature angle $\alpha = 90^\circ$ and relative radius $r_u = R_u/H = 6$. No planar extension.

$r_u = 1, b=1.5$ & $\alpha = 180^\circ$

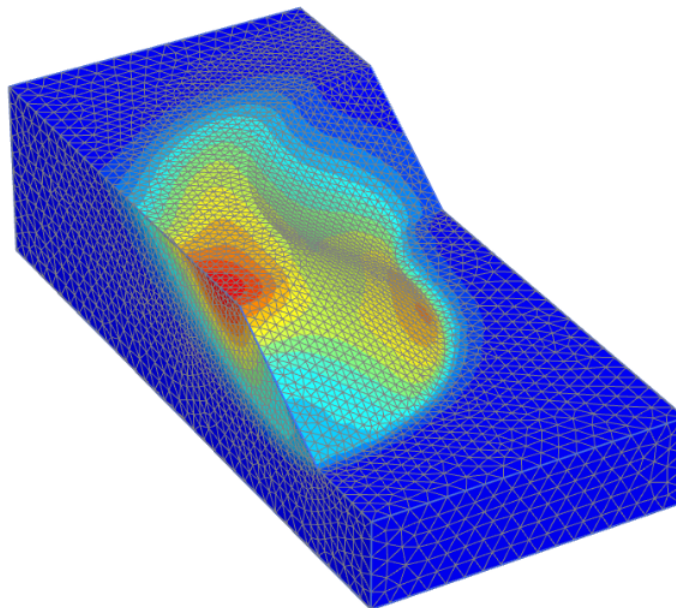


Figure F5: Incremental displacements from PLAXIS 3D for a convex slope with inclination $b = 1.5$, curvature angle $\alpha = 180^\circ$ and relative radius $r_u = R_u/H = 1$. No planar extension.

$r_u = 2, b=1.5$ & $\alpha = 180^\circ$

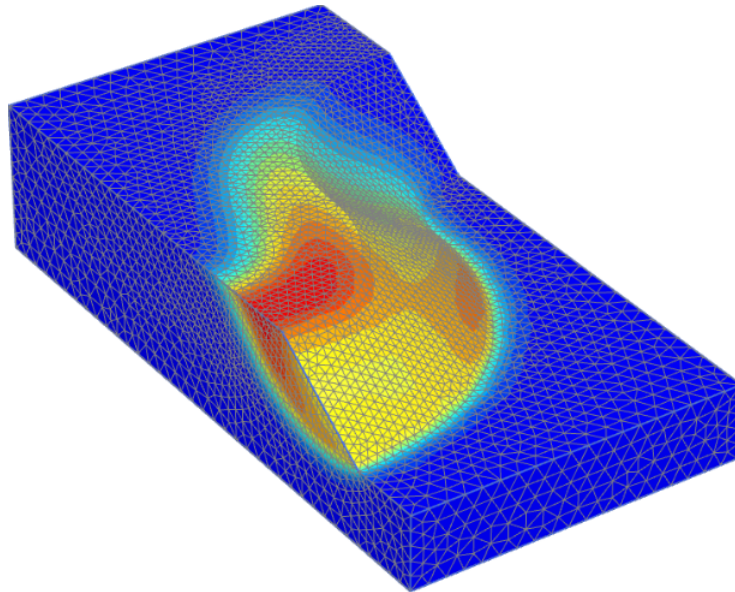


Figure E6: Incremental displacements from PLAXIS 3D for a convex slope with inclination $b = 1.5$, curvature angle $\alpha = 180^\circ$ and relative radius $r_u = R_u/H = 2$. No planar extension.

$r_u = 4, b=1.5$ & $\alpha = 180^\circ$

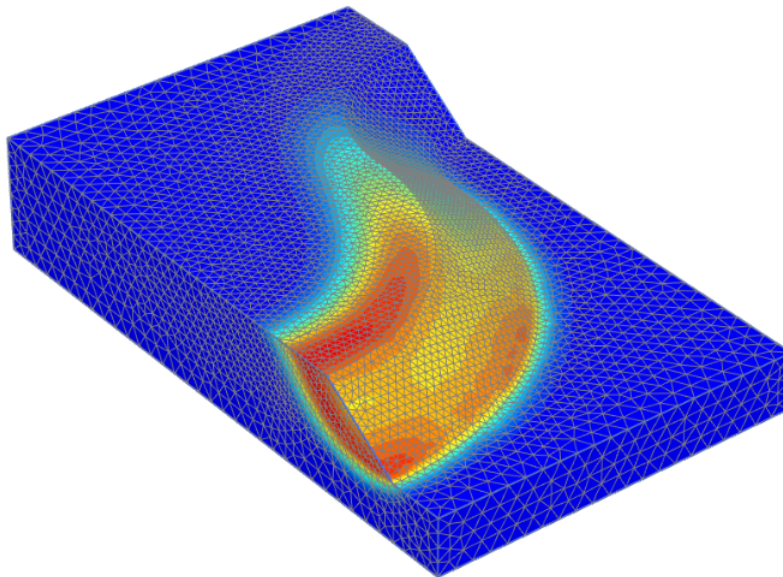


Figure E7: Incremental displacements from PLAXIS 3D for a convex slope with inclination $b = 1.5$, curvature angle $\alpha = 180^\circ$ and relative radius $r_u = R_u/H = 4$. No planar extension.

$r_u = 6, b=1.5$ & $\alpha = 180^\circ$

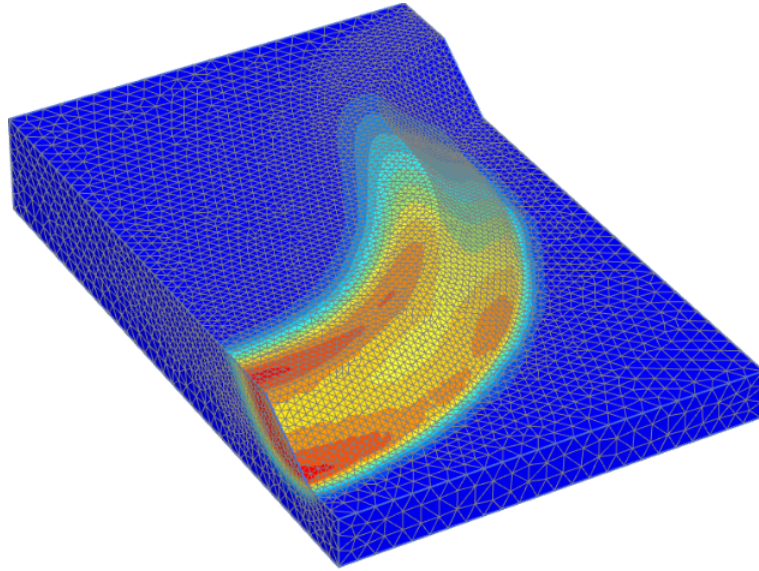


Figure E8: Incremental displacements from PLAXIS 3D for a convex slope with inclination $b = 1.5$, curvature angle $\alpha = 180^\circ$ and relative radius $r_u = R_u/H = 6$. No planar extension.

E.2 Convex - $b=3$

$r_u = 1, b=3$ & $\alpha = 90^\circ$

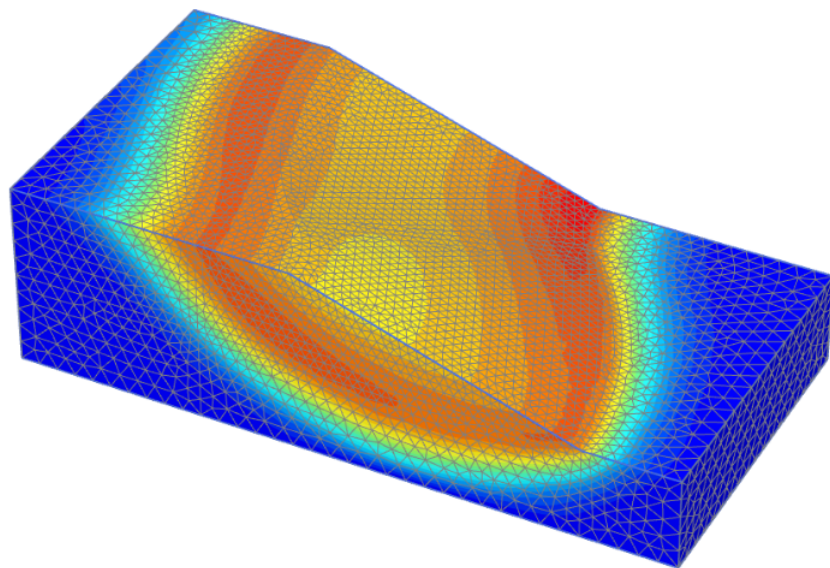


Figure E9: Incremental displacements from PLAXIS 3D for a convex slope with inclination $b = 3$, curvature angle $\alpha = 90^\circ$ and relative radius $r_u = R_u/H = 1$. No planar extension.

$r_u = 2, b=3$ & $\alpha = 90^\circ$

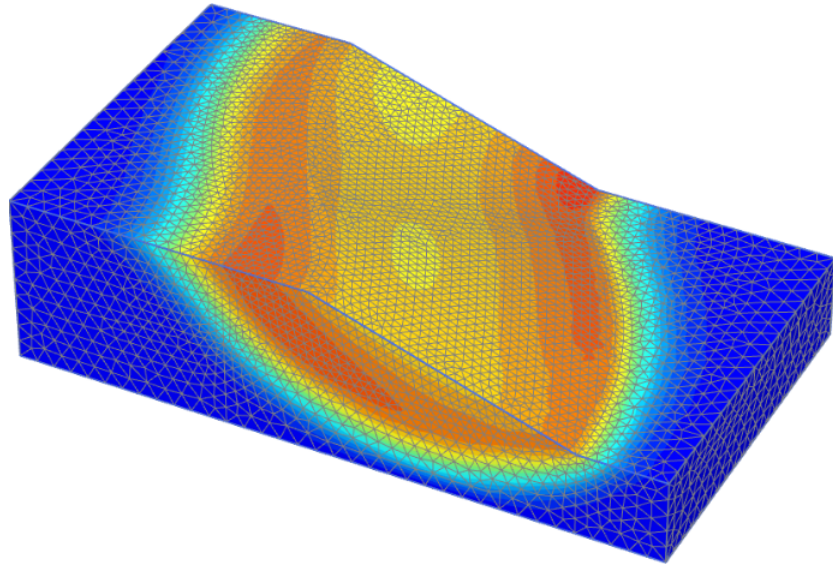


Figure F.10: Incremental displacements from PLAXIS 3D for a convex slope with inclination $b = 3$, curvature angle $\alpha = 90^\circ$ and relative radius $r_u = R_u/H = 2$. No planar extension.

$r_u = 4, b=3$ & $\alpha = 90^\circ$

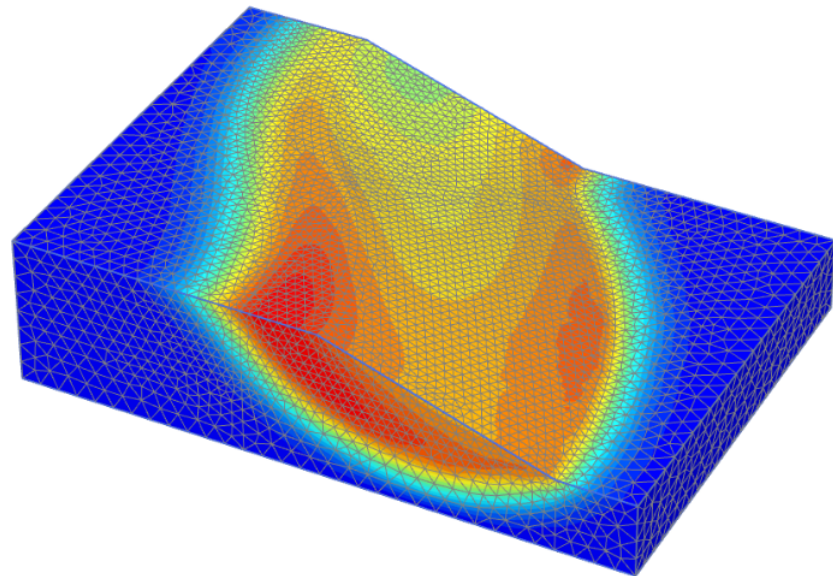


Figure F.11: Incremental displacements from PLAXIS 3D for a convex slope with inclination $b = 3$, curvature angle $\alpha = 90^\circ$ and relative radius $r_u = R_u/H = 4$. No planar extension.

$r_u = 6, b=3$ & $\alpha = 90^\circ$

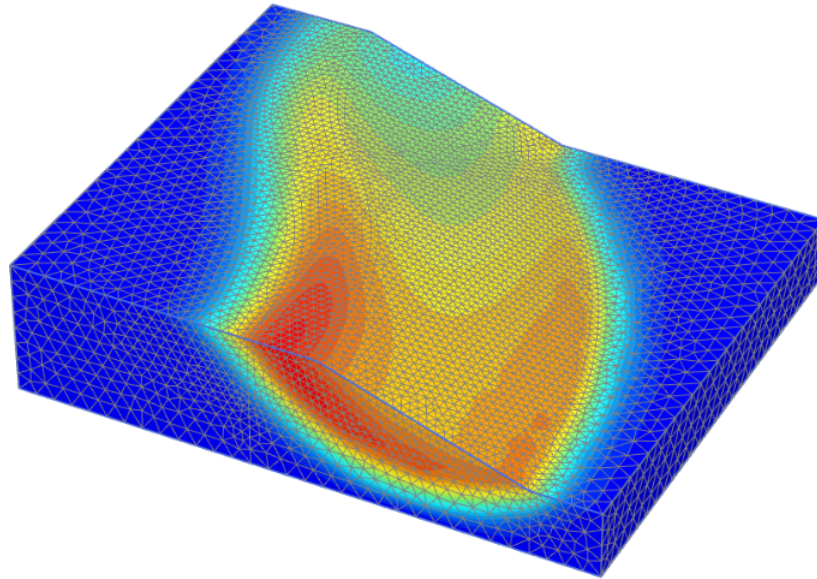


Figure E.12: Incremental displacements from PLAXIS 3D for a convex slope with inclination $b = 3$, curvature angle $\alpha = 90^\circ$ and relative radius $r_u = R_u/H = 6$. No planar extension.

$r_u = 1, b=3$ & $\alpha = 180^\circ$

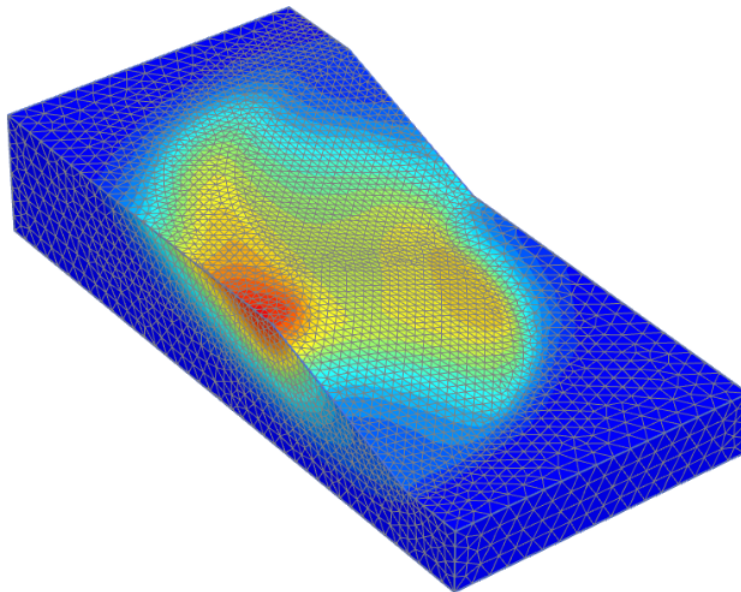


Figure E.13: Incremental displacements from PLAXIS 3D for a convex slope with inclination $b = 3$, curvature angle $\alpha = 180^\circ$ and relative radius $r_u = R_u/H = 1$. No planar extension.

$r_u = 2, b=3$ & $\alpha = 180^\circ$

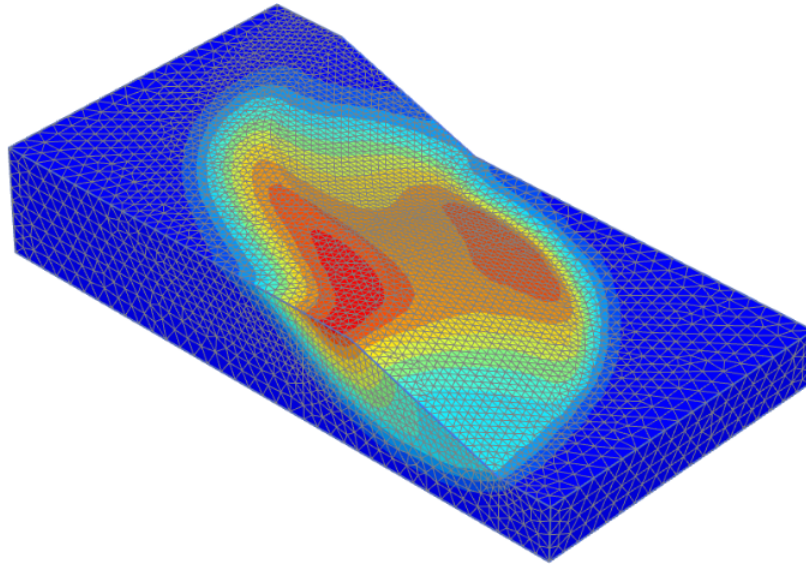


Figure E.14: Incremental displacements from PLAXIS 3D for a convex slope with inclination $b = 3$, curvature angle $\alpha = 180^\circ$ and relative radius $r_u = R_u/H = 2$. No planar extension.

$r_u = 4, b=3$ & $\alpha = 180^\circ$

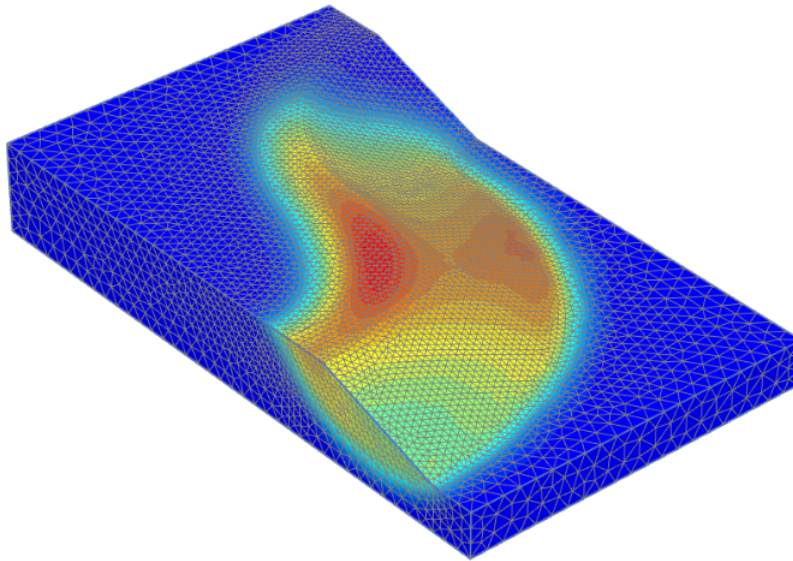


Figure E.15: Incremental displacements from PLAXIS 3D for a convex slope with inclination $b = 3$, curvature angle $\alpha = 180^\circ$ and relative radius $r_u = R_u/H = 4$. No planar extension.

$r_u = 6, b=3$ & $\alpha = 180^\circ$

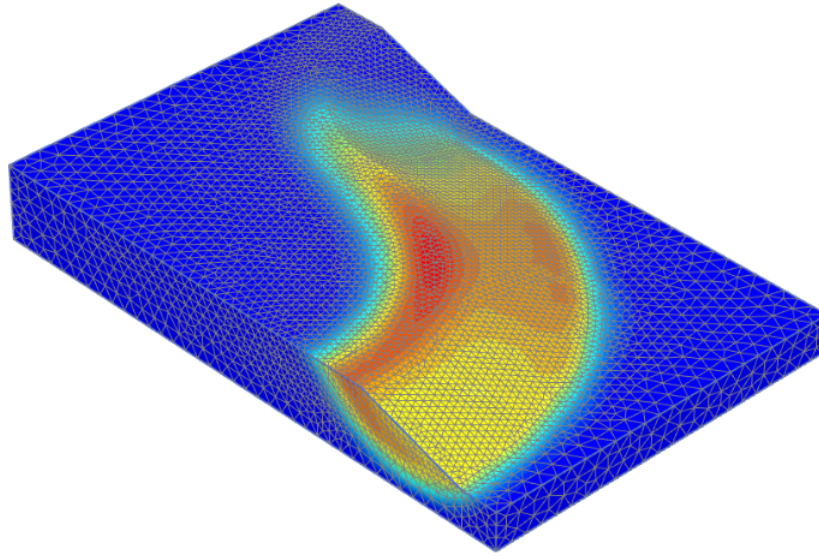


Figure E.16: Incremental displacements from PLAXIS 3D for a convex slope with inclination $b = 3$, curvature angle $\alpha = 180^\circ$ and relative radius $r_u = R_u/H = 6$. No planar extension.

E.3 Concave - $b=1.5$

$r_l = 1, b=1.5$ & $\alpha = 90^\circ$

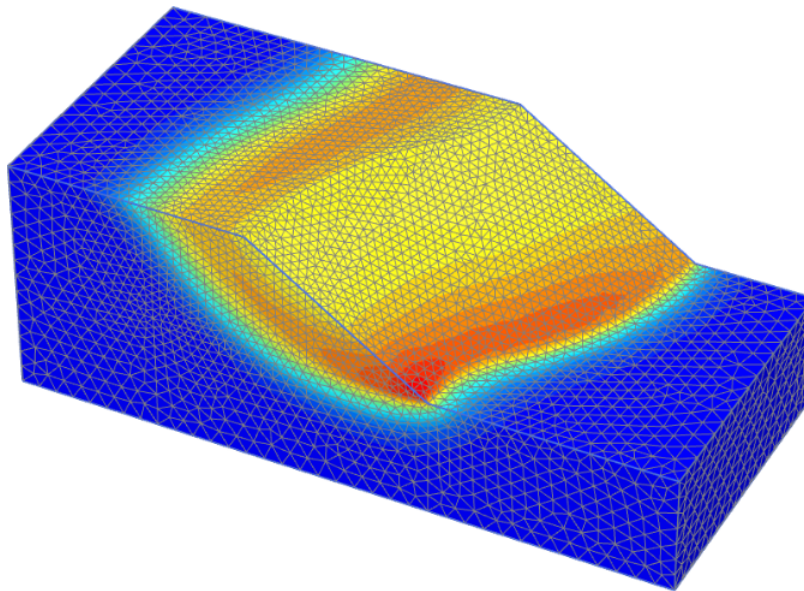


Figure E.17: Incremental displacements from PLAXIS 3D for a concave slope with inclination $b = 1.5$, curvature angle $\alpha = 90^\circ$ and relative radius $r_l = R_l/H = 1$. No planar extension.

$r_l = 2, b=1.5$ & $\alpha = 90^\circ$

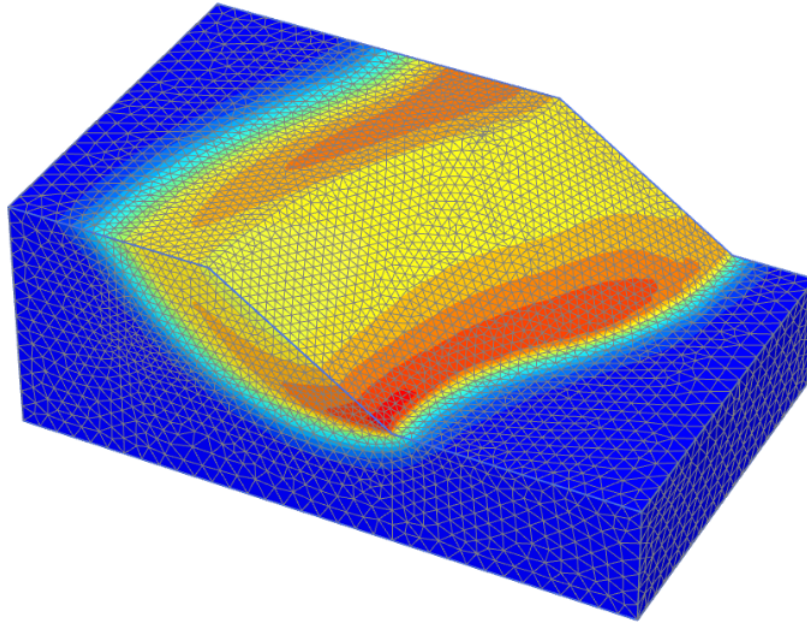


Figure F.18: Incremental displacements from PLAXIS 3D for a concave slope with inclination $b = 1.5$, curvature angle $\alpha = 90^\circ$ and relative radius $r_l = R_l/H = 2$. No planar extension.

$r_l = 4, b=1.5$ & $\alpha = 90^\circ$

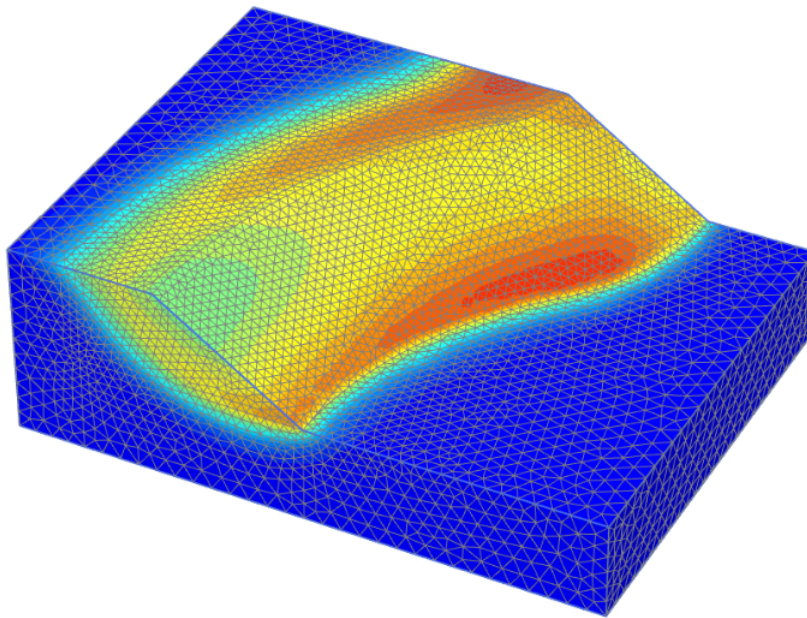


Figure F.19: Incremental displacements from PLAXIS 3D for a concave slope with inclination $b = 1.5$, curvature angle $\alpha = 90^\circ$ and relative radius $r_l = R_l/H = 4$. No planar extension.

$r_l = 6, b=1.5$ & $\alpha = 90^\circ$

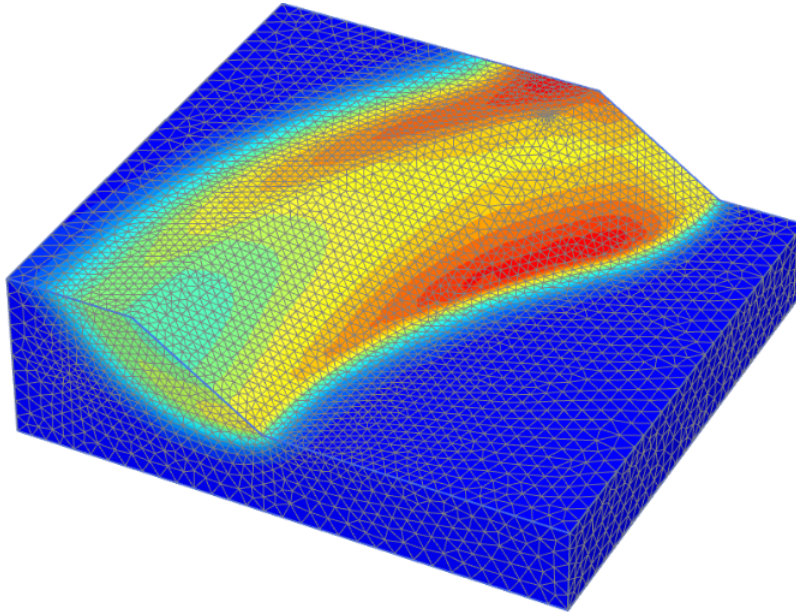


Figure E.20: Incremental displacements from PLAXIS 3D for a concave slope with inclination $b = 1.5$, curvature angle $\alpha = 90^\circ$ and relative radius $r_l = R_l/H = 6$. No planar extension..

$r_l = 1, b=1.5$ & $\alpha = 180^\circ$

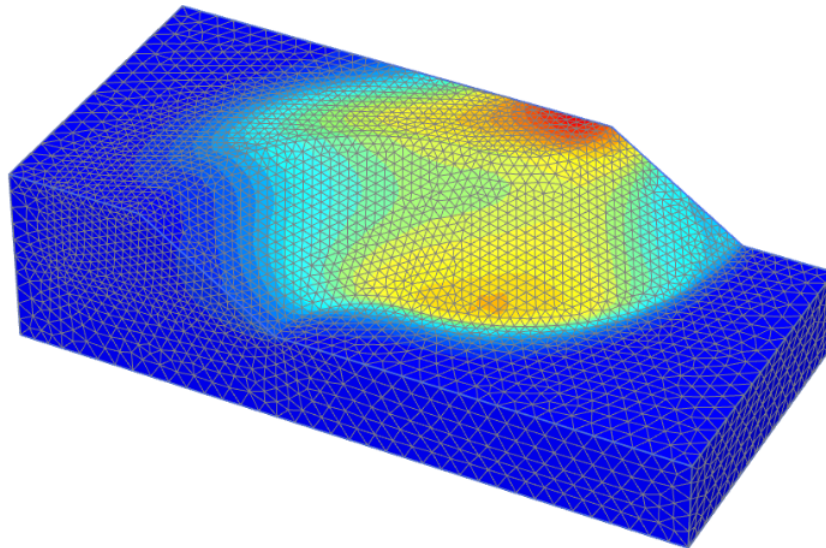


Figure E.21: Incremental displacements from PLAXIS 3D for a concave slope with inclination $b = 1.5$, curvature angle $\alpha = 180^\circ$ and relative radius $r_l = R_l/H = 1$. No planar extension..

$r_l = 2, b=1.5$ & $\alpha = 180^\circ$

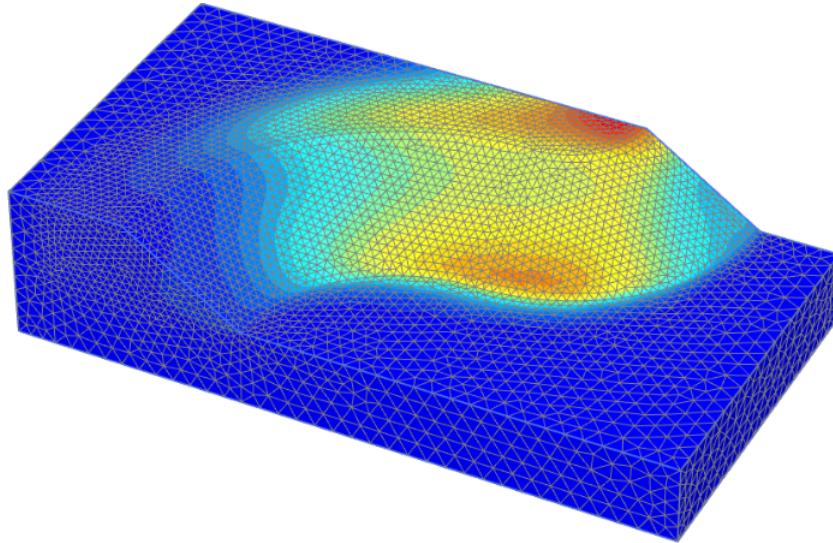


Figure E22: Incremental displacements from PLAXIS 3D for a concave slope with inclination $b = 1.5$, curvature angle $\alpha = 180^\circ$ and relative radius $r_l = R_l/H = 2$. No planar extension.

$r_l = 4, b=1.5$ & $\alpha = 180^\circ$

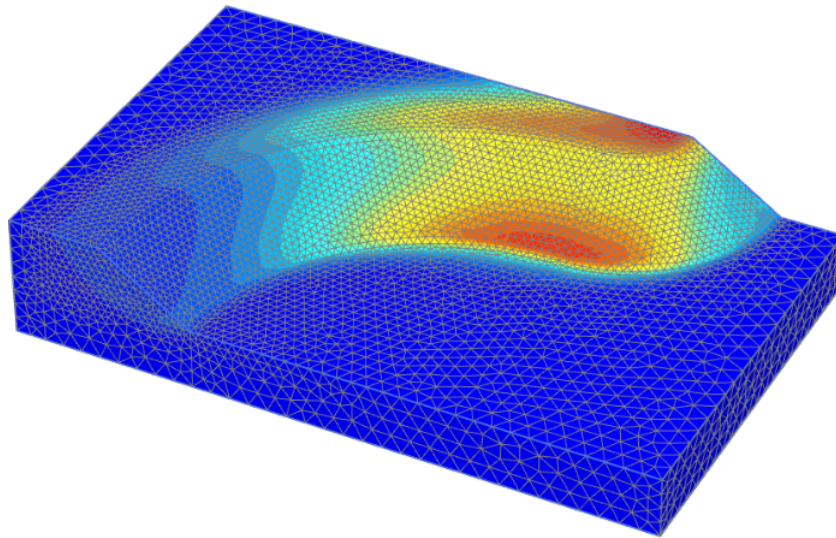


Figure E23: Incremental displacements from PLAXIS 3D for a concave slope with inclination $b = 1.5$, curvature angle $\alpha = 180^\circ$ and relative radius $r_l = R_l/H = 4$. No planar extension.

$r_l = 6, b=1.5$ & $\alpha = 180^\circ$

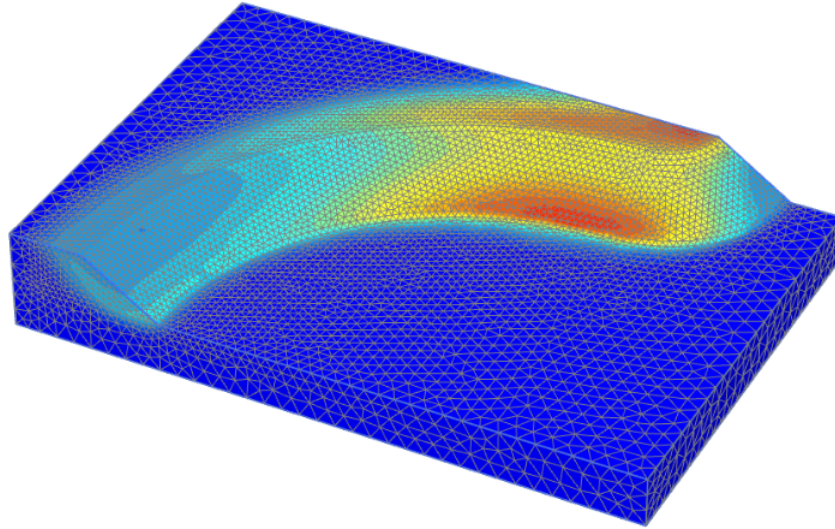


Figure E24: Incremental displacements from PLAXIS 3D for a concave slope with inclination $b = 1.5$, curvature angle $\alpha = 180^\circ$ and relative radius $r_l = R_l/H = 6$. No planar extension.

F.4 Concave - $b=3$

$r_l = 1, b=3$ & $\alpha = 90^\circ$

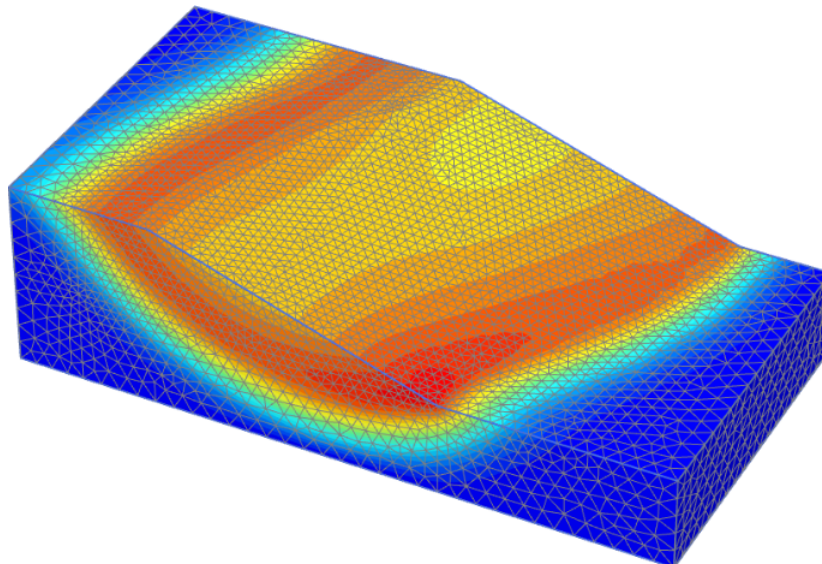


Figure E25: Incremental displacements from PLAXIS 3D for a concave slope with inclination $b = 3$, curvature angle $\alpha = 90^\circ$ and relative radius $r_l = R_l/H = 1$. No planar extension.

$r_l = 2, b=3$ & $\alpha = 90^\circ$

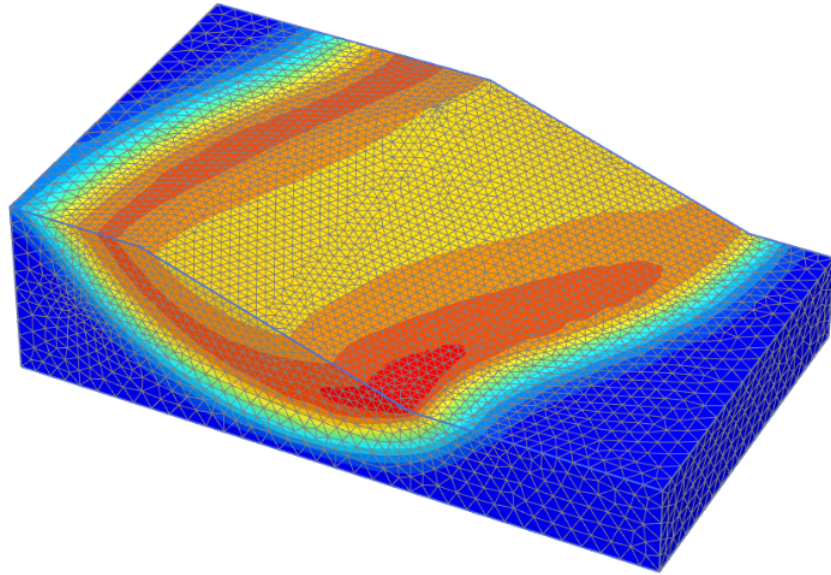


Figure E.26: Incremental displacements from PLAXIS 3D for a concave slope with inclination $b = 3$, curvature angle $\alpha = 90^\circ$ and relative radius $r_l = R_l/H = 2$. No planar extension.

$r_l = 4, b=3$ & $\alpha = 90^\circ$

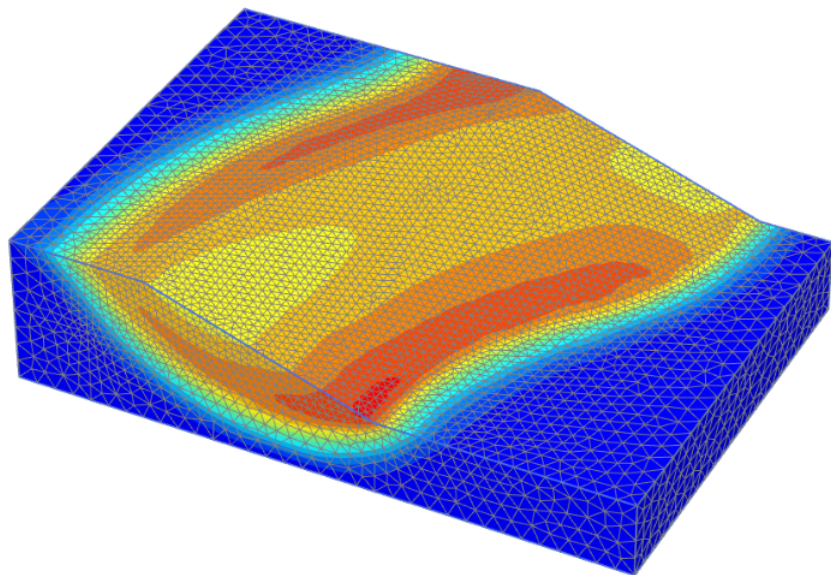


Figure E.27: Incremental displacements from PLAXIS 3D for a concave slope with inclination $b = 3$, curvature angle $\alpha = 90^\circ$ and relative radius $r_l = R_l/H = 4$. No planar extension.

$r_l = 6, b=3$ & $\alpha = 90^\circ$

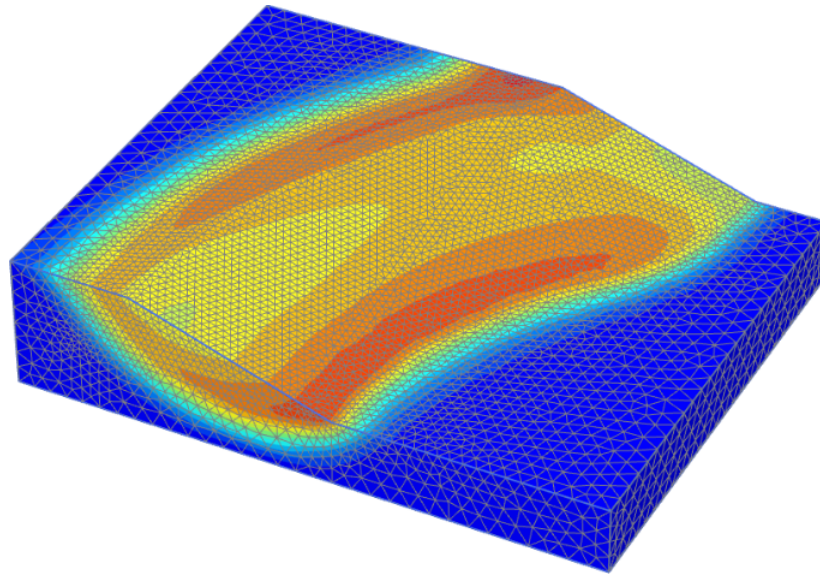


Figure E.28: Incremental displacements from PLAXIS 3D for a concave slope with inclination $b = 3$, curvature angle $\alpha = 90^\circ$ and relative radius $r_l = R_l/H = 6$. No planar extension.

$r_l = 1, b=3$ & $\alpha = 180^\circ$

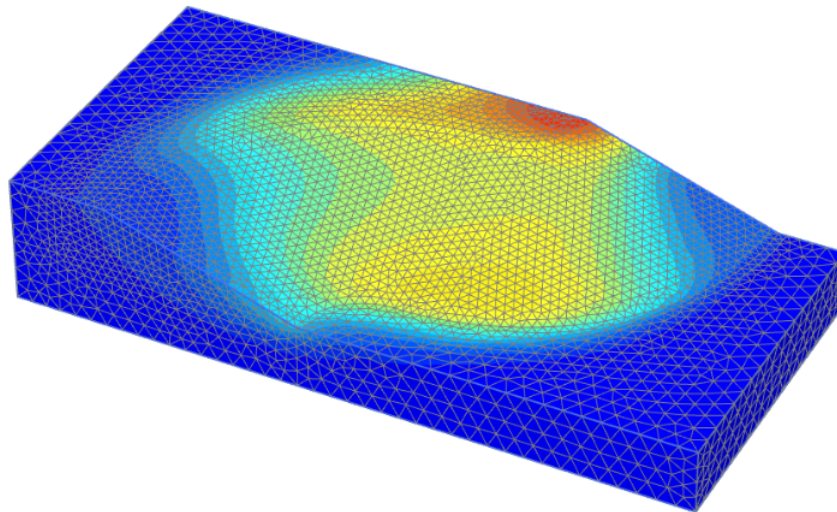


Figure E.29: Incremental displacements from PLAXIS 3D for a concave slope with inclination $b = 3$, curvature angle $\alpha = 180^\circ$ and relative radius $r_l = R_l/H = 1$. No planar extension.

$r_l = 2, b=3$ & $\alpha = 180^\circ$

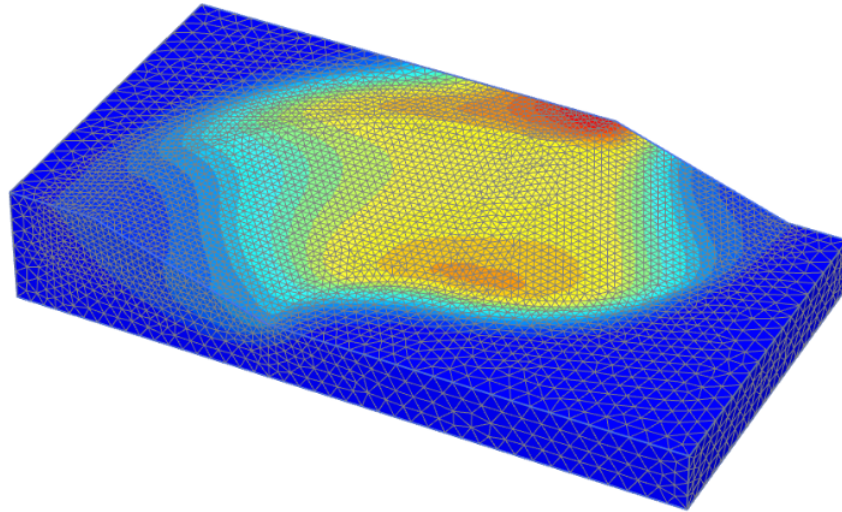


Figure E30: Incremental displacements from PLAXIS 3D for a concave slope with inclination $b = 3$, curvature angle $\alpha = 180^\circ$ and relative radius $r_l = R_l/H = 2$. No planar extension.

$r_l = 4, b=3$ & $\alpha = 180^\circ$

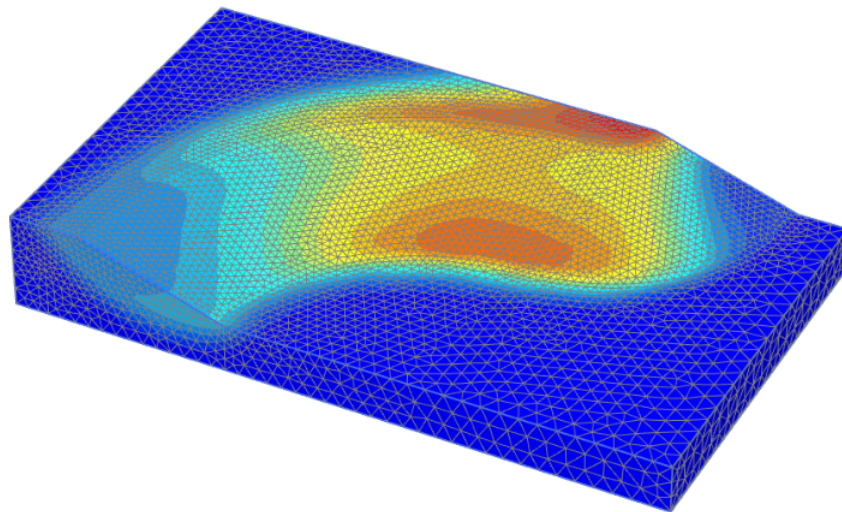


Figure E31: Incremental displacements from PLAXIS 3D for a concave slope with inclination $b = 3$, curvature angle $\alpha = 180^\circ$ and relative radius $r_l = R_l/H = 4$. No planar extension.

$r_l = 6, b=3$ & $\alpha = 180^\circ$

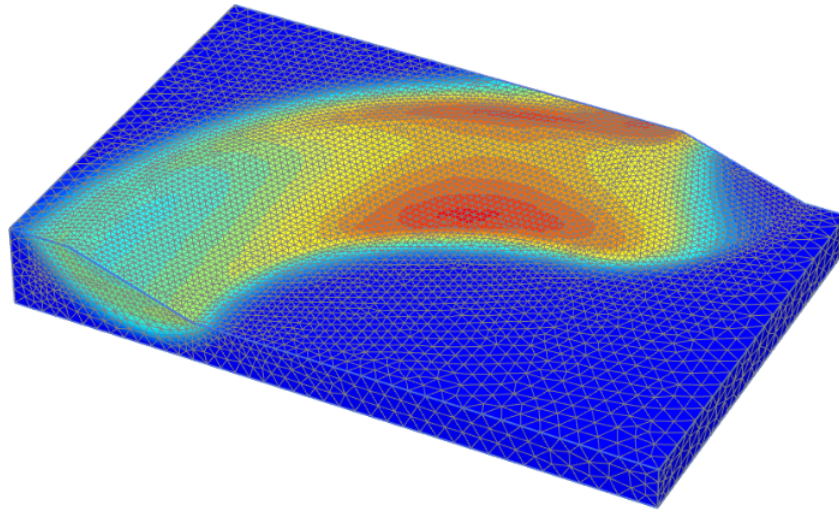


Figure E32: Incremental displacements from PLAXIS 3D for a concave slope with inclination $b = 3$, curvature angle $\alpha = 180^\circ$ and relative radius $r_l = R_l/H = 6$. No planar extension.

E5 Convex - 10 m extension

Extended - $r_u = 1, b=1.5$ & $\alpha = 90^\circ$

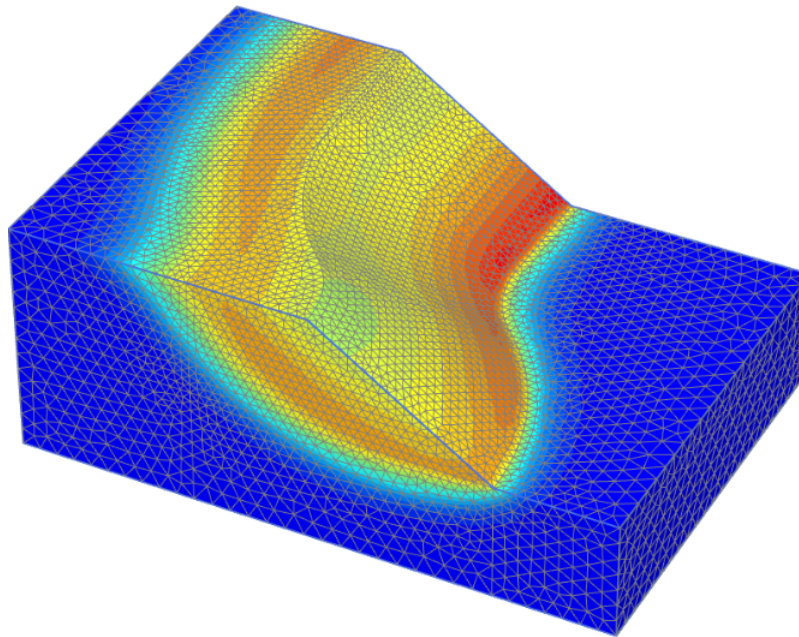


Figure E33: Incremental displacements from PLAXIS 3D for a convex slope with a 10 m planar side extension, for inclination $b = 1.5$, curvature angle $\alpha = 90^\circ$ and relative radius $r_u = R_u/H = 1$.

Extended - $r_u = 2$, $b=1.5$ & $\alpha = 90^\circ$

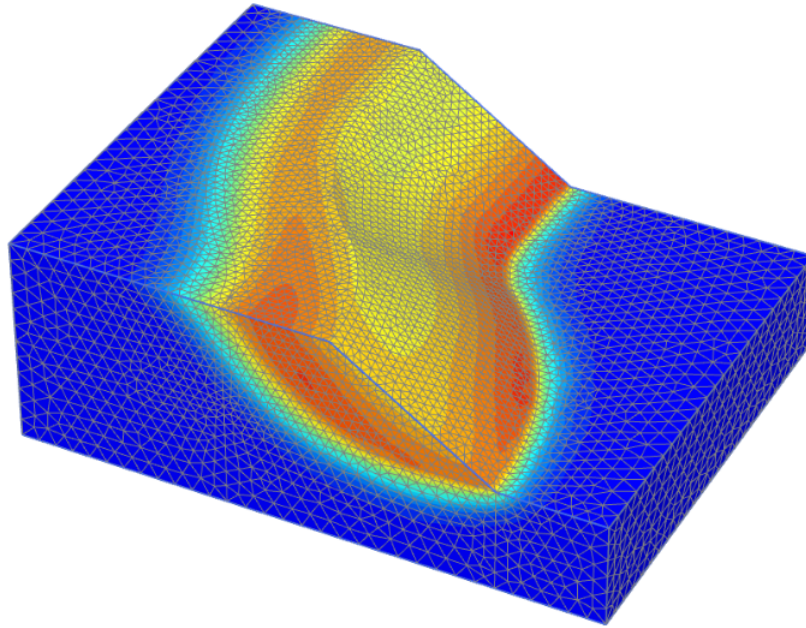


Figure E34: Incremental displacements from PLAXIS 3D for a convex slope with a 10 m planar side extension, for inclination $b = 1.5$, curvature angle $\alpha = 90^\circ$ and relative radius $r_u = R_u/H = 2$.

Extended - $r_u = 4$, $b=1.5$ & $\alpha = 90^\circ$

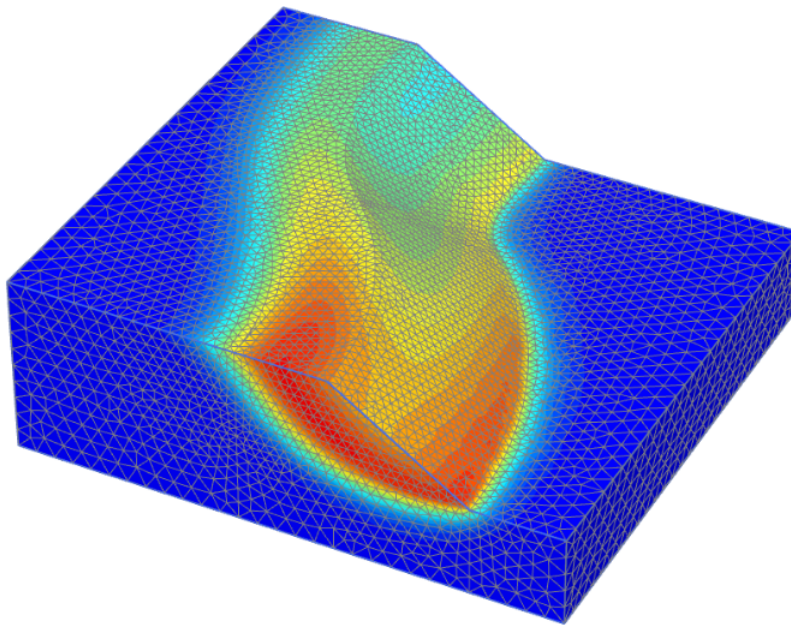


Figure E35: Incremental displacements from PLAXIS 3D for a convex slope with a 10 m planar side extension, for inclination $b = 1.5$, curvature angle $\alpha = 90^\circ$ and relative radius $r_u = R_u/H = 4$.

Extended - $r_u = 6$, $b=1.5$ & $\alpha = 90^\circ$

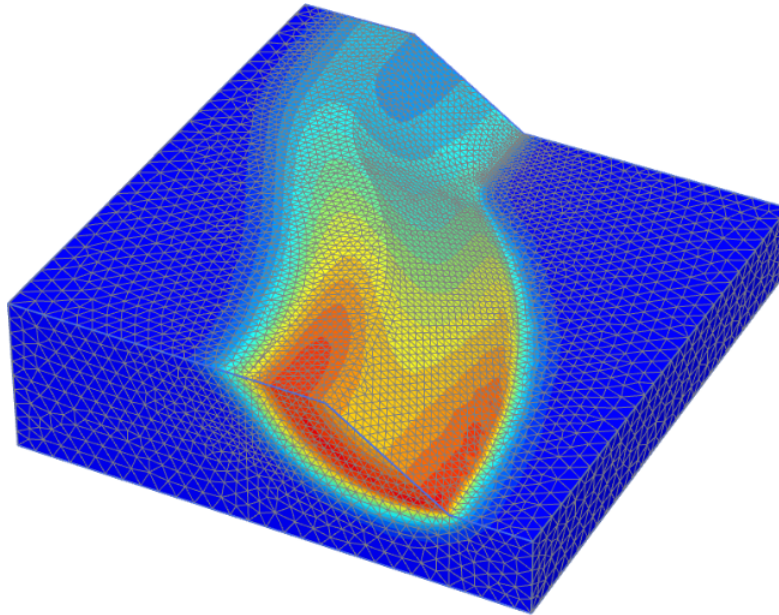


Figure E36: Incremental displacements from PLAXIS 3D for a convex slope with a 10 m planar side extension, for inclination $b = 1.5$, curvature angle $\alpha = 90^\circ$ and relative radius $r_u = R_u/H = 6$.

Extended - $r_u = 1$, $b=1.5$ & $\alpha = 180^\circ$

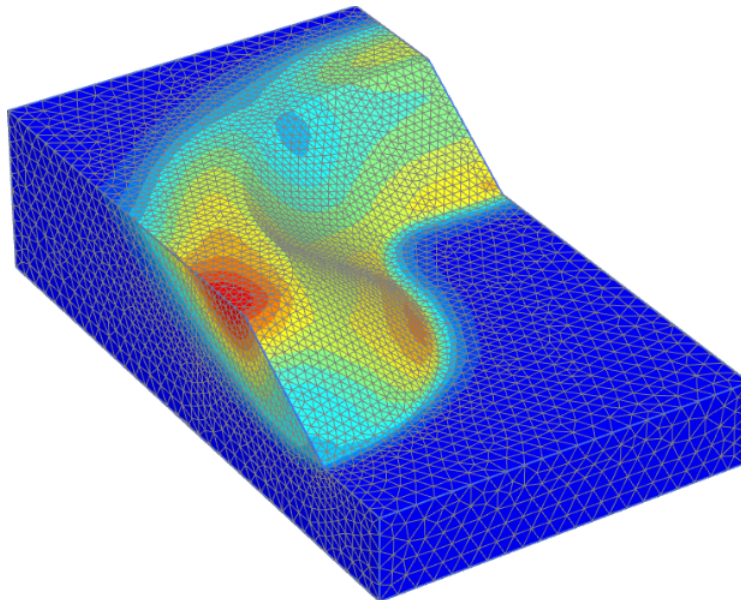


Figure E37: Incremental displacements from PLAXIS 3D for a convex slope with a 10 m planar side extension, for inclination $b = 1.5$, curvature angle $\alpha = 180^\circ$ and relative radius $r_u = R_u/H = 1$.

Extended - $r_u = 2$, $b=1.5$ & $\alpha = 180^\circ$

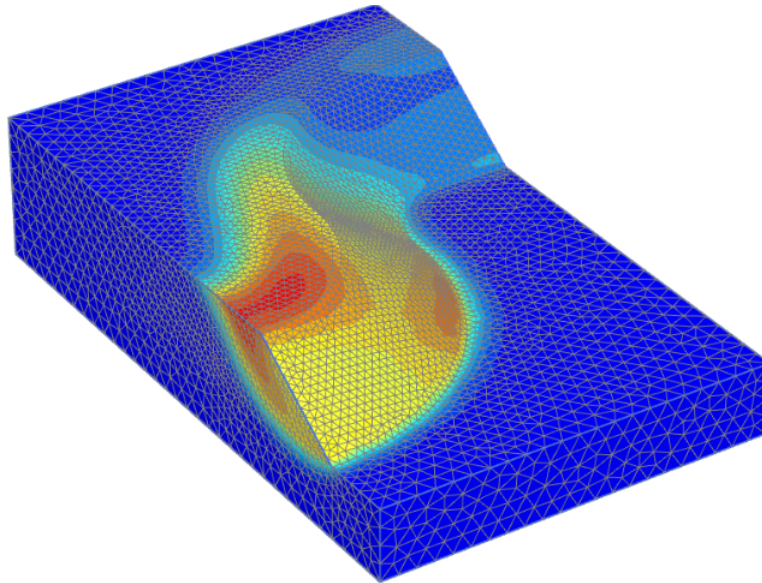


Figure E38: Incremental displacements from PLAXIS 3D for a convex slope with a 10 m planar side extension, for inclination $b = 1.5$, curvature angle $\alpha = 180^\circ$ and relative radius $r_u = R_u/H = 2$.

Extended - $r_u = 4$, $b=1.5$ & $\alpha = 180^\circ$

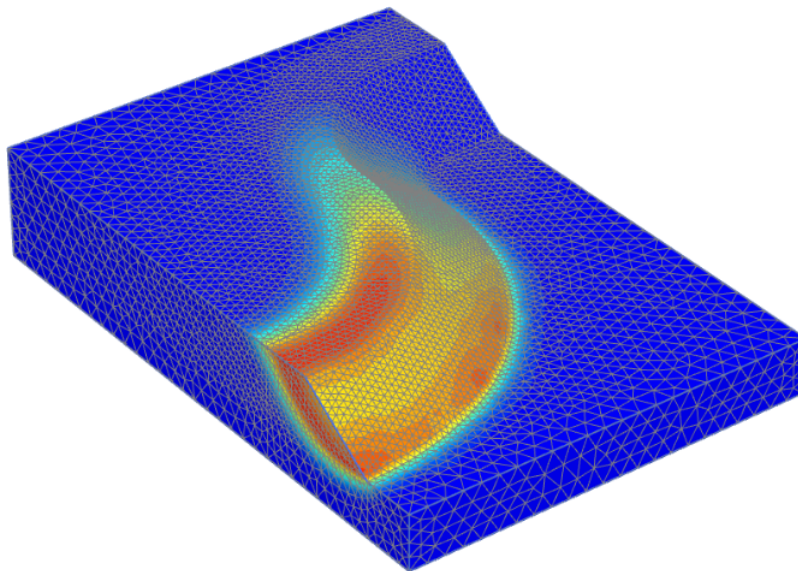


Figure E39: Incremental displacements from PLAXIS 3D for a convex slope with a 10 m planar side extension, for inclination $b = 1.5$, curvature angle $\alpha = 180^\circ$ and relative radius $r_u = R_u/H = 4$.

Extended - $r_u = 6$, $b=1.5$ & $\alpha = 180^\circ$

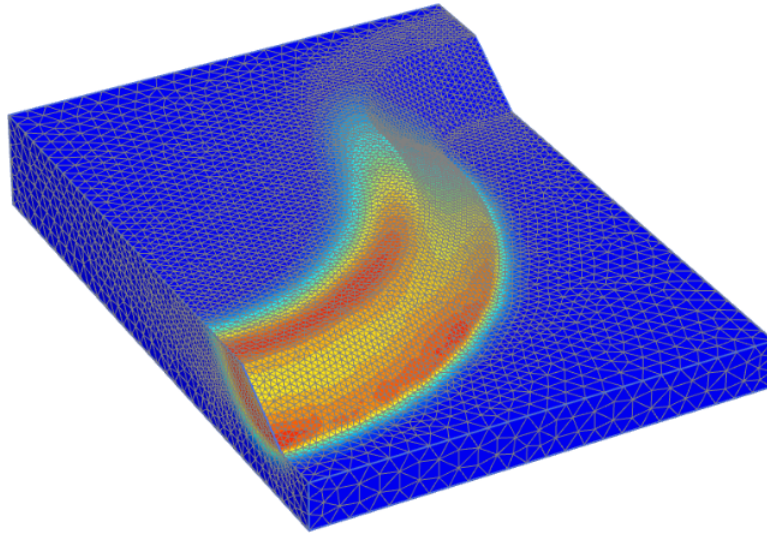


Figure E40: Incremental displacements from PLAXIS 3D for a convex slope with a 10 m planar side extension, for inclination $b = 1.5$, curvature angle $\alpha = 180^\circ$ and relative radius $r_u = R_u/H = 6$.

F6 Concave - 10 m extension

Extended - $r_l = 1$, $b=1.5$ & $\alpha = 90^\circ$

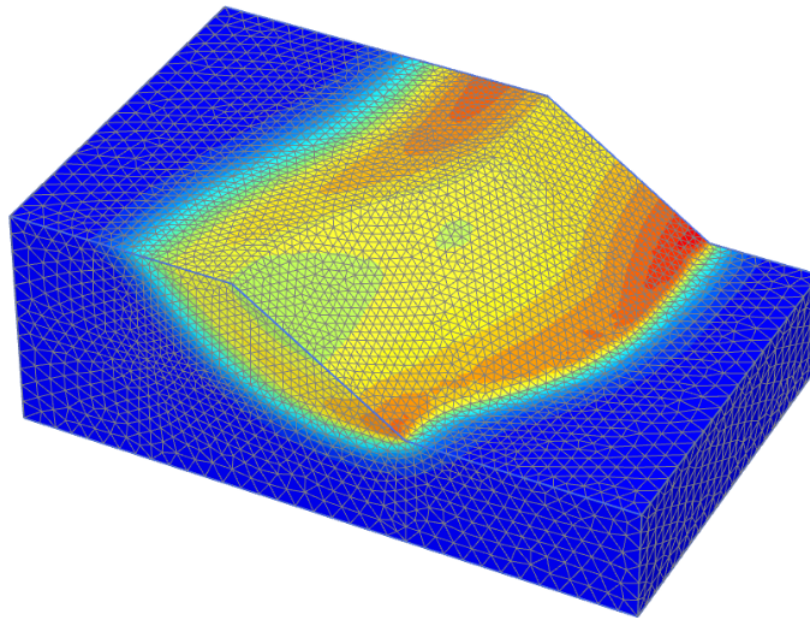


Figure E41: Incremental displacements from PLAXIS 3D for a concave slope with a 10 m planar side extension, for inclination $b = 1.5$, curvature angle $\alpha = 90^\circ$ and relative radius $r_l = R_l/H = 1$.

Extended - $r_l = 2$, $b=1.5$ & $\alpha = 90^\circ$

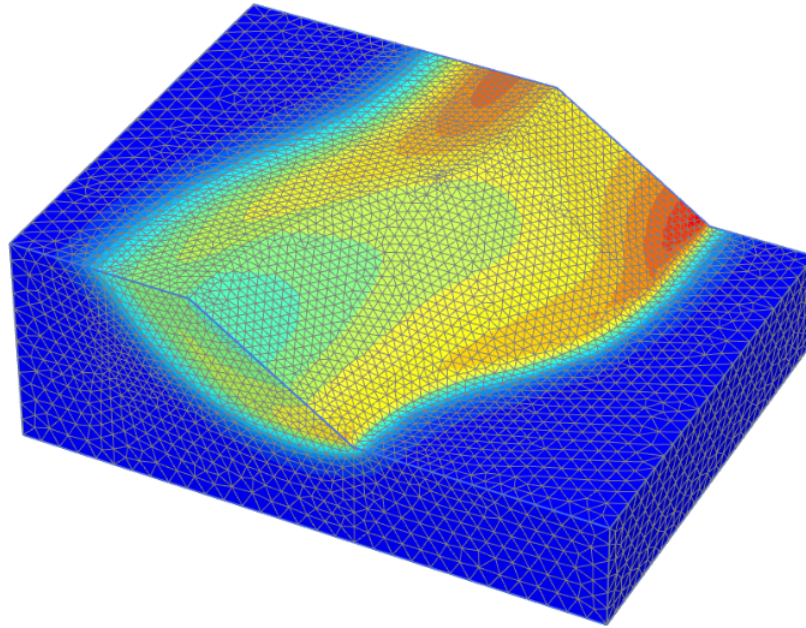


Figure E42: Incremental displacements from PLAXIS 3D for a concave slope with a 10 m planar side extension, for inclination $b = 1.5$, curvature angle $\alpha = 90^\circ$ and relative radius $r_l = R_l/H = 2$.

Extended - $r_l = 4$, $b=1.5$ & $\alpha = 90^\circ$

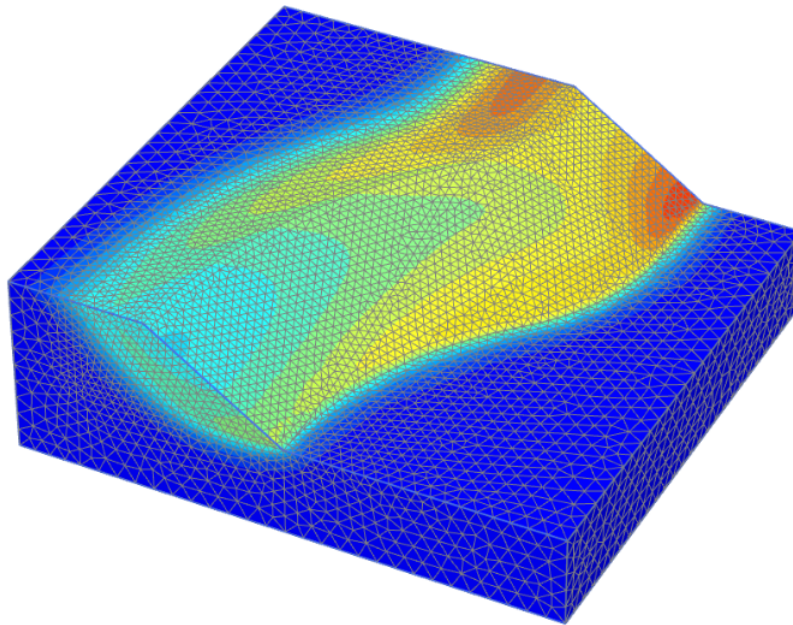


Figure E43: Incremental displacements from PLAXIS 3D for a concave slope with a 10 m planar side extension, for inclination $b = 1.5$, curvature angle $\alpha = 90^\circ$ and relative radius $r_l = R_l/H = 4$.

Extended - $r_l = 6$, $b=1.5$ & $\alpha = 90^\circ$

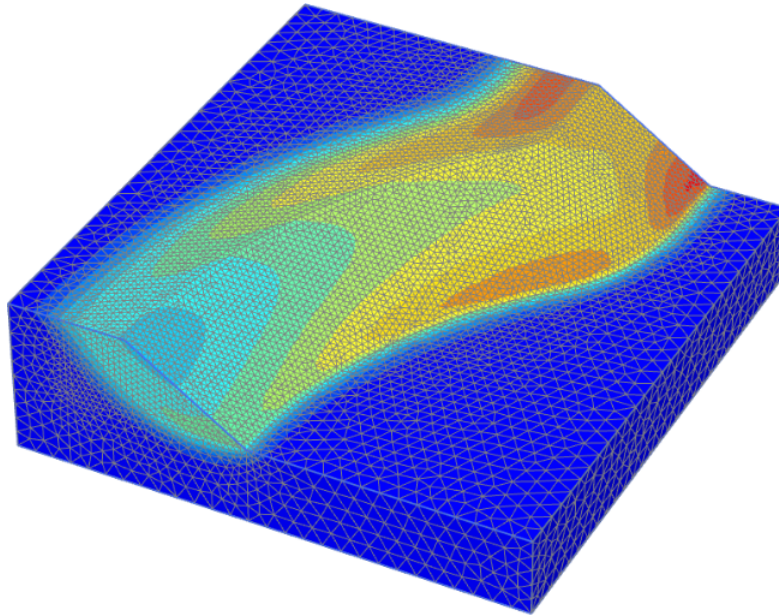


Figure F44: Incremental displacements from PLAXIS 3D for a concave slope with a 10 m planar side extension, for inclination $b = 1.5$, curvature angle $\alpha = 90^\circ$ and relative radius $r_l = R_l/H = 6$.

Extended - $r_l = 1$, $b=1.5$ & $\alpha = 180^\circ$

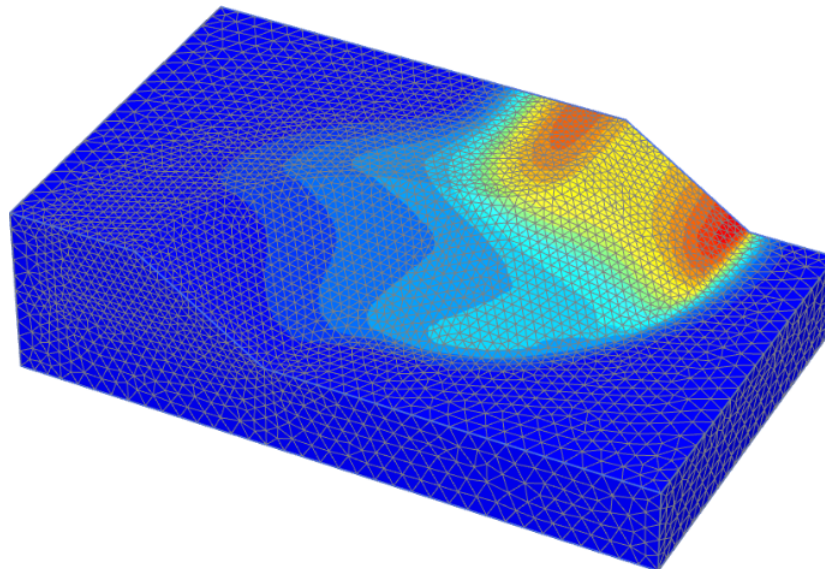


Figure F45: Incremental displacements from PLAXIS 3D for a concave slope with a 10 m planar side extension, for inclination $b = 1.5$, curvature angle $\alpha = 180^\circ$ and relative radius $r_l = R_l/H = 1$.

Extended - $r_l = 2$, $b=1.5$ & $\alpha = 180^\circ$

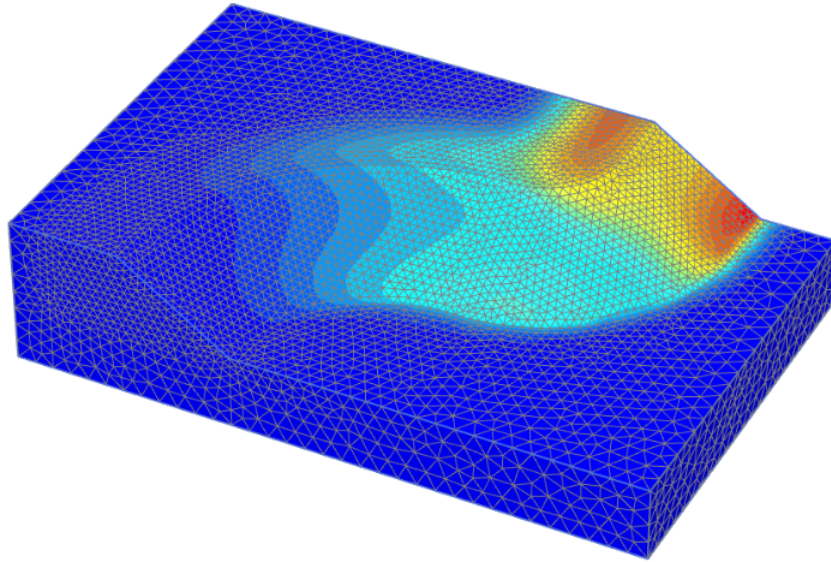


Figure E46: Incremental displacements from PLAXIS 3D for a concave slope with a 10 m planar side extension, for inclination $b = 1.5$, curvature angle $\alpha = 180^\circ$ and relative radius $r_l = R_l/H = 2$.

Extended - $r_l = 4$, $b=1.5$ & $\alpha = 180^\circ$

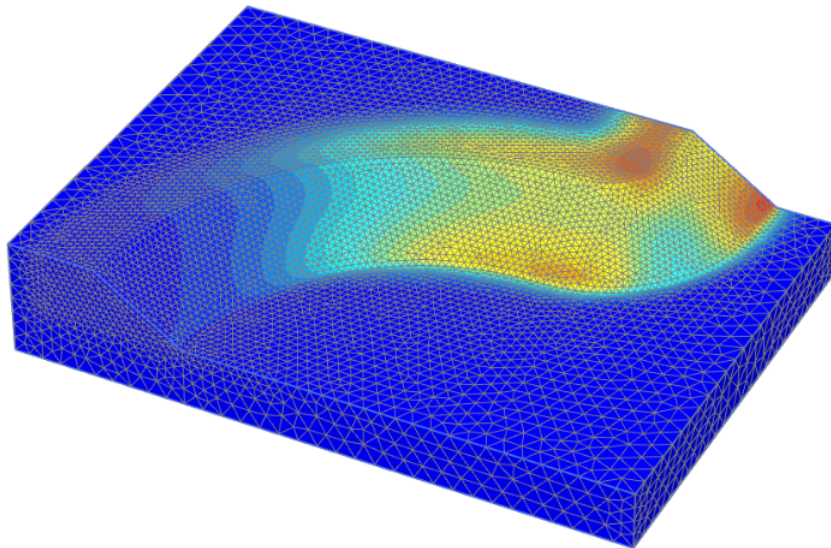


Figure E47: Incremental displacements from PLAXIS 3D for a concave slope with a 10 m planar side extension, for inclination $b = 1.5$, curvature angle $\alpha = 180^\circ$ and relative radius $r_l = R_l/H = 4$.

Extended - $r_l = 6$, $b=1.5$ & $\alpha = 180^\circ$

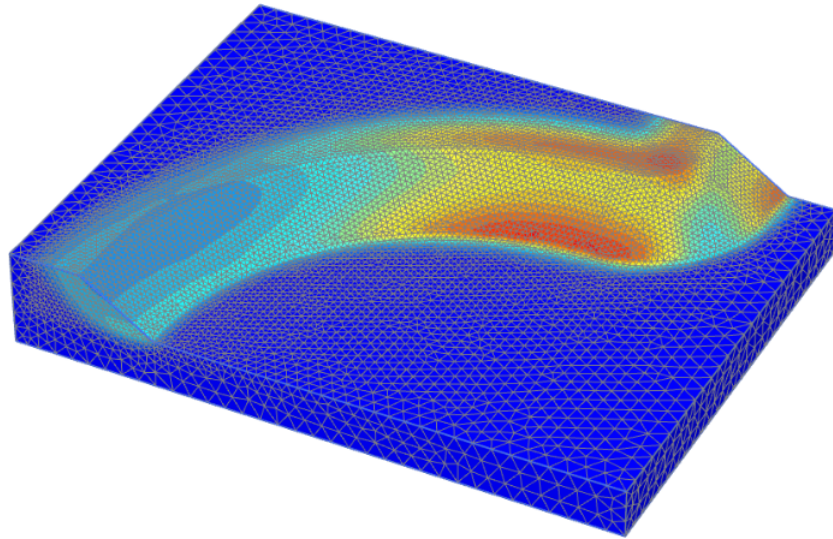


Figure F48: Incremental displacements from PLAXIS 3D for a concave slope with a 10 m planar side extension, for inclination $b = 1.5$, curvature angle $\alpha = 180^\circ$ and relative radius $r_l = R_l/H = 6$.